Advancing Neutrinoless Double Beta Decay Search with LEGEND and MONUMENT, and Exploring Passive Neutrino Detectors with PALEOCCENE

Dissertation

zur

Erlangung der naturwissenschaftlichen Doktorwürde
(Dr. sc. nat.)

vorgelegt der

Mathematisch-naturwissenschaftlichen Fakultät

der

Universität Zürich

von

Gabriela Rodrigues Araujo

aus

Brasilien

Promotionskommission

Prof. Dr. Laura Baudis (Vorsitz)

Prof. Dr. Florencia Canelli

Dr. Pin-Jung Chiu

Dr. Michelle Galloway

Zürich, 2023

ABSTRACT

Neutrino mass is the sole experimental evidence of physics beyond the Standard Model of particle physics. The quest for understanding the mechanism by which neutrinos gain mass drives the search for neutrinoless double beta ($0\nu\beta\beta$) decay, a process that would indicate a Majorana mass term as the origin for the tiny neutrino masses. The potential of $0\nu\beta\beta$ decay to distinguish between normal and inverted neutrino mass orderings further highlights its significance and emphasizes the necessity of accurately calculating the nuclear matrix elements (NMEs) necessary to translate the experimental observable of the decay half-life ($T^{0\nu}_{1/2}$) to the effective Majorana mass ($m_{\beta\beta}$).

In this context, this thesis presents advancements in $0\nu\beta\beta$-decay search with GERDA and LEGEND, alongside ordinary muon capture (OMC) measurements conducted by MONUMENT, intended to reduce uncertainties in NME calculations for $0\nu\beta\beta$ decay.

GERDA, a pioneering experiment in probing $0\nu\beta\beta$ decay of ^{76}Ge with high-purity germanium (HPGe) detectors, concluded its Phase II data taking after accumulating over 100 kg.yr of data. Operating in liquid argon (LAr), GERDA achieved the lowest background index in the field, setting stringent constraints on $T^{0\nu}_{1/2}$. In this work, the characterization of background rates during Phase II was conducted, providing essential information regarding its background uniformity.

Building upon GERDA, LEGEND-200 similarly employs arrays of HPGe detectors immersed in LAr and surrounded by an instrumentation system that collects LAr scintillation light. This LAr system proved itself very effective in vetoeing background events in GERDA, playing a major role in obtaining the remarkably low background index. To facilitate the collection and detection of scintillation light resulting from radioactive decays in LAr, wavelength shifting materials such as tetraphenyl butadiene (TPB) are employed to convert 128 nm scintillation light into visible wavelengths.

While GERDA also incorporated wavelength shifters, LEGEND-200 introduced a novel feature surrounding the HPGe detector arrays: a wavelength-shifting reflector (WLSR) composed of Tetratex® (TTX) reflective film coated with TPB. Designed with the primary goal of enhancing light collection efficiency, this WLSR contributes to improving background suppression achieved with the LAr instrumentation.

Crucial efforts in attaining this enhancement compose a central part of this work, which included the WLSR design followed by the successful coating of 13 m^2 of TTX with TPB. A sample extracted from the resulting WLSR was characterized with microscopy and in LAr. The coating demonstrated satisfactory uniformity, with an estimated quantum efficiency of approximately 85% at LAr temperatures.

For even larger surfaces, the complexity of TPB coating presents a challenge, prompting the need for scalable alternatives, such as the plastic wavelength shifter polyethylene naphthalate (PEN). This alternative is particularly relevant for the forthcoming LEGEND-1000 experiment, which aims to escalate the deployment of HPGe detectors from 200 kg (as in LEGEND-200) to 1000 kg, necessitating extensive WLSR coverage. While the optimization of PEN-based WLSR is still an ongoing effort, this work demonstrates its potential and identifies opportunities for enhancing its light yield, including the reduction of effective light absorption within the PEN-based WLSR combinations and tackling challenges posed by the installation of thin films.

Within the context of the MONUMENT experiment, OMC was measured in ^{76}Se and ^{136}Ba, with the goal of providing OMC rates for refining the calculations of NMEs associated with the $0\nu\beta\beta$ decay of ^{76}Ge and ^{136}Xe – the leading isotopes in the field. This work primarily focused on analyzing OMC in ^{136}Ba, identifying over one hundred γ and x-ray emission lines in the measured energy spectrum, thereby laying the foundation for obtaining the OMC rates required to refine the relevant NME calculations.

Beyond the scope of $0\nu\beta\beta$ decay research, this thesis explored the potential of crystals read out by light-sheet fluorescence microscopy (LSFM) as passive particle detectors. This work was performed in the context of PALEOCCENE, which is based on the utilization of color centers (CC) as potential indicators of nuclear recoils induced by dark matter and coherent elastic neutrino-nucleus scattering (CEvNS). This thesis presents the first measurements utilizing state-of-the-art LSFM microscopes to read out radiation-induced CCs in transparent crystals, demonstrating the feasibility of CC imaging with LSFM, a pivotal component of the PALEOCCENE concept.

PREFACE

This thesis consists of five parts, all dedicated to exploring neutrino properties via $0\nu\beta\beta$ decay or their direct detection via coherent elastic scattering with nuclei. The thesis discusses many experiments dedicated to these two topics, namely GERDA, LEGEND, MONUMENT, and PALEOCCENE, all of which I have actively participated in during my PhD journey.

Part I (Chapters 1 to 3) introduces the theory and current experimental status of the search for $0\nu\beta\beta$ decay. It highlights the elusiveness of this decay and the role of effective background suppression, which is a key focus of this work. Additionally, Part I discusses the uncertainties in nuclear matrix elements for $0\nu\beta\beta$ decay and provides the theoretical foundations for measurements aimed at refining the calculations of these elements, which are the focus of MONUMENT.

Part II (Chapters 4 to 6) focuses on experimental aspects relevant to GERDA and LEGEND, along with overall considerations affecting the data from all discussed experiments. Chapter 4 examines sources of background. Chapter 5 describes the properties of liquid argon (LAr) and the use of wavelength shifters to facilitate the detection of its scintillation light. Chapter 6 provides an overview of high-purity germanium (HPGe) detectors, which are employed not only in GERDA and LEGEND but also in MONUMENT and in the γ spectrometry facility Gator used for radiopurity assays. This chapter covers the experimental approach common for both GERDA and LEGEND, including the background suppression performed through the LAr instrumentation.

Part III (Chapters 7 to 11) is dedicated to the search for $0\nu\beta\beta$ decay with GERDA and LEGEND. These chapters are presented in an chronological order, corresponding to the transition from GERDA to LEGEND and my related contributions. At the time GERDA resumed data-taking, by the end of 2019, I became a collaboration member and contributed to the characterization of GERDA's legacy data. Chapter 7 details my specific contributions and presents the results obtained from this data, including the (by then) record-setting lower limit on the half-life of $0\nu\beta\beta$ decay and the remarkably low background index achieved. These results were published in *Phys. Rev. Lett.* 125(25), 2020 [1].

During the same period, I joined the R&D work for LEGEND, which was entering its construction phase. My focus for LEGEND was on improving background suppression achieved through the LAr instrumentation, by introducing wavelength-shifting reflectors (WLSR). This work, spanning Chapters 8 to 11, was carried out during the entire duration of my PhD.

Chapter 8 provides an overview of LEGEND and the principle behind the WLSR. Chapter 9 details the R&D of the WLSR for LEGEND-200, including the radiopurity assay of materials using Gator. The analyses, simulations, and the updated baseline analysis methods I conducted or developed for

samples measured with Gator are summarized in Appendix A, in addition to a publication in the *J. Inst.* 17(08), 2022 [2].

Chapter 10 focuses on the in-situ evaporation for the LEGEND-200 WLSR, detailing my contributions in the R&D and construction of the evaporation system. I carried out the described work in collaboration with the electronic and mechanical workshops, and assistance from Yannick Müller.

Chapter 11 describes the characterization of the in-situ evaporated WLSR, along with a subsequent campaign dedicated to the R&D of WLSR for LEGEND-1000. During the LAr measurements of the first campaign, I collaborated with MSc student Vera Wu, where I played the role of planning the measurements, conducting simulations, assisting with experimental setup operation, supervising her work, and performing analysis cross-checks. Vera Wu conducted the primary analysis of the LAr data, which is part of her MSc thesis [3] and is not covered in this thesis. Instead, I describe the data analysis I performed for the second campaign. This campaign involved the collaboration of Dr. Pin-Jung Chiu and PhD students from other institutions, who, alongside me, assembled and operated the setup.

The results obtained from the measurements and simulations of the first campaign were published in the *Eur. Phys. J. C* 82(5), 2022 [4]. As the first author of that publication, certain sections of the text I authored for the paper are reproduced in Chapters 9 and 11.

Part IV (Chapter 12) shifts the focus to the study of ordinary muon capture (OMC) with MONUMENT. In this chapter, I describe the experimental setup and the data analysis I performed, focusing on the identification of γ and x-ray lines following OMC in ^{136}Ba. This work represents the first steps towards obtaining partial and total OMC rates that can serve as inputs in the calculation of NMEs for the $0\nu\beta\beta$ decay of ^{136}Xe.

Part V (Chapter 13) describes PALEOCCENE, which focuses on nuclear reactor neutrino detection rather than the search for 'neutrinoless' processes. Although distinct from the $0\nu\beta\beta$ research, this project shares a common thread with the investigation of fluorescence in wavelength shifters, as fluorescence is the signal observed from passive PALEOCCENE detectors. This chapter stands as self-contained, including introduction, results, and conclusion. Certain sections of this text resemble my contributions to [5], published in *Phys. of the Dark Univ.* 41, 2023, and to [6] submitted to *Nat. Comm*. The latter involved collaboration with MSc student Valentino Aerne, where I took charge of planning and executing the measurements while supervising his data analysis. The results from his analysis are part of his MSc thesis and are not covered within this thesis.

The concluding Chapter 14 summarizes the work presented throughout this thesis. Unless specified, all plots and schematics are authored by me.

CONTENTS

ABBREVIATIONS LIST

$m_{\beta\beta}$	effective Majorana mass
$T^{0\nu}_{1/2}$	$0\nu\beta\beta$-decay half-life
$2\nu\beta\beta$	double beta decay
$0\nu\beta\beta$	neutrinoless double beta decay
BEGe	broad energy germanium detector
BI	background index
BSM	beyond Standard Model
CC	color centers
CEvNS	coherent elastic neutrino-nucleus scattering
CL	confidence level
Coax	coaxial germanium detector
DAQ	data acquisition
ESR	enhanced specular reflector
FEP	full-energy peak
FWHM	full width at half maximum
HPGe	high-purity germanium
HS	hand sanded
IBD	inverse beta decay
IC	inverted coaxial germanium detector
ICPMS	inductively coupled plasma mass spectrometry
IO	inverted ordering
IS	integrating sphere
ISM	interacting shell model
KL2Z	KamLAND2-Zen
KLZ-800	KamLAND-Zen-800
LAr	liquid argon
LN2	liquid nitrogen
LNGS	Laboratori Nazionali del Gran Sasso
LOI	line of interest
LSFM	light-sheet fluorescence microscopy

LY	light yield
MS	machine sanded
NMEs	nuclear matrix elements
NO	normal ordering
OMC	ordinary muon capture
PE	number of photoelectrons
PEN	polyethylene naphthalate
PMT	photomultiplier tube
PSD	pulse shape discrimination
PSI	Paul Scherrer Institut
QE	quantum efficiency
QRPA	quasiparticle random-phase approximation
RGA	residual gas analyzer
ROI	region of interest
RT	room temperature
SEM	scanning electron microscopy
SIS	source insertion system
SM	Standard Model of particle physics
SMP	shape memory polymer
sPE	single photoelectrons
SPIM	selective plane illumination microscopy
SY	scintillation yield
TPB	tetraphenyl butadiene
TTX	Tetratex®
TUM	Technical University of Munich
UV	ultraviolet
UZH	University of Zurich
vis	visible ($\sim$ at WLS emission) wavelengths
VUV	vacuum ultraviolet
WIMP	weakly interacting massive particle
WLS	wavelength shifter
WLSR	wavelength-shifting reflector

PART I

THEORY & EXPERIMENTAL STATUS

"About 100 billion neutrinos pass through an average fingernail every second. They pass through the Earth as if it weren't there, and the atoms in the human body capture a neutrino about every seventy years, or once in a lifetime. As we will see, neutrinos captured me early in my career."

– A quote by Raymond Davis, extracted from his Nobel lecture [7].

1

NEUTRINOS & PHYSICS BEYOND THE STANDARD MODEL OF PARTICLE PHYSICS

1.1 BRIEF HISTORICAL OVERVIEW

Neutrinos have been at the center of numerous enigmas in particle physics. The postulation of neutrinos by Pauli in 1930 came as a "desperate remedy to save the law of energy conservation" [8]. Addressing his fellow physicists at a conference, whom he humorously referred to as "radioactive ladies and gentlemen", he explained that the emission of a neutral light particle along with the electron in a nuclear beta decay could solve the long-standing problem of the continuous energy spectrum of the electron. While the summed energy from the electron and neutral particle remains constant (the Q-value of the decay), the charge-neutral particle could carry momentum, causing the broad energy spectrum of the electron. This particle was later named 'neutrino' by E. Fermi, who also provided the theoretical framework for beta decay processes [9].

The proof neutrinos existed only came a few decades later, in 1956, when Reines and Cowan detected antineutrinos from a nuclear reactor at Savannah River [10]. Ten years later, neutrinos were part of yet another conundrum: the solar electron neutrino flux measured by Raymond Davis and collaborators at the Homestake mine did not agree with predictions by the standard solar model. The measured flux was only a third of the predicted value: either the solar model was wrong, or neutrinos could change their flavor via oscillations [11]. This flavor oscillation had been theorized by Pontecorvo years before [12–14] and implies that neutrinos have mass.

The oscillation hypothesis was however difficult to test and the final proof took decades to come. Probing neutrinos is challenging because of their 'difficult-to-catch' nature: neutrinos have no electric charge, and do not participate in strong interaction. They only interact (and can thus be detected) via gravity or weak interaction. The proof that neutrinos oscillate was achieved around the turn of the millennium when the Super-Kamiokande and the SNO experiments measured oscillations from atmospheric and solar neutrinos [15, 16]. The confirmation of neutrino mass led to another puzzle: the Standard Model (SM) of particle physics lacked a compelling mechanism for generating their mass. In this chapter, we discuss the current status of the SM, the unsolved riddle of neutrino mass, and its solution in the case neutrinos have a Majorana mass component. We will also discuss the relation of these subjects to the matter-antimatter asymmetry of the universe.

When Pauli proposed the existence of neutrinos, he initially dubbed them 'neutrons', given that neutral nucleons – the actual neutrons – had not been discovered at the time. This changed in the 1930s: when the palette of known particles expanded to include neutrons, positrons, and muons. While positrons had been predicted by Dirac's wave equation in the late 1920s, the first observation of muons was unexpected, prompting the question "Who ordered that?" [17].

As more particles were discovered, a theoretical framework was needed to understand the growing 'zoo' of particles. This led to the development of the Standard Model (SM) of particle physics, a theory of particles and fields, which describes three out of the known four forces and classifies the most elementary particles as depicted in Figure 1.1.

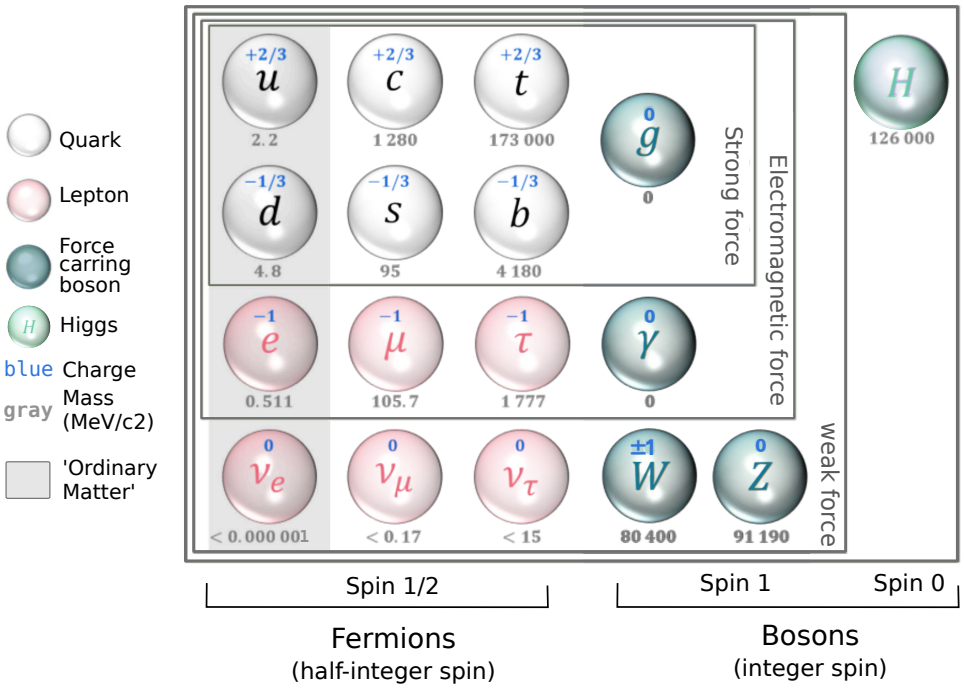

Figure 1.1: Elementary particles of the SM. Adapted from [18].

In the SM, spin 1/2 particles are classified into quarks and leptons of three generations. The first generation of these particles corresponds to what we call 'ordinary matter', given that they make up matter which is stable. Bosons with spin 1 are the carriers of the forces that act upon fermions (particles with half-integer spins). The SM includes the strong force (mediated by massless gluons), the electromagnetic force (mediated by massless photons), and the weak force, mediated by the massive W and Z bosons[1]. Only the W bosons have electric charge. The Higgs boson has neither charge nor color. Particles however interact with it via the Higgs field.

1 The SM does not include gravity.

The interaction with the Higgs field is precisely what gives particles[2] their mass, according to the SM, as depicted in Figure 1.2. The absolute mass value is proportional to the coupling strength, and particles that do not interact with the Higgs field have no mass as a result. This is the case for photons and gluons. The neutrino case is yet unsolved: while the SM initially did not predict the interaction of neutrinos with the Higgs field, neutrinos were proved to have tiny masses [8, 16, 19]. These masses are much lower than the MeV to TeV mass scale of most elementary particles, as shown in Figure 1.2 (d).

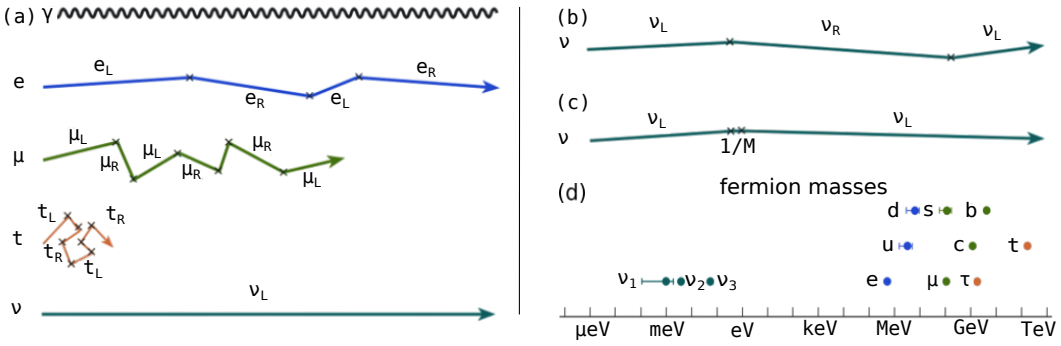

Figure 1.2: Schematic of particles in vacuum, interacting (or not) with the Higgs boson and acquiring mass (or not) as a result. The handedness of the particles changes after the interaction. In (a), the SM picture is shown: neutrinos are always left-handed and do not have mass. In (b) and (c), extensions of the SM are shown, where neutrinos have a Dirac or a Majorana nature. In (d), the scale of neutrino mass is shown compared to the masses of other elementary particles. Figures modified from [8].

The smallness of these masses is the reason why the SM falls short in generating neutrino masses: an unnaturally weak coupling to the Higgs field would be required to result in very light neutrinos. To address this neutrino mass issue, beyond Standard Model (BSM) theories have been proposed. Some of them are discussed in the next section.

1.3 NEUTRINO MASS: DIRAC VS. MAJORANA

Theories and mechanisms to generate neutrino mass are BSM physics [19]. In this section, we discuss two possible mass generation frameworks: i) neutrinos are Dirac fermions and acquire mass similarly to other SM particles; ii) neutrinos are their own anti-particle[3] and their mass is explained via the see-saw mechanism, which arises with the incorporation of a Majorana mass term [20]. Both cases introduce a right-handed neutrino, and in either theory, the concept of handedness (or helicity) plays a key role.

2 As well as antiparticles, which are also included in the SM.

3 This means that their current classification and detection as particles (ν) and antiparticles ($\bar{\nu}$) simply correspond to different helicity states.

Helicity is related to the projection of the spin vector on the direction of the particle's motion: particles with positive (negative) helicity are right-handed (left-handed). For massless particles, helicity is equivalent to chirality, an intrinsic (Lorentz invariant) property of particles that is related to the weak charge [21, 22]. Only left-handed particles participate in the weak interaction, which is chiral (not symmetric under parity transformation), as demonstrated by Wu's experiment in 1957[4] [24].

For massive particles, helicity is not an intrinsic particle property: it depends on the frame of reference. In the SM, massive particles acquire their mass via interactions with the Higgs field and have their helicity changed as a result (as shown in Figure 1.2). The interaction of fermions with the Higgs scalar doublet Φ is given via the Yukawa coupling Y^l of the left and right-handed fermion components (L_L and E_R) with Φ:

$$-\mathcal{L}_{\text{Yukawa,lep}} = Y^{\ell} \bar{L}_L^{\ell} \phi E_R^{\ell} + h.c., \tag{1.1}$$

where $\bar{L}_L$ is the left-handed lepton doublet, E_R is the right-handed lepton field (a singlet), and ℓ corresponds to the lepton flavor (e, μ, τ) [19]. The particle masses result from spontaneous electroweak symmetry breaking and are proportional to the coupling strength and the vacuum expectation value of the Higgs field (v):

$$m^{\ell} = Y^{\ell} \frac{v}{\sqrt{2}}. \tag{1.2}$$

While no right-handed field of neutrinos is included in the SM, one can incorporate the component ν_R in addition to the left-handed ν_L [8, 19, 20]. The handedness change after the interaction with the Higgs field is exemplified in Figure 1.2 (b), and the resulting Dirac mass (m_D) is obtained analogously to Equation 1.1 and Equation 1.2:

$$-\mathcal{L}_{\text{D}} = m_D \bar{\nu}_L \nu_R + h.c., \tag{1.3}$$

$$m_D = Y^{\nu} \frac{v}{\sqrt{2}}. \tag{1.4}$$

Obtaining the observed tiny masses via this mechanism however requires unnaturally small coupling strengths. The Majorana hypothesis can solve this problem. In this case, we can apply a charge conjugation operation to ν_L. The resulting field, ν_L^C, takes the place of the right-handed component, leading to the left-handed Majorana mass term [20, 25]:

$$-\mathcal{L}_{\text{M}'} = \frac{1}{2} m' \bar{\nu}_L \nu_L^C + h.c. \tag{1.5}$$

A Majorana mass term and the assumption of particle-anti-particle equivalence, can only be applied to neutrinos, as they do not have electric charge.

4 and further confirmed by the Goldhaber's experiment, which showed that neutrinos are left-handed [23].

While a left-handed Majorana mass term does not require adding right-handed fields, it violates gauge invariance [25, 26]. But once the right-handed singlet has been introduced (Equation 1.3), we can preserve gauge invariance without further compromise. We then obtain a general neutrino mass with both Dirac and Majorana contributions [20, 25, 26]:

$$-\mathcal{L}_{\text{M+D}} = \frac{1}{2} m' \bar{\nu}_L \nu_L^C + m_D \bar{\nu}_L \nu_R + \frac{1}{2} M \bar{\nu}_R^C \nu_R + h.c.$$

$$= \frac{1}{2} \overline{n_L} \mathcal{M}_{\text{M+D}} n_L^c + \text{ h.c.} \tag{1.6}$$

$$with \;\; \mathcal{M}_{\text{M+D}} = \begin{pmatrix} m' & m_D \\ m_D & M \end{pmatrix}, \; n_L = \begin{pmatrix} \nu_L \\ \nu_R^c \end{pmatrix}, \;\; and \;\; m' = 0, \tag{1.7}$$

where the gauge invariance is preserved by setting m' to zero. The Majorana mass term leads to the Majorana mass M, which can take large values, as it is not constrained by interactions with the Higgs field [8]. In this scenario, neutrinos interact with the Higgs field as shown in Figure 1.2 (c): first, a Dirac mass is generated via interactions with the Higgs field; then, a heavy neutrino partner is created for a very brief time, suppressed by the large M [8]. This results in the see-saw mechanism: the mass of neutrinos observed over time is so small due to the heavy mass of the right-handed neutrino[5] [8]. In this case, the Yukawa coupling strength is similar to those from other fermions, and the masses of the 'light' and 'heavy' Majorana neutrinos are [25]:

$$m_{light} \approx \frac{m_D^2}{M}, \;\; m_{heavy} \approx M, \;\; and \;\; m_D \ll M, \tag{1.8}$$

where M is $\mathcal{O}(10^{14}\,\text{GeV})$ so that m_{light} results in sub-eV masses, considering m_D of the order of the electroweak scale (100 GeV) [28]. The heavy neutrino partner is dubbed sterile as it does not interact via the weak force. Its lack of interaction would explain why right-handed neutrinos were not observed so far. Furthermore, the right-handed Majorana mass term allows for $\nu \leftrightarrow \bar{\nu}$ mixing, which violates lepton-number [20, 25]. This could possibly explain the asymmetry between matter and antimatter in the universe, which is discussed in the next section.

5 There are many types of see-saw mechanisms. The one described here, and discussed throughout this thesis, is called 'type-I' [25, 27].

"Do we all descend from neutrinos?" [27]

1.4 MATTER-ANTIMATTER ASYMMETRY IN THE UNIVERSE

It is believed that equal amounts of matter and antimatter originated in the Big Bang. According to the current understanding of symmetries in the SM, particle creation and annihilation would naturally occur in a balanced manner [28]. However, the Universe is matter dominated. As such, there should be a BSM mechanism that produces more matter than antimatter. A lepton-number (L) violating process, such as the Majorana mass of neutrinos, could be the key to solving this problem.

The understanding of particle interactions is strongly based on symmetries. Although L is an accidental symmetry in the SM[6] [29], no process has ever been observed to violate it: the difference in the number of leptons in elementary particle reactions has never deviated from zero ($\Delta L = 0$) [27].

By searching for symmetry-breaking processes, scientists have been trying to understand the genesis of the surplus of baryonic matter. Three essential processes are required to account for it: i) violation of baryon (B) number; ii) violations of charge symmetry and charge-parity (CP) symmetry; iii) interactions out of thermal equilibrium.

Although not explicitly included in the *Sakharov conditions* mentioned above, L-violation could induce B-violation via leptogenesis, provided that CP-violation and out-of-equilibrium reactions are also present, as outlined above [29]. Specifically, lepton asymmetries originating from the potential decay of heavy neutrinos involving CP-violating phases in the early universe could transmute into baryon asymmetry via sphaleron processes [28].

A crucial element in leptogenesis is L-violation. In the specific above-mentioned scenario, the existence of heavy neutrinos would further provide a candidate for a decay that could have occurred out of equilibrium (since at a certain point, the inverse decay process becomes energetically forbidden).

Testing the conservation of L would thus provide an answer whether this is a fundamental symmetry of nature. The most sensitive probe of L-violation, which simultaneously hints at the existence of heavy right-handed neutrinos, is $0\nu\beta\beta$ decay [29].

Hence, a central objective of investigating $0\nu\beta\beta$ decay is to provide insights into whether Majorana neutrinos could explain the matter excess in the universe. That is, "Could neutrinos be the underlying reason for the presence of matter in the universe?" Another way to frame this question is: "Do we trace our origins back to neutrinos?". A profound question comparable to the well-known "Are we all stardust?" [27]. Shedding light on this open problem through the search for the 'matter-creating' process of $0\nu\beta\beta$ decay is an active area of research in elementary physics [30] and one of the main focuses of this thesis.

6 This also applies to baryon number, but both can be violated at the perturbative level, with only $B - L$ being conserved in the SM [29].

2

NEUTRINOLESS DOUBLE BETA ($0\nu\beta\beta$) DECAY

A $0\nu\beta\beta$ decay is a process that could occur in double-beta ($2\nu\beta\beta$) decay isotopes if neutrinos are Majorana particles. In this case, the number of antineutrinos emitted in a double beta decay has a certain probability of being zero. The amplitude of this probability is related to that of the 'helicity flip' of the Majorana neutrinos involved in the process. This can be seen as a $\bar{\nu} \leftrightarrow \nu$ mixing, which leads to the neutrino exchange schematically shown in Figure 2.1. No antineutrinos are emitted as a result, and L-violation occurs:

$$2\nu\beta\beta : (A, Z) \rightarrow (A, Z+2) + 2e^- + 2\bar{\nu}_e, \qquad \Delta L = 0$$

$$0\nu\beta\beta : (A, Z) \rightarrow (A, Z+2) + 2e^-, \qquad \Delta L = +2. \tag{2.1}$$

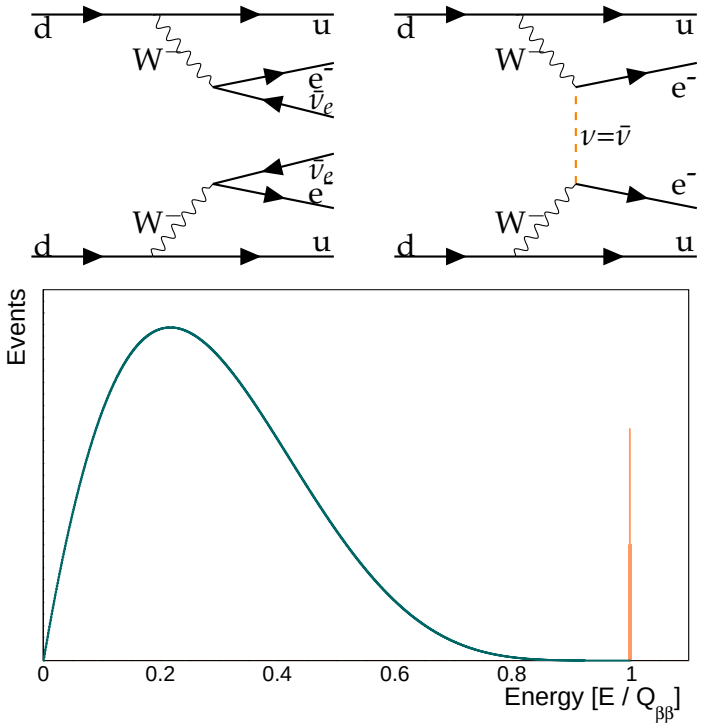

Figure 2.1: Top: Feynman Diagrams of $2\nu\beta\beta$ and $0\nu\beta\beta$ decays, based on [29, 31]. In $2\nu\beta\beta$, two neutrons in a nucleus decay into two protons, two antineutrinos, and two electrons. In $0\nu\beta\beta$, virtual light ($\lesssim$10 MeV) Majorana neutrinos are exchanged[1], resulting in no neutrino emission. Bottom: Continuous energy spectrum of the two electrons emitted in a $2\nu\beta\beta$ decay, where electrons share the energy with neutrinos, and the hypothetical $0\nu\beta\beta$-decay peak at the Q-value, for an energy resolution (σ/E) of 0.2% at $Q_{\beta\beta}$. The calculation for the continuous spectrum is based on [31].

The electrons emitted in the $0\nu\beta\beta$ decay take the full energy of the decay and produce a peak at $Q_{\beta\beta}$, the endpoint of the $2\nu\beta\beta$-decay spectrum, as shown in Figure 2.1. Besides shedding light on the origin of the matter-antimatter asymmetry of the universe, an observation of $0\nu\beta\beta$ decay could serve as a measure of the neutrino absolute mass scale, since its effective Majorana mass ($m_{\beta\beta}$) is related to the neutrino mass eigenstates[2] m_i [27]:

$$m_{\beta\beta} = \left| \sum_{i=1,2,3} \left| U_{ei}^2 \right| e^{i\alpha_i} m_i \right|, \tag{2.2}$$

where U_{ei} represent the neutrino mixing elements[3] and $e^{i\alpha_i}$ the Majorana phases. The individual masses of neutrinos are not known, and oscillation experiments only measure the squared difference of the masses. The ordering of the mass eigenstates m_i is also not yet determined. In the normal ordering (NO), m_3 is the heaviest, while in the inverted ordering (IO), m_3 is the lightest. The different ordering scenarios result in two bands of the parameter space relating the $m_{\beta\beta}$ mass to the lightest neutrino mass [29], as shown in Figure 2.2.

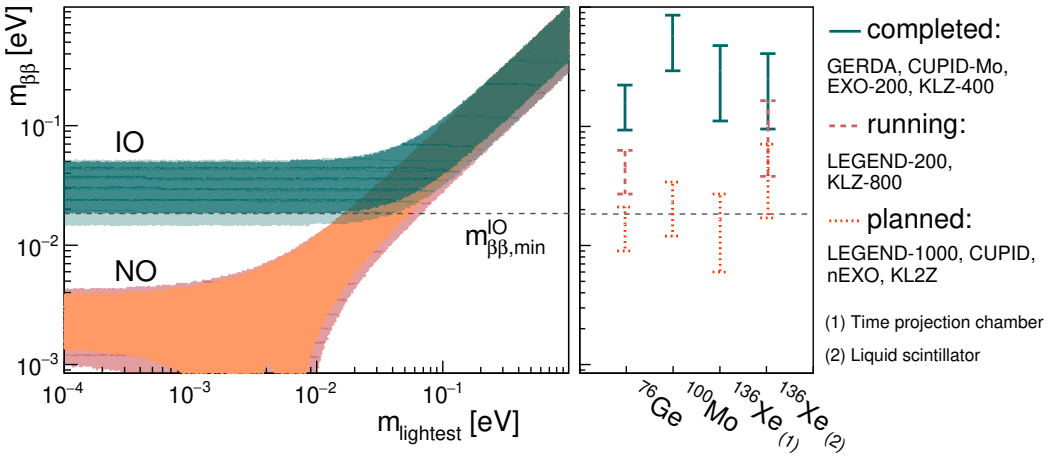

Figure 2.2: $m_{\beta\beta}$ vs. the mass of the lightest neutrino, using the central values of oscillation parameters from [33] along with their 3σ uncertainties (shaded bands) for the IO and NO scenarios. The minimum $m_{\beta\beta}$ value for the IO region is also indicated. The width of the bands reflects the uncertainty from the unknown Majorana phases, which are uniformly varied across all possible values (as in [34]). The overlap region is where $m_1 \sim m_2 \sim m_3$. On the right side, the excluded or projected sensitivity values of $m_{\beta\beta}$ for selected isotopes and their respective generation of experiments are displayed (values from [30], discussed in Section 2.2). The uncertainties on these values derive from the calculation of the $0\nu\beta\beta$ nuclear transition (Section 2.1).

1 There are other mechanisms that could mediate the $0\nu\beta\beta$ process [27, 30]. Only the light neutrino exchange is discussed throughout this thesis.

2 As aforementioned, we discuss here light neutrino exchange as the mechanism dominating $0\nu\beta\beta$ decay, but note that other BSM physics may result in $0\nu\beta\beta$ decay with $m_{\beta\beta}$ masses that are too small to relate to the neutrino masses [32].

3 from the Pontecorvo–Maki–Nakagawa–Sakata matrix, which describes neutrino oscillations.

These regions can be explored by probing $m_{\beta\beta}$ via the measurement of the $0\nu\beta\beta$-decay half-life ($T^{0\nu}_{1/2}$). The next sections discuss the sensitivity of $0\nu\beta\beta$ experiments in testing these mass regions, the uncertainties associated with it, and how GERDA, LEGEND, and MONUMENT advance this research.

2.1 EXPERIMENTAL SENSITIVITY & THEORETICAL UNCERTAINTIES

At the time of its discovery, the $2\nu\beta\beta$ decay was the rarest process ever observed [35]. If existent in any form, a $0\nu\beta\beta$ decay is even rarer, given the low probability of observing a 'flipped' helicity. Current estimates for the half-lives $T^{0\nu}_{1/2}$ surpass 10^{26} years (a value 10^{16} times greater than the age of the universe!). To detect this highly elusive decay, experiments strive to achieve a *background free* state or to minimize background, while optimizing the energy resolution (ΔE), the detection efficiency (ε), and exposure (Mt). The interplay between these factors and the sensitivity to probing the half-life of this process for a given isotope is:

$$\left(T^{0\nu}_{1/2}\right) \propto \begin{cases} a\varepsilon M\, t & \text{background free case,} \\ a\varepsilon\sqrt{\frac{Mt}{BI\Delta E}} & \text{in the presence of background,} \end{cases} \tag{2.3}$$

where a is the isotopic abundance, M is the target mass, and t is the measuring time [36]. The background index (BI) is normalized per exposure and to the width of the region of interest (ROI), which is the energy region around $Q_{\beta\beta}$. While all $0\nu\beta\beta$ experiments primarily measure the energy of the emitted electrons, they significantly vary in the approaches to achieve high sensitivity. Some focus on large target masses, some on measuring the angular distribution of emitted electrons [37], and some others prioritize energy resolution. References [27, 36] provide a comprehensive review of these approaches. A non-exhaustive summary is presented below:

- **Background suppression**: passive shielding (deployment deep underground within lead, copper, water, or cryogenic liquid layers); active vetoing (via the instrumentation of the scintillating medium or water shields); use of self-vetoing (such as scintillating plastics) or radio-pure materials (such as electroformed copper, materials with low levels of cosmic activation obtained from underground, and materials selected via radiopurity assays); event discrimination (via position reconstruction, topology, timing); choice of intrinsically radio-pure detector or target (such as semiconducting crystals) and of isotopes with high Q-value and long $2\nu\beta\beta$-decay half-lives.
- **Energy resolution:** choice of detectors with intrinsic good energy resolution, usually optimized when $2\nu\beta\beta$ source and detector are the same.
- **Detection efficiency:** dense instrumentation of target (e.g., photodetectors surrounding a scintillator) or use of source material as detector medium; minimization of dead-layers or need for fiducialization.

- **Exposure:** High isotopic abundance; target availability and cost; ease of construction.

The $0\nu\beta\beta$-decay search experiments discussed in this thesis fulfill most of the above-mentioned requirements by operating ^{76}Ge-enriched high-purity germanium (HPGe) crystals immersed in liquid argon (LAr), which serves as both an active and a passive shield. While not the most scalable approach due to detector costs and crystal granularity[4], HPGe-based experiments have achieved some of the best results despite smaller target masses [1]. This feat is attributed to their superior resolution and lowest background indices in the field [1, 36, 38].

The combination of $\sim$ 0.1% full width at half maximum (FWHM) resolution at $Q_{\beta\beta}$ with active vetoes, and pulse-shape discrimination, renders this technique highly effective in mitigating major background sources, such as natural radioactivity, cosmic rays, and the $2\nu\beta\beta$ decays. While some experiments rely on a higher Q-value to avoid background from natural radioactivity associated with ^{208}Tl and ^{214}Bi decays, accurately distinguishing the $2\nu\beta\beta$ spectrum from the expected signal ultimately depends on good energy resolution. This clear distinction for HPGe detectors is exemplified in Figure 2.3.

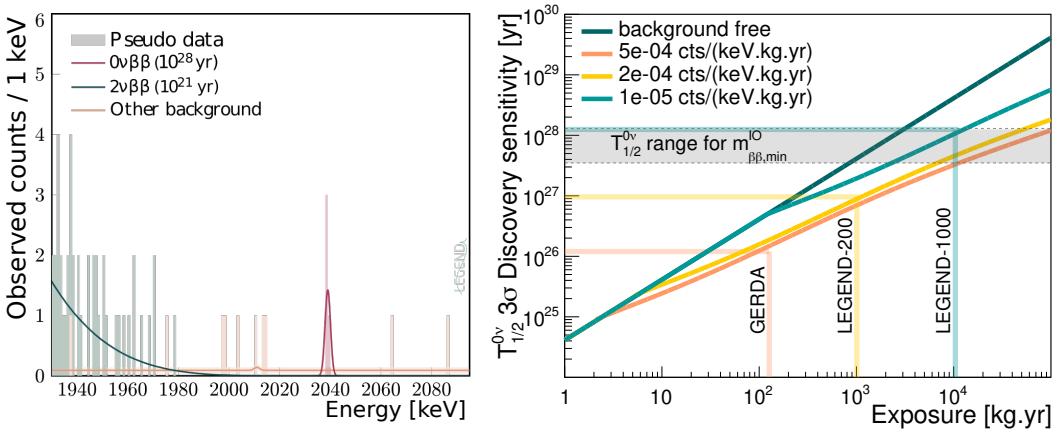

Figure 2.3: Left: Simulated energy spectrum for LEGEND-1000, for an exposure of 10 ton.yr and 2.5 keV FWHM at $Q_{\beta\beta}$ (figure from [39]). In this spectrum, neither events from $2\nu\beta\beta$ nor from the nearby ^{214}Bi γ line leak into the signal region. The $0\nu\beta\beta$ peak, if present, would be clear and sharp, even with only a handful of events. Right: 3σ discovery sensitivity to $0\nu\beta\beta$ decay as a function of exposure, considering $a\varepsilon$=70% and various background scenarios, calculated based on [30]. The exposures and sensitivities achieved (or planned) in GERDA and LEGEND are indicated, as well as the range of $T^{0\nu}_{1/2}$ values corresponding to the minimum $m_{\beta\beta}$ value shown in Figure 2.2.

Figure 2.3 (right) illustrates the background regimes of Equation 2.3 and the respective discovery sensitivities. At lower exposures, it is relatively

4 It also does not present a large natural abundance. However, only ^{130}Te has natural abundance over 10% [27].

easier to achieve a background-free or 'quasi'[5] background-free state. As the exposure increases, reducing the background is crucial to attaining the desired sensitivity level. For LEGEND-200, a modest improvement of BI, relative to GERDA, can allow for a $T^{0\nu}_{1/2}$ sensitivity better than 10^{27} yr.

For the LEGEND-1000 experiment to achieve a discovery sensitivity that fully covers the IO scenario, a strict BI lower than 0.01 count/(keV.ton.yr) is required. Some of the background-suppression techniques crucial for LEGEND to achieve the target sensitivities are discussed in this thesis. These are namely the material selection via HPGe γ-spectroscopy and the R&D and construction of instrumentation for the LAr system.

This thesis also addresses a critical aspect in determining the $0\nu\beta\beta$-decay discovery sensitivity: the significant theoretical uncertainty in translating measured $T^{0\nu}_{1/2}$ values into the effective Majorana mass ($m_{\beta\beta}$). The $m_{\beta\beta}$ parameter is crucial as it directly relates to the absolute scale of neutrino masses and the different mass ordering scenarios. The uncertainty in the excluded or projected values of $m_{\beta\beta}$ primarily stems from theory, namely from the nuclear matrix elements (NMEs), $\mathcal{M}^{0\nu}$, required to convert measured $T^{0\nu}_{1/2}$ (or rates $\Gamma^{0\nu}$) into $m_{\beta\beta}$:

$$\Gamma^{0\nu} = (T^{0\nu}_{1/2})^{-1} = G^{0\nu}(Q_{\beta\beta}, Z) \left|\mathcal{M}^{0\nu}\right|^2 \frac{m^2_{\beta\beta}}{m^2_e}, \tag{2.4}$$

where m_e is the electron mass, $G^{0\nu}(Q_{\beta\beta}, Z)$ is the phase space factor, and $\mathcal{M}^{0\nu}$ represents the amplitude for the transition probability between the initial and final states of the mother and daughter nuclei. Given the large number of nucleon interactions, the calculation of $\mathcal{M}^{0\nu}$ is a complex many-body problem, which has no exact solution. Its calculation using first-principle (ab-initio) methods demands high computational power, which rapidly grows with the number of nucleons.

The NMEs of the isotopes commonly employed in $0\nu\beta\beta$-decay searches have been thus mostly calculated with phenomenological models, which yield values that differ by a factor larger than two [39]. This uncertainty directly impacts the assessment of sensitivity required to cover the inverted mass ordering, as observed in the images shown on the right of Figures 2.2 and 2.3. Additionally, the uncertainty in NMEs also complicates the comparison among different isotopes, a topic further discussed in the following section.

2.2 CURRENT STATUS OF THE $0\nu\beta\beta$-DECAY SEARCH

The current lower limits on $T^{0\nu}_{1/2}$ are at the level of 10^{26} yr [40]. The most stringent results were obtained by KamLAND-Zen-800 (KLZ-800) with $\sim$1 ton yr exposure of ^{136}Xe [41]. Remarkbly, GERDA achieved a similar result despite having only approximately one-tenth of the exposure, being also the first $0\nu\beta\beta$-decay experiment to operate "background-free up to its design exposure" [1].

5 high probability of observing zero background counts in the ROI.

The success of GERDA can be attributed to the high resolution and purity of HPGe detectors, the use of ultra-radio-pure materials, and sophisticated background vetoes and rejection techniques (discussed in Section 6.2). Other leading results in the search for $0\nu\beta\beta$ decay have been obtained by experiments utilizing ^{100}Mo and ^{130}Te isotopes [42, 43]. Figure 2.2 (right) presents some of these results, including projections from experiments that are transitioning to or commencing their upscaled versions.

Besides the variety of isotopes, the panorama of $0\nu\beta\beta$-decay search involves various experimental techniques. The SNO+ and CUORE experiments use ^{130}Te as a target, loaded in a scintillating medium or as crystalline bolometers, respectively [43, 44]. The planned KamLAND2-Zen (KL2Z) and nEXO will use ^{136}Xe, loaded in a scintillator within a balloon or in liquid within a time-projection chamber [45, 46]. LEGEND is the only dedicated experiment using ^{76}Ge targets. Its current phase, LEGEND-200, aims to achieve a sensitivity to $T^{0\nu}_{1/2}$ larger than 10^{27} yr within five years. With this sensitivity, LEGEND-200 may start exploring the IO parameter space, as shown in Figure 2.2. Its successor, LEGEND-1000, aims for $T^{0\nu}_{1/2}$ greater than 10^{28} yr, which is the largest value targeted by any planned experiment. This is likely to cover the entire IO region, as evidenced in Figure 2.3 (right).

The nEXO experiment also aims to cover this region, albeit at lower $T^{0\nu}_{1/2}$ values. That is, the highest $T^{0\nu}_{1/2}$ values do not directly translate into the best sensitivity to $m_{\beta\beta}$, which is typically quoted as a range of values (Figure 2.2, right). The translation to $m_{\beta\beta}$ depends on isotopic specific parameters such as the phase space factor and NMEs (Equation 2.4). The wide range of quoted $m_{\beta\beta}$ values reflects the large uncertainties associated with the NMEs.

The identification of the isotope or future experiment that will achieve the best sensitivity to $m_{\beta\beta}$ thus remains an open question that relies on better constraints on NMEs. Therefore, the pursuit of $0\nu\beta\beta$-decay search with various isotopes is important, as well as efforts to constrain NMEs. The latter is explored in this work through ordinary muon capture (OMC), which is described in the next chapter.

3

ORDINARY MUON CAPTURE (OMC) FOR $0\nu\beta\beta$ DECAY

The previous chapter discussed the impact of NMEs on the uncertainty in determining the effective indicator of new physics, $m_{\beta\beta}$. Since this parameter is directly related to neutrino masses, a large uncertainty in its value leads to a poorer understanding of the sensitivity of future $0\nu\beta\beta$-decay searches to covering the different mass ordering scenarios (Figure 2.2). This uncertainty is primarily driven by the discrepancies of NMEs obtained using different methods, which, in turn, stems from the lack of experimental inputs needed to constrain the phenomenological calculation methods.

This chapter discusses OMC as an approach to address this issue by providing experimental rates of high-lying excited states produced through OMC in $2\nu\beta\beta$-decay daughters. Since $0\nu\beta\beta$ decay is also expected to involve high-lying excited states (albeit virtual), the OMC rates serve as benchmark inputs for its NME, helping to reduce its uncertainty and leading to more precise values for $m_{\beta\beta}$. Before discussing the details of OMC rates, this chapter examines the rates of $2\nu\beta\beta$ and $0\nu\beta\beta$ decays, discussing their similarities, differences, and associated NMEs, as well as describing their differences regarding the 'g_A quenching' problem, and how OMC could help in this regard.

3.1 RATES & NMES FOR $2\nu\beta\beta$ & $0\nu\beta\beta$ DECAYS

We begin with the simpler case, the rate $\Gamma^{2\nu}$ of $2\nu\beta\beta$ decays, which can be calculated using Fermi's Golden Rule:

$$\Gamma^{2\nu} = (T^{2\nu}_{1/2})^{-1} = G^{2\nu}(Q_{\beta\beta}, Z) \left|\mathcal{M}^{2\nu}\right|^2, \tag{3.1}$$

where $G^{2\nu}(Q_{\beta\beta}, Z)$ is the phase-space factor [47] and $\mathcal{M}^{2\nu}$ represent the NMEs. The NMEs are related to the probability amplitude for the transition between the initial and final states of the mother and daughter nuclei. In a broader context, matrix elements link a final eigenstate Ψ_f resulting from a transition of the initial eigenstate Ψ_i to the operators driving the transition. For instance, a general matrix element M for a transition induced by a Hamiltonian $\hat{H}$, acting on quantum states as described by the Schrödinger equation, is expressed as: $M = \left\langle \Psi_f | \hat{H} | \Psi_i \right\rangle$.

We can express the NMEs for $2\nu\beta\beta$ decay in a similar form. First, we have to consider that the decay occurs through virtual intermediate states with angular momentum and parity $J^\pi = 1^+$, as schematically shown in Figure 3.1.

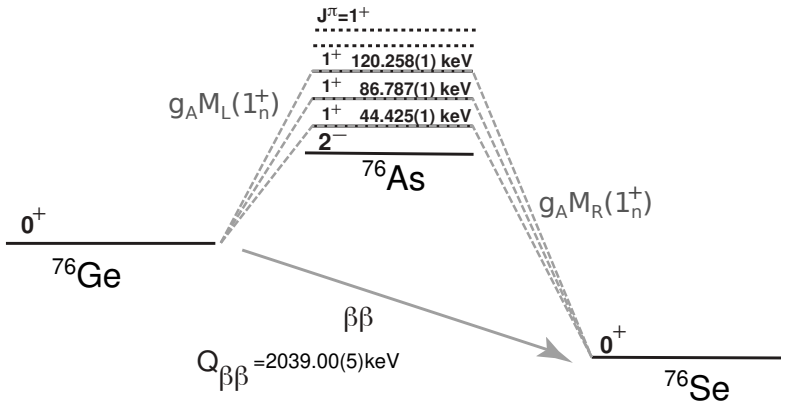

Figure 3.1: Schematic of the $2\nu\beta\beta$ transition from the ground state 0^+ of ^{76}Ge to the ground state 0^+ of the final nucleus ^{76}Se. The transition is described as proceeding through virtual 1^+ states of the intermediate odd-odd nucleus[1] and can be divided into left and right transition branches, each with a set of NMEs $M_{(L/R)}$ [48, 49]. Schematic based on [48, 52].

Consequently, the NMEs $\mathcal{M}^{2\nu}$ take the form of a summation across the n intermediate states with energy E_n participating in the process [47–51]:

$$\mathcal{M}^{2\nu} = \sum_n \frac{\left\langle 0_f^+ | T_{GT}^{\pm} | 1_n^+ \right\rangle \left\langle 1_n^+ | T_{GT}^{\pm} | 0_i^+ \right\rangle}{E_n(1_n^+) - [m_i + m_f]/2}, \quad \text{with } T_{GT}^{\pm} = g_A \sum_j \sigma_j \tau_j^{\pm}, \tag{3.2}$$

where $m_{i(f)}$ is the mass of the initial (final) nucleus and $T_{GT}^{\pm}$ is the one-body Gamow-Teller (GT) operator, which is the product of the summation of GT-type spin-isospin operators across all nucleons with the axial coupling constant g_A [49].

Given the proportionality of each NME branch to the coupling g_A, as evidenced in Equation 3.2 and Figure 3.1, we can factor out this coupling[2] and express $\mathcal{M}^{2\nu}$ as:

$$\mathcal{M}^{2\nu} \equiv g_A^2 M_{\mathrm{GT}}^{(2v)}, \tag{3.3}$$

where $M_{\mathrm{GT}}^{(2v)}$ are the GT matrix elements between initial and final states.

In $0\nu\beta\beta$ decay, the NMEs $\mathcal{M}^{0\nu}$ additionally include the Fermi $M_F^{(0\nu)}$, and Tensor $M_T^{(0\nu)}$ components [50]:

$$\begin{aligned} \mathcal{M}^{0\nu} &\equiv g_A^2 \mathcal{M}_{0\nu} \\ &= g_A^2 \left(M_{\mathrm{GT}}^{(0\nu)} - \left(\frac{g_V}{g_A} \right)^2 M_F^{(0\nu)} + M_T^{(0\nu)} \right), \end{aligned} \tag{3.4}$$

1 Given that contributions from forbidden transitions are negligible [49].

2 For simplicity, we will often neglect other coupling terms in this discussion. Details can be found in [30, 51].

where g_V is the vector coupling constant, and the Tensor operator $M_T^{(0\nu)}$ can be regarded as a second-order correction to $\mathcal{M}^{0\nu}$, having thus a negligible contribution [30, 36]. As the GT component is dominant[3] [36, 48], we write $\mathcal{M}^{0\nu}$ approximately as:

$$\mathcal{M}^{0\nu} \sim g_A^2 M_{\mathrm{GT}}^{(0\nu)},$$

with

$$M_{\mathrm{GT}}^{(0\nu)} = \sum_{J^\pi} \left\langle 0_f^+ \left| \mathcal{O}_{GT}^{(0\nu)}(J^\pi) \right| 0_i^+ \right\rangle, \tag{3.5}$$

$$\mathcal{O}_{GT}^{(0\nu)}(J^\pi) = \sum_{a,b} H(J^\pi) \vec{\sigma}_a \cdot \vec{\sigma}_b \tau_a^+ \tau_b^+,$$

where the sum goes over all J^π multipolarity states involved in the transition and $\mathcal{O}_{\mathrm{GT}}^{(0\nu)}$ is a two-body transition operator that incorporates all the transition details, including the potential for each state [48]. With the approximate proportionality between $\mathcal{M}^{0\nu}$ and g_A^2, the decay rate $\Gamma^{0\nu}$ is approximately proportional to g_A^4. This becomes especially relevant when considering the impact of potential uncertainties in g_A, which will be addressed in this chapter.

In summary, the primary differences between the NMEs (and decay rates) for $0\nu\beta\beta$ and $2\nu\beta\beta$ decays, described by Equations 3.5 and 3.2 (2.4 and 3.1), are as follows:

- The $0\nu\beta\beta$ decay entails $m_{\beta\beta}$, a parameter that characterizes the Majorana nature of neutrinos. In this case, neutrinos are not emitted but virtually exchanged, as shown in the Feynman diagram of Figure 2.1. This means that neutrinos act as effective propagators, which are accounted for in the NMEs of the process.

- The virtual exchange of neutrinos in $0\nu\beta\beta$ decay results in a large momentum transfer between the two involved nucleons, $\sim$100 MeV, determined by the inverse of the distance between nucleons within the nucleus [50]. This large momentum transfer can lead to virtual transitions through high-lying ($J^\pi > 1^+$) excited states of the intermediate nucleus. In contrast, $2\nu\beta\beta$ decay involves transitions only to multipole states 1^+ [30, 49], leading to the pure Gamow-Teller contribution to $\mathcal{M}^{2\nu}$ [47].

- The axial coupling constant g_A may exhibit a different value for $0\nu\beta\beta$ decay, given its possible dependence on the momentum transfer [36, 50].

In the next section, we discuss the impact of the differences outlined above in the calculation of NMEs for $0\nu\beta\beta$ decay and in the determination of g_A.

3 Given that Fermi transitions require the total angular momentum to remain unchanged, all the Fermi strength goes to the isobar analog state in the daughter [51].

NME calculations & g_A quenching

Calculating NMEs for both $0\nu\beta\beta$ and $2\nu\beta\beta$ decays is not straightforward, given the complexity of solving the Schrödinger equation for all nucleons within the nuclear medium where these decays could occur. Solving this many-body problem is in fact not analytically possible. Consequently, phenomenological models that consider only a limited number of states are employed to calculate NMEs [27, 47]. However, these models rely on experimental benchmarks in order to yield NMEs that accurately reproduce measured decay rates. This is especially problematic for $0\nu\beta\beta$ decay, as no experimental data is available for the states with multipolarity J^π larger than 1^+ involved in the process.

Various nuclear models are employed for the complex many-body calculations of NMEs. While a detailed discussion of these methods exceeds the scope of this thesis[4], we distinguish here between the two main approaches: ab-initio and phenomenological NME calculation methods.

Ab-initio methods rely on 'first-principles', describing nuclear interactions based on the underlying theory of nuclear forces; quantum chromodynamics. In these methods, no average interaction potentials are used. Instead, interactions among all nucleons are described using bare nucleon-nucleon and three-nucleon interactions within the framework of chiral effective field theory [30, 53]. While successful for light and mid-mass nuclei, for which predictions of β and $2\nu\beta\beta$ decays agree well with data [30], the computational power required for ab-initio calculations has long rendered this method impractical for large nuclei[5].

To address these issues, calculations are performed using phenomenological methods, such as the interacting shell model (ISM), the interacting boson model (IBM), and quasiparticle random-phase approximation (QRPA) [27, 30, 50]. These methods approximate the interaction among nucleons using average and residual potentials or other simplified approaches. However, these methods introduce additional uncertainties and necessitate experimental inputs to obtain NMEs that accurately predict decay rates. One significant source of uncertainty arises from their incomplete modeling of nuclear many-body interactions[6]. This problem is addressed by quenching the axial coupling constant g_A, which is represented as $g_A^{eff} = q \cdot g_A^{free}$, where g_A^{free} is obtained from the decay of free neutrons, with a precise value of 1.27 [30, 48].

However, interactions of neutrinos with the decaying nucleons involve all other nucleons in the nuclear medium. These interactions influence the charges that couple to the weak interaction, leading to a quenched ($q < 1$) value of g_A^{eff} in nuclei [47].

4 For details, refer to [27, 30, 50].

5 As of writing this thesis, the first ab-initio calculations for the heavy ^{136}Xe and ^{130}Te nuclei have become available. However, these results are not final, as uncertainties, such as those from the truncation of calculations, still need further assessment [53].

6 This 'incompleteness' stems from limiting the number of eigenstates calculated or missing interactions and correlations, depending on the specific method employed [27, 50].

Recent ab-initio calculations of β decays have addressed the issue of g_A quenching by including previously neglected nuclear effects, such as two-body meson-exchange currents and additional nuclear correlations [30]. This indicates that the quenching of g_A is only necessary when nuclear medium effects are not fully considered in the calculations.

However, for many $0\nu\beta\beta$-decay candidate isotopes, the behavior of g_A quenching is not yet well-known, given the lack of precise ab-initio calculations or experimental benchmarks for phenomenological models. Moreover, phenomenological models often rely on $2\nu\beta\beta$ data, despite the higher momentum transfers involved in $0\nu\beta\beta$ decay, which may affect g_A [27].

The impact of high momentum transfer extends to the calculation of NMEs, as shown in Equation 3.5, where all the multipole J^π intermediate virtual states involved in the $0\nu\beta\beta$ decay must be incorporated into the NME sum. The challenge arises from the lack of knowledge of the individual probabilities of exciting these intermediate states and the uncertainty as to whether phenomenological methods accurately predict such excitations [50]. Unlike $2\nu\beta\beta$ and β decays, $0\nu\beta\beta$ decay has not been measured, thus there is no experimental data to constrain its NMEs or g_A. Hence, methods that help precisely determining these values are crucial for achieving more accurate predictions of $m_{\beta\beta}$. This is especially important, considering that g_A appears to the fourth power and the NMEs are squared in the calculations relating the experimental rates to $m_{\beta\beta}$ (Equations 2.4 and 3.5).

In the next section, we discuss OMC as a tool to constrain these values, given the provided high momentum transfer necessary to probe the high-energy states of the intermediate odd-odd nucleus.

3.2 OMC AS A BENCHMARK FOR NMES

Ordinary muon capture (OMC) by a nucleus in an irradiated target follows the capture of the muon by an atom, as described below:

1. Muon captured within an atomic orbit: As a muon traverses the target, it slows down due to interactions with the outer atomic electrons, eventually coming to a stop, as it is 'captured' within a muonic orbit, forming a muonic atom. The captured muon then transitions to lower-energy orbits, emitting X-rays and Auger electrons along the way, until it reaches the ground state. This process occurs on a timescale of $\mathcal{O}(10^{-13}\,\mathrm{s})$ [54]. When the lowest orbit K (1s) is reached, the muonic wavefunction strongly overlaps with that of the nucleus.

2. Muon captured by the nucleus: The large overlap of nuclear and muonic wavefunctions enhances the probability of the nucleus capturing the muon. This capture becomes more likely than the ordinary muon decay, which has a lifetime of 2.2 µs, while the lifetime for nuclear capture is $\mathcal{O}(100\,\mathrm{ns})$ [54]. The capture process results in a proton transforming

into a neutron inside the nucleus through the charged current weak interaction, as described by Equation 3.6 and shown in Figure 3.2.

$$\mu^- + p \rightarrow n + \nu_\mu. \tag{3.6}$$

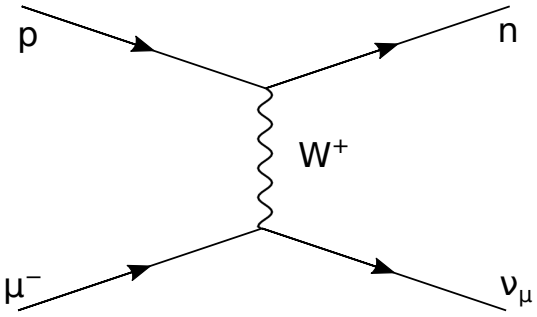

Figure 3.2: Feynman diagram of a muon capture: A proton in the nucleus transforms into a neutron, emitting a neutrino.

If no γ ray is directly emitted in this process, the capture is referred to as non-radiative muon capture, or ordinary muon capture (OMC). The reaction often results in the excitation of the odd-odd daughter nucleus to a J^π state:

$$\mu^- + {}^{A}_{Z}X(0^+) \rightarrow {}^{A}_{Z-1}Y^*(J^\pi) + \nu_\mu,$$

where 0^+ is the ground state of the even-even parent isotope [55]. The amount of energy transferred into the nuclear excitation following OMC depends on the energy taken by ν_μ [54]. The total available energy for nuclear excitation is approximately limited by the mass of the muon ($\sim$100 MeV). The probability of exciting the nucleus ${}^{A}_{Z-1}Y$ is further restricted by the concurrent, more often, reaction of $n = 1, 2, 3$ (or larger) neutron emission, resulting in ${}^{A-n}_{Z-1}Y$ [56].

However, a significant fraction of OMC results in the formation of ${}^{A}_{Z-1}Y^*$ at high excited levels, providing an opportunity to study high excited states of isotopes of interest, such as the virtual intermediate odd-odd ${}^{A}_{Z-1}Y^*$ isotopes involved in $0\nu\beta\beta$ decay, schematically illustrated in Figure 3.3.

Table 3.1: Examples of $2\nu\beta\beta$ daughter isotopes ${}^{A}_{Z}X$ used as OMC targets to study the states ${}^{A}_{Z-1}Y^*(J^\pi)$.

Daughter ${}^{A}_{Z}X$	odd-odd ${}^{A}_{Z-1}Y$	$2\nu\beta\beta$ parent ${}^{A}_{Z-2}W$
^{136}Ba	^{136}Cs	^{136}Xe
^{76}Se	^{76}As	^{76}Ge
^{130}Xe	^{130}I	^{130}Te
^{48}Ti	^{48}Sc	^{48}Ca

The exact experimental method to measure OMC rates in targets such as the ones listed in Table 3.1 is described in Chapter 12. It involves measuring

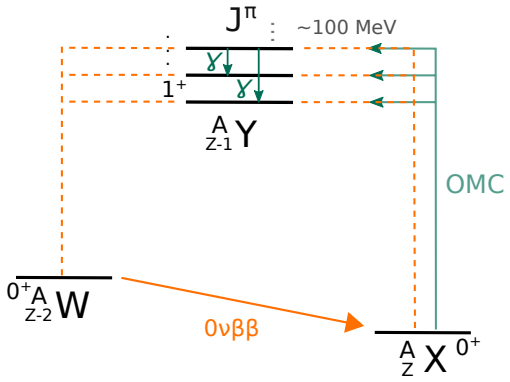

Figure 3.3: Schematic of a $0\nu\beta\beta$ decay, transitioning through virtual states of the odd-odd ${}^{A}_{Z-1}Y$ isotope up to large excitation levels (orange) and access to high excitation levels of ${}^{A}_{Z-1}Y$ via OMC in a $2\nu\beta\beta$ daughter isotope (green).

the γ rays resulting from the de-excitation of the several multipole states of the ${}^{A}_{Z-1}Y^{*}(J^{\pi})$ odd-odd isotope. Through this measurement, both the total OMC rate and the partial rates to each excited state can be determined.

The measured total OMC rate serves as a benchmark for the values of coupling constants such as g_A, helping to validate whether it is quenched at high momentum transfer [55]. The measured partial rates to individual states can be compared to the values predicted by a given calculation framework, providing a way to further benchmark the model. For instance, the partial OMC rates in ^{136}Ba to low-energy ^{136}Cs states calculated using the ISM and proton-neutron QRPA models yield results that differ by a factor of four [55]. The comparison between theoretical and experimental results can be used to fine-tune and provide insight into NME calculations involving large momentum transfer in heavy nuclei, such $0\nu\beta\beta$ decay [54].

By providing information on both the quenching of coupling constants and improving the accuracy of NMEs, OMC proves itself a valuable tool for $0\nu\beta\beta$-decay searches. The sensitivity of these searches is heavily influenced by the current uncertainties in these values, where even marginal uncertainties in g_A coupled with an uncertainty factor of two in NMEs can result in an order of magnitude larger exposure required to achieve the same sensitivity.

PART II

BACKGROUND SOURCES, PARTICLE INTERACTIONS, & EXPERIMENTAL APPROACH

4

PARTICLE INTERACTIONS & BACKGROUND SOURCES

This thesis focuses on highly sensitive particle detectors, which are susceptible to various background sources that must be minimized. To reduce cosmic background, detectors like GERDA, LEGEND, Gator, and the proposed PALEOCCENE are placed underground. MONUMENT is the only experiment in this thesis that does not need overburden shielding. In either case, even after the effective shielding provided by the underground location, muons, muon-induced neutrons and natural radioactivity can contribute to the signals, requiring characterization and further suppression. Strategies to mitigate these background signals depend on their origin and type of interaction within the detector. These are discussed in a non-exhaustive manner in this overview chapter, focusing on the mentioned experiments.

4.1 RADIOGENIC ALPHA, BETA & GAMMA BACKGROUND SOURCES

Nuclei in unstable states spontaneously decay. The instability is caused by some excess of total energy, often related to an imbalance in the number of nucleons or their arrangement within the nucleus. This process, known as radioactivity, is present everywhere in nature: in buildings, soil, food, and gases. The emitted radiation are usually α or β particles, followed by γ rays.

Various sources contribute to environmental radioactivity. The dominant contributing radioisotopes are: i) the four shortest-lived primordial nuclides (^{238}U, ^{235}U, ^{232}Th, and ^{40}K), which have half-lives comparable to the age of the Earth $\mathcal{O}(10^9\,\mathrm{y})$; ii) their radiogenic daughters, such as ^{226}Ra and ^{228}Th; iii) the cosmogenic isotopes, produced by the interaction of cosmic rays with gases or other materials (e.g., ^{39}Ar, ^{46}Sc, and ^{60}Co); and iv) anthropogenic nuclides, mainly arising from nuclear testing and power plants, such as ^{137}Cs and ^{85}Kr.

Many of these isotopes, especially the ones of geological origin (^{40}K, ^{238}U, and ^{232}Th), are present as trace elements in materials used in the construction of detectors. The decay of ^{40}K emits 1.46 MeV γ rays, for the electron capture decay mode, and electrons with energy below 1.31 MeV, for the β mode. The ^{238}U, and ^{232}Th chains produce a series of α, and β particles, followed by γ rays, as shown in Figure 4.1. Many of the γ lines marked in this figure, as well as the γ rays from ^{40}K are observed in the energy spectra of all the HPGe detectors discussed in this work.

Despite the long half-lives of the parent isotopes at the beginning of the chain, the secular equilibrium may be broken, changing the relative content of isotopes from the same chain. This equilibrium disruption may be caused by material processing or by the introduction of radon daughters. Radon gas can

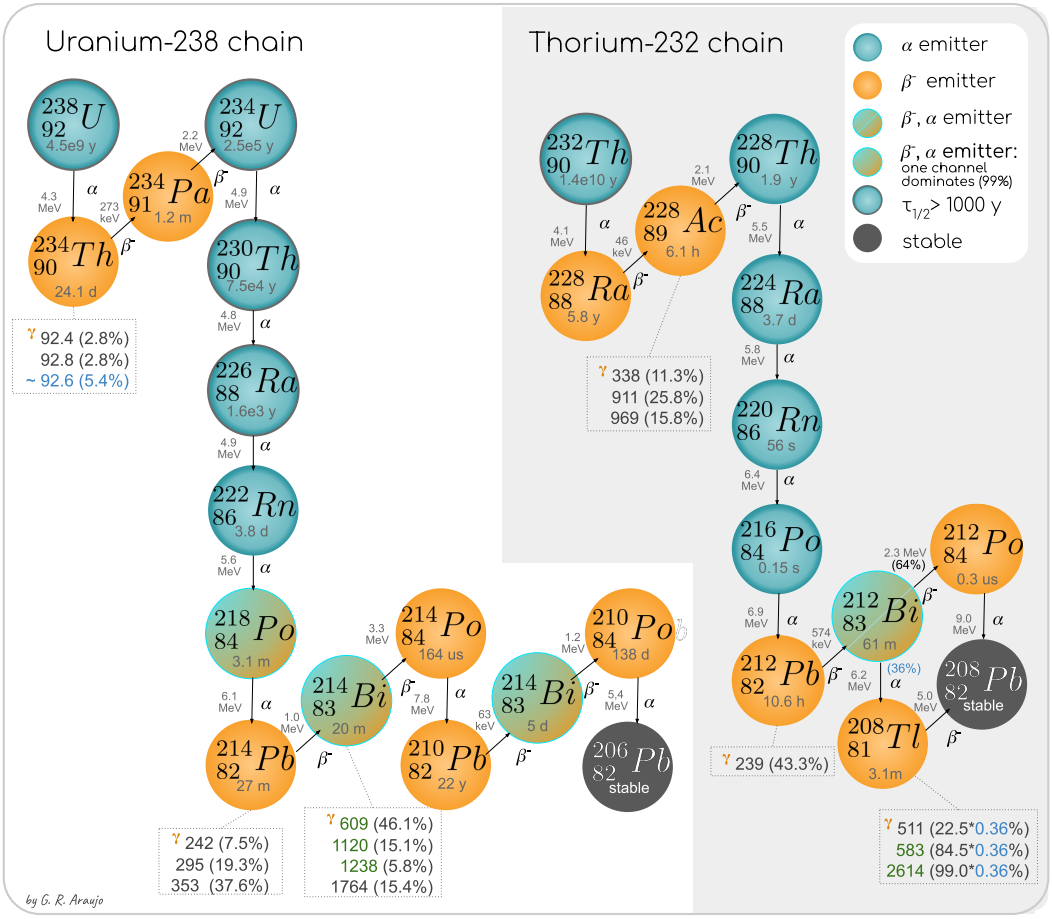

Figure 4.1: ^{238}U and ^{232}Th decay chains. Half-lives, Q-values, γ ray emission, and branching fractions (f_B) extracted from [57]. Secondary decay channels with f_B <0.2% are not shown (such as the α-decay of ^{214}Bi, or the decay of ^{234m}Pa through its ground state). Only γ rays above 90 keV with a total f_B >5.2% are shown – the ones that undergo summation effects are marked in green. For ^{234}Th, the lines around 92 keV are usually observed together, resulting in a total f_B of ∼5.4%.

emanate from surfaces and decay into radioactive daughters that may adhere to other surfaces – an effect known as plate-out[1], which is an important effect when analysing surface backgrounds. Alpha decays originating from this surface/dust contamination are for instance observed in the GERDA data and discussed in Chapter 7.

Some of the cosmogenic isotopes in HPGe detectors are ^{68}Ge ($T_{1/2}$=271 d), and ^{60}Co ($T_{1/2}$=5.3 yr), which is also present in copper (often present around HPGe crystals[2]). Some of the cosmogenic isotopes present in trace amounts in atmospheric argon are ^{39}Ar and ^{42}Ar. The former emits β particles out of the ROI, as discussed in Chapter 5. The latter produces ^{42}K, which decays with $T_{1/2}$=12.4 h, via a β emission (with and endpoint of up to 3.5 MeV), often

1 This mostly happens for ^{222}Rn, which has a longer half-life than ^{220}Rn, being thus more commonly present in the environment [58].

2 For instance, in the WLSR shroud of LEGEND and in the sample chamber of Gator.

accompanied by a γ ray. ^{42}K was the primary contributor to the background index in GERDA, and its 1525 keV γ ray is studied in detail in Chapter 7.

Interactions & observed signals

Among the HPGe detectors discussed here, all of them detect γ rays originating from natural radioactivity, but only the ones in GERDA and LEGEND exhibit a clear signal from α decays. This is mainly due to their low background and 'bare' approach. While the detectors employed in MONUMENT and Gator are housed in a vacuum cryostat that blocks external α particles, the HPGe detectors in GERDA and LEGEND are not encased. Although the dead layer of HPGe crystals are thick enough ($\sim$1 mm) to hinder the penetration of α particles, these particles are not completely shielded by the thin (sub-µm) passivated and boron implantation layers (described in Chapter 6). The ranges of α and β particles, and the attenuation length of γ rays in different detector materials are listed in Table 4.1.

Table 4.1: Range (R) of α and β particles, and attenuation length (λ_{att}) of γ rays in germanium (Z=32, ρ=5.3 g cm^{-3}) and in liquid argon (Z=18, ρ=1.4 g cm^{-3}) for various energies. Data from [59–61].

In germanium			
Energy [MeV]	R_α [µm]	R_β [mm]	$\lambda_{att}\gamma$ [cm]
0.5	1.7	0.5	2.4
1.0	3.1	1.2	3.3
2.6	7.9	3.5	5.1
3.5	11.2	4.7	5.5
In liquid argon			
Energy [MeV]	R_α [µm]	R_β [mm]	$\lambda_{att}\gamma$ [cm]
0.5	4.2	0.6	9.1
1.0	6.9	1.5	12.4
2.6	18.7	4.5	19.7
3.5	27.6	6.1	22.4

The different ranges of these particles are a result of their distinct dominant interaction mechanisms. Alphas are highly ionizing particles that rapidly lose energy through a high energy loss per unit distance. As a result, their range is only a few micrometers in most of the detector materials. Electrons in the MeV range primarily lose energy through collisions with atomic electrons, and to a lesser extent via radiation emission (Bremsstrahlung or Cherenkov) [60]. Their range in Ge and LAr is a few millimeters.

Gamma rays penetrate deeper (several centimeters), losing energy via various mechanisms: the photoelectric effect (predominant at energies below MeV), Compton scattering (around 1 MeV), and pair production (above MeV energies). Details on the probabilities for these different γ ray interactions in

HPGe are provided in Appendix A, in the context of γ ray simulations for Gator, and illustrated in Figure A.6 therein.

Of particular concern for $0\nu\beta\beta$-decay search are the Compton interactions of the ^{214}Bi and ^{208}Tl γ rays (such as the 2.6 MeV line), and β or α emissions above the $Q_{\beta\beta}$ value (2.039 MeV) [62]. A few major examples of the latter are: β emissions from ^{42}K, ^{214}Bi, and ^{208}Tl, which have sufficient energy to penetrate millimeters beyond the HPGe dead layer[3]; and α particles from ^{210}Po decay depositing energy in the p^+ contact or passivated layer.

Although the full energy of these γ rays and α decays are not close to $Q_{\beta\beta}$, their partial energy deposition in the HPGe detectors may result in events within the $0\nu\beta\beta$-decay ROI. Features observed in the HPGe spectra resulting from partial energy depositions from γ rays are presented and analyzed in detail in the aforementioned Appendix A and in [64]. These features are namely the Compton continuum, the Compton edges, and the backscatter, the single, and the double escape peaks, which all contrast to the full energy peak, where all the energy is deposited and collected within the sensitive volume of the HPGe crystal.

These concepts will be extensively utilized throughout the subsequent chapters, as the detection of γ rays plays a central role in various topics, including the LAr system, HPGe γ spectroscopy, background characterization in GERDA, and the study of excited states with MONUMENT.

Background suppression

To minimize the effect of radiogenic α, β and γ ray background sources, components used in the construction of the detectors undergo a selection campaign: the maximum allowable radiogenic background is estimated via Monte Carlo simulations, and materials are selected based on radiopurity assays conducted using HPGe γ spectroscopy or mass spectroscopy [39, 65]. The HPGe γ screening of materials for LEGEND with Gator is discussed in Appendix A. Additionally, certain materials are subjected to radon emanation tests, and dedicated ventilation systems are implemented to mitigate the presence of radon within the laboratory facilities and detector assembly sites [2].

Materials that do not meet radiopurity requirements for close-detector parts, such as the stainless steel used in the GERDA cryostat or the Gator enclosure, are kept at a moderate distance and shielded by more radio pure materials such as oxygen-free copper [66]. Additional measures involve the use of active (scintillating) materials and vetoes, which are major topics in this thesis, as well as particle discrimination analysis methods, discussed in Section 6.1.

3 As shown in Table 4.1, a 3.5 MeV β from ^{42}K can penetrate $\sim$5 mm into Ge. Furthermore, these particles can produce Bremsstrahlung photons which can penetrate several cm [63].

Although HPGe detectors are inherently pure[4], they can be activated by cosmic rays. Minimizing the exposure of these detectors to above-ground conditions effectively reduces their background levels. For instance, the γ ray from the cosmogenic ^{65}Zn was observed only in detectors newly introduced in GERDA (see Chapter 7), and the background in Gator was observed to decrease after years underground, primarily due to the reduction in isotopes with half-lives below ten years, such as the cosmogenic ^{58}Co ($T_{1/2}$=70.9 d), ^{54}Mn ($T_{1/2}$=312.3 d), and ^{60}Co ($T_{1/2}$=5.3 yr) [2]. The contribution from the short-lived cosmogenic ^{68}Ge ($T_{1/2}$=271 d) was found to be negligible in GERDA detectors, given their long storage underground [63].

To prevent the presence of cosmogenic isotopes from argon in LEGEND-1000, the employment of underground argon is foreseen. This is especially important to reduce the background index from ^{42}K in the $0\nu\beta\beta$-decay ROI, but also to reduce the decay rate from ^{39}Ar, enabling other exotic searches at lower energies [39].

4.2 NEUTRONS & MUONS

The production of neutrons can occur through various processes: (α, n) reactions, the spontaneous fission of heavy elements, such as ^{235}U, and muon spallation. The latter process is significant and results in the production rate of neutrons being related to the flux of muons reaching the detectors.

Muons are created in the decay of pions originated from high-energy collisions, such as those of protons from an accelerator with a solid target, or those from cosmic rays with atoms in the Earth's atmosphere. In the previous section, we discussed the activation of isotopes caused by both primary and secondary cosmic rays in the atmosphere and materials above ground. In this section, we focus on the secondary muonic component, relevant for experiments operated underground.

At the Laboratori Nazionali del Gran Sasso (LNGS), located under $\sim$1400 m of rock ($\sim$3500 meter water equivalent), the muon flux is of approximately 1.25 $m^{-2}\,h^{-1}$ [65], a reduction of about 1 million in comparison with the flux at ground level. Yet, muons still pose a concern for many experiments, which mitigate these by operating muon vetoes based on scintillating panels or Cherenkov light produced in water tanks.

Once muon vetoes are in place, the prompt electromagnetic signal induced by the passage of a muon is negligible, as these are recorded with high energies and efficiently tagged by vetoes [39, 62]. The real concern lies rather in the activation of isotopes by muon-induced neutrons, which can yield delayed events.

An example is the process of ^{76}Ge capturing a neutron (^{76}Ge+n $\rightarrow^{77(m)}$Ge), resulting in ^{77}Ge and ^{77m}Ge, which have half-lives ranging from 55 s to 11.2 h. These delayed decays are often not promptly correlated with the passage of a

4 Thanks to the zone-refining and crystal growing processes, as well as the enrichment process in the case of enriched detectors [39, 62].

muon and, as a result, not vetoed [67]. Despite their β emissions above $Q_{\beta\beta}$, this background is not yet significant for the current experiments [62], but could become concerning for the sensitivity of future Ge-based detectors. To mitigate them, either laboratories at greater underground depths or additional neutron background suppression measures are pursued for LEGEND-1000 [39]. These include the use of delayed tagging provided by the muon veto and LAr instrumentation [67] and the implementation of neutron moderators, which will be shown in Chapter 8.

5

LIQUID ARGON

Liquid argon (LAr) is widely used as a scintillating medium in particle physics experiments [39, 68–76]. A few of its key features are the high photon yield in response to radiation (tens of photons/eV [77]), high transparency, and low cost, compared to other noble liquids. In GERDA, LAr was used as a cooling, shielding, and scintillating medium, playing a major role in its background-free operation [1, 66].

In LEGEND, LAr is similarly employed, but underground argon is the one procured for LEGEND-1000 [39], given the presence of cosmogenic isotopes in atmospheric argon. The most important ones are listed in Table 5.1. Although present with the largest abundances, the radioactive isotopes ^{39}Ar and ^{85}Kr are not major concerns for LEGEND-200, as the Q-value of their β emissions (565 keV and 687 keV, respectively [57]) are well below the $0\nu\beta\beta$-decay ROI[1]. ^{37}Ar is also negligible, since it quickly decays once underground[2]. The only significant concern is ^{42}Ar, not because of its β emission, which has a Q-value of 599 keV, but rather due to the decay of its progeny ^{42}K, discussed in the previous chapter.

Table 5.1: Liquid argon properties.

atomic and physical properties [79]	
melting point (at 1 atm)	83.8 K
boiling point (at 1 atm)	87.3 K
density (at b.p.)	1.395 g/cm^3
main isotope	^{40}Ar (99.6%)
radioactive isotopes	
^{85}Kr	$\sim$ 0.1 Bq kg^{-1} [80]
^{37}Ar	time-dependent ($T_{1/2}$ =35 d) [57]
^{42}Ar	$\sim$40 µBq kg^{-1} (atmospheric Ar) [81]
^{39}Ar	$\sim$ 1 Bq kg^{-1} (atmospheric Ar) [80, 82]
	$\sim$ 6.5 mBq kg^{-1} (underground Ar) [83]

1 However, their presence decrease the sensitivity to BSM searches at low energies [39].

2 Isotopes for which a decay is predicted but has not yet been detected, such as ^{36}Ar [78], are also negligible.

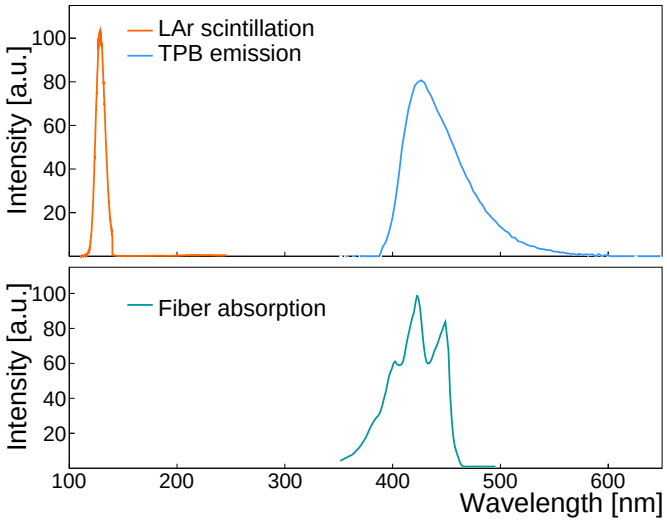

Figure 5.1: VUV scintillation from LAr [85], TPB emission, and absorption of wavelength-shifting fibers used in LEGEND-200 [86,87].

5.1 SCINTILLATION & WAVELENGTH SHIFT

Scintillation in LAr occurs when radiation ionizes and excites argon atoms, leading to the formation of ionized or excited dimers. If the ionization electrons are not drifted out of the detector medium (via strong electric fields), they thermalize and recombine. Excited dimers can exist in a singlet or triplet molecular electronic states, which subsequently de-excite by emitting photons with a fast ($\tau_{singlet}$~6 ns) or long ($\tau_{triplet}$~1.5 µs) decay times[3] [77]. The prompt light component is less affected by quenching resulting from collisions with impurities, while the triplet component is more affected and is often used as a measure of purity and light yield levels [84]. The probability of inducing singlet or triplet states depends on the excitation density and, therefore, on the type of interaction. For instance, electron recoils induce a larger fraction of triplet states compared to nuclear recoils. This discrimination can be used to distinguish interactions caused by γs, βs and muons from those caused by neutrons or α particles.

The scintillation light is emitted in the vacuum ultraviolet (VUV) spectral region, peaked at 128 nm [85]. This wavelength is commonly absorbed by plastics, glass, and quartz – materials often employed as photodetector windows, light guides, and optical fibers. To facilitate the detection of this scintillation, wavelength shifters, such as tetraphenyl butadiene (TPB), are often used [65,68–73,76]. Figure 5.1 (top) shows the TPB re-emission of VUV light in a region between 380 nm and 600 nm.

The emission in the blue spectral region is of advantage: it matches well the quantum efficiency of commercial photodetectors, which typically peak in this range [72,88], the efficiency of reflectors, as it will be shown in this work, and the absorption of wavelength-shifting fibers, such as those used in LEGEND-200, shown in Figure 5.1.

3 With the latter being longer given the necessary spin-flip for the transition to the ground state.

Furthermore, the emission in the blue region is beneficial in terms of transparency. While impurities in LAr (such as oxygen and nitrogen) can reduce its effective transparency to its own VUV scintillation light [89, 90], the transparency to blue light remains unaffected. The lower refractive index of LAr for blue light compared to VUV light also contributes to reduced scattering. As a result, the emitted blue light can propagate through LAr with minimal absorption or scattering, leading to better light collection. The detailed optical properties of LAr are extensively discussed in Chapter 11.

5.2 TPB & PEN as wavelength shifters

TPB is widely employed as a wavelength shifter (WLS) in LAr-based experiments [65, 68–76, 91]. For the LAr instrumentation of GERDA, TPB was applied to several surfaces through solvent-based dip-coating, brushing, or vacuum evaporation methods [65]. These methods, however, have limitations in terms of uniformity or labor-intensiveness [4, 92]. These limitations render the use of TPB in experiments requiring extensive surface coverage, such as DarkSide and LEGEND-1000, impractical. As an alternative, the blue scintillating material polyethylene naphthalate (PEN) became a promising substitute.

PEN is a commercially available plastic film that offers ease of manipulation at room temperatures while featuring high tensile strength at cryogenic temperatures [93, 94]. This in contrast to TPB, which is a powder that requires specific coating techniques and can emanate into LAr [95].

TPB has been however extensively characterized [95–101], and its quantum efficiency (QE) at 128 nm was measured to be $(60 \pm 4)\%$ at room temperature [96]. This value had not yet been measured in LAr, but its efficiency was observed to increase at low temperatures [98, 102].

Prior to the work presented in this thesis, the efficiency of PEN had been only measured relative to TPB [92, 94, 103, 104]. The complication of relative measurements is that the light yield from TPB coatings is sample-dependent, with large variations for different coating methods, thickness and substrates [87, 96, 97, 105].

The QE (or quantum yield) represents better the true efficiency, given that it is an intrinsic characteristic of the molecules – namely, the ratio between the average number of photons emitted and absorbed [96, 106, 107]. It is thus not dependent on specific parameters of the sample, such as its thickness, and setup, such as detector position and coverage. In this thesis, the QE and other optical properties of these WLS materials were investigated in detail in the context of the R&D of WLS reflectors for LEGEND.

6

HIGH-PURITY GERMANIUM (HPGE) DETECTORS

High-purity germanium (HPGe) detectors are semiconductor diodes biased at a reverse voltage. Their detection principle is based on collecting charges induced by radiation. The passage of ionizing irradiation through the active detector volume excites electrons to the conduction band, creating electron-hole pairs at numbers proportional to the energy deposited.

In the most common p-type detectors, the holes are collected at the p^+ contact, which is produced by boron implantation. The n^+ contact, where the positive voltage is applied, is produced via lithium implantation, and surrounds most of the surface of the detector. The reverse-bias voltage yields a depleted volume and causes newly created electron-hole pairs to drift toward the respective electrodes. This is schematically shown in Figure 6.1, along with the different types of detectors used in LEGEND.

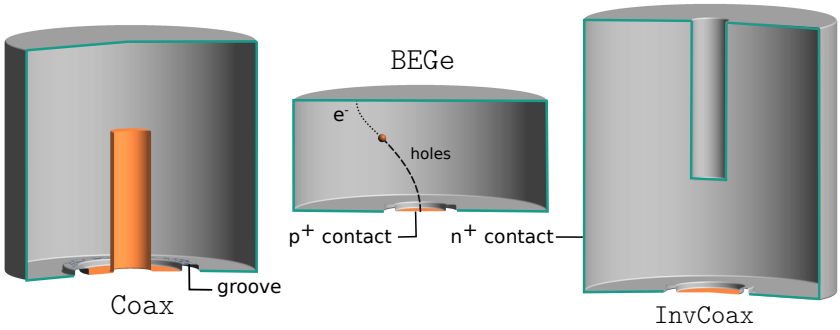

Figure 6.1: Different shapes and contacts of p-type detectors. In the (Semi-) Coaxial (Coax) detector, the p^+ contact covers its axial borehole. This borehole helps to maintain full depletion of the detector, even for large sizes reaching up to 3 kg [108]. In the broad energy germanium detector (BEGe), the p^+ contact is small ($\varnothing$ 15 mm). This design reduces the capacitance of the contact, leading to improved energy resolution, but results in lower detector mass, which is on average 0.7 kg [31, 109]. In the Inverted Coaxial (InvCoax, or IC) detector, the enhanced resolution is guaranteed by the'point-like' contact as in the BEGe, and the full depletion by the borehole, which is not boron-implanted, as opposed to the Coax. The drifts of electrons and holes to the respective electrodes are schematically shown at the center. Detector schematics modified from [108][1].

Although the deposited layer of lithium is thin, it diffuses up to 1 mm deep into the detector producing a 'dead' layer, where the collection of charge is ineffective. However, this dead layer serves as an advantage by shielding the detector from α particles. Once the full depletion voltage is applied, the bulk of the detector becomes fully sensitive. The signals are read out by charge-sensitive preamplifiers, which output a voltage pulse [66].

1 All the HPGe schematics were made with the code kindly made public by L. Pertoldi [110].

The low energy of 2.96 eV required to create electron-hole ($e^- h^+$) pairs, coupled with a Fano factor (F) of 0.13, results in relatively small statistical fluctuations from signals in HPGe detectors ($\sigma = \sqrt{N_{e^- h^+} . F}$), and thus in energy resolutions of fractions of a percent at energies around the MeV range [109]. This enhanced energy resolution, combined with their energy linearity, establishes HPGe detectors as preferred choices for γ spectroscopy.

Experiments aiming for efficient and high-resolution detection of γ rays, such as MONUMENT and Gator, therefore employ HPGe diodes. HPGe detectors are also advantageous for low-background γ ray counting because of their high purity, which has been optimized during the production of detectors with low leakage currents.

Being a semiconductor, the band gap for Ge is small (0.66 eV) [109]. Consequently, thermal excitations can bring electrons to the conduction band, and the detectors must be cooled, often to liquid-nitrogen or liquid-argon temperatures. The commercially available method to operate and cool these detectors is housing the HPGe crystals in a vacuum cryostat, which is electrically cooled by a pulse tube cooler or connected to a liquid nitrogen dewar. This approach is employed by Gator and MONUMENT to operate their HPGe detectors. GERDA and LEGEND operate the crystals bare, without mechanical housing, in liquid argon, as is described in the next section.

6.1 $0\nu\beta\beta$-DECAY SEARCH WITH HPGE

The advantageous performance parameters of HPGe diodes, rendered this technology attractive for the search of the $0\nu\beta\beta$ decay of ^{76}Ge:

$$^{76}\mathrm{Ge} \rightarrow ^{76}\mathrm{Se} + 2e^- . \tag{6.1}$$

Table 6.1: Parameters for $0\nu\beta\beta$ search with ^{76}Ge. While its $Q_{\beta\beta}$ value and $G_{0\nu}$ are not as high as for other isotopes (Section 2.2), the detection efficiency of HPGe detectors is high, and their energy resolution and BI around $Q_{\beta\beta}$ are the best in the field [1, 36].

Physics Parameters	
$0\nu\beta\beta$ Isotope	^{76}Ge
$Q_{\beta\beta}$	2039 keV
$M_{0\nu}$	2.7 – 6.0 [39]
$G_{0\nu}$	$2.4 \cdot 10^{15}\,\mathrm{yr}^{-1}$ [39]
g_A	1.27 [111]
nat. abundance	7.8 % [66]
enrichment up to	92% [39]
HPGe performance parameters	
FWHM at $Q_{\beta\beta}$	2.5 keV [39]
containment efficiency	∼100% [111]
achieved BI	5×10^{-4} cts/(keV·kg·y) [1]

The search for $0\nu\beta\beta$ decay using HPGe detectors began in the late 1960s with natural detectors and later transitioned to enriched ^{76}Ge crystals in the 1990s [66, 108]. The field has since then experienced many technological advancements. For both GERDA and MAJORANA experiments, new detectors with enhanced performance were developed, such as the BEGe and IC detectors shown in Figure 6.1.

The point-like contact feature of these detectors not only provides enhanced resolution but also allows for pulse shape discrimination (PSD): the distances charge travel from different multi-scatter interaction points within the detector yield pulses clearly distinct from the ones expected from the $0\nu\beta\beta$-decay signal, which is a single-site interaction. This distinction is made more clear by point-contact detectors, as the electric field throughout the bulk is lower and much more intense around the point contact [112]. This results in a slower drift of charges and a sharp signal amplitude change only when the holes are collected at the contact, as shown in Figure 6.2.

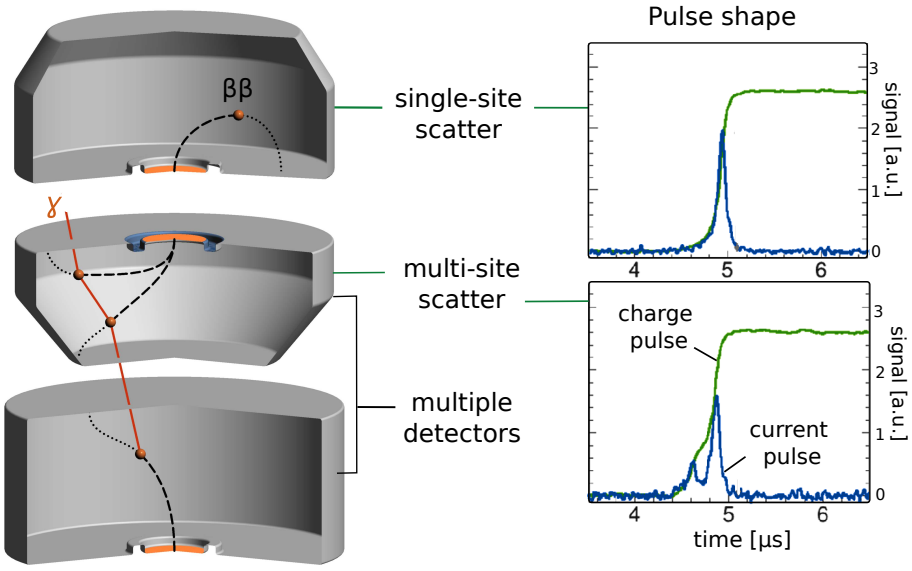

Figure 6.2: Single-site scatter: the $\beta\beta$ signal is a single-site event, given the small ($\sim$1 mm) travel range of the electrons in Ge, as listed in Table 4.1. This event is observed as a sharp step-like charge pulse, as all the charges are collected approximately at once. Multi-site scatter: γ rays in the MeV range often deposit energy in multiple sites, as they lose energy via Compton scatters, often spaced by several cm. The charge pulse observed will reflect the arrival of different charge clouds originating from the mulitple depositions. Another possibility is that part of this energy is depositied at another detector. Such an event is flagged as a multiple-detector deposition. Surface events, like those from αs (not shown), can also be identified via PSD because of the delay in their charge collection. For details on the PSD methods for αs and βs, see references [108, 112]. PSD graphs were modified from [112] and detector schematics were modified from [108].

It has been demonstrated within the GERDA experiment and by dedicated studies that the PSD capability of IC detectors is comparable to that of the well-established BEGes [39, 112, 113]. The IC detectors have thus become the

primary choice for LEGEND. Their larger size compared to BEGes allows for a reduction in support material and cabling in close proximity to the detectors, decreasing the background rate per mass. Additionally, the lower surface-to-volume ratio of the IC detectors results in less surface background. Ultimately, the background suppression technique of immersing bare HPGe crystals in a cooling and scintillation medium has further enhanced the capabilities of $0\nu\beta\beta$-decay searches with HPGe. This approach is discussed in the following section.

6.2 $0\nu\beta\beta$-DECAY SEARCH WITH HPGE CRYSTALS IN LIQUID ARGON

GERDA has pioneered the employment of HPGe crystals in LAr [65]. LEGEND follows in its footsteps, incorporating the LAr system in its current phase, LEGEND-200, and the future stage, LEGEND-1000. The working principles of the LAr system and the water muon veto are depicted in Figure 6.3.

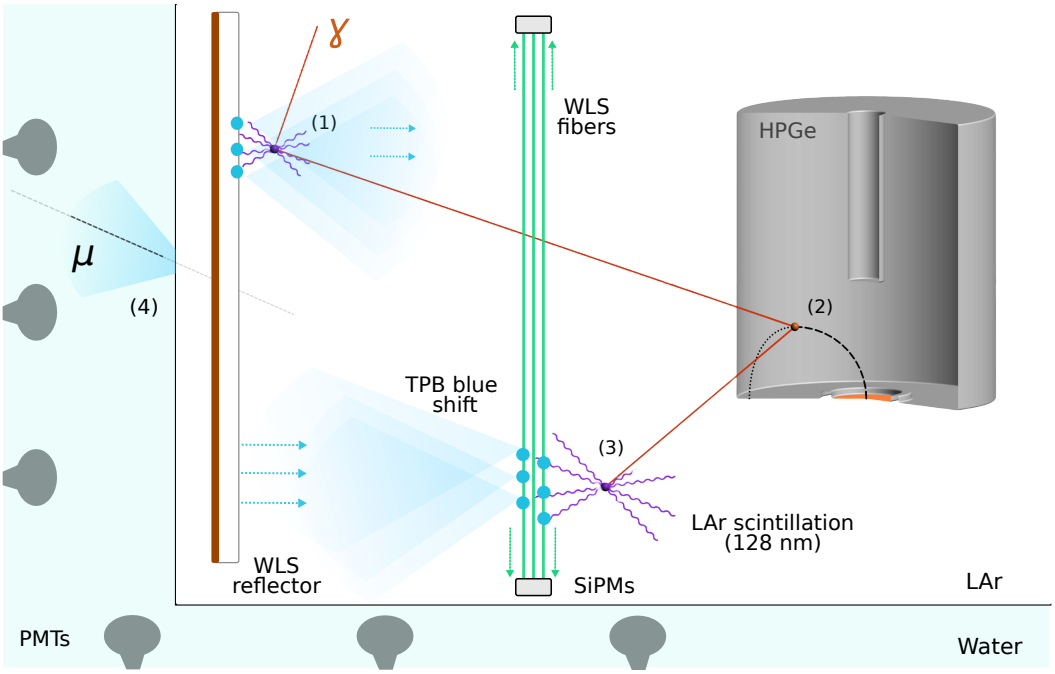

Figure 6.3: Schematic of the background suppression performed by the LAr and muon veto systems. The HPGe crystals are immersed in LAr contained in a cryostat. Energy depositions in LAr (1,3) induce its VUV scintillation. To shift this scintillation light to the blue region, TPB is applied to various surfaces, including the fibers. The WLS fibers absorb the blue light, re-emit it in green, and guide it towards the SiPMs. If the detected light signal is above a certain threshold, the energy deposition in the Ge crystal (2) is tagged. WLS reflectors increase the light collection by shifting VUV light and reflecting blue light towards the fibers. An interaction of a muon within a crystal (not shown) is similarly tagged if it induces LAr scintillation or if the PMTs in the water tank detect Cherenkov light from its passage (4).

The working principle and design of the muon veto system are the same for both GERDA and LEGEND-200. As discussed in Chapter 4, the underground

depth of the LNGS laboratory significantly reduces the muon flux by six orders of magnitude. However, for LEGEND-1000, a few additions will be implemented to mitigate the impact of muon-induced neutrons. One of these is the use of neutron moderating panels, shown in Chapter 8.

LAr serves multiple purposes in combination with HPGe detectors: it cools the crystals to their operating temperature, shields them from radioactive decays originating from the cryostat walls, and serves as an active veto by scintillating in response to energy depositions. This is illustrated in Figure 6.3 by the Compton scatters of a γ ray both in the LAr (1,3) and in the Ge crystal (2). If solely the interaction within the HPGe diode was recorded, this event could lie within the $0\nu\beta\beta$ ROI. This is because the full energy of the γ ray would not be accurately reconstructed due to the partial energy deposition.

Furthermore, this event would not be rejected by PSD, as it produces a single-site scatter within the HPGe crystal, resembling the expected $\beta\beta$ signal (Figure 6.2). By surrounding the detectors and efficiently collecting light from events with partial energy deposition in the HPGe crystal, the LAr system significantly complements the PSD and multiplicity background suppression methods, effectively reducing the Compton background within the ROI.

While the LAr instrumentation design implemented in GERDA was effective in achieving a background-free state, several improvements have been introduced for LEGEND-200. These modifications, as well as future implementations for LEGEND-1000 are discussed in detail in Chapter 8. One notable improvement shown in Figure 6.3 is the WLS reflector, which enhances light collection. This is accomplished by reflecting the light emitted by TPB back to the fibers, as shown in (3), and by shifting and reflecting light induced by events that scatter at a greater distance from the fibers, as shown in (1). The R&D and characterization of these WLS reflectors are among the main topics discussed throughout this thesis, spanning from Chapter 8 to Chapter 11.

PART III

$0\nu\beta\beta$-DECAY SEARCH WITH GERDA AND LEGEND

7

CHARACTERIZATION OF GERDA'S FINAL DATA SET

7.1 THE GERDA EXPERIMENT

The GERmanium Detector Array (GERDA) operated at LNGS for approximately eight years searching for $0\nu\beta\beta$ decay of ^{76}Ge in HPGe crystals [1, 66]. GERDA was the first experiment to employ bare HPGe detectors immersed in LAr [65]. The experiment acquired data during two phases: Phase I, where LAr was employed solely as a coolant and passive shield [66], and Phase II, where a system was introduced to collect scintillation induced by coincident background events in LAr [65], as illustrated in Figure 7.1, and discussed in Section 6.2.

For its Phase II, GERDA incorporated 20 kg of enriched BEGe (^{enr}BEGe) detectors, expanding the total amount of enriched HPGe crystals to ∼36 kg. These HPGe crystals were of various types, including also Coax, and later IC detectors, all of which are described in Chapter 6. The distribution of these detectors within the experimental setup is illustrated in Figure 7.1.

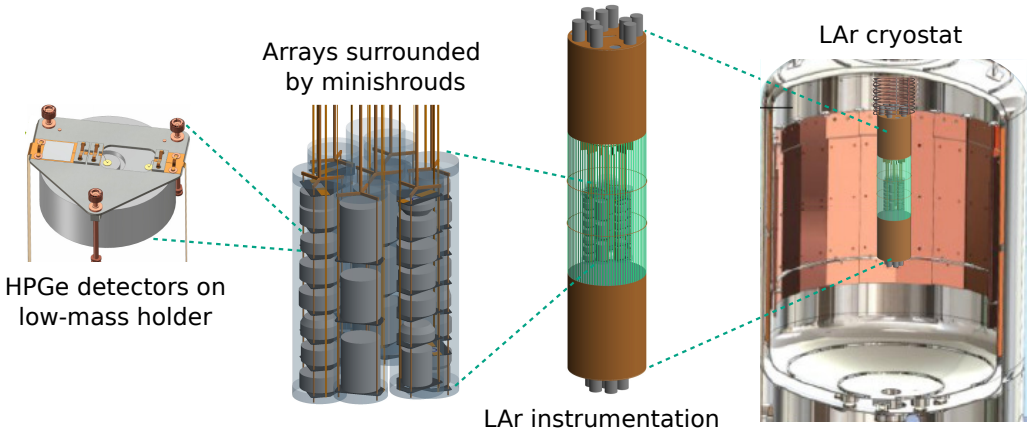

Figure 7.1: Schematic view of the GERDA experiment during Phase II: The HPGe crystals were supported by low-mass ultra-pure silicon plates held by copper strings, and enclosed by TPB-coated nylon minishrouds. Surrounding the seven-string array was the LAr instrumentation, consisting of a curtain of TPB-coated WLS fibers coupled to SiPMs. This setup was contained within two copper shrouds equipped with PMTs, with the inner parts covered in reflective TPB-coated Tetratex. The entire configuration was immersed in 64 m^3 of LAr housed within a stainless steel cryostat lined with copper to reduce radioactivity. Additionally, a 590 m^3 water tank instrumented with PMTs (not shown) served as a muon veto. The ∼1400 m of rock above the lab provides passive shielding against atmospheric muons. Image credit: Ge crystal and cryostat modified from [65], other figures from [63].

Phase II of GERDA began in 2015 and lasted until 2019 when its target exposure of 100 kg·yr was achieved. This chapter is dedicated solely to this period, which was important for the subsequent LEGEND experiment. Besides the LAr instrumentation, several detectors currently operated in LEGEND were introduced and tested during Phase II. The addition of these detectors in GERDA occurred during an upgrade in 2018, which involved some other hardware modifications. The details of this upgrade are discussed in the following section.

7.2 UPGRADE OF GERDA PHASE II

The 2018 upgrade in GERDA can be considered minor compared to the Phase II upgrade conducted in 2015. Although the data-taking period after the 2018 upgrade is still referred to as 'Phase II', when comparing data before and after the upgrade, we refer to the post-upgrade period as Phase II+. The modifications carried out during this 2018 upgrade included:

- introduction of five new IC detectors (9.6 kg), replacing some existing detectors, as shown in Figure 7.2;
- vertical flipping of some detectors, as shown in Figure 7.2;
- addition of new detector holders and cables;
- replacement of the LAr system with a new fiber curtain featuring a higher density of fibers and including a central fiber shroud;
- minor modifications to the mini-shrouds.

One of the main objectives of the work described in the upcoming sections was to characterize the data obtained after these minor upgrades and conduct data quality checks prior to the final data release.

7.3 CHARACTERIZATION OF DATA BEFORE & AFTER THE UPGRADE

This section presents the characterization and stability studies conducted on the legacy dataset of GERDA Phase II. The focus of these studies was to assess any changes in the background following the upgrade works in 2018. For this task, the stability and homogeneity of the complete dataset were examined both before and after the upgrade, taking into account analysis cuts such as PSD and LAr veto.

Datasets, structure & quality cuts

The Phase II data was categorized into before and after the upgrade, and among different types of HPGe detectors, as presented in Table 7.1.

1 Apart from detectors referred to as 'natural', all the discussed detectors discussed in this section are enriched.

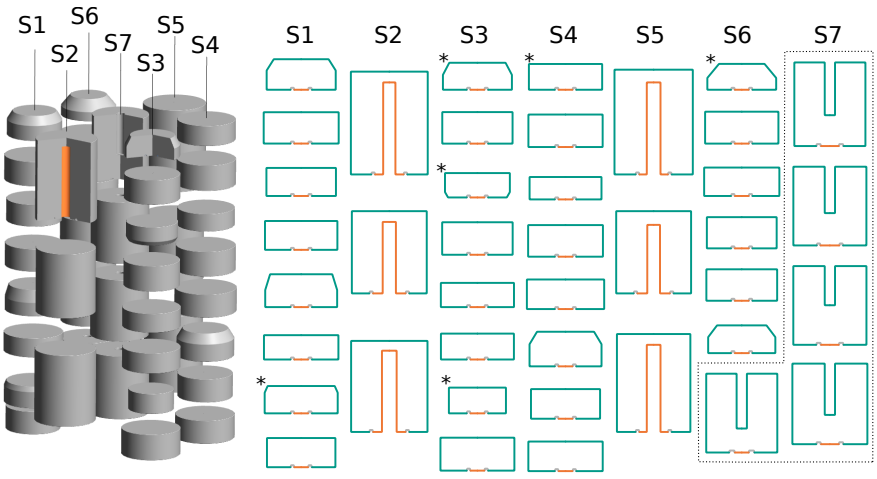

Figure 7.2: Detector configuration during Phase II+: A total of 41 detectors were distributed among seven strings. Most of the detectors, 30 BEGe detectors and 6 Coax detectors, remained installed in the same positions as before the upgrade. A few of the BEGes were however flipped horizontally, which is indicated by (*). The dashed lines highlight the 5 IC detectors, which replaced the natural[1] detectors in the central string (S7), as well as one Coax detector in string S6. Image modified from [108], produced with the code available at [110].

Table 7.1: Datasets and exposure of Phase II & Phase II+ (before & after the upgrade). Exposure values exclude the natural detectors and data where PSD was not applicable.

	Phase II	Phase II+
run numbers	53 to 93	95 to 114
^{enr}BEGe exposure [kg·yr]	31.46	21.87
^{enr}Coax exposure [kg·yr]	28.64	13.18
^{enr}IC exposure [kg·yr]	0.00	8.54
total exposure [kg·yr]:	60.10	43.59

In this study, only high-level blinded data (after processing and energy calibration) was utilized[2]. This data includes flags from analysis cuts and vetoes. To ensure the quality of the data, several cuts were applied. These quality cuts removed non-operational or unstable detectors from the analysis and filtered out the following events: unphysical events such as test pulses, baseline-only events, pile-up events, muon-vetoed events, and events with energy deposition in multiple detectors.

The identification of muon-vetoed events and the discrimination of particles using multiplicity, PSD, and the LAr veto cuts are part of the particle discrimination schemes common to both GERDA and LEGEND, described in detail in Sections 6.1 and 6.2. The LAr and PSD cuts are considered higher-level analysis cuts and are applied later in the data analysis, which is then labeled

2 For a thorough description of the data structure, as well as analysis software, cuts, and blinding procedures, see [109, 114].

as 'after analysis cuts'. The next sections provide energy spectra and rates both before and after applying these analysis cuts.

Combined spectra

Figures 7.3 to 7.5 display the combined spectra of the ^{enr}Coax and ^{enr}BEGe detectors before the upgrade and ^{enr}Coax, ^{enr}BEGe, and ^{enr}IC detectors after the upgrade. The spectra are presented before applying analysis cuts (but including quality cuts) and after implementing PSD, LAr, and both PSD and LAr veto cuts.

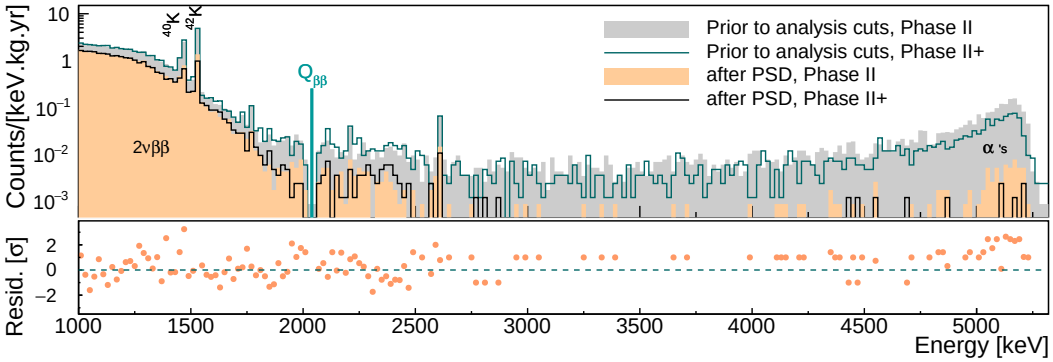

Figure 7.3: Spectra before and after PSD cut, both before and after the upgrade (and prior to unblinding the ROI around $Q_{\beta\beta}$). The subplot shows the number of standard deviations by which the residuals of the spectra (after cut) before and after the upgrade differ from zero[3].

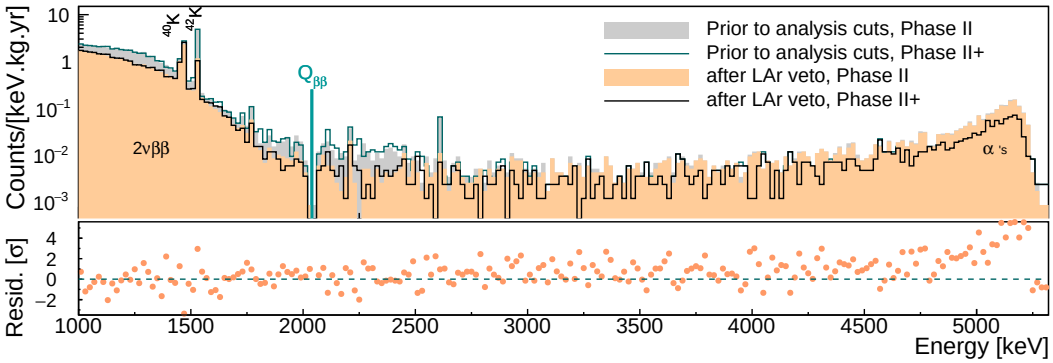

Figure 7.4: Spectra before and after LAr cut, both before and after the upgrade. The subplot shows the number of standard deviations by which the residuals of the spectra (after cut) before and after the upgrade differ from zero.

3 To calculate the residuals in each bin i, the number of counts (N^i) in the spectrum before the upgrade is divided by the respective exposure and subtracted from the same quantity after the upgrade. The uncertainties are calculated as $\Delta N^i = \sqrt{N^i}$, normalized for the respective

Figure 7.3 shows the effectiveness of the PSD cut in suppressing background events from α decays, which dominate the spectrum at high energies (around 5 MeV). The PSD cut also effectively reduces the Compton background, especially below the ^{208}Tl line at 2.6 MeV. This background is also suppressed by the LAr veto cut, as observed in Figure 7.4. Given the complementarity of the cuts, the combined suppression of the Compton background is larger than the individual suppression achieved by each cut, as shown by Figure 7.5.

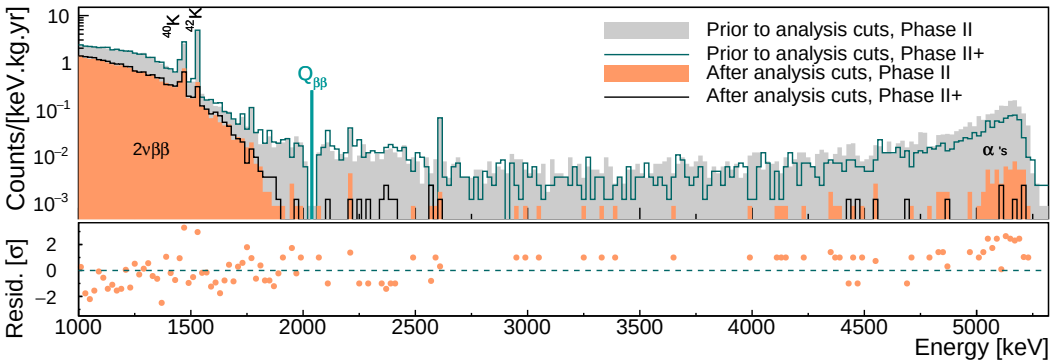

Figure 7.5: Spectra before and after analysis cuts, both before and after the upgrade. The $Q_{\beta\beta}$ energy region, as well as the most prominent spectral features, are marked. The subplot shows the number of standard deviations by which the residuals of the spectra before and after the upgrade differ from zero. For this comparison, only the spectra after analysis cuts are considered.

The residuals of Figure 7.5 show that the event rates before and after the upgrade mostly agree within less than three standard deviations, except for the potassium γ lines at 1461 keV and 1525 keV, as well as around 5 MeV, where the spectrum is dominated by α decays from ^{210}Po. Although the dead layer of the detectors stops most of the α particles (Chapter 4), their decays on the p^+ contact are still detected, often with degraded energy. While ^{210}Po is commonly present in materials as part of the uranium decay chain, direct contamination with ^{210}Po through dust can occur (Chapter 4). The activity from this contamination decays over time with the time constant of ^{210}Po (135.4 d), resulting in a continuous decrease in events in this region.

To further investigate the slight discrepancies around the potassium γ lines, we analyzed the event rates before and after the upgrade, taking into account the following factors: i) detector type, ii) time, and iii) position of the detectors within the arrays. These investigations are discussed in the next sections.

Spectra per detector type

The spectra before and after the upgrade for the ^{enr}BEGe and the ^{enr}Coax detectors, before analysis cuts, are shown in Figure 7.6 and Figure 7.7.

exposure, and propagated in the calculation of the total residual uncertainty which normalizes the residual values.

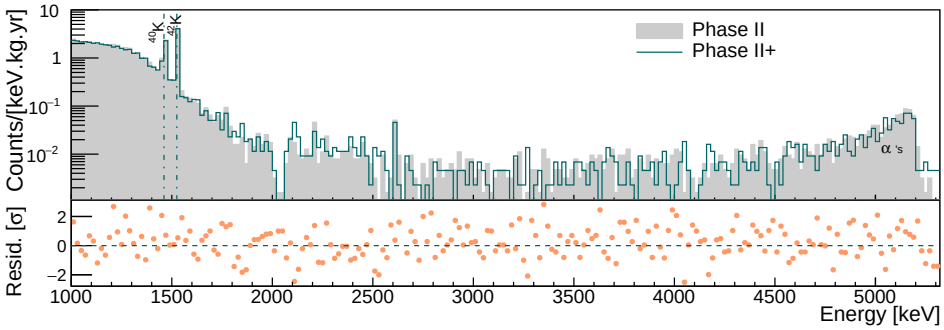

Figure 7.6: Spectra before and after the upgrade for the ^{enr}BEGe detectors.

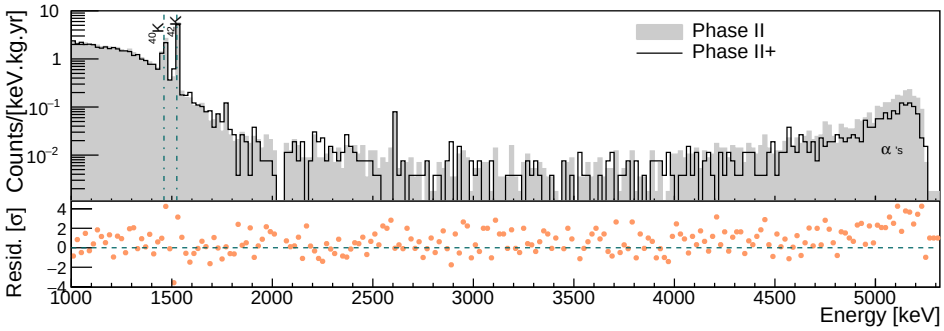

Figure 7.7: Spectra before and after the upgrade for the ^{enr}Coax detectors.

For the ^{enr}BEGe detectors, the spectra before and after the upgrade exhibit good agreement within 3σ, as indicated by the residual subplot. For the ^{enr}Coax detectors, the spectra mostly agree within 3σ, except for the region around the potassium γ lines and the high-energy region dominated by αs. This discrepancy suggests a larger initial contribution of surface αs on the p^+ contact of the Coax detectors. This observation is expected due to the larger size of the p^+ contact in these detectors.

Since there were no ^{enr}IC detectors before the upgrade, their spectrum is compared to that of the ^{enr}BEGe detectors after the upgrade, as shown in Figure 7.8. The differences in this comparison are more significant: the IC detectors exhibit a higher rate of ^{42}K and ^{40}K events, as well as lower contamination from α particles. Furthermore, a pronounced fluctuation around 1.12 MeV is attributed to the presence of the cosmogenic isotope ^{65}Zn, which has a half-life of 224.3 days and decays to ^{65}Cu, which is stable.

The higher cosmogenic component for IC detectors is expected since these detectors were the last ones to be installed underground. The lower rate from α decays for ^{enr}IC detectors may indicate that these detectors were handled in a cleaner manner, avoiding radon plate-out (discussed in Chapter 4).

To gain a better understanding of the discrepancies around the potassium γ lines, particularly for the ^{enr}Coax detectors before and after the upgrade,

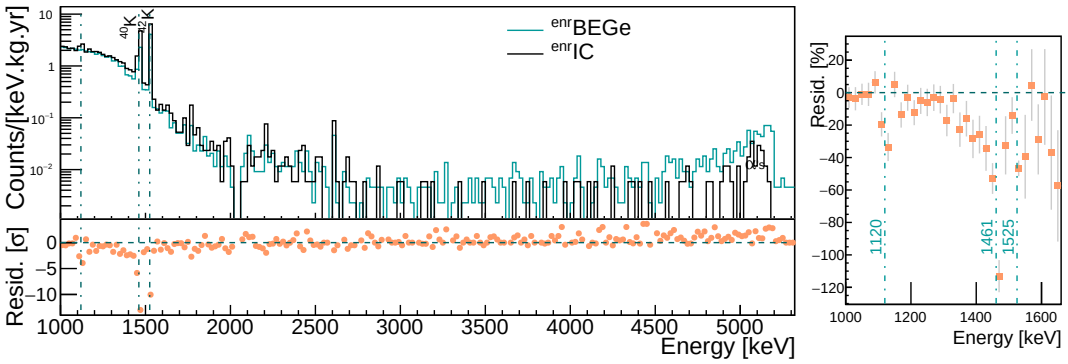

Figure 7.8: Spectra comparison between $^{\text{enr}}$IC and $^{\text{enr}}$BEGe. The panel on the right shows their normalized residuals in % ($^{\text{enr}}$BEGe minus $^{\text{enr}}$IC, normalized by the $^{\text{enr}}$BEGe) zoomed around the large residual discrepancies. The energies of γ lines around these regions are also indicated.

the event rates around these lines were investigated per detector position, as discussed in the next section.

Event rates per detector & position

The left images of Figures 7.9 and 7.10 present the event rates (before analysis cuts) of the ^{40}K and ^{42}K γ lines per detector, both before and after the upgrade. These rates were calculated by summing up the counts within a 20 keV window centered at the nominal γ line energies and subtracting a flat background extracted from neighboring 5 keV bins. The event rates around the $Q_{\beta\beta}$ analysis region were calculated by summing up the counts from 1930 keV to 2190 keV[4], and are shown in Figure 7.13. All rates are normalized by the exposure.

The lower panels of each plot show the number of standard deviations (nσ) by which the residuals differ from zero. The gray line represents the expected mean of zero when there are no differences between the before and after the upgrade. The orange line represents a zero-order linear fit of the nσ values.

To gain a better understanding of the relationship between these event rates and the positions of the detectors in the array, the rates are displayed on a map according to the string and z-position of each detector. These maps are provided in Figures 7.9 and 7.10 (right). Additionally, the same maps after applying the LAr veto cut are displayed in Figure 7.11.

Based on the presented maps and graphs, we can observe the following features:

- Prior to applying the LAr veto cut, the rates from the 1461 keV line from ^{40}K are more intense for the central string (S7). This γ line is not suppressed by the LAr veto.

4 Excluding 5 keV regions around the 2104 keV and 2119 keV γ lines from ^{208}Tl and ^{214}Bi, as well as 25 keV around $Q_{\beta\beta}$ since this window was blinded.

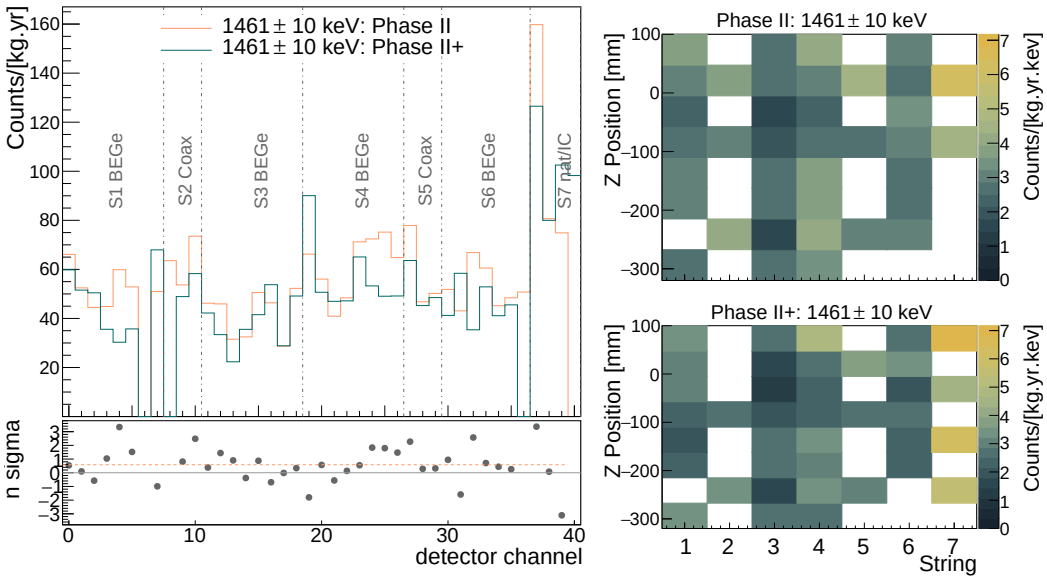

Figure 7.9: Left: Event rate around the 1461 keV line from ^{40}K displayed per detector before and after the upgrade. The detectors are shown per channel number, and the vertical lines and labels indicate the distributions within the strings S1 to S7. While most of the detector channels remained the same after the upgrade, string 7 has been largely modified, as illustrated in Figure 7.2. The subplot shows the residuals between the two graphs and a linear fit. Right: The same event rates are displayed per detector central Z-position and string, both before (top) and after the upgrade (bottom). Bin sizes do not correspond to detector sizes, thus strings with a lower number of detectors show more empty bins. One top detector in string 2 is empty in the Phase II+ graphs since it stopped taking physics data after the upgrade.

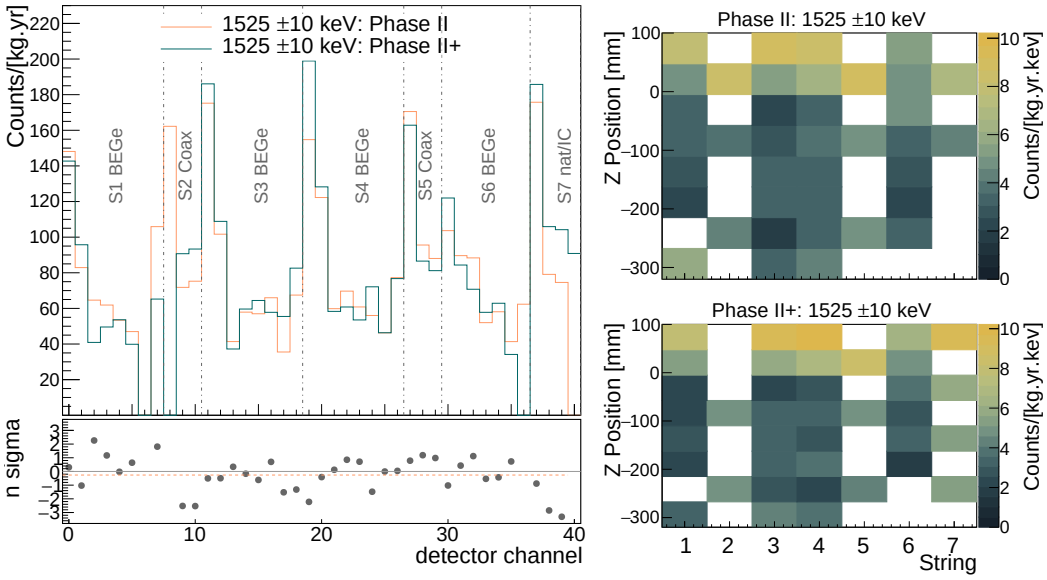

Figure 7.10: Left: Event rate around the 1525 keV line from ^{42}K displayed per detector before and after the upgrade. Right: The same event rates are displayed per detector Z-position and string, both before (top) and after the upgrade (bottom).

- The rates from the 1525 keV γ line from ^{42}K are higher for the top detectors, but they are significantly suppressed by the LAr veto, leading to a more uniform distribution after applying the LAr veto cut.

- The patterns in the maps and graphs are mostly consistent before and after the upgrade, with residuals mostly within 3σ, and the fitted nσ values close to zero.

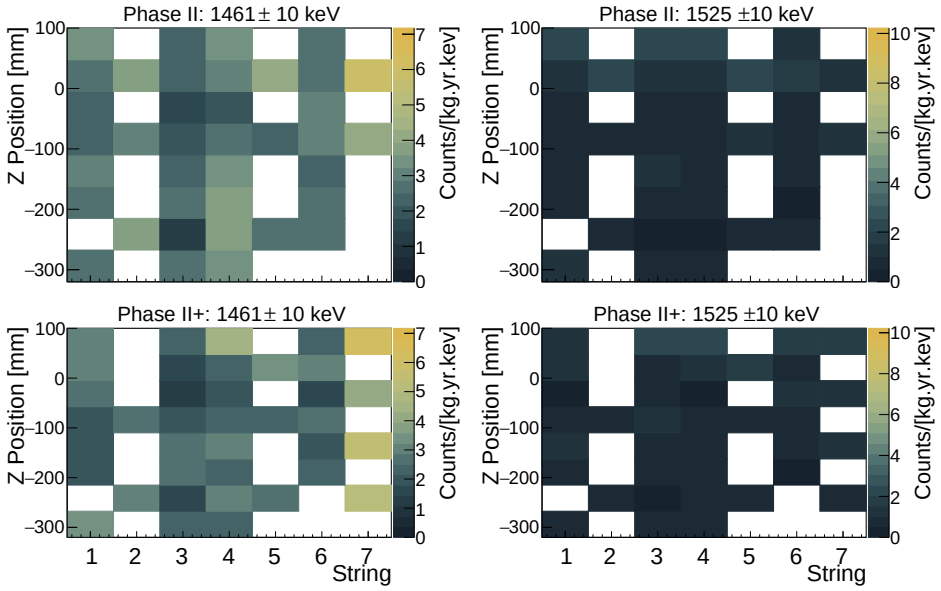

Figure 7.11: Event rate around the 1461 keV (left) and 1525 keV line (right) per detector Z-position and string both before and after the upgrade. All rates are shown after the LAr veto cut was applied.

The higher rates of potassium lines observed in the IC detectors compared to BEGe detectors can be explained by their position in the central string. The rates from the IC detectors are approximately as high as those previously observed from the natural detectors in the same string. The rate of the ^{40}K line is related to the natural radioactivity of materials surrounding the detectors, such as cables, fibers, and minishrouds. In the case of the central string, the content of these materials was likely higher. Although the LAr veto does not suppress the γ line of ^{40}K given it is a single gamma emission, background suppression was achieved through the PSD cut, as demonstrated in Figure 7.5. Given its lower energy, this γ line does not contribute to background events within the ROI for the $Q_{\beta\beta}$ search [63].

The rate from the decay of ^{42}K was higher in the top detectors, potentially due to convection and the electric field generated by the detectors and cables, which can drift ions in that direction [63]. The LAr veto effectively suppressed this line, with an efficiency of approximately 75%, because the decay involves a β-γ cascade, resulting in energy deposition by the β particle in the LAr. Both βs and γs from ^{42}K are further suppressed by the PSD cut (Section 6.1).

Time stability of event rate

To assess the stability of the rates per detector, the rates are plotted per run for each detector. This analysis is performed both before and after applying the LAr veto cut, considering four energy regions: i-ii) a 20 keV window centered around the 1525 keV and 1461 keV potassium γ lines, iii) 1000 keV to 5500 keV, and iv) 1000 keV to 1300 keV. The last region serves as a reference for stable event rates, as this region is dominated by $2\nu\beta\beta$ events.

The rates and their errors are calculated following the aforementioned methodology. An illustrative example showing the time stability for an $^{\text{enr}}$Coax detector is presented in Figure 7.12.

Similar graphs were constructed for each detector and subsequently analysed. Runs exhibiting rates deviating more than 3σ from the mean were identified as outliers and documented in Table 7.2 and Table 7.3 for the pre-LAr veto and post-LAr veto cuts, respectively.

Table 7.2: Summary table of the outliers observed in the time stability check of Phase II data for three relevant energy regions. Detectors are identified by their channel numbers. Values for which the total number of events (N) is <= 10 are marked with "Y".

Channel	Energy range	Run number	N_σ away from mean	N <= 10
12	1525 ± 10 keV	63	3.5	Y
20	1525 ± 10 keV	87	3.6	Y
29	1525 ± 10 keV	95	3.3	N
31	1525 ± 10 keV	109	3.1	Y
37	1461 ± 10 keV	55	4.8	Y
37	1461 ± 10 keV	101	4.6	Y
38	1461 ± 10 keV	97	3.8	Y

Table 7.3: Summary table as before, but after LAr veto.

Channel	Energy range	Run number	N_σ away from mean	N <= 10
37	1461 ± 10 keV	55	4.6	Y
37	1461 ± 10 keV	101	4.2	Y
38	1461 ± 10 keV	97	4.0	Y

The summary tables show that no statistically significant outlier was found. The majority of the initially flagged rates correspond to shorter runs characterized by a low count rate. The event rates were thus found to be consistent during each of the investigated periods (Phase II and Phase II+).

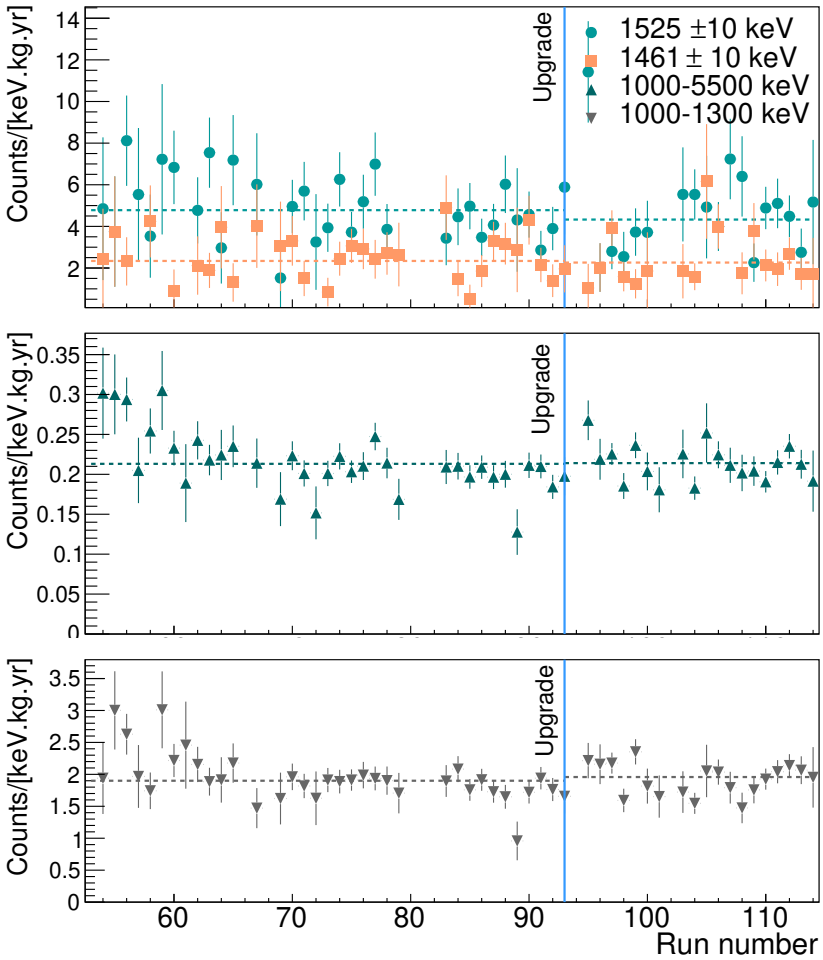

Figure 7.12: Event rate, prior to analysis cuts, per run for an ^{enr}Coax detector (ch 27).

Discussion

The initial discrepancies observed in the rates of the potassium lines for Coax and IC detectors were found to be dependent on the positions of the detectors and were not caused by the upgrade. Although the detector positions generally remained unchanged after the upgrade, it is worth noting that one Coax detector with a high ^{42}K rate (due to its top position) became non-operational for physics data taking after the upgrade. This accounts for the observed difference when comparing the Coax combined spectra. Thus no actual discrepancy was observed when comparing the rates per detector before and after the upgrade. Additionally, no discrepancies were observed in the event rates per detector over time.

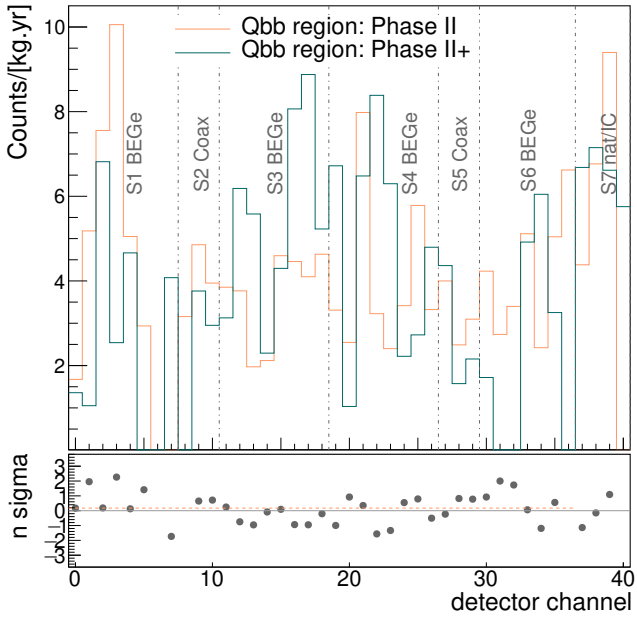

Figure 7.13: Event rate (before analysis cuts) around the $Q_{\beta\beta}$ region displayed per detector before and after the upgrade. The residuals agree within less than 3σ.

Similar studies of rate stability were conducted for other energy regions and after applying PSD (or PSD & LAr veto) cuts and the conclusions remained consistent. Apart from the decrease in α decays, there was no significant indication of a change in the background after the upgrade. Furthermore, the slight decrease in the background from α decays did not result in noticeable differences in the background around the $Q_{\beta\beta}$ region after the upgrade, as illustrated in Figure 7.13.

It is important to note that both α decays and ^{42}K decays, which have the potential to contribute to the background in the $0\nu\beta\beta$-decay ROI (Chapter 4), are effectively suppressed by the PSD and LAr cuts. The effectiveness of this suppression, as observed in Figure 7.5, played a crucial role in achieving the lowest background in the field by GERDA. These remarkable results obtained from the Phase II data are discussed in the next section.

This chapter presented the characterization of the Phase II legacy data from GERDA, focusing on the stability and the homogeneity of the datasets before and after the 2018 upgrade, considering detector type, time, and detector positions within the array.

The results indicated overall agreement between event rates pre- and post-upgrade, with overall homogeneity across different detector positions. Although slightly different rates were observed for detectors at the top and center of the array, these differences were not significant, as the rates became more homogeneous after applying analysis cuts. The slight decrease in α decays also had no impact on the background around the $Q_{\beta\beta}$ region.

The findings of this analysis, along with dedicated analyses performed by collaborators[5], supported the implementation of a single BI for all detectors, irrespective of their type, position within the array, or time, improving upon past analyses that utilized different BI for different detector types [115, 116].

The legacy Phase II data, comprising over 100 kg·yr of exposure, was analyzed using a single BI and published in 2020 as *Editor's Suggestion* in Physical Review Letters [1]. The energy distribution of events in this data is displayed in Figure 7.14. After applying all analysis cuts, the background rate within the analysis window was remarkably low: 5.2×10^{-4} counts/(keV.kg.yr), as observed in the corresponding bottom panel.

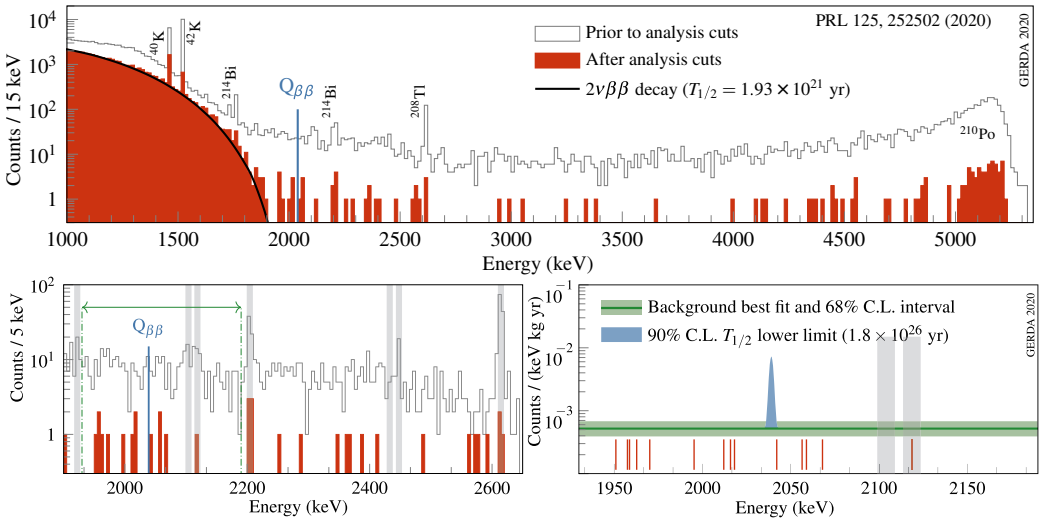

Figure 7.14: Top: Energy distribution of GERDA Phase II events (103.7 kg·yr of exposure) before and after analysis cuts. The main background contributions to the spectra are labeled. Bottom: enlarged views of the energy spectra including the full analysis window marked by dashed lines (left); and zoomed within this window (right), normalized to the exposure and including both the extended likelihood fit and the expected $0\nu\beta\beta$-decay signal for $T^{0\nu}_{1/2}$ equal to $1.8 \cdot 10^{26}$ yr. Figures from [1].

5 Other collaborators specifically worked on quantifying the statistical significance of the homogeneous background hypothesis, focusing around the $Q_{\beta\beta}$ region. Their results also showed no significant indication of non-homogeneities.

The analysis of the remaining events after all cuts and unblinding of the 25 keV window around $Q_{\beta\beta}$ favored the no-signal hypothesis, resulting in the strongest lower limit on $T^{0\nu}_{1/2}$ at that time. Combining with Phase I data, a total exposure of 127.2 kg·yr yielded a result of $T^{0\nu}_{1/2} > 1.8 \cdot 10^{26}$ yr (at 90% C.L.).

This lower limit was subsequently translated into upper limits on the effective Majorana mass, using the relations and assumptions described in Chapter 2 and in [1]. The obtained result is $\langle m_{\beta\beta} \rangle < 79 - 180$ meV (at 90% C.L.). This range incorporates the uncertainties in nuclear matrix elements, which are a central topic of investigation in this thesis and for the MONUMENT experiment.

Although another $0\nu\beta\beta$-decay-search experiment has recently surpassed these limits on $T^{0\nu}_{1/2}$ and $m_{\beta\beta}$ [41], the background index achieved by GERDA remains the lowest in the field, demonstrating the combined power of high-resolution HPGe detectors and effective background suppression techniques. This achievement paved the way for the subsequent LEGEND experiment, which is the focus of the next chapters.

8

THE LEGEND EXPERIMENT

The Large Enriched Germanium Experiment for Neutrinoless $\beta\beta$ Decay (LEGEND) is a collaborative effort that brings together the expertise and resources of the GERDA and MAJORANA experiments. The primary objective of LEGEND is to achieve a high sensitivity to $0\nu\beta\beta$ decay and potentially make a groundbreaking discovery.

By targeting a sensitivity to $T^{0\nu}_{1/2}$ beyond 10^{28} yr, LEGEND aims to cover the entire inverted mass ordering scenario (Figure 2.3). This goal is pursued through two phases: LEGEND-200, with a target mass of 200 kg of enriched HPGe, and LEGEND-1000, which aims to operate 1000 kg of enriched HPGe for ten years. LEGEND-200 started physics data taking this spring with a HPGe mass of about 140 kg. The experiment was built and commissioned between 2020 and 2023, re-utilizing most of the infrastructure from GERDA at LNGS, including the instrumented water tank and the cryostat, shown in Figure 8.1.

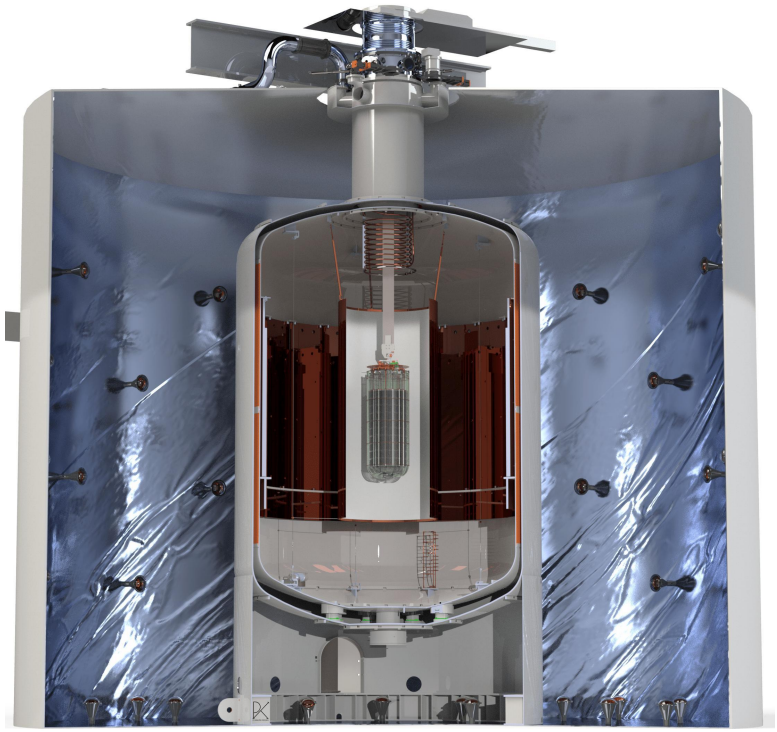

Figure 8.1: LEGEND's cryostat inside the water tank: the tank is instrumented with PMTs and serves as a muon veto. The cryostat contains the HPGe detectors immersed in LAr and surrounded by the fiber instrumentation of the LAr system. Wavelength shifting (WLS) reflectors further surround the detectors and fibers. At the top of the cryostat, a shutter gives access to a lock (not shown), which can be accessed from the clean room above the tank. Figure credit: P. Krause.

LEGEND-200 aims for a sensitivity to $T^{0\nu}_{1/2}$ beyond 10^{27} yr within five years of operation. This requires a modest background reduction of 2.5 compared to GERDA's [39]. To achieve this background level, some of the improvements LEGEND employs are:

- Newly developed IC detectors with enrichment up to 92%. These large detectors provide excellent energy resolution and PSD at a reduced background rate per mass (Chapter 6) [39, 113];
- Self-vetoing radio-pure detector holders made of PEN [117];
- Low-background near-detector parts from MAJORANA, such as the electroformed copper and low-noise front-end electronics [39];
- Improvements in the LAr system, which we discuss below.

8.1 WLS REFLECTORS FOR THE LAR INSTRUMENTATION OF LEGEND

The LAr system has played a major role in suppressing background in GERDA[1]. For LEGEND-200, the LAr instrumentation was modified in order to decrease its radioactivity while increasing its efficiency. These modifications included:

- Removal of top and bottom PMTs, due to their lower radio-purity compared to the fibers.
- Increase in the fiber density to guarantee efficient light collection despite the removal of the PMTs.
- SiPM readout on the bottom sides of the fibers, in addition to the readout at the top, further improving the efficiency of light collection.
- Installation of a system that monitors the attenuation length and triplet lifetime of LAr, key indicators of the optical quality and light yield of the LAr [87].
- Installation of a WLS reflector surrounding the fiber array in order to enhance the light collection, as illustrated in Figure 8.2.

The WLS reflector (or short WLSR) is essential for LEGEND-200, as the fibers are now much closer to the HPGe detectors and collect less direct light from events that scatter at greater distances. The WLSR was thus optimized to be at an approximate distance of 40 cm from the HPGe crystals – a value about twice the attenuation length of 2.6 MeV γ rays in LAr (Table 4.1). By shifting VUV light towards the blue and reflecting it towards the fibers, the WLSR not only enhances the light collection from the scatters a bit further away, but also from nearby ones. This is because the WLSR 'recovers' blue light emitted

1 The exact suppression factor depends on the specific type of background and its location within the experiment. Estimations from [118] indicated survival probability (after LAr veto in the $0\nu\beta\beta$-decay analysis window) of 0.3% for ^{228}Th, 15% for ^{238}U and 10% for ^{60}Co.

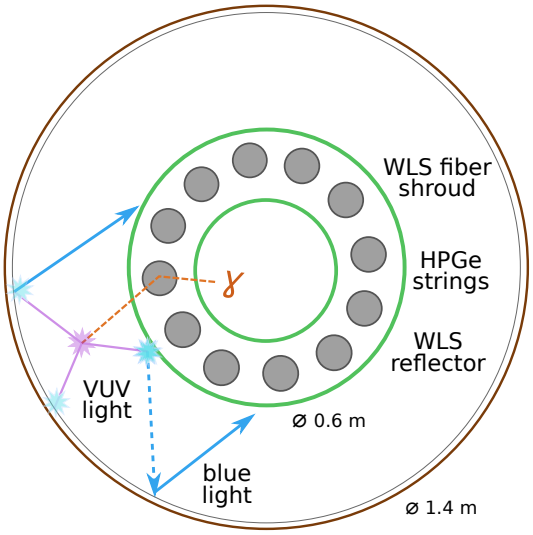

Figure 8.2: The strings of HPGe crystals are surrounded by WLS fibers arranged in two concentric cylinders. The fibers are coated with TPB, which absorbs the VUV light induced by an event in LAr and re-emits it at wavelengths that can be absorbed and re-emitted by the fibers (as in Figure 5.1). The fibers re-emit the light in green, which undergoes internal reflections until reaching the SiPMs. TPB-coated WLS reflectors surround the fibers, shifting VUV scintillation light and reflecting visible light towards the fibers[2].

in all directions by TPB by reflecting it towards the fibers. This process is represented by the reflection of the dashed arrow in Figure 8.2. Furthermore, the WLSR reduces the dead time from the LAr system by preventing light from external ^{39}Ar decays from reaching the fibers within the shroud.

For the large scale of LEGEND-1000, extensive coverage of WLSR will be required. In the baseline design, 400 HPGe crystals (1000 kg) are housed within an electroformed copper reentrant tube [39], contained within a cryostat filled with atmospheric LAr, as depicted in Figure 8.3.

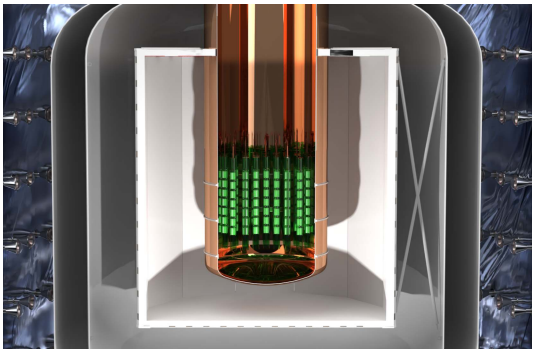

Figure 8.3: LEGEND-1000 design. The inner copper tube (⌀ 1.9 m) houses the detectors and the fiber instrumentation submerged in ∼20 tons of underground LAr. The tube is inside a 10 m tall (⌀6 m) cryostat, instrumented with neutron moderating panels, filled with ∼180 tons of atmospheric LAr. A PMT-instrumented water tank contains the cryostat and serves as a muon veto. Experimental site: LNGS. Fig. credit: P. Krause.

The volume within the copper tube is filled with underground LAr, which has lower levels of cosmogenic ^{39}Ar and ^{42}Ar isotopes[3]. In order to maximize light collection within this volume, the inner copper walls will be covered with WLSR, similar to the current implementation in LEGEND-200. For LEGEND-1000, a TPB in-situ coating is not viable. While the copper tube (⌀ 1.9 m) is

2 Further details on on the cooling, shielding, and vetoing capabilities of the LAr instrumentation, as well as the muon veto, are provided in Section 6.2. Further technical specifications of the fibers, SiPMs and monitoring system are provided in [87], and the LAr scintillation and WLS mechanisms are detailed in Chapter 5.

3 This depletion of cosmogenic isotopes in LAr is crucial for LEGEND-1000 to achieve the ∼ 10 fold background reduction, compared to LEGEND-200.

not much larger than the WLSR (⌀ 1.4 m), its distinct inner volume poses challenges for the vacuum and setup necessary for in-situ evaporation.

In the atmospheric argon part, the light collection system serves multiple purposes. Firstly, it allows for tagging γs that interact outside the copper tube, but could still reach the HPGe crystals. Secondly, the system plays a crucial role in detecting events correlated with neutron capture in HPGe. As discussed in Section 4.2, the suppression of this background, mostly caused by muon-induced neutrons, is essential for operating LEGEND-1000 at LNGS. These neutrons are primarily produced within the LAr and its cryostat [67]. While neutron moderators can partially prevent them from reaching the HPGe crystals, the instrumentation of the atmospheric LAr volume further enhances background suppression by tagging γs resulting from neutron interactions, such as the production of ^{41}Ar, which is often associated with the neutron-induced background in the HPGe detectors, as detailed in [39, 67].

The design of the instrumentation for this component is still ongoing, and various possibilities are considered, such as surrounding the neutron moderators and the outer part of the copper tube using WLS fibers or light guides covered with WLS while covering the tube and cryostat walls with WLSR. Regardless of the design, the atmospheric argon system requires extensive WLS and WLSR coverage, approximately ten times larger (or more) than the currently employed. To meet these requirements, alternative scalable options for WLSR based on PEN films have been tested.

The next three chapters of this thesis present the characterization of several TPB coatings and PEN films combined with reflectors. The goal was to develop and characterize an efficient WLSR not only for LEGEND but also for future large-scale LAr-based experiments or practical UV-light detectors. These chapters are presented in a sequential manner, following the timeline illustrated in Figure 8.4.

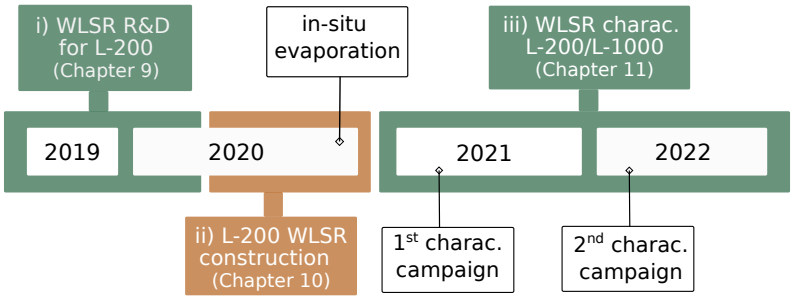

Figure 8.4: The WLSR work for LEGEND is presented here in three parts. The first two chapters describe the R&D, construction, and characterization of the WLSR specifically designed for LEGEND-200: Chapter 9 presents the measurements conducted to select efficient and radiopure WLSR materials; Chapter 10 focuses on the construction of a setup for the in-situ evaporation of TPB inside the LEGEND-200 cryostat. Chapter 11 details the characterization of the WLSR with microscopy and in LAr, including a comprehensive investigation of PEN thin films, which was conducted during two separate measurement campaigns.

9

R&D OF WAVELENGTH-SHIFTING REFLECTORS FOR LEGEND-200

In GERDA, TPB was applied to the WLS fibers through vacuum evaporation, and to the Tetratex® (TTX) of the copper shrouds by dipping. These coatings were performed ex situ, and the coated materials were later installed in the cryostat via the lock system. For the $\sim$13 m^2 of WLSR required for LEGEND, the installation via the lock system ($\varnothing$ 0.8 m) was not possible without bending the materials due to the larger diameter of the WLSR.

As discussed in Section 5.2, TPB coatings are highly efficient, especially when applied through vacuum evaporation. While TPB could still be applied to the WLS fibers in LEGEND, its fragile vacuum-evaporated coatings would not withstand the bending and rolling required for the WLSR installation. The design considerations for the WLSR thus included the mechanical stability of the WLS coating and the preservation of the WLSR quality after installation. On the reflector side, TTX is highly reflective but thin and flexible, necessitating additional mechanical support.

To address the challenges of installing a large WLSR in LEGEND, various options for reflectors, WLS materials, and coating thickness were explored. The goal was to investigate the optical properties of more mechanically stable materials, such as PEN films and standalone copper reflective foils, and to evaluate the trade-off between optical efficiency and mechanical stability. The results of this study are presented in the following sections. For more information on TPB and PEN, please refer to Section 5.2.

9.1 OPTICAL CHARACTERIZATION OF WLSR MATERIALS WITH UV-VIS LIGHT

An efficient PEN or TPB-based WLSR should efficiently reflect the light re-emitted at wavelengths from 360 nm to 600 nm. As a first R&D step, we thus measured the reflectance of a few substrates and quantified the effective absorption of the TPB and PEN films in response to these wavelengths. This range corresponds to the visible spectrum where the shifters predominantly emit light – this will be referred to as vis throughout our discussion.

Samples

The samples investigated in this chapter are listed in Table 9.1. The microporous PTFE-based film TTX was acquired from Donaldson with a thickness of 254 µm [119]. Pieces of TTX were attached to copper plates, which served as mechanical support for the thin reflective film (Figure 9.1, left). Given

Table 9.1: Sample list: the short sample names are shown in the first column. The WLS and reflective films were first measured separately (bare samples). Then, the combinations of WLS films on reflective films (WLSR samples) were measured. All PEN samples are sanded. TPB$^{(*)}$ was deposited on thin low-reflective glass, and its measurement is thus considered to be approximately that of 'bare' TPB.

Bare Samples

Sample name	Film material	Film thickness
TTX	Tetratex®	254 µm
Cu foil	Copper thin foil	50 µm
PEN	Polyethylene Naphthalate	125 µm
TPB$^{(*)}$	Tetraphenyl Butadiene	3.0 µm

WLSR samples

Sample name	Reflective film	WLS film	WLS thickness
TTX + TPB	TTX	TPB	0.2, 0.8, 1.0 µm
TTX + PEN	TTX	PEN	125 µm
Cu foil + TPB	Cu foil	TPB	0.8 µm

its advantageous mechanical stability and radiopurity, the copper foil was also investigated as a reflective substrate for TPB deposition. TPB was then vacuum evaporated onto the surfaces of the copper foil (shown in Figure 9.1, right), TTX, and glass substrates. The glass substrates were used to obtain TPB samples without reflective backing and for later measurement of the evaporation thickness (performed with a profilometer as in [120]).

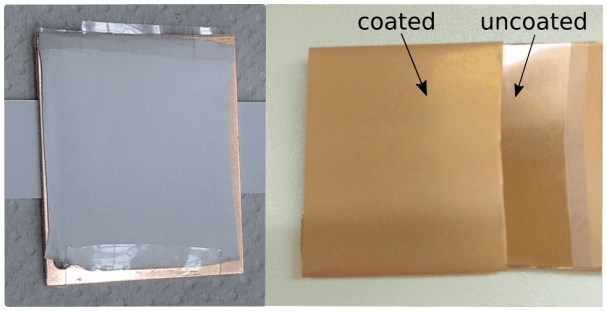

Figure 9.1: TTX sample attached to a copper plate (left) and a copper foil partially evaporated with TPB (right). The TPB coating changes the appearance of the foil, which becomes slightly white and diffusive.

Teonex® PEN film was acquired from Goodfellow [121] with a thickness of 125 µm, biaxial orientation and grade Q53. The film was sanded with grade P240 sandpaper in random directions, then ultrasonic cleaned in a bath of isopropanol. One piece of PEN was attached (with an air gap in between) to TTX.

Setups

These measurements were performed at the Technical University of Munich (TUM) using a LAMBDA 850 UV/vis spectrophotometer from PerkinElmer with a 150 mm integrating sphere (IS) and a Cary Eclipse spectrophotometer. In the IS, the light reflected (or re-emitted) by the samples is integrated at all

angles. As part of the light from samples with TPB or PEN is absorbed by them and shifted to longer wavelengths, we used the Cary Eclipse spectrophotometer to resolve the emission wavelengths and decouple these components. As shown schematically in Figure 9.2, both setups have monochromators that precisely select the wavelength of light that is directed towards the sample. However, while the first provides the integrated angular response (hemispherical reflectivity), only the latter can resolve the wavelength of light that exits the sample.

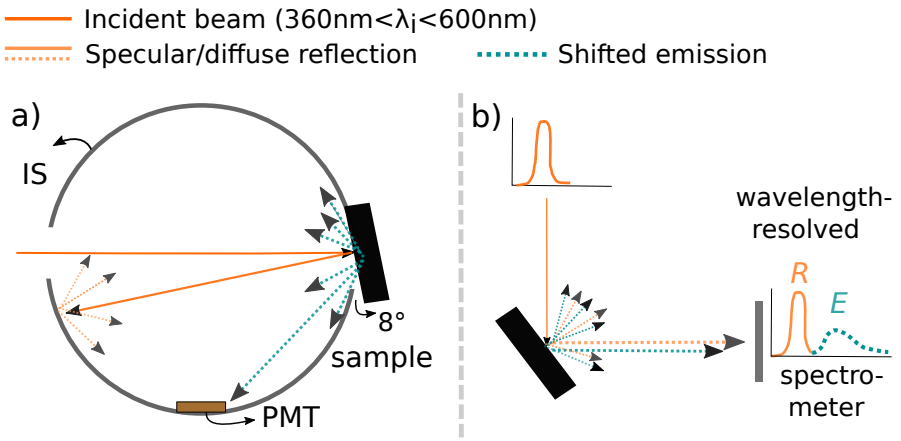

Figure 9.2: a) In the integrated measurement, the light enters the IS and reaches the sample, which is at an angle of 8°. Most of the diffuse and specular reflection of the sample are integrated by the IS before detection by a Hamamatsu R955 PMT [122]. b) In the wavelength-resolved measurement, the spectra of the reflected/scattered light (R) and shifted emission (E) are measured by a calibrated spectrometer. In both setups, the sample holder backing the sample was not reflective[1].

Procedures, Analysis and Results

The samples listed in Table 9.1 were measured in air at room temperature. The setup with the IS was first calibrated using a spectralon standard reflector. The TTX sample was repeatedly measured as a control of systematic uncertainties, which were found to be negligible. Figure 9.3 shows the integrated intensity measured with the IS.

For the samples that do not shift light, the measured intensity is the absolute reflectance of the sample. For the samples with WLS, this intensity is the sum of the light reflected (or back-scattered) by the sample and the light absorbed by the WLS and then emitted at longer wavelengths. To decouple these contributions, we used the wavelength-resolved measurements shown in Figure 9.2 (b). In these measurements, a total of 12 spectra were acquired

1 To additionally prevent stray light and second-order peaks from reaching the photodetector in (b), excitation and emission filters were used, which blocked light outside the ranges from 335 nm to 620 nm and from 360 nm to 600 nm, respectively.

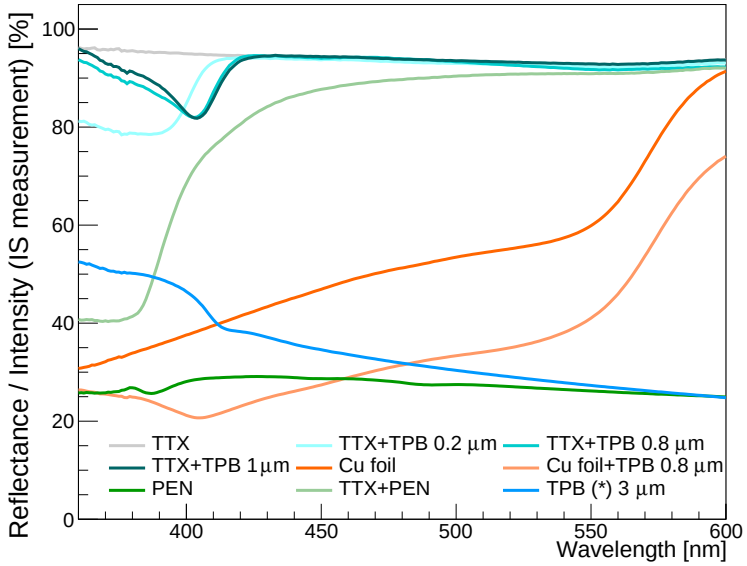

Figure 9.3: Absolute reflectance (or intensity) measured with the IS.

for each sample: one per incident wavelength (λ_i) from 370 nm to 590 nm, with a 20 nm step[2]. An example is shown in Figure 9.4, top.

We then integrated the reflection $R(\lambda_i)$ and emission $E(\lambda_i)$ components of each λ_i-spectrum and calculated the fraction due to the emission component:

$$E_f(\lambda_i) = \frac{E(\lambda_i)}{E(\lambda_i) + R(\lambda_i)}. \tag{9.1}$$

This fraction is used to correct the integrated intensity $I_{IS}(\lambda_i)$ of WLS samples measured with the IS as shown in Figure 9.4 (bottom) and described by the following equation:

$$I_{IS}^{corr}(\lambda_i) = I_{IS}(\lambda_i) \cdot [1 - E_f(\lambda_i) \cdot \mathcal{F}(\lambda_i)], \tag{9.2}$$

where $\mathcal{F}(\lambda_i)$ is a correction for the PMT response in the wavelength regions of the two components [122]. For the TTX+WLS samples, $I_{IS}^{corr}(\lambda_i)$ can be written as:

$$I_{IS}^{corr}(\lambda_i) = I_R^W(\lambda_i) + I_{TR}^*(\lambda_i), \tag{9.3}$$

where $I_R^W(\lambda_i)$ is the portion of light that is directly reflected (or scattered) by the WLS film, which corresponds to the $I_{IS}^{corr}(\lambda_i)$ of the shifters measured without reflective backing. $I_{TR}^*(\lambda_i)$ is a more complex convolution of processes: a fraction of the total light intensity traverses the WLS film (with probability $I_T^W(\lambda_i)$), is reflected by TTX with probability $R_{TTX}(\lambda_i)$ (known from Figure 9.3), and then traverses the film again. This can be approximately described as:

$$I_{TR}^*(\lambda_i) \approx I_T^W(\lambda_i) \cdot R_{TTX}(\lambda_i) \cdot I_{T'}^W(\lambda_i) \cdot [1 + I_\Gamma(\lambda_i)], \tag{9.4}$$

2 The entire procedure was performed at 30° and 45°: no significant dependence on the angles of incidence was observed.

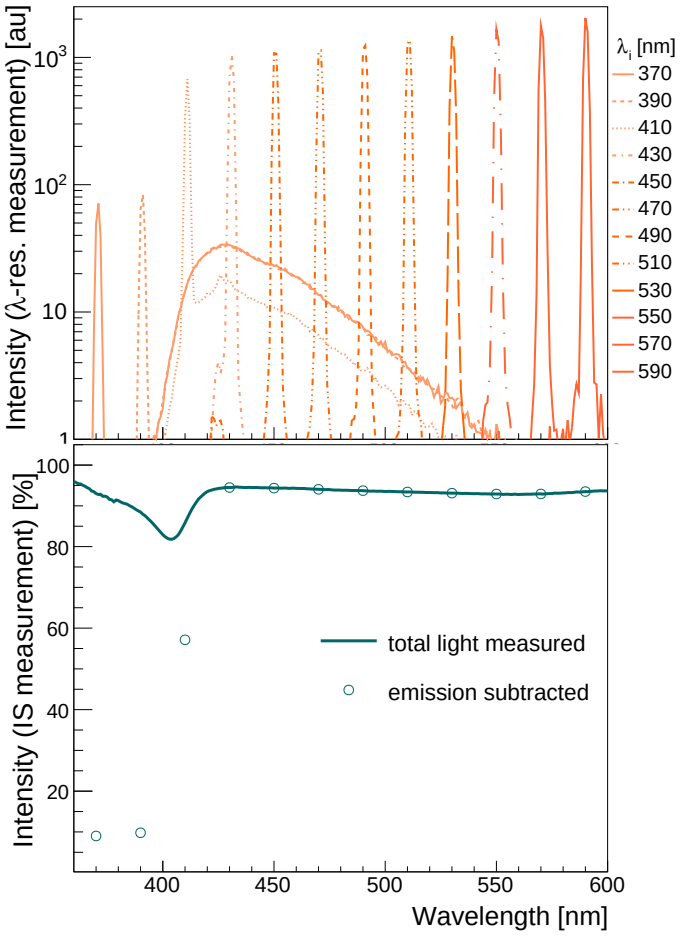

Figure 9.4: Measurements of a TTX+TPB sample. Top: Wavelength-resolved spectra for each λ_i. The peak of reflected light $R(\lambda_i)$ is at the position of λ_i, and for $\lambda_i \lesssim 410\,\text{nm}$, a broad peak of shifted emission $E(\lambda_i)$ is also present. Bottom: Integrated intensity $I_{IS}(\lambda_i)$ before (solid line) and after (○) correction of the emission fraction. Error bars are not shown given they are negligible, as aforementioned.

where $I_\Gamma(\lambda_i)$ is a correction factor that accounts for multiple scatters between the film and TTX[3], and we consider $I^W_{T'} \approx I^W_T$. Equation 9.3 and Equation 9.4 show that the $I^{corr}_{IS}(\lambda_i)$ of the WLSR combinations is a measure of both their efficiency in reflecting vis light, and the vis transparency of the WLS films, $I^W_T(\lambda_i)$ - which can be thus extracted from these equations. We can then obtain the effective absorption fraction of the PEN and TPB films for the vis wavelengths:

$$I^W_\alpha(\lambda_i) = 1 - I^W_R(\lambda_i) - I^W_T(\lambda_i). \tag{9.5}$$

The results are shown in Figure 9.5. For the absorption fraction of the TPB films, we assumed a ±60% uncertainty on the estimation of $I^W_R(\lambda_i)$ from TPB$^{(*)}$ - given that the TPB thickness was larger and its substrate was not completely non-reflective[4]. The resulting errors (shaded bands) are small at wavelengths that are mostly absorbed and large above ∼420 nm, where the

3 A photon could scatter n-times between the WLS film and TTX, adding $[R_{TTX}(\lambda_i) \cdot I^W_{R'}(\lambda_i)]^n$ terms to I_Γ. We neglect high orders (n>3) of these reflections, as the vis-reflectance of PEN or TPB is not high.

4 The thin glass substrate might contribute to up ∼25% of the I^W_R measured from TPB$^{(*)}$ (assuming the reflectance of the glass is <8%).

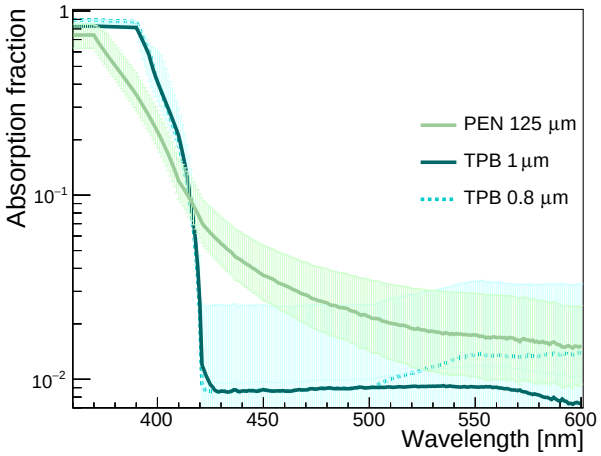

Figure 9.5: Absorption fraction of PEN and TPB films. The line from TPB 0.8 µm is only clearly visible above 500 nm (the lines almost overlay below this value). The uncertainty bands are discussed in the text.

absorption fraction is low. For the absorption fraction of PEN, we also assume a conservative ±60% uncertainty on $I_R^W(\lambda_i)$[5].

Discussion

The reflectance and absorption spectra are important parameters for the design and material selection of an efficient WLSR. The reflectance of TTX - shown in Figure 9.3 - is $\gtrsim$94.5% at the emission peak of TPB at $\sim$ 425 nm. The combination of WLS and reflector that presents the best reflectance (and lowest absorption) is TPB on TTX. TTX, however, requires a material for the mechanical support. Coating TPB directly on radiopure and mechanically stable copper, or coupling TTX to PEN would avoid needing a three-layered structure (copper plate + TTX + TPB). However, the reflectance of TPB coatings on Cu foils was low: less than half of that from TPB on TTX, as shown in the same figure.

Given the white appearance of thick coatings of TPB, we investigated whether a 3 µm layer of TPB could act as the reflector of visible light. The results from TPB$^{(*)}$ 3 µm show that TPB alone is not a good reflector; its reflectance is below 40%.

The integrated intensity from the TPB coatings on TTX was approximately independent of coating thickness for light above 420 nm: the values were almost as intense as the ones from the bare TTX. Thus, thicker ($\sim$ 1 µm) coatings of TPB are preferred for a TTX-based WLSR: the coating is thick enough to fully absorb the VUV light[6] while the light is not significantly lost to scattering and absorption.

The absorption of light above 420 nm by 1 µm of TPB might be well below 1%, as shown by the lower error bands of Figure 9.5: thin TPB films might be

5 Although this I_R^W is from the bare PEN, slight differences in its sanded surface and total internal reflection within the film may lead to uncertainties. We thus assume a conservative uncertainty on it.

6 The optimum light yield was measured for thickness between 0.5 and 1 µm of TPB on TTX [87].

thus ∼ absorption free in this region. Below 420 nm, TPB absorbs part of the light and partially re-emits it. The absorption edge of Figure 9.5 agrees with those measured by [123] and [100].

While sanded PEN reflected ∼30% of the light above 420 nm, TTX+PEN reflected more than 80%: similarly to TPB+TTX, the reflectivity is dominated by the TTX backing. Both PEN and TPB films absorb more than 10% of the light below 410 nm. Around the emission peak of the shifters (∼ 425 nm), the PEN film absorbs significantly more than the thin TPB films. This effect is also seen in Figure 9.3: the lower intensity of PEN+TTX (compared to bare TTX, or TTX+TPB) is due to the absorption of photons, either by PEN and/or by both PEN and TTX[7] after multiple reflections (within the PEN film or between PEN and TTX).

While TTX+PEN reflects more vis light than Cu foil + TPB, there is room for improvement in the performance of a PEN-based WLSR. This improvement could be achieved by finding better coupling methods to the reflector, exploring reflector materials, or decreasing its effective light absorption (for example, by using a thinner film or employing optical coupling).

These results show that even if the QE of PEN was the same of TPB's, the light yield of a PEN-based WLSR would still be lower since more of the shifted light is lost within it. Therefore, TPB vacuum coated on TTX demonstrated to be significantly superior in terms of optical properties.

9.2 RADIOPURITY & OUTGASSING CHARACTERIZATION

Besides the optical and mechanical considerations, the materials for the WLSR are also selected in terms of radio-purity and outgassing. The requirement for low outgassing is driven by the LAr quality. Materials can emit gases, such as nitrogen or water vapor, which can degrade the light yield and transparency of LAr to its own scintillation [62, 124].

Therefore, materials immersed in LAr must undergo testing to evaluate their outgassing rate and ensure they do not introduce impurities into the LAr. This aspect was important in the R&D of WLSR materials for LEGEND, particularly considering the large surface area covered by the WLSR. In general, metals are expected to exhibit lower outgassing compared to plastics, which tend to be porous. As TTX is a porous material, it underwent outgassing testing, which is described in Appendix B.

Radiopurity measurements

The important role the selection of radio-pure materials plays in the sensitivity of the experiment was discussed in Chapter 4. While copper was selected for its radio purity, TTX had the potential to contribute significantly to the background in LEGEND-200 if not sufficiently pure. To assess its radio-purity, a sample of TTX, weighting 930 g, with a surface density of approximately

7 TTX either absorbs or transmits the 1-R_{TTX} fraction of photons.

$100\,\mathrm{g\,m^{-2}}$, was screened for 53 d using the HPGe γ spectrometer Gator. The details about the setup, the analysis methods and simulations, are described in Appendix A, while here we show the results and discuss them.

Table 9.2 lists the values and upper limits of activity measured in the screening of the LEGEND-200 TTX sample in comparison to the values measured from the GERDA batch of TPB dip-coated TTX in 2015.

Isotope	LEGEND-200 Batch (this work)		GERDA Batch [105]	
	HPGe [mBq/kg]	HPGe [mBq/m^2]	HPGe [mBq/kg^2]	ICPMs [mBq/m^2]
^{238}U	<26.4	<2.64	<115	0.15
^{226}Ra	0.97 ± 0.38	0.097 ± 0.038	<11.6	-
^{228}Ra (^{232}Th)	<1.56	<0.156	<15.3	0.07
^{228}Th	<1.48	<0.148	<9.79	-
^{235}U	<1.21	<0.121	<6.68	-
^{60}Co	<0.29	<0.029	<3.43	-
^{40}K	7.20 ± 2.10	0.720 ± 0.210	<54.3	2.3
^{137}Cs	<0.48	<0.048	<3.58	-

Table 9.2: Upper limits (90% CL) and values of activities measured in the γ-ray HPGe screening of the TTX sample and values measured with HPGe and ICPMS for the TPB dip-coated TTX from GERDA. Units of the second and fourth column are shown in mBq/m^2. Both HPGe screenings were performed with Gator.

The values obtained for the LEGEND-200 batch are consistent with the upper limits obtained in the screening of the GERDA TTX. The latter values are larger due to the lower exposure: only ∼200 g of material were screened for 10 d, as compared to ∼1 kg for over 50 d in this work.

The limits here obtained for ^{238}U and ^{232}Th are orders of magnitudes larger than the activities of these isotopes measured in the nylon used in the minishrouds of LEGEND-200, which are $\mathcal{O}(100\,\mu\mathrm{Bq\,kg^{-1}})$ [125][8]. While the total mass of TTX deployed in LEGEND-200 is similar to that of nylon[9], the distance between TTX and the detectors is much larger: over 40 cm, compared to ∼1 cm for the nylon minishrouds. The flux of particles at this larger distance is further reduced as a result of attenuation in LAr (Chapter 5).

Therefore, the background contribution from TTX is negligible compared to that of nylon. The dominating contributions to the background in LEGEND-200 are expected to come from cables and ^{42}K from the LAr [126]. The values and limits measured in this work show that TTX fulfills the radiopurity requirements for LEGEND-200. This assessment was not performed for TPB, as it is employed in very small amounts (only a few grams in total).

8 Assuming the radiopurity of Nylon did not improve since GERDA.

9 The total mass of nylon deployed in the seven strings of GERDA was ∼200 g. This value scaled to LEGEND-200, amounts to around 1 kg of nylon, which is approximately the mass of TTX deployed in LEGEND-200 (1.32 kg).

9.3 CONCLUSION

In this R&D study, the reflectance and absorption spectra of different WLSR materials were investigated. TTX alone showed high reflectance, which was mostly kept when TPB layers were present. Coating TPB directly on copper or coupling TTX with PEN were explored as alternatives. However, TPB on copper had low reflectance, while PEN showed higher reflectance but significant effective absorption. TPB vacuum coated on TTX was thus the superior choice for the WLSR in LEGEND-200, considering its optical properties. PEN was later further investigated as a candidate for LEGEND-1000.

Regarding the radiopurity and outgassing requirements, the respective measurements from TTX yielded satisfying results. Thus, we selected TTX coated with a thickness of 600 nm of TPB for the WLSR of LEGEND-200.

To ensure the mechanical stability of the WLSR during installation and maintain a high-quality coating, we adopted a specific approach: ex-situ attachment of TTX to copper, followed by the installation of this assembly inside the cryostat, and finally, in-situ evaporation of TPB on the TTX surface. The details regarding this process are provided in the next chapter.

10 CONSTRUCTION OF THE WLSR FOR LEGEND-200

The WLSR of LEGEND-200 consists of a three-layer structure: copper foils for mechanical support, TTX as a reflector, and TPB as a WLS layer. The WLSR production involved attaching TTX to copper foils in a clean room, assembling them inside the cryostat, and coating them with TPB in situ.

The task of attaching TTX to copper foils and installing them inside the cryostat was undertaken by collaborators and is detailed elsewhere [127]. The TTX used in this assembly came from the same batch used for the optical, outgassing, and radio-purity characterizations discussed in the previous chapter. This chapter describes the construction of a system for evaporating TPB onto $\sim$13 m^2 reflective TTX shroud assembled inside the cryostat.

10.1 CONSTRUCTION OF A TPB VACUUM EVAPORATION SYSTEM

The R&D and construction of the evaporation system involved collaboration between the TUM and UZH. The TUM team built the evaporation crucible, a container with a cylindrical (2π) opening used to heat TPB to its sublimation temperature [127]. The work presented here was performed at the UZH and focused on the cabling, feed-throughs, and, most importantly, the system that moved the crucible and cables along the reflective shroud, depicted in Figure 10.1.

Coating such a large surface in situ was challenging due to the tight constraints imposed by the vacuum level and by installing the structure inside the cryostat. The various aspects considered in the design of the evaporation system are described below.

Evaporation requirements

- Vacuum level: To ensure effective deposition of TPB onto the TTX within a distance of approximately 0.7 m, a vacuum level of 10^{-5} mbar was necessary during the evaporation. This is the vacuum level described in [128, 129] as ideal for an evaporation distance of 0.85 m, resulting in a mean free path of TPB molecules of $\sim$1.5 m.

- Deposition rate and temperature: Several factors influence the deposition rate, including the opening size of the crucible, the distance between the crucible and the surface, and the heating temperature of the crucible. The latter is crucial as it determines the kinetic energy of TPB molecules, ensuring that they reach the TTX surface with adequate energy for proper adhesion rather than undergoing elastic collisions.

- Homogeneity and axial positioning: to guarantee a homogeneous deposition, the evaporator should move precisely along the vertical axis, maintaining a centered position with centimeter precision. This movement should repeat multiple times, ensuring that the coating is consistent throughout the entire z-length and compensating for any potential variations in the deposition rate.

- TPB thickness, crucible volume, and opening: The amount of TPB necessary for coating $\sim$1 µm of TPB on the surface of TTX was $\sim$20 g. The crucible was thus designed to accommodate this amount and allow TPB to exit through the lateral of a cylindrical opening. The crucible was divided into a body and a lid, both heated separately to maintain a consistent temperature. No obstructions were allowed around the cylindrical 2π opening to ensure the unimpeded exit of TPB molecules.

While these considerations were most relevant for the design of the crucible, they also had implications for the design of the system to move the evaporator. For instance, they influenced the precision of crucible movement, power, and weight requirements for the crucible and cables, as well as the vacuum requirements for all components involved. Therefore, considering these aspects was essential for the design of the evaporation system. The crucible, constructed with aluminum and surrounded by heating coils, was built and tested by the TUM team. The setup to move the evaporator is described below.

Evaporator moving system

To ensure a uniform coating, the movement of the evaporator within the WLSR was crucial. The system depicted in Figure 10.1 was designed to achieve this goal with centimeter precision in all axes. The several components of this system are described below.

1. **A modified version of the source insertion system (SIS):** This system was employed for the precise and automated movement of the crucible within the WLSR center during evaporation. Originally designed for moving sources along a stainless steel band [64, 130], the SIS underwent several modifications to repurpose it for this specific task:

    - An additional gear was incorporated and the clutch was modified accordingly to increase the torque output, allowing the system to handle heavier loads;
    - A deviation piece with two rollers was added to redirect the steel band to a central position. This was necessary because a central flange was unavailable, requiring an alternative arrangement;
    - New attachment pieces were designed to secure the crucible to the steel band and to initialize the system via a new switch.

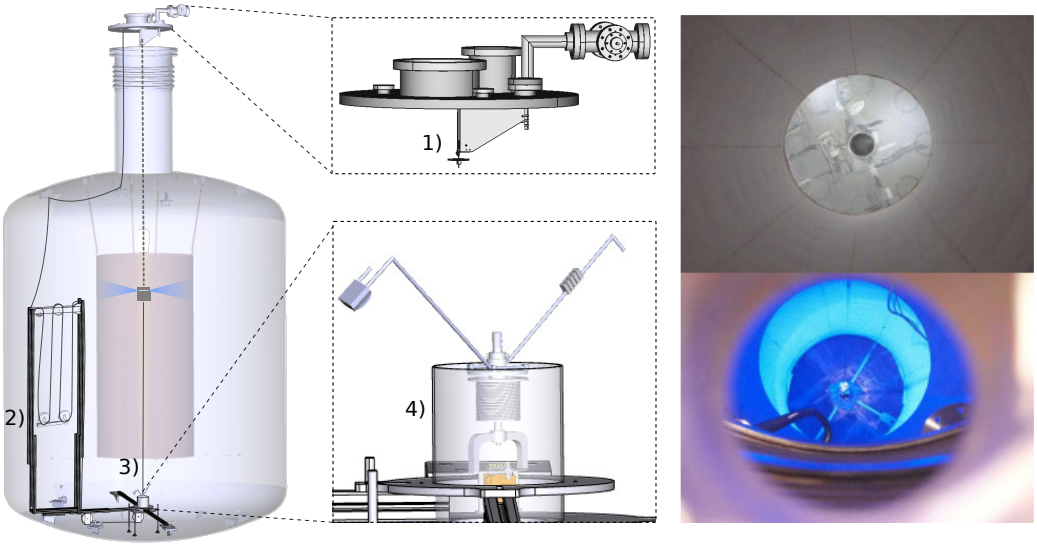

Figure 10.1: Left: Schematic of the TPB evaporator being lifted inside the LEGEND-200 cryostat by the modified insertion system mounted to the flange (1). During this movement, a cable support structure (2) steadily pulled its cable bundle (3). The bottom inset shows the evaporator in its parking place (4), where the rods shown hold a quartz monitoring crystal and a counterweight. Right: TTX Reflective shroud inside the cryostat as viewed from above before (top) and during (bottom) the TPB evaporation. The latter was photographed under UV illumination.

Following these modifications, the system was able to reliably pull the additional weight and cable pull of the evaporation system ($\sim$5 kg) with a speed of 3 mm s^{-1} and a tested maximum pull capacity of 15 kg.

2. **Cable support structure:** Considering the inherent torsion of the cables and the flexibility of the SIS steel band, a system was implemented to maintain the cables straight, facilitating their movement alongside the evaporator. The structure consisted of two pulleys connected to 1.8 kg and 2.4 kg weights. These weights caused the pulleys to move up and down in coordination with the crucible attached to the SIS. The masses of these weights were optimized to ensure smooth cable movement while minimizing the exerted force on the SIS[1].

   The cable support structure, measuring 2.6 m in size, accommodated the 10 m cable length when the evaporator was positioned at its lowest point. Despite the WLSR spanning 3 m, the evaporator and cabling had to cover a distance of over 8 m from the starting position at the flange to the bottom parking position.

3. **Cable bundle:** The system required ten cables for temperature and deposition monitoring, along with four thicker cables for power supply.

1 To measure the pull exerted by the pulley system on the SIS, the SIS current was calibrated against different weights. The measured pull ranged from 1.2 kg to 2.5 kg, with variations attributed to friction within the system.

Given the extensive travel distance of the evaporator, the combined weight of the cables was over 1 kg. However, much of the force exerted on the SIS resulted from the pull applied by the pulley system to straighten the cables. Especially if the cable bundle was not uniform, the tension on the SIS spiked to much higher values. To minimize this issue, several bundling methods were tested, with the pull on the SIS being monitored while the system moved the bundle. The optimal strategy was to bundle the cables with 0.5 cm thick heat shrink attachments spaced at approximately 10 cm intervals. Cables with polyurethane insulation were selected for their flexibility and low outgassing rate.

4. **Evaporator parking place:** While heating up the crucible to its operating temperature, it was necessary to cover its opening to prevent the dispersion of TPB inside the cryostat. For this purpose, a cylindrical 'parking place' cover was built. To ensure the SIS band would not continue moving the evaporator down after reaching the parking position, a switch was installed. This switch sent a signal to the system upon contact with the parked evaporator.

The evaporation system was designed to meet strict spatial constraints and facilitate the installation process. The cryostat, approximately 8 m tall (including the neck) and 4 m wide, could only be accessed from the top through a $\varnothing$ 0.8 m hole. All structural components thus had to pass through the cryostat opening, be carried inside using a human lift, and fit within the limited space under the WLSR (around 1 m).

All parts were thus selected to facilitate their mounting within the limited space of the cryostat, which had a curved floor. Moreover, the outgassing properties of these materials were considered, as the goal was to achieve a vacuum level of $\sim 10^{-5}$ mbar within the large cryostat within a day, utilizing a turbo pump with a pumping speed of 900 l/s. Materials containing plastics, such as cables and pulleys, underwent outgassing tests as described in Appendix B.

To develop the system, a test setup was utilized during the design phase, conducting tests in the assembly hall of the UZH using the 7 m high platform to place the SIS. Once the components were manufactured, their assembly and stability were thoroughly tested to ensure proper functionality and reliability.

10.2 IN-SITU EVAPORATION

The evaporation procedure happened in December 2020. The TUM team entered the cryostat through the cylindrical reflective shroud and assembled the cable support structure. The UZH team provided support on the upper part of the cryostat and assembled all the SIS and flange components. The evaporator crucible was filled with 25 g of TPB. The cryostat flange was closed, and the TPB evaporator was lowered into the cryostat to its designated

parking position. The cryostat was pumped to $\sim 10^{-5}$ mbar, and the crucible was heated to $\sim 150\,^{\circ}$C.

Once the desired temperature was reached, the crucible was moved to the starting position of the WLSR. The SIS was setup to continuously move the crucible along the WLSR, with steps of 10 mm and short pauses of few seconds. The evaporation rate was verified using the quartz deposition monitor. The blue emission of TPB covering the reflector was also observed using a UV lamp, as shown in Figure 10.1 (right).

The evaporation process was conducted in two runs. In the first run, technical issues led to a very low evaporation rate, with only ~ 1.5 g of TPB evaporated within ~ 30 h. The primary issue was that the target temperature of the crucible was not achieved. Especially its lid was not warm enough, leading to the accumulation of TPB on its surface, blocking the evaporator opening. The cause of the overall lower temperature was the faulty readout of the temperature sensors. This issue was promptly identified and resolved. Additionally, the stainless steel piece holding the evaporator to the steel band was modified to minimize heat transfer and decrease the temperature gradient between the body and lid of the crucible.

The second run began the same day with the cryostat being pumped again. The same procedures were followed, but this time a 20-times higher evaporation rate was achieved. After ~ 15 h, the full content of the crucible was evaporated, and the reflector was covered with 600 nm of TPB. Samples of the coated reflector, called 'witness' samples, were taken for optical characterization using VUV light at TUM and in LAr at UZH.

10.3 CONCLUSION

This chapter described the construction process of the WLSR, focusing on the in-situ TPB coating on the reflective TTX shroud inside the cryostat. To accomplish this task, a TPB vacuum evaporation system was designed, taking into consideration the spatial and vacuum requirements associated with executing a vacuum evaporation inside a cryostat. This system was employed in December 2020, and the large-scale coating of the TTX shroud inside the LEGEND-200 cryostat was successfully achieved. The resulting TPB coating is highly uniform, and presents a high light yield, as described in the next chapter.

11

WLSR CHARACTERIZATION FOR LEGEND-200 AND R&D FOR LEGEND-1000

This chapter describes the optical characterization of the specific WLSR of LEGEND-200, along with the R&D of PEN-based alternatives for LEGEND-1000 and other large-scale LAr-based experiments. The characterization work was conducted during two campaigns, between 2020 and the beginning of 2021, and in spring 2022.

During the first campaign, microscopy and LAr measurements were performed on TTX, the LEGEND-200 WLSR, and a PEN film. These measurements served as inputs for Geant4 simulations, where the simulated parameters were tuned to match the measured response of TTX, TPB, and PEN. The aim was to extract the reflectivity or quantum efficiency (QE) of these materials in response to LAr scintillation. The findings of this campaign, summarized in [4] and in this chapter, revealed that PEN exhibited a good efficiency in shifting VUV photons. However, there were still unresolved questions regarding the optimization of the light yield (LY) from a PEN-based WLSR.

Motivated by these questions, the second characterization campaign focused on testing various PEN films of different material grades, film thickness, surface treatments, and coupling with different reflectors. Microscopy was employed to characterize the different surface treatments and measurements in LAr were conducted to directly compare PEN-based WLSRs.

As many of the procedures of both campaigns are similar, they are described in parallel in this chapter. Section 11.1 presents the characterization with microscopy, Section 11.2 describes the measurements in LAr and their data analysis. While the assembly and operation of the LAr apparatus were alike in both campaigns, the primary analysis approaches differed. This chapter provides a detailed description of the analysis developed for the second campaign[1].

Section 11.3 describes the LAr simulations conducted to complement the results of the first campaign. Since the optical parameters of interest were already extracted using these simulations, and the focus of the 2022 campaign was on directly comparing PEN-based WLSRs, no further simulations were performed. Each section is accompanied by its results, which are collectively discussed in the final section.

1 In the first campaign, the main analysis of the LAr data was conducted by Vera Wu as part of her MSc thesis [3]. During the second campaign, PhD students from other institutions assisted with the operation of the setup at UZH for a few weeks, but only the analyses performed by myself are described here. For more information, please refer to the preface.

In order to examine the uniformity of TPB coverage on the in-situ evaporated TTX of LEGEND-200, a 'witness' sample was imaged with microscopes. This characterization served two purposes: to verify the quality of the evaporation process and to ensure that the sample met the requirements for accurate QE estimation in this study, as a non-uniform TPB coverage on the sample could lead to an underestimation of its QE.

Since a single TPB molecule is much smaller than the pores of TTX (1 nm compared to 250 nm [131] for the pores[2]), scanning electron microscopy (SEM) was employed to assess whether TPB effectively filled the pores in TTX. To evaluate the coating uniformity at larger scales, fluorescence microscopy was employed.

Additionally, PEN films were imaged to investigate their surface and how the photons emitted by it reflected within the film, with the aim to gain more understanding about light trapping within the film. For this purpose, fluorescence microscopy was employed.

11.1.1 *Samples, procedures & setups*

The measurements were performed on various samples, which are described in Table 11.1. TTX+TPB (L) is a 'witness' sample of the in-situ evaporated LEGEND-200 WLSR. To investigate the effects of LAr immersion and ambient light exposure on this sample, one piece went through two five-day-long immersions in LAr, while another sample was partially exposed to ambient light for approximately two weeks[3].

To compare the quality of the TTX+TPB (L) coating achieved in the in-situ evaporation, a sample of TTX dip-coated with TPB, TTX+TPB (D), was also measured. This sample was prepared for GERDA, as described in [130], and has been kept since then inside a container in a cupboard at UZH.

The PEN samples, all biaxially oriented Q53 grade films from Teonex® (as in Chapter 9), initially have a smooth surface. As described in this previous chapter, they were sanded to create a rougher surface on both sides, using a P240 grit sandpaper. For the second campaign, additional 25 µm films of the same type were acquired and sanded using a machine with P400 and P600 grit sandpaper, but only one side of the films was sanded.

The samples imaged with SEM were sputter coated with 2 nm of platinum using a safematic sputter coater. Each sample was scanned in 3 to 4 spots with a Zeiss GeminiSEM 450 field emission SEM. The image sizes varied, ranging from around 1 mm to 1 µm, with a resolution on the order of 10 nm.

2 The value of 1 nm was estimated by the sum of benzene rings and C-C bonds, or by dividing its molar mass by its density.

3 The sample was kept inside a glass box and half of it was covered, so that half of the sample was exposed to light, but none of it was directly exposed to humidity and dust.

Table 11.1: Description of the samples measured with microscopes.

Name	description	measurement
TTX	bare Tetratex® 254 µm film	SEM
TTX + TPB (L)	evaporation witness sample, kept in dark	SEM & fluorescence mic.
TTX + TPB (L)(2)	TTX+TPB (L) after 2 immersions in LAr	SEM
TTX + TPB (L)(E)	TTX+TPB (L) partially exposed to ambient light	fluorescence mic.
TTX+TPB (D)	TPB dip-coated, kept in dark	fluorescence mic.
PEN (HS)	bare 125 µm film, 'hand-sanded'	fluorescence mic.
PEN (MS)	bare 25 µm film, 'machine-sanded'	fluorescence mic.

For the fluorescence microscopy imaging, a Widefield Leica Thunder Imager 3D was used. The wavelength of the excitation light was 390 nm, and an additional filter with a range of 375 nm to 405 nm ensured the light was monochromatic. To prevent the 390 nm excitation light from reaching the detectors in case of reflection by the sample, a dichroic mirror with a cutoff at 415 nm was employed. The fluorescence response from the sample, with a wavelength above 415 nm, was collected by the objective and recorded using the setup's camera.

11.1.2 *Results*

Figure 11.1 shows SEM images of bare and TPB-coated TTX samples. The tubular structures of TTX are shown in yellow, with a diameter consistent with the measurements reported in [131] (∼250 nm). The pores of TTX are well covered with TPB (shown in blue), indicating a homogeneous coating.

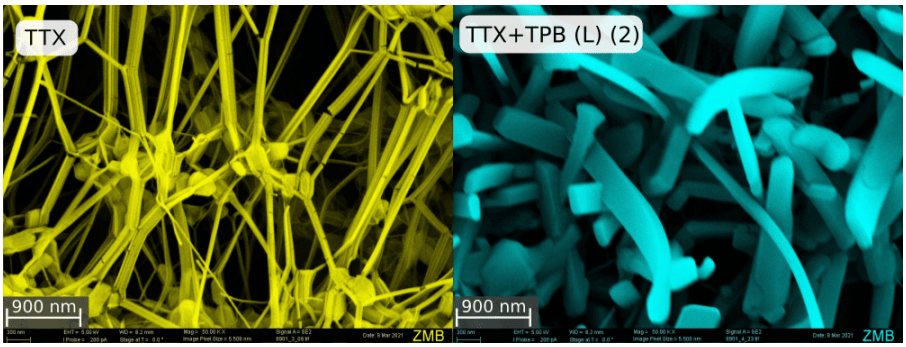

Figure 11.1: SEM images (900 nm scale bar) of TTX and TTX+TPB (L)(2). The respective images were colored in yellow and blue to ease the observation of their structures.

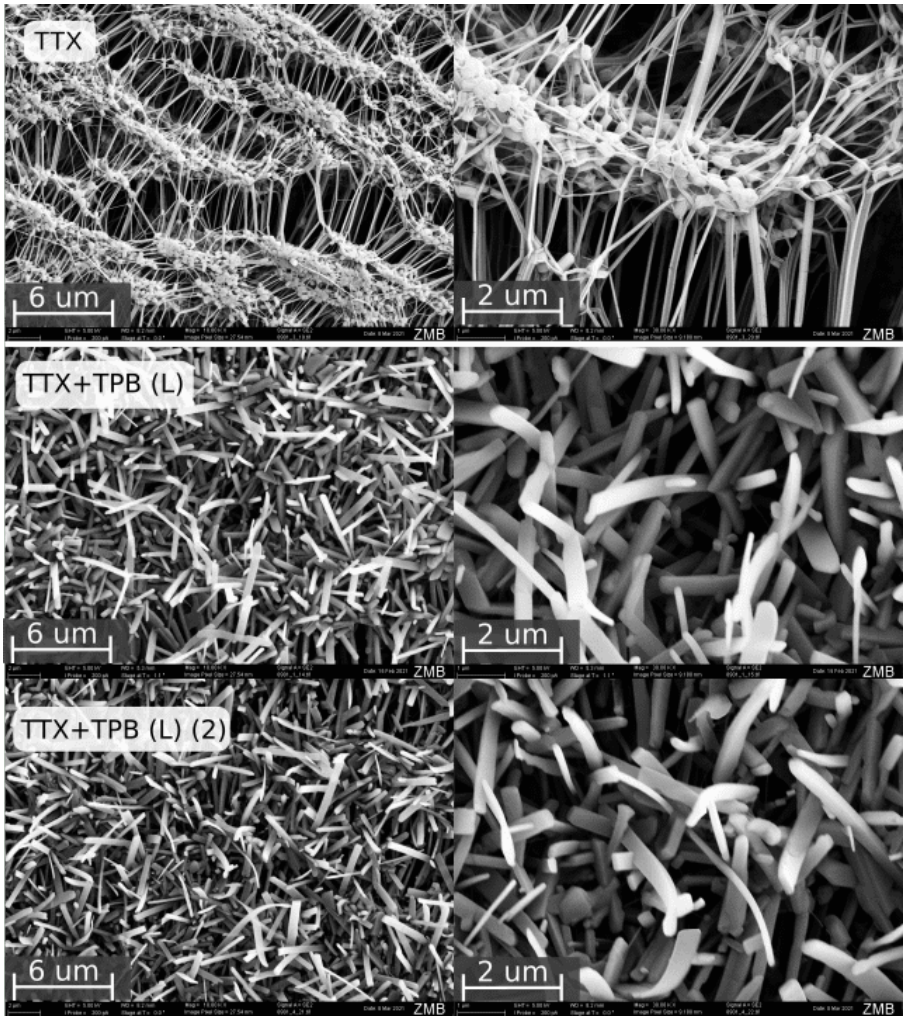

Figure 11.2: SEM images of TTX (top), and TTX+TPB (L) before and after two immersions in LAr (middle and bottom, respectively). The scale bars of the figures on the left and right are 6 µm and 2 µm respectively.

The images in Figure 11.2 further confirm the homogeneous distribution of TPB at larger scales (several µm), with no regions lacking TPB[4].

These SEM images also enable the visualization of the TPB structure, which can vary depending on the coating technique and cooling rate [132–134]. The crystalline shape of TPB observed from these samples is needle-like, which is the common shape of the alpha-form of TPB [133]. Among the reported TPB structures [132–134], the alpha is the most frequent and stable at room temperature [133]. It exhibits a tighter packing and has a different UV-vis absorption spectrum than other crystalline forms [134]. The needle-like structures observed in the images have sizes up to a few µm, being thus larger than the nominal coated thickness (600 nm), an observation also reported by [128, 135].

4 It is important to note that not all structures may be visible in SEM images due to the reduced scattering of electrons from areas with less or no platinum coating.

While the alpha-form is dominant in films produced by sublimation [132, 133], vacuum-evaporated TPB samples may not always exhibit needle-like structures, and the homogeneity and light yield of the coating can vary depending on the evaporation conditions [87, 136, 137].

The third row of images in Figure 11.2 shows TTX+TPB (L)(2). Consistent with the observations in [128], no clear damage to the needle-like TPB structures is observed after immersions in LAr[5].

The left figures of Figure 11.3 and Figure 11.4 show the single and multiple fluorescence microscopy scans of TTX+TPB (L). The scans of dip-coated TTX+TPB are shown on the right for comparison. The dip-coated sample exhibits several large crystals and areas with less TPB coverage, leading to inconsistent light emission. Quantifying the QE of TPB from such a sample would introduce large errors due to the uneven TPB coverage.

In contrast, TTX+TPB (L) shows homogeneity at both the sub-µm scales observed with SEM and at much larger scales (investigated with fluorescence microscopy up to several cm^2). The fluorescence intensity does not approach zero or decrease significantly at any point. This uniformity of TPB can be better visualized in the light intensity profiles of the microscopy scans, as demonstrated by the bottom images of Figure 11.3.

The bottom image of Figure 11.4 demonstrates that a moderate two-week-long exposure of one side of the TTX+TPB (L) sample to ambient light did not affect its fluorescence intensity in response to UV light (390 nm). This was further confirmed by analyzing the shape of the microscopy z-profiles.

Figures 11.5 and 11.6 provide detailed views of the scratches resulting from sanding PEN films. While the exact width of the scratches appears to depend on the sandpaper grit, their spacing is rather influenced by the sanding method (machine or by hand).

Upon visual inspection under ambient light, the sanded films appeared less transparent. However, in fluorescence microscopy, the light originates within the film, with more light exiting the film through the scratches. This indicates that the emitted photons by PEN may become 'trapped' inside the film due to total internal reflection[6]. This is also expected to happen in LAr, since the refractive index of LAr at visible wavelengths is only slightly higher than that of air [138] and still significantly lower than that of PEN [139].

The effect of reduced transparency (to external light) caused by the scratches can be observed in the middle image of Figure 11.6, taken in bright field mode: the sample is illuminated from the back and less light is transmitted through the scratches, giving them a dark appearance. While the microscopy images helped to visualize the surface effects of PEN films in air, their response in LAr was investigated with dedicated measurements described in the next section.

5 This however does not provide quantitative information about the potential diffusion of TPB into LAr, studied by [95].

6 While the probability of total internal reflection of light in the *vis* measurements of Chapter 9 was not high (the angle of incidence was 8°), the probability of total internal reflection by photons emitted isotropically inside the film is much larger.

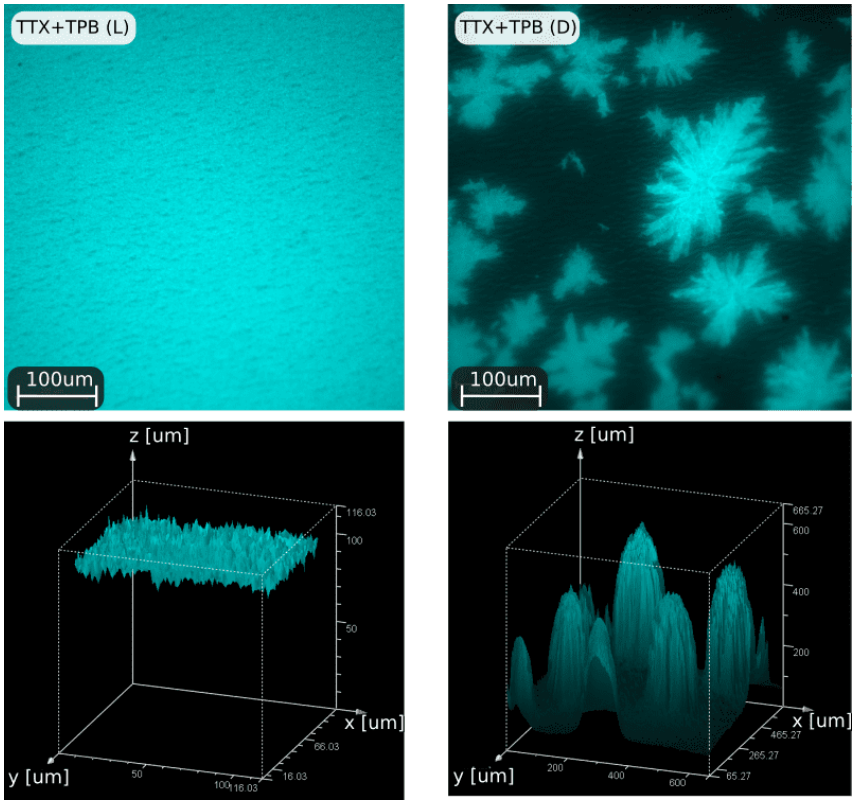

Figure 11.3: Fluorescence microscopy images of TTX+TPB (L) and dip-coated TTX+TPB (D). The images on the bottom show examples of the intensity 'z-profile' of the light detected from the respective samples.

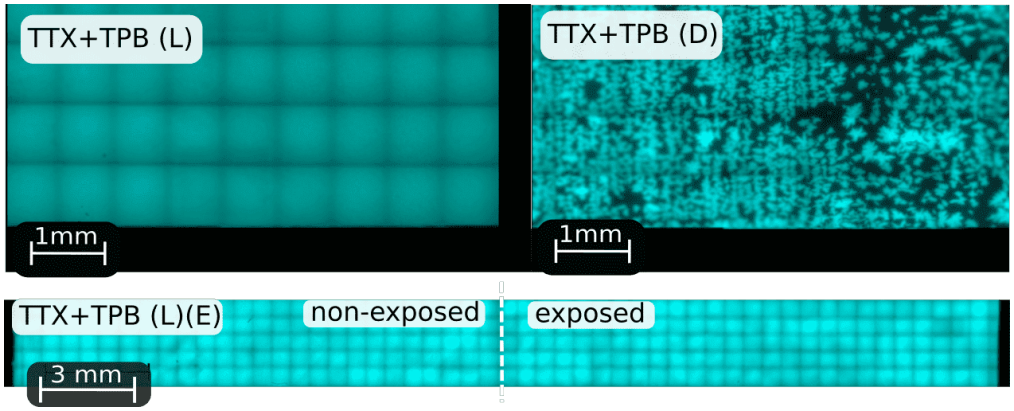

Figure 11.4: Top: Fluorescence microscopy images of TTX+TPB (L) and TTX+TPB (D). Images are composed of multiple scans ('tiles'). The shadowing on the edges of each tile is an effect of the central focusing point. Bottom: Tile scan of TTX+TPB (L)(E). The left half of it underwent exposure to ambient light for two weeks. A shaded line in the middle identifies the border between exposed and non-exposed areas.

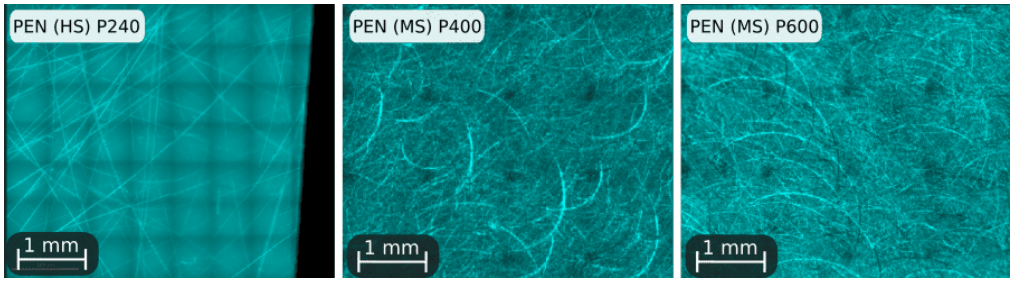

Figure 11.5: Tile fluorescence microscopy scans of PEN sanded by different methods (HS, MS) and sandpaper grit (P240-600).

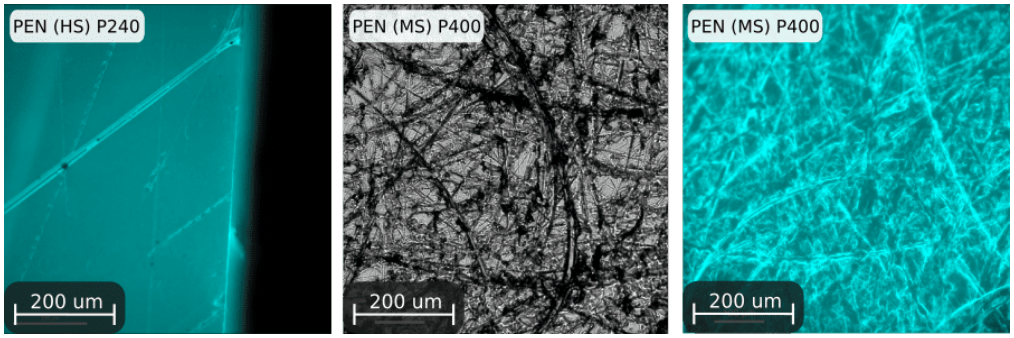

Figure 11.6: Microscopy images of PEN (HS) and (MS). The latter was imaged both in fluorescence and in bright-field mode (shown in the middle).

11.2 LIQUID ARGON MEASUREMENTS

To develop and optimize WLSR materials for use in LAr, it is essential to study their properties directly in LAr, as no other setup can provide the specific refractive indices, VUV scintillation at 128 nm, and cryogenic temperature at the same time. Key optical properties, such as reflectivity and absorption, depend on the wavelength. The refractive index of the medium also influences reflectivity, while QE often depends on temperature. Moreover, when optimizing the LY of WLSR combinations, it is important to consider mechanisms of light trapping within the WLSR materials, which are strongly influenced by the medium.

In our first campaign, we thus characterized the reflectivity of TTX and the QE of TPB and PEN in response to 128 nm light in LAr. For this purpose, we initially characterized the setup using an absorber with known optical parameters. Subsequently, we measured the reflective and WLSR samples, which resulted in enhanced light detection compared to the absorber. The measured LY was then used to tune a detailed optical simulation of the setup, allowing us to extract the optical properties from the samples.

In the second campaign, we focused on testing various WLSR combinations based on PEN. The primary objective was to understand the impact of optical coupling, surfaces, and reflectors on the LY. These factors are strongly influenced by the medium, emphasizing the importance of studying them in the actual LAr environment.

11.2.1 *Samples, procedures & setup*

The samples for measurements in LAr are listed in Table 11.2. To characterize the LAr setup, a reference measurement was conducted using the Metal Velvet™ foil from Acktar [140]. This foil is suitable for these measurements due to its compatibility with low-temperature applications, minimal outgassing properties, and reflectivity below 1% across a wide range of wavelengths, from extreme UV to infrared [140].

Table 11.2: Samples measured in LAr in the first and second characterization campaigns. All PEN films are from Teonex®. The dashes indicate that no optical coupling or surface sanding method was employed. See text for details.

Reference Sample

Sample name	Material
Absorber	Metal Velvet™

Samples of 1st campaign

Sample name	WLS thickness
TTX	bare, no WLS
TTX+TPB (L)	0.6 µm
TTX+PEN (HS)	125 µm

PEN-based WLSRs of 2nd campaign

Sample name	reflector	grade	thickness	coupling	sanding
TTX+Q53-25 (MS)	TTX	Q53	25 µm	-	MS P500
TTX+Q51-50 (HS)	TTX	Q51	50 µm	-	HS P240
TTX+Q53-125 (MS)	TTX	Q53	125 µm	-	MS P500
TTX+Q53-125	TTX	Q53	125 µm	-	-
TTX+Q53-125 (HS)	TTX	Q53	125 µm	-	HS P240
ESR+Q53-125	ESR	Q53	125 µm	-	-
Al+Q53-12 (HS)	Alu	Q53	12 µm	epoxy adh.	HS P240
Tyvek+Q53-25	Tyvek®	Q53	25 µm	SMP glue	-

Among the samples included in the measurements are TTX and TTX+TPB (L), which were previously described in the earlier sections and chapters. The bare TTX sample was measured in LAr to understand its reflectivity of VUV light. The TTX+TPB (L) sample from LEGEND-200 was measured not only to characterize the specific WLSR of LEGEND-200, but also to quantify the QE of TPB. Additionally, PEN-based samples were included as part of the R&D for large-scale WLSR coverage.

The TTX+PEN (HS) sample was prepared as described in Chapter 9: Teonex® Q53 grade film was hand-sanded with P240 grit sandpaper and attached to TTX without optical coupling. In the second campaign, most samples followed the same procedure, but with only one side of the sample being sanded while the side attached to the reflector remained untreated. Different sanding methods, including machine sanding (MS), described in the previous section, were employed.

Besides different surface treatments, the sample list included various PEN thicknesses (ranging from 12 µm to 125 µm), PEN grades (Q51 and Q53), and reflectors such as the diffuse reflector Tyvek® from DuPont™ and the Vikuiti™

enhanced specular reflector (ESR) from 3M®, also known as VM2000. These reflectors, employed in many experiments, present high efficiency at visible wavelengths [66, 141].

For one of these samples, ESR (without adhesive or optical coupling) with a thickness of 38 µm was attached to PEN. To optically couple the PEN film to Tyvek (type 1082D, 275 µm), various adhesives and glues were tested as part of an optimization campaign for optical couplings, described in Appendix C. The Poly Max® shape memory polymer (SMP) glue showed the best performance for coupling Tyvek and PEN. The process to produce this laminate is detailed in the same appendix.

A commercial laminate consisting of a thin PEN layer coupled to an aluminum backing with an epoxy adhesive was also tested. Although aluminum is less reflective than other reflectors [141], this laminate was investigated due to its simplicity, availability, and suitability for experiments requiring large WLSR coverage but not prioritizing LY.

Before attachment, Tyvek and all PEN films were cleaned ultrasonically in an isopropanol bath and dried with a nitrogen gun. TTX and ESR were considered clean and did not undergo further cleaning. Each sample had a rectangular size of 110 mm x 350 mm and was wrapped around the cylindrical sample holder. Two ring-shaped aluminum clips were used to hold the sample against the top and bottom parts of the holder.

While the 125 µm thick PEN films adhered well to the reflectors without the need for optical coupling, resulting in a flat WLSR sample as observed in Figure 11.7 (1, 3), the thin films were held together mainly by the aluminum clip and their surface was not as stable and flat.

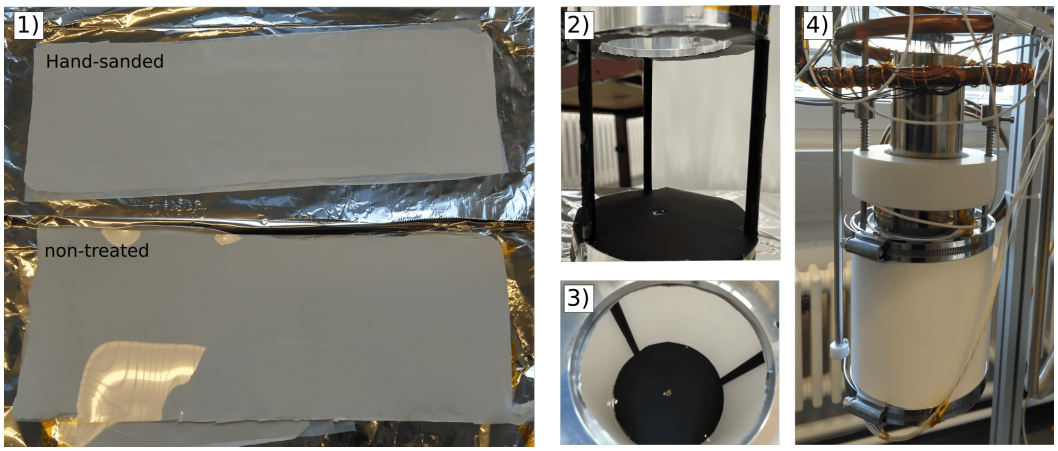

Figure 11.7: 1) Examples of 125 µm PEN films attached to TTX by manually pressing both films together. The specular surface of non-treated PEN is clearly seen on the top of white TTX. 2-4) The sample holder is shown: before (2) and after (3) a sample is installed surrounding it, and then attached to the PMT in the setup (4).

Figure 11.7 (4) shows the attachment of the sample holder to the PMT of the setup. The schematic of the LAr setup is shown in Figure 11.8: it includes a

cryostat equipped with a cooling system, level meter and temperature sensors, as well as a sample cell delimited by a sample holder, an α source, and a VUV-sensitive PMT.

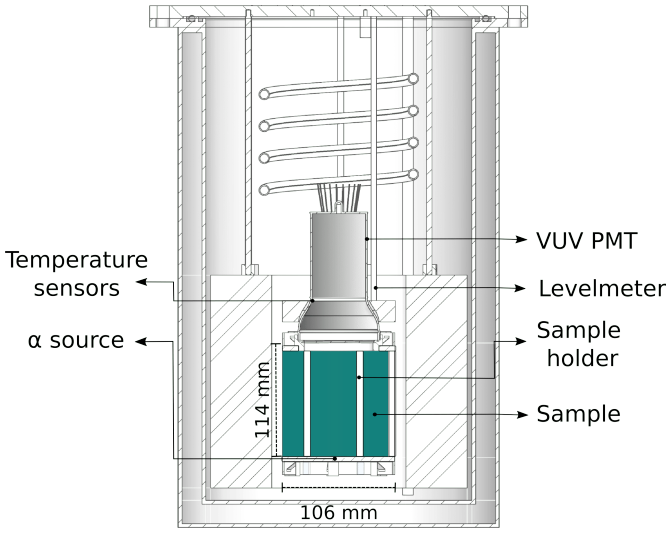

Figure 11.8: Schematic cut of the LAr setup with its main components indicated.

The 3" PMT (R11065 model from Hamamatsu modified with a MgF_2 window) is sensitive to both VUV and visible light and designed for operation in LAr temperatures.

The α source used in the setup is ^{241}Am deposited on a thin stainless steel disk [105]. The source has an activity of 30 Bq and emits 5.5 MeV α particles, without any encapsulation. This source of scintillation photons is ideal, providing well-localized and high-energy emissions that can be distinguished from most background sources. The source was located at the base of the sample cell, allowing the scintillation photons from α decays to either reach the sample or be directly detected by the PMT. In the second campaign, a blue LED was also installed in close proximity to the source.

To avoid uncertainties caused by the reflectivity of materials, all inner structural parts of the sample cell, except for a small opening ($\sim$7 mm diameter) for the source and LED, were covered with the low-outgassing absorber, as shown in Figure 11.7 (2).

Once a sample was mounted, the cryostat was sealed and evacuated to a pressure of approximately 10^{-5} mbar. Then, it was filled with gaseous argon with 99.9999% purity, which was liquefied inside the cryostat using liquid nitrogen as the cooling agent within a copper cooling coil situated within the cryostat (as described in [3, 105, 130]). The gas was added until the LAr level in the cryostat was a few cm above the PMT window, maintaining an over-pressure condition (above 1 and below 1.3 bar). The liquid level was continuously monitored using a level meter and a temperature sensor located on the PMT. The operational temperature ranged from 87 to 89 K.

The PMT was biased at 1500 V and set to trigger on single photoelectrons (sPE), which were later used for the signal calibration. The signals were acquired without amplification using a CAEN V1724 module with an acquisition rate of 100 MHz, an acquisition window of 8 µs, a pre-trigger of 1 µs, and a trigger level set to a few sigma above the mean fluctuation of the baseline. All waveforms were saved for subsequent processing.

During the first campaign, the samples were measured in three different modes: i) VUV-only: used to characterize bare TTX sample and the setup with the reference absorber; ii) VUV+vis: measurement of both the VUV light directly reaching the PMT and the visible light shifted by the WLSR samples; and iii) vis-only: measurement of only shifted light, as the direct VUV component was blocked by an acrylic filter placed before the PMT window. In the second campaign, the acrylic filter of the latter mode was not utilized.

At the end of a sample measurement, the LAr was evaporated and not reused to prevent the accumulation of impurities in LAr that could decrease its scintillation yield [84]. To avoid variations of the purity level, the material content and vacuum level of the cryostat at the time of filling were always roughly the same. A few measurements were repeated to assess the systematic uncertainty on the effective scintillation yield.

11.2.2 *Data analysis*

The goal of the analysis is to determine the mean light yield (LY) in each sample measurement in response to α decays from the source, in units of number of photoelectrons (PE). The first step towards this goal was processing the raw data to identify pulses in each event trace using a derivative method, described in [142]. This method identifies the pulses by setting thresholds based on the values the derivative function should cross, typically around four times the root mean square (RMS) value of the noise [142, 143].

To determine the charge produced by single photoelectrons (sPE), the integrals of individual pulses were utilized. Figure 11.9 displays a histogram of these integrals, exhibiting a distinct sPE peak. To obtain the integral charges of the full waveforms, all pulses within the 7 µs post-trigger window were integrated, as shown in Figure 11.9 (right).

The prominent peak observed above the exponential background represents the signal detected when α particles deposit 5.5 MeV in the LAr of the cell. This spectrum was fitted for each set of five million traces, and calibrated to PE values using the sPE peak. This individual calibration ensured that potential drifts in the voltage and gain of the PMT did not affect the final results. The mean PE value of the α peak was derived from the mean of the Gaussian function and its statistical uncertainty for each sample measurement was calculated from the distribution of the fit results obtained from multiple datasets of five million traces.

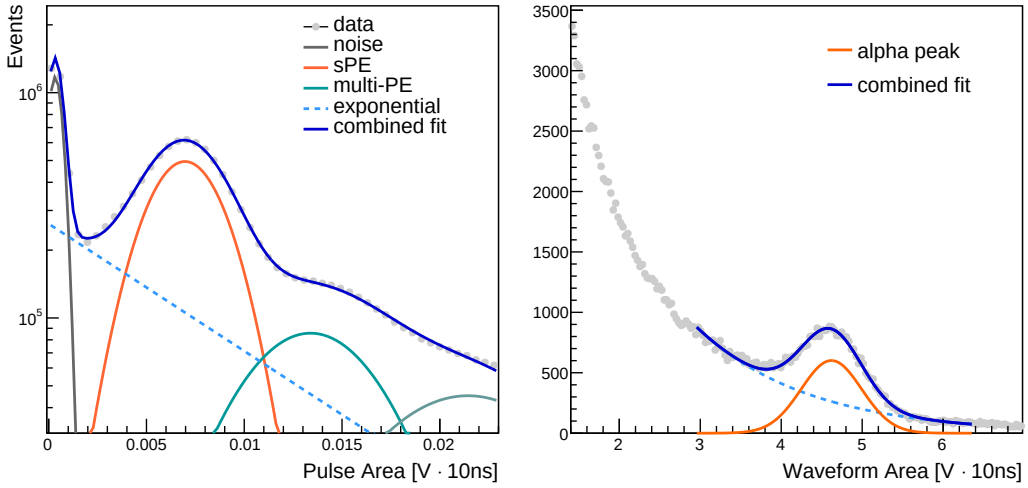

Figure 11.9: Left: Spectrum of pulse integrals fit with a sum of gaussian and exponential functions used to describe the noise, the sPE and multi-PE peaks. The relative mean (μ) and deviations σ of the gaussian peaks is fixed to $\mu_{\text{2PE}} = 2\mu_{\text{sPE}}$, $\mu_{\text{3PE}} = 3\mu_{\text{sPE}}$, $\sigma_{\text{2PE}} = \sqrt{2}\sigma_{\text{sPE}}$, $\sigma_{\text{3PE}} = \sqrt{3}\sigma_{\text{sPE}}$. Right: Spectrum of waveform integrals fit with the sum of Gaussian and exponential functions.

The main systematic uncertainty in repeated measurements in LAr arises from the quenching of the LAr scintillation yield (SY) due to impurities. This quenching primarily affects the long-lived triplet component, leading to variations in its observed lifetime ($\tau_{triplet}$) and SY (Chapter 5). This variation of SY is a concern if it significantly varies across different measurements, impacting the measured LY in different degrees. To assess the stability of SY, we monitor $\tau_{triplet}$ and perform repeated measurements.

In the first campaign, measurements in different VUV and vis modes were affected differently by the re-emission of the WLSs, which can influence the measured $\tau_{triplet}$. Consequently, the estimated $\tau_{triplet}$ was only indicative of the stability of SY within each measurement mode (see [3, 4]). To validate the stability of SY across all measurements and confirm the detection of shifted light, the measurements of TPB and PEN samples were repeated in the vis-only mode.

Using simulations, an effective value for SY was determined, and its systematic uncertainty was derived (as it will be shown in Section 11.3). The agreement of VUV-vis and vis-only measurements within one sigma demonstrated a systematic uncertainty on SY below 3%. The analysis of the relative ratios of the prompt light component, which is minimally affected by quenching, was additionally employed to assess measurement stability. Further details on these analyses can be found in [3, 4].

In the second campaign, increased outgassing due to shorter pumping times and material variability resulted in greater variations in impurity levels and SY compared to the first campaign. To correct for these variations, the relationship

between the measured PE and $\tau_{triplet}$ was analyzed. This assessment, detailed in Appendix C, yielded a correction function for the LY in each measurement based on their measured $\tau_{triplet}$. Measurements with low $\tau_{triplet}$, caused by impurity quenching, had their LY scaled using the correction function. In the next section, the results for the second campaign will be presented both before and after this correction. The correction was particularly important for the repeated measurement of TTX+Q53-125, where an accidental introduction of impurities led to a reduction in $\tau_{triplet}$ and measured PE.

11.2.3 *Results*

The results from the first campaign were obtained using LAr data collected over several days, including measurements at different PMT voltages and integration time windows (see [3, 4] for details). For the results presented here, only a few datasets were processed and analyzed as described earlier. Yet, they show good agreement (within fractions of a percent) with the results published in [3, 4], confirming the reliability of both methods. The results are presented in Figure 11.10 (left).

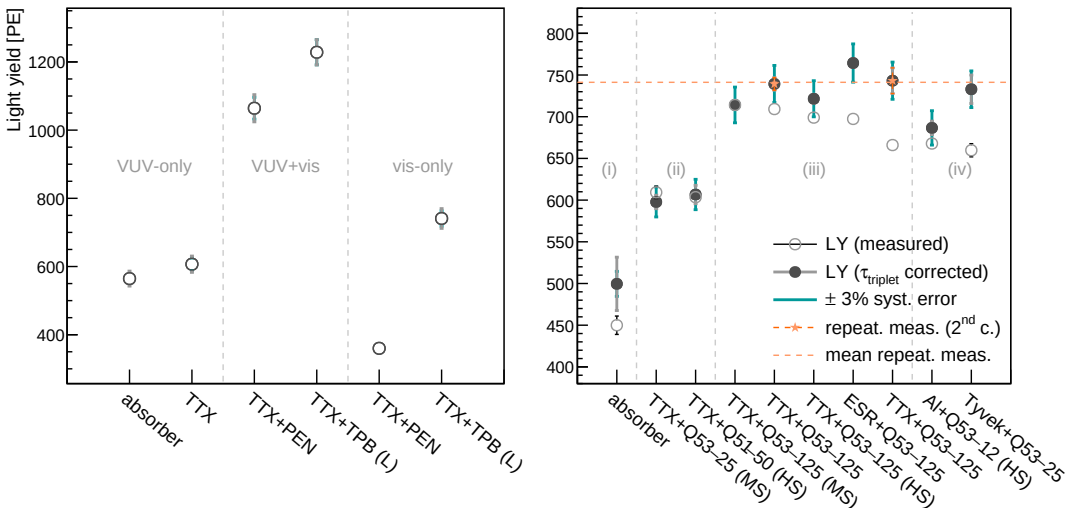

Figure 11.10: Left: LY measured in the first campaign in the VUV, VUV+vis and vis-only modes. Right: Measured and corrected LY for the second campaign . The repeated measurements and their mean value are marked. The four regions represent: i) reference measurement; ii) thin films not optically coupled; iii) 125 µm films with varying surface treatment and reflectors; iv) thin films optically coupled.

In the VUV-only mode, no significant enhancement in LY was observed from TTX, suggesting that TTX does not reflect LAr VUV scintillation to a significant extent. The exact value and limit of its VUV reflectivity are calculated using simulations in the next section.

In the VUV+vis mode, a substantial increase in LY was observed, particularly for the WLSR witness sample, TTX+TPB (L), indicating efficient wavelength shifting and reflection. The vis-only measurements served as a cross-check for the magnitude of shifted light. The derived systematic uncertainty of 3% for SY is represented by the colored error bars. The QE of TPB and PEN were later determined based on simulations (next section).

For the second campaign, shorter data acquisition times were employed, and only datasets obtained within the first six hours of operation, after the level and temperature stabilization, were analyzed. This resulted in approximately six datasets of five million traces for each sample measurement. The results, including the LY values corrected for $\tau_{triplet}$, are shown in Figure 11.10 (right).

Once the LY values are corrected for $\tau_{triplet}$, the LY values from repeated measurements agree well, within a fraction of the 3% systematic uncertainty derived from the first campaign.

The measurements within region (iii) in Figure 11.10 demonstrate that the LY from 125 µm films does not significantly differ for different sanding methods (non-treated, HS, MS) or reflectors (TTX or ESR), within the limits of the systematic uncertainty. While a rough or smooth surface may impact the amount of light measured from a specific angle using an optical setup (as in [120]), it does not seem to significantly affect the LY measured in this configuration, where light scatters multiple times.

Additionally, the LY measured from combinations with ESR and TTX were comparable. However, it should be noted that this result is valid only for non-optical coupling and is dependent on the geometry of the setup, given that the reflectivity of ESR is specular, while the reflective of TTX is diffuse.

A clear difference in performance is observed between the samples in region (iii) and the thinner films in region (ii). While both sets of films are not optically coupled, the lower performance of the thinner films may be related to their installation. The thin films are rather flexible, mechanically unstable, and their surfaces do not adhere to the TTX when manually pressed against it. This results in a rugged film surface when installed on the sample holder, contrasting to the 125 µm films, which do not require optical coupling to the reflector to be flat and well aligned, as shown in Figure 11.7.

To address this issue, several optical couplings were tested (Appendix C), and SMP glue was used to couple a thin PEN film to Tyvek. This laminate, Tyvek+Q53-25, performed as well as the non-optically coupled 125 µm films, despite the introduction of the glue, which may introduce absorption. Optical couplings to ESR were not tested, as ESR appeared to become more transparent in LAr (see Appendix C).

Another sample tested was the commercial aluminum-based laminate (Al+Q53-12). Despite the lower reflectivity of aluminum, its LY was not much lower than that of the best-performing combinations and still significantly higher than that of non-optically coupled combinations. The higher LY of the optically-coupled thin films in region (iv) compared to those in region

(ii) further supports the assumption that the rugged surface of the thin films after installation in the sample holder led to their lower LY.

11.3 LIQUID ARGON OPTICAL SIMULATIONS

To extract intrinsic optical parameters of TTX, TPB and PEN in LAr, a Monte Carlo simulation was conducted using the Geant4 toolkit [144]. This simulation accurately replicated the geometry, optics, and material properties of the experimental setup, including the interactions of α particles in LAr and the resulting scintillation photons. The setup optical parameters for the simulation are described in Section 11.3.1. To extract the desired optical parameters, the simulation was fine-tuned using data from the first campaign. This calibration process involved the following steps:

1. Estimation of the effective VUV photon yield (PY_{eff}): The absorber measurement provided a known reference for determining the effective VUV photon yield resulting from an α decay in the sample cell. Section 11.3.2 elaborates on the details of this estimation, and the resulting value was used as an input parameter for the subsequent simulations.

2. Tuning the VUV reflectivity of TTX: By iteratively adjusting the simulation parameters, the measured LY of the TTX measurement is matched to extract the VUV reflectivity of TTX. Section 11.3.3 outlines this iterative process, which resulted in an accurate parameter for subsequent simulations.

3. Estimation of the QE of TPB and PEN: Similarly, the simulation parameters for the QE of TPB and PEN were iteratively adjusted to reproduce the measured LY values and extract their intrinsic QE, as discussed in Section 11.3.4

By combining the LAr measurements with the Geant4 simulation, it was possible to extract the intrinsic QE of TPB and PEN, as well as the reflectivity of TTX in response to LAr scintillation. The upcoming sections provide a detailed description of each step and the discussion of the obtained results.

11.3.1 *Optical parameters & their uncertainties*

The simulation incorporated various optical parameters to accurately model the experimental setup and interactions with LAr scintillation photons. The following parameters and associated uncertainties were considered:

1. Scintillation spectrum and yield: The scintillation spectrum of LAr (shown in Figure 5.1) was obtained from [85], and its scintillation yield (SY_{LAr}) was tuned in the simulation using the absorber measurement.

2. Refractive indices (n_i) of LAr: These values were calculated using the Sellmeier coefficients measured by [138]. These indices were then used to

calculate the Rayleigh scattering length for each wavelength, resulting in a length of 99 cm at 128 nm.

3. Absorption length of LAr: The absorption length of LAr was set to 60 cm in the VUV range[7] and 10 m in the visible range. To account for uncertainties, simulations were also performed with lengths of 30 cm for VUV and 200 cm for visible light, but the effects were negligible given the size of the setup.

4. PMT efficiency: The QE of the PMT (QE_{PMT}) was set according to the values provided in its data sheet [147], 22% at 128 nm and 27% at 420 nm. The VUV QE was degenerate with SY_{LAr} (Section 11.3.2), so no additional uncertainty was added to it. The effect of the PMT's MgF_2 window on its wavelength-dependent QE in LAr was investigated by modeling the window using the refractive indices of MgF_2 from [148] and [149]. The resulting low reflectance was consistent with expectations for MgF_2. The transmission of the window in LAr, particularly in the VUV region, could be slightly higher [89]. This source of uncertainty is further discussed in Section 11.3.4.

5. Reflectivity of the absorber: These values were set according to is data sheet, 0.7% from the VUV to the visible region [140]. Increasing the reflectivity up to 2% had a negligible effect on the resulting LY since photons either bounced multiple times on the absorber or went directly to the PMT.

6. VUV reflectivity of the source disk (SD_{ref}): The optics of the source disk was determined by its surface composition (∼70% stainless steel and ∼30% black source material). Using the measured VUV reflectivity of stainless steel at 128 nm from [150] and assuming zero reflectivity for the black source material, SD_{ref} was estimated to be (16 ± 4)%. Its vis-reflectivity was considered negligible due to the small size of the disk. Since scintillation photons originated close to the source disk (at a few µm distance), the SD_{ref} VUV reflectivity was important. This value was degenerate with other parameters like QE_{PMT}, and uncertainties were associated with it only in the case of specular reflection, as discussed in Section 11.3.2.

7. Reflectivity of TTX: The reflectivity of TTX in the visible range was measured in this work (Chapter 9). As the refractive indices of LAr are slightly higher than those of air [138], the reflectivity of TTX in LAr could be slightly lower. Uncertainties in this value are discussed alongside the results. Initially, the VUV reflectivity of TTX was unknown but its measurement in LAr provided the value utilized in the simulations. The refractive index of TTX is not relevant as the reflectivity was fixed in this simulation, with the surface set to absorb photons that are not reflected.

7 While ref. [89] set a lower limit of 110 cm on the attenuation length of 128 nm photons by pure LAr (a value consistent with zero absorption), the values of 66 and 50 cm measured by [145, 146] indicate varying absorption lengths for different LAr batches (and impurity levels).

8. VUV absorption length (VUV-λ_{abs}) of TPB and PEN: A conservative range of values for the absorption of 128 nm photons by TPB, spanning from 250 nm to 450 nm, was considered. This range is based on the ~400 nm value measured by [96], and on the observation that the efficiency saturation from TTX+TPB samples in response to VUV was achieved at thickness under 1 µm [87, 137], compared to ~2 µm measured in [96][8]. The VUV absorption of PEN was assumed to be 100%, since the absorption of PEN was observed to be high at lower wavelengths (Chapter 9).

9. Visible absorption length (vis-λ_{abs}) of TPB and PEN: The measured vis-absorption of TPB and PEN films (Chapter 9) was used to estimate the mean values (M_v) of their effective vis-λ_{abs}[9]. Upper and lower limits ($M_v \pm \delta$) on vis-λ_{abs} were calculated considering the uncertainties in the measurements, with an additional 10% systematic uncertainty. The resulting upper values ($M_v + \delta$) were implemented in the simulation to provide a conservative lower limit on the QE of the shifters. The conservative vis-λ_{abs} limits for wavelengths from 425 to 600 nm are 2 to 10 mm for PEN and ~1 mm for TPB, indicating TPB's thin film is nearly absorption-free in this range. Incorporating scattering lengths above 50 µm for PEN and 2 µm for TPB[10] [136] did not result in significant changes.

10. Re-emission spectra of TPB and PEN: The emission spectrum from TPB at 87 K was taken from [102], while the PEN spectrum was measured at room temperature (Chapter 9). We did not utilize the spectrum from [151], taken at 93 K, because both the room temperature and 93 K spectra from that reference exhibit slight shifts towards lower wavelengths compared to the spectra obtained in this work and in [94, 120]. While this uncertainty in the spectrum could introduce an error in the QE of PEN estimated from the vis-only measurement (some of the spectrum might be attenuated by the acrylic window, as shown in Figure 11.11), the error in the VUV+vis measurement was negligible. The spectrum used in the simulation provided a slightly more conservative estimation of the QE of PEN.

11. Refractive indices of TPB and PEN at visible wavelengths: These values were set to 1.62 and 1.51, respectively, based on [123] and [139]. Varying these values within ±0.1 for TPB and ±0.2 for PEN did not result in significant changes, since the reflectance of visible photons by WLSR samples is dominated by the reflectance of TTX and the absorption of the films (Chapter 9). The refractive indices of TPB and PEN at VUV wavelengths are unknown. Therefore, the surfaces were set not to reflect VUV photons. Although this

8 These differences in absorption may be due to variations in coating technique, substrate, and perfect sample coverage, as discussed in the microscopy study of Section 11.1.

9 For this, we use $I_\alpha^W = (1 - I_R^W) \cdot (1 - e^{-d/\lambda_{abs}})$. As there is no knowledge of the exact path of the photon after entering the film, we attribute the absorption to a path length equal to the thickness of the film (d). This is an approximation valid for the simulation, as it reproduces the effective absorption observed.

10 Lower values (fractions of the film thickness) were not considered as they were not included in the calculation of effective absorption.

approach could lead to an overestimation of absorbed photons, it ensured a conservative estimation of the minimum QE of the shifters.

12. Transmittance of the acrylic window: To incorporate the properties of the poly(methyl methacrylate) acrylic window into the simulation of the vis-only mode, we measured its transmittance, shown in Figure 11.11. The 92.3% value in the plateau region is consistent with attenuation caused only by reflection, considering the material's refractive index of approximately 1.5 [152]. Consequently, the absorption length of the window was set to 1 m in this region. For values between the plateau and 350 nm, the absorbance was calculated by subtracting the transmittance and reflectance from one. Below 350 nm, all light is absorbed. The window modeling was validated by simulating the absorber measurement with the window, which resulted in an expected yield of zero PE.

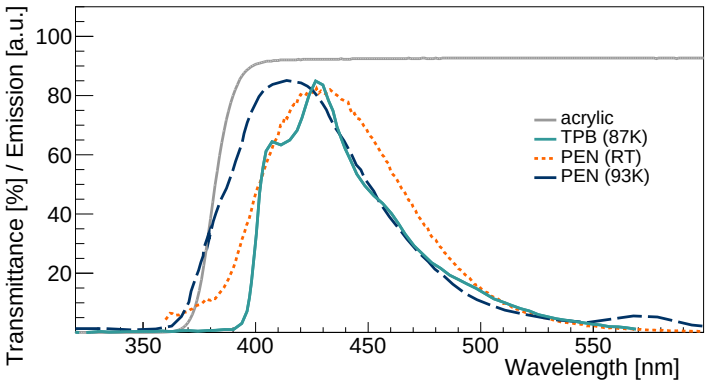

Figure 11.11: Transmittance of the acrylic window and emission spectra of TPB at 87 K [102], of PEN at 93 K [151] and PEN at RT (this work).

11.3.2 *Effective photon yield in the sample cell*

The effective VUV photon yield (PY_{eff}) resulting from an α decay in the sample cell is quantified using the VUV-only measurement of the absorber. While this value is extracted from the simulation framework, we provide an analytical description in this section to examine its degeneracy with other optical parameters and evaluate associated uncertainties.

PY_{eff} is related to the number of photons detected by the PMT (N_{det}), according to the equation:

$$N_{det} = PY_{eff} \cdot QE^{VUV}_{PMT} \cdot \Omega, \tag{11.1}$$

where QE^{VUV}_{PMT} is the QE of the PMT at 128 nm and Ω is the solid angle covered by the PMT in the hemisphere above the source disk. A schematic of Ω for the absorber measurement is shown in Figure 11.12 (1).

PY_{eff} depends on the photon yield from an α particle depositing $E = 5.5$ MeV in LAr ($PY^{\alpha}_{LAr} = E \cdot SY_{LAr}$), but considers that some of the scintillation

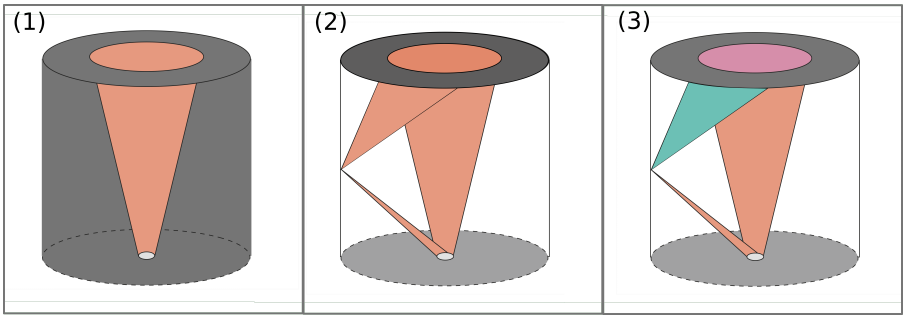

Figure 11.12: Schematic of the light produced by the α source in the bottom and detected by the PMT at the top in the measurement of the absorber (1), a reflector (2) and a WLSR sample (3). For (1,2), only VUV light is detected. For the WLSR, part of the VUV light is absorbed, re-emitted in blue and reflected. This can be measured in the VUV+vis or vis-only mode, using the acrylic filter to block the VUV component. Schematic modified from [3].

photons may be reflected by the source disk. For the isotropic emission of photons around the α decay, half of the photons can directly propagate through the cell, while the other half reach the surface of the source disk, where they are either absorbed or reflected, with a probability according to the reflectivity of the source disk, SD_{ref}. PY_{eff} is thus defined as:

$$PY_{eff} = PY^{\alpha}_{LAr} \cdot \frac{1}{2} \cdot (1 + SD_{ref}), \tag{11.2}$$

which can be expressed in terms of the scintillation yield (SY_{LAr}),

$$PY_{eff} = E \cdot SY_{LAr} \cdot \frac{1}{2} \cdot (1 + SD_{ref}). \tag{11.3}$$

Equation 11.3 shows that SY_{LAr} and SD_{ref} are degenerate components of PY_{eff}, implying that their specific values are not crucial as long as PY_{eff} is accurately determined. However, when the reflectivity of the source disk, SD_{ref}, includes a specular component, PY_{eff} is non-isotropic. To investigate this uncertainty, we set SD_{ref} according to the parameters described in Section 11.3.1 and simulate different scenarios by varying the reflection components of SD_{ref}, including a portion that is Lambertian and the remaining portions with 25%, 40%, or 60% specular reflection.

This introduces a systematic uncertainty in determining PY_{eff} from the absorber measurement. Combined with the uncertainty arising from the measured PE value of the absorber, it results in a total systematic uncertainty of $\pm 5\%$ on PY_{eff}. Since the impurity level remains relatively stable across these measurements, uncertainties related to variations in SY_{LAr} due to impurities are likely included within the $\pm 5\%$ uncertainty on PY_{eff}[11].

11 In cases where the PY_{eff} uncertainty is estimated through repeated measurements in the vis-mode, the results agree within less than one sigma for a systematic error of less than 3%, as discussed in Section 11.3.4.

According to Equation 11.1, different values of PY_{eff} and QE_{PMT}^{VUV} can result in the measured N_{det}. We chose to fix the value of QE_{PMT}^{VUV} as specified in Section 11.3.1 and determine the remaining free parameter, SY_{LAr}, by matching N_{det} to the measured PE value. The resulting SY_{LAr} is ∼25 ph/keV. It is worth noting that fixing QE_{PMT}^{VUV} to estimate PY_{eff} does not introduce any uncertainty in the estimation of efficiencies for other WLS samples, as long as the ratio q_{QE} between the true QE_{PMT}^{vis} and QE_{PMT}^{VUV} remains the same. In other words, if the overall QE of the PMT increases in LAr (as discussed in Section 11.3.1), the relative value of q_{QE} should remain unchanged. This relationship can be expressed as:

$$QE_{PMT}^{vis} = q_{QE} \cdot QE_{PMT}^{VUV}. \tag{11.4}$$

In this case, the number of scintillation photons detected from any sample can be described similarly to the Equation 11.1:

$$N_{det} = PY_{eff} \cdot QE_{PMT}^{VUV} \cdot (\Omega + \epsilon \cdot q_{QE}^{s}), \tag{11.5}$$

where ϵ is the sample enhancement factor: more photons reach the PMT due to shifting and/or reflection from the sample, as illustrated in Figure 11.12, (2, 3). The term q_{QE}^{s} is equal to q_{QE} for the VUV+vis measurements or equal to unity for the VUV-only measurements. The extra LY can be used to determine the QE or the VUV reflectivity of the samples. Since these parameters involve the geometry and optics of the samples, we extract these values from the simulations, as explained in the next sections.

11.3.3 *VUV-reflectivity of TTX*

To extract the VUV reflectivity of TTX, we simulated the TTX sample in the setup for different values of its VUV reflectivity. An example of the VUV photons being reflected by the TTX in the simulation is shown in Figure 11.13.

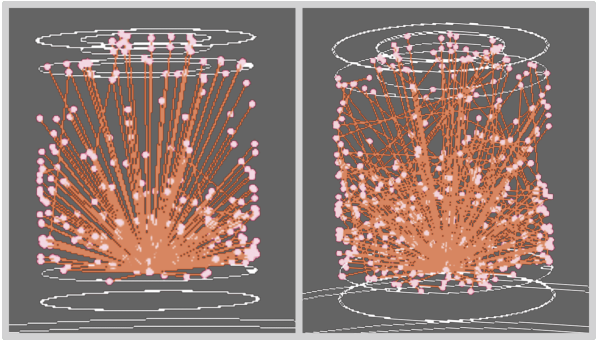

Figure 11.13: Left: Simulation of an α decay in the LAr setup covered by the absorber. The α particle is not visible, only VUV photons (in a reduced number, for clarity). Right: Simulation of TTX surface with non-zero reflectivity, resulting in photons being reflected by its surface.

We then find the reflectivity value that matches the measured PE of TTX. To account for the systematic uncertainty, we run the simulation for the mean and limit (±5%) values of PY_{eff}. The uncertainty arising from the measured PE of the sample represents the statistical uncertainty. The obtained VUV reflectivity is $9 \pm 6(stat) \pm 2(syst)$%. This result indicates that, although the measured mean PE value from TTX is higher than that of the absorber, we cannot confirm a non-zero reflectivity from TTX. Hence, we establish an upper limit (at 90% CL) that the VUV reflectivity of TTX is below 17%.

11.3.4 *Quantum efficiency of TPB & PEN*

To determine the QE of TPB and PEN, a similar approach is followed. The simulation is configured with the specified geometry and optical parameters, and then run for various QE values of the shifters until the measured PE value is reproduced. However, in this case, uncertainties related to the samples themselves are incorporated into the simulations, in addition to the systematic uncertainty on PY_{eff}. These uncertainties have been extensively discussed in Section 11.3.1. The main ones are summarized in Table 11.3.

Table 11.3: Range of expected and limit values of the optical parameters of the WLSR samples, given their uncertainties. Values in bold are used for the *low limit* case of QE. See text for details.

TPB

parameter	lower value	expected value	upper value
VUV-λ_{abs}	**250 nm**	350 nm	450 nm
vis-λ_{abs}	$M_v - \delta$	M_v	$\mathbf{M_v}+\boldsymbol{\delta}$
VUV-ref. TTX	0%	9%	**17%**
vis-ref. TTX	unconstrained	95%	**95%**

PEN

parameter	lower value	expected value	upper value
vis-λ_{abs}	$M_v - \delta$	M_v	$\mathbf{M_v}+\boldsymbol{\delta}$
vis-ref TTX	unconstrained	95%	**95%**

For the TPB-based sample, we consider the uncertainties associated with the VUV and vis-λ_{abs}, as well as the VUV to vis-reflectivity of TTX. For the PEN-based sample, the VUV parameters are not relevant since we assumed that all VUV light is absorbed.

For both samples, we consider the mean value (M_v) of vis-λ_{abs} and its $\pm\delta$ uncertainty as described in Section 11.3.1. The uncertainties on the VUV-reflectivity of TTX in LAr were discussed in the previous section, while the lower value of its vis-reflectivity is left unconstrained (since its reflectivity could be lower in LAr in comparison to ∼95% measured in air). When the vis-reflectivity of TTX is lowered, it results in an increased estimated QE of TPB, which can exceed unity for reflectivity values below 80%. This implies

that the vis-reflectivity of TTX in LAr[12] is likely higher than 80%, but it is not possible to confidently constrain the upper value of the QE of TPB in LAr.

We thus performed the analysis considering two cases: the *expected case*, which utilized the expected values of the optical parameters, and the *lower limit case*, which incorporated the lower or upper values of these parameters, highlighted in bold in Table 11.3. The estimation of the QE for the *lower limit* yielded the most conservative value, which was used to obtain 90% CL lower limits on the QE of TPB and PEN, shown in Table 11.4.

Table 11.4: QE of TPB and PEN using the expected values of the optical parameters and 90% CL lower limit on the QE of TPB and PEN taking all investigated uncertainties into account.

QE	*expected* value	90% CL *lower limit*
TPB	$85 \pm 5(stat) \pm 6(syst)\%$	67%
PEN	$69 \pm 4(stat) \pm 5(syst)\%$	49%

While the *expected case* considered only the uncertainties on the measured PE and on PY_{eff}, the *lower limit case* incorporated all the uncertainties on the optical parameters of the shifters and reflector, and uncertainties that potentially increase the estimated QE if introduced in the simulation. These included the potential enhancement of the PMT's QE in the VUV range (discussed in Section 11.3.2), uncertainties on the emission spectrum of PEN, and on the VUV refractive indices of TPB and PEN (discussed in Section 11.3.1). Consequently, these lower limits are conservative. All values were obtained using measurements and simulations in the VUV+vis mode.

In the vis-only mode, simulations including the acrylic window yielded expected QE values of $91 \pm 4(stat) \pm 4(syst)\%$ for TPB and $57 \pm 3(stat) \pm 4(syst)\%$ for PEN. These values agree within errors with the expected values presented in Table 11.4[13]. The estimations from the vis-only mode served as a cross-check of stability and shifted light, but were not further considered in the determination of the lower limits, given the additional optical uncertainties introduced by the acrylic window[14].

11.4 DISCUSSION & CONCLUSION

This section discusses the results of the two characterization campaigns of WLSR materials involving microscopy imaging and measurements in LAr.

In the first campaign, microscopy imaging confirmed the homogeneous distribution of TPB achieved through the in-situ evaporation, validating sample quality for the QE estimation. TTX, TPB, and PEN samples were

12 While one surface of TTX faces LAr and the other surface boundary is TPB, most of TTX is rather in LAr, since it is a porous material with thickness much larger than the TPB coating.
13 Note that the agreement remains valid for lower values of the systematic uncertainty (∼2.5%).
14 Particularly for PEN, which has some uncertainty in its emission spectrum (Section 11.3.1)

measured with a VUV-vis sensitive PMT in a LAr setup, and their optical parameters were characterized through LY comparison and simulations.

The results showed that TTX has a lower capability to reflect LAr scintillation compared to other PTFE-based materials used to reflect liquid xenon scintillation: 17% for TTX in LAr compared to over 95% for PTFE in liquid xenon [153]. This reduced reflectance of TTX may be attributed to the absorption edge of PTFE at ∼160 nm [154]. When TTX was coupled to shifters, it demonstrated a reflection response to shifted light of over 80% in LAr, potentially reaching the high values measured in air (∼95%).

The obtained QE values for TPB are consistent with previous measurements, matching the 73 ± 9% value from [96] corrected for the increase in efficiency at 87 K measured by [98]. While the measurements in this work indicated an expected TPB QE lower than unity, they did not establish an upper limit.

Regarding PEN, its efficiency was previously reported only relative to TPB. This work thus provided the first independent measurements of PEN's performance. Its LY relative to TPB was additionally obtained by using the measured PE values from PEN and TPB in the VUV+vis mode subtracted by the PE value measured from the absorber. Table 11.5 presents this relative LY value along with values from the literature.

Table 11.5: LY from PEN relative to TPB in response to 128 nm (LAr scintillation) light, at room temperature (RT) or LAr temperature (∼87 K). All the films are biaxially oriented: a few of them backed by a reflector, and a few sanded (marked with (s)). Geometry of the setups vary. Values from this work are shown in bold.

PEN sample	relative LY	Reflector	temperature
molded PEN	∼ 50% [94]	no	RT
Film (125 µm)$^{(s)}$	∼ 50% [120]	no	RT
Film (125 µm)	80(23)% [92]	no	LAr[15]
Film (125 µm)	34(1)% [103]	ESR	LAr
Film (25 µm)	39(2)% [104]	ESR	LAr
Film (125 µm)$^{(s)}$	**75(7)%**	**TTX**	**LAr**

It is noteworthy that these LY ratios are not directly comparable: while the QE is an intrinsic property of the material, the measured LY depends on the setup geometry and sample optics. For instance, the photodetector coverage in the setup of [104] was ∼1%, resulting in multiple scattering of photons and a LY more dependent on the reflectivity and absorption of the sample. In this work, the photodetector coverage was ∼6% and photons were less likely to scatter multiple times because the bottom was covered with absorber.

LY variations have been observed in different studies for TPB with varying thickness and PEN of different thicknesses and types [87, 96, 97, 103, 105]. This sample dependence is among the causes for the differences in the relative LY values shown in Table 11.5. The highest LY from PEN relative to TPB,

15 The value from [92] was measured at RT and projected at LAr temperature.

directly measured in LAr, was obtained in this work[16]. This remains true for the analysis of the vis-only mode, which results in a relative LY $>$ 48%, despite the acrylic window partially attenuating the emission from PEN (an effect that is only modeled in the simulation).

After the first campaign, questions remained regarding the higher LY observed from TTX+PEN (HS). Among these questions were: whether sanding PEN increased its LY, by facilitating light to exit the film or removing some degraded layer, and whether uncoupled combinations performed better, given that some optically coupled combinations were observed to become transparent in LAr [103]. Finally, the main question was how to optimize a PEN-based WLSR, for instance, whether thinner PEN films would perform better due to their enhanced transparency.

To address these questions, the second campaign focused on PEN-based WLSRs, examining several PEN thicknesses, grades, reflectors, and couplings. The results from 125 µm films in LAr indicated that neither the sanding method nor the specific reflector (TTX or ESR) significantly affected the LY in the employed setup configuration, where light scattered several times.

Non-optically coupled thin films presented installation challenges that affected their results. To address this issue, various optical couplings were tested, and an optimized laminate of thin PEN film glued to Tyvek was measured. This laminated performed as well as the most efficient WLSR combinations. Additionally, a commercial aluminum-based laminate was tested for the first time and exhibited a higher LY compared to non-optically coupled thin films, proving itself as a practical option for experiments without strict radiopurity requirements that prioritize ease of use.

The PEN films measured in this campaign are currently undergoing further characterization using ICPMS measurements and a VUV optical setup [137] to determine the batch-dependency of PEN efficiency and the presence of VUV-absorbing materials on the film surface that possibly reduce its LY.

Overall, the characterization campaigns yielded important results for detector designs and optical simulations in experiments such as LEGEND-200, LEGEND-1000, and others employing TTX, TPB, or PEN in LAr. Constraining the QE of shifters is crucial to accurately determine other optical parameters in simulations of detectors that employ these films.

The estimated QE values suggest that the intrinsic QE of PEN may not significantly differ from TPB's, with a mean relative expected value of $\sim 81 \pm 10\%$. This indicates potential for improving the LY from a PEN-based WLSR by reducing effective absorption and optimizing coupling to the reflector. While some applications may require the efficiency of PEN to closely match that of TPB, the obtained lower limit of 49% on the QE of PEN may be sufficient for certain applications. For such cases, the commercial laminate tested in this work could serve as a viable option.

16 The TPB WLSR used for comparison had already demonstrated high efficiency [87], so a high relative value should not be attributed to lower performance of the specific TPB WLSR.

The wide range of PEN combinations measured in this study highlights the versatility of PEN as a WLS material, providing flexibility for various experimental requirements. It offers options that balance ease of use and efficiency, making it suitable for a variety of applications. This comprehensive characterization of PEN opens up possibilities for a wider range of applications and expands the choices available to experimenters working with WLS materials.

PART IV

ORDINARY MUON CAPTURE FOR $0\nu\beta\beta$ DECAY WITH MONUMENT

12

ORDINARY MUON CAPTURE FOR $0\nu\beta\beta$ DECAY

As discussed in Chapters 2 and 3, reducing the uncertainty in NMEs for $0\nu\beta\beta$ decay is crucial to precisely assess the sensitivity of experiments searching for this process and provide accurate estimates of $m_{\beta\beta}$ if $0\nu\beta\beta$ decay is observed. The MONUMENT experiment plays a pivotal role in this pursuit by measuring ordinary muon capture (OMC) in selected targets, providing total and partial OMC rates that serve as key inputs for NME calculations. The methodologies employed for obtaining these rates are described in [56]. This chapter present the initial steps towards this goal with a specific focus on the measurement and analysis of ^{136}Ba carried out as part of this thesis.

12.1 THE MONUMENT EXPERIMENT

MONUMENT (Muon Ordinary capture for NUclear Matrix elemENTs) is a collaborative effort established in 2020 with the aim of measuring OMC in various isotopes, focusing on the daughters of $0\nu\beta\beta$-decay candidates. I joined this collaboration for its first irradiation campaign in 2021, when we irradiated ^{76}Se and ^{136}Ba. The measurements consisted of irradiating the target isotopes with muons and recording the energy and time distribution of γ rays emitted during the de-excitation of states produced by OMC. This process is illustrated for ^{136}Ba in Eq. 12.1 and Figure 12.1.

$$\text{OMC: } {}^{136}Ba + \mu^- \rightarrow {}^{136}Cs^* + \nu_\mu \rightarrow {}^{136}Cs + \gamma. \tag{12.1}$$

$$0\nu\beta\beta : {}^{136}Xe \rightarrow [virtual({}^{136}Cs^*)] \rightarrow {}^{136}Ba + 2e^-. \tag{12.2}$$

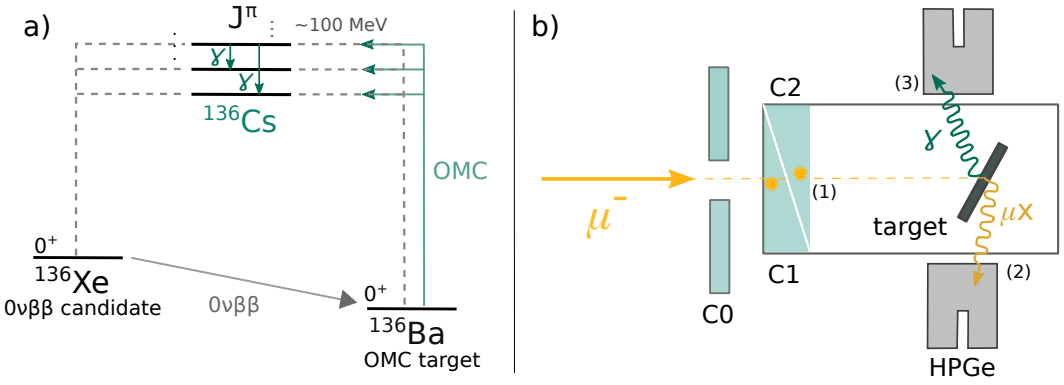

Figure 12.1: a) The $0\nu\beta\beta$ decay of ^{136}Xe could occur via transitions through high-energy virtual states of ^{136}Cs, which can be accessed via OMC in ^{136}Ba. b) Schematic of the MONUMENT experimental approach: A target, surrounded by HPGe detectors and scintillating counters (C0, C1, and C2), is irradiated with muons, which induce a scintillation signal (1) when crossing C1 and C2, and emit muonic X-rays (μX) after forming muonic atoms. These μX are promptly detected (2), while γ rays from the de-excitation of the isotope produced by OMC are detected as delayed signals (3).

To irradiate the selected targets, MONUMENT utilizes negative muons from the πE1-2 beamline of the high-intensity proton accelerator facility at the Paul Scherrer Institut (PSI). This beamline provides $\mathcal{O}(10^4)$ μ^-/s with momentum around 30 MeV/c. To measure the time relative to an incoming muon, scintillating counters coupled to PMTs are used. These counters, labeled as C0, C1, and C2 in Figure 12.1, trigger a signal when a muon passes through them, as indicated by (1) in the figure[1].

To precisely measure γ rays emitted during the de-excitation following OMC, MONUMENT utilizes HPGe detectors, which offer superior performance for γ spectroscopy, as discussed in Chapter 6. These detectors also record the high-energy muonic X-rays (μX) emitted by the produced muonic atoms (as described in Section 3.2). These represent a 'prompt' HPGe signal, indicated by (2), followed by 'delayed' γ rays (3), which come from the de-excitation following OMC.

A variety of HPGe detectors were utilized in the 2021 campaign: two Coax and two BEGe detectors of p-type, and four n-type Coax detectors. Each detector has its characteristic features: the Coax detectors generally have better time resolution, while the BEGes provide better energy resolution. The sensitivity to low or high energies was dominated by either the specific window type or the size of the detectors (detailed in Appendix D). The HPGe detectors assembled in the beam hall are shown in Figure 12.2.

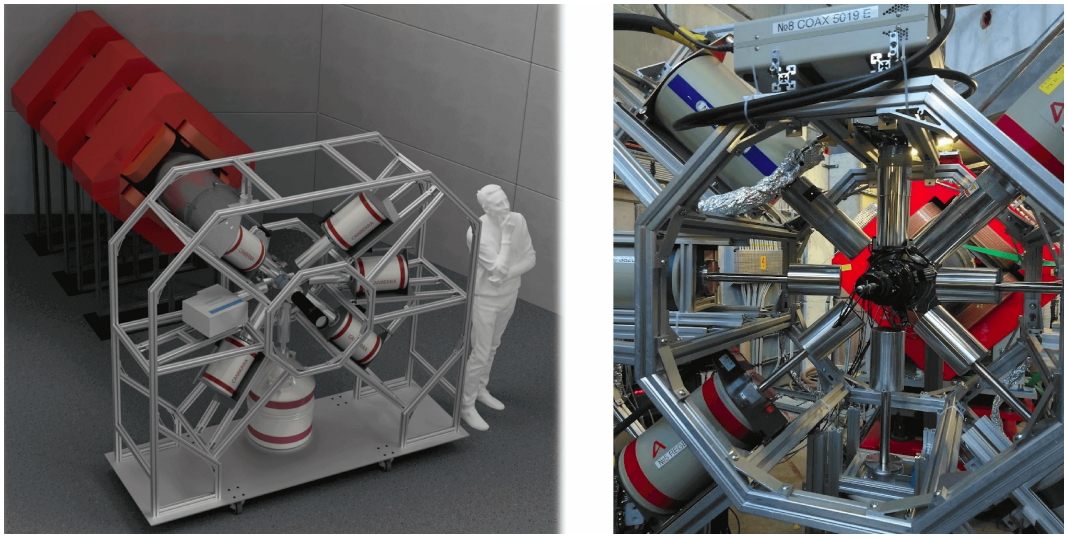

Figure 12.2: Left: Schematic of the MONUMENT experiment. Right: During the 2021 run, eight HPGe detectors surrounded the target sample placed at the front of the beamline, which can be seen at the back of the support frame. Credit for the schematic: MONUMENT collaboration.

The setup remained mostly unchanged during the 2022 irradiation campaign, when ^{100}Mo was measured. However, this campaign is not covered in this work, as this thesis primarily focuses on the data analysis of ^{136}Ba taken during the first campaign, described in more detail in the next section.

1 An additional counter, C3, is not shown, as it was mostly not relevant for this analysis.

The enriched Ba target (^{enr}Ba) was prepared by depositing a solution of $BaCO_3$ powder dissolved in isopropanol onto a holder and allowing it to dry. The resulting target consisted of 2 g of $BaCO_3$. The Ba component of the powder was primarily composed of ^{136}Ba (95.3%), followed by ^{138}Ba (2.4%), ^{137}Ba (1.5%), and $^{A<136}$Ba (0.8%). The enrichment in ^{136}Ba was important to avoid populating the excitation state of interest through concurrent neutron emission reaction following OMC in more massive isotopes[2], as in:

$$^{137}\text{Ba} + \mu^- \rightarrow ^{136}\text{Cs}^* + \text{n}.$$

Although the target also contained CO_3, these atoms are much smaller in size and have a weaker Coulomb potential. Therefore most of the muons are expected to be captured in ^{136}Ba[3]. The measurements were conducted in three modes, listed below.

1. *Beam-on:* This is the main data-taking phase, during which the target was irradiated with muons, as illustrated in Figure 12.1. The muon energy was adjusted so that most of them (∼95%) stopped in the target [56].

2. *Beam-off:* After the beam-on phases, a short (∼24 h) data-taking period followed. The target remained in place, but the beam shutter was closed. The HPGe detectors continued detecting activity from beam-related mid-lived isotopes in the target.

3. *Offline:* For this measurement, the target was removed from the setup in the beam hall and measured using a HPGe detector located at the radiochemistry department of PSI. This offline data-taking allowed further measuring radioactivity from isotopes with half-lives on the order of days to weeks.

Beam-on data from the enriched ^{136}Ba target was collected in two periods: from October 21st to October 27th, and again from November 4th to 7th. *Beam-off* data was acquired following both periods, while *offline* data was taken only after the first. To acquire *offline* data, a Canberra ADC board controlled by the Genie 2000 Basic Spectroscopy Software was utilized.

For *beam-on* and *beam-off* data acquisition with the full MONUMENT setup, two DAQ systems were employed: MIDAS and LLAMA (also known as ALPACA). MIDAS, a DAQ system developed at PSI and TRIUMF [155] and employed by other PSI-based experiments [156], recorded trigger timestamps and signal pulse heights obtained using an online trapezoidal filter. To allow for improved offline adjustment of time resolution, MIDAS also recorded the first 1.4 µs of each raw HPGe waveform. By providing an online signal processing and analyzer, MIDAS enabled real-time monitoring of ongoing

2 To understand and quantify this effect, a natural Ba target was also measured as a comparison. However, the analysis of this data is not discussed in this work.

3 It is known that even if a muon is captured in the muonic orbit of a light atom, it may still migrate to the orbits of surrounding heavy atoms [54].

measurements. LLAMA, a system specifically dedicated to MONUMENT [157], focused on recording raw traces for later optimization of filtering parameters and detailed offline analysis. More information about these systems, including their trigger schemes, signal processing, and calibration, can be found in [155–159]. In this work, only data acquired with MIDAS is analyzed.

12.3 DATA PROCESSING & SELECTION

Data pre-processing & preliminary run selection

The data acquired with the MIDAS DAQ was processed into ROOT trees [160] containing various parameters for each event, such as the ID channel of the HPGe detector (1 to 8) or scintillating counter (0 to 3), pre-calibrated energy (applicable only for HPGe events), timestamps, and status flags indicating events such as pileup[4], underflow or overflow.

MIDAS runs were pre-selected based on log notes taken during the beam-time. Criteria to exclude runs included the presence of calibration sources or a significant drop in beam current. A total of 2898 *beam-on* runs were classified as satisfactory, each with a livetime of $\sim$300 s. All the *beam-off* runs were classified as satisfactory and were used for this analysis, each with a livetime of $\sim$1 h[5]. While these initial data selection and processing were performed by collaborators, the analysis presented in this work required further processing the data to extract the events and parameters of interest, as described in the next section.

Time distributions, event selection & classification

The time difference ($t_{\mu\gamma}$) between a signal in a HPGe detector (Ge hit) and the passage of a muon through a scintillating counter (C# hit) is a crucial parameter for analyzing OMC data. Events with large $t_{\mu\gamma}$ are less likely to have been caused by a muon. To pre-select muon-correlated events, a correlation window is defined as follows:

$$t_{\text{corr}}^{\text{min}} < t_{\mu\gamma} < t_{\text{corr}}^{\text{max}}, \text{ where } t_{\mu\gamma} = t_{\text{Ge}} - t_{\text{C\#}} \tag{12.3}$$

$$\text{and } t_{\text{corr}}^{\text{min}} = -100\,\text{ns and } t_{\text{corr}}^{\text{max}} = 1000\,\text{ns}.$$

The definition of $t_{\text{corr}}^{\text{min}}$ accounts for the $\pm$100 ns uncertainty in the time measurement of C# hits[6], while the definition of $t_{\text{corr}}^{\text{max}}$ considers the muon capture lifetime, which is typically between 80 ns and 200 ns for heavy targets [56]. Ge events that satisfy all status flag criteria are then classified into two main categories based on the correlation window:

4 The acquired traces were $\sim$15 µs for HPGe events and $\sim$1.4 µs for the scintillating counters.
5 MIDAS runs re-start at a fixed file size, which is reached faster during the beam-on phase.
6 Although a muon takes less than a nanosecond to go through the counters, the analysis of time between C# hits (t_{C2}-t_{C1}) reveals events distributed within approximately $\pm$100 ns from the mean of zero.

1a. **Uncorrelated:** Ge events with no C# hit within the correlation window.

1b. **Correlated**: Ge events that are timely correlated with a muon. This correlation is further defined by the condition:

$$\overline{C0} \wedge C1 \wedge C2, \tag{12.4}$$

where $\overline{C0}$ means that no C0 hit was observed within the time correlation window, and C1 $\wedge$ C2 means that one C2 and one C1 hit were observed within the correlation window, where

$$t_{corr}^{min} < t_{Ge} - t_{C2} < t_{corr}^{max} \text{ and } |t_{C2} - t_{C1}| < 100\,\text{ns}.$$

This classification of events is depicted in Figure 12.3, showing the procedure to obtain the distribution of $t_{\mu\gamma}$ by scanning Ge events from the ROOT trees, categorizing them as **correlated** or **uncorrelated**, and then summarizing their information into arrays containing the recorded energy E and $t_{\mu\gamma}$ for each Ge channel. Events falling outside these two categories are not further analyzed.

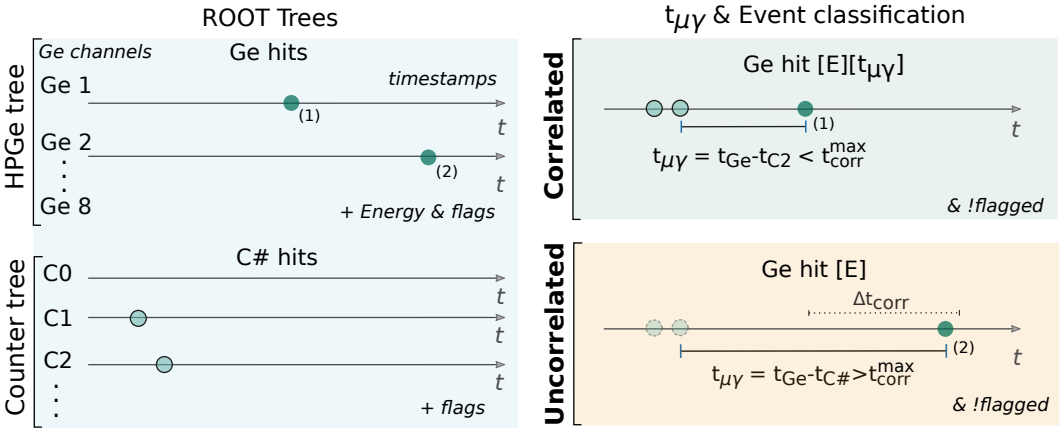

Figure 12.3: The Ge hits in the HPGe tree are sorted according to their timestamps, which are compared to those of the C# hits from the scintillating counter. If a Ge hit, such as (1), fulfills the **correlated** criterion, it is categorized as such and its energy and $t_{\mu\gamma}$ values are stored in an array. If a Ge hit, such as (2), is not correlated with any C# hit, it is classified as **uncorrelated** and saved in a separate array.

Final run selection & Re-calibration

After the initial data pre-selection, a further stability check was performed. The rates from the scintillating counters and HPGe detectors were analyzed per run: Runs with rates deviating by more than 3.5σ from the mean value of a local group of approximately 70 runs were flagged[7]. Out of the total 2898 runs, only eight runs were excluded, leaving 2890 runs for further analysis.

7 The use of mean rates from local groups is necessary due to long-period decrease of beam intensity (several hours or days), making the average and standard deviation of all runs together misleading when searching for outliers (such as runs taken during sudden drops of beam intensity).

The mean rates from these selected runs are displayed in Figure 12.4 for the three scintillating counters and six HPGe detectors used in this analysis. Ge channels 2 and 6 were excluded due to the need for further tuning in the pre-processing stage (from raw data to ROOT trees), which is ongoing work. The high count rates of C1 and C2 ($\sim$ the rate of muons provided by the beamline) indicate that most of the muons passed through the central opening to the target. The last two bins of the figure represent the **correlated** and **uncorrelated** events used in this analysis. Comparing their sum to the total number of events shows that the majority of events were accepted.

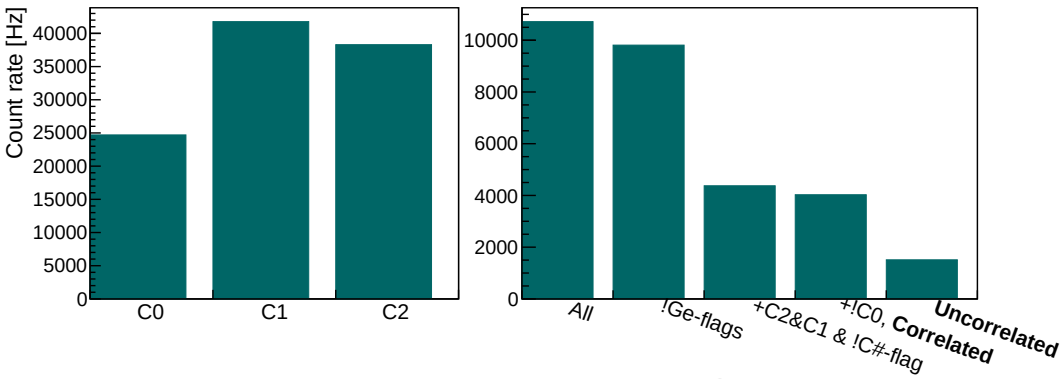

Figure 12.4: Count rates of accepted (non-flagged) events from each scintillation counter and total rates within [100, 4500] keV from six HPGe detectors. All events are shown initially, followed by the selections: non-flagged events, which are further separated into **uncorrelated** or into C2&C1 correlation, followed by the additional anti-coincidence with C0.

After this selection process, a second calibration was applied to the pre-calibrated data. For this calibration, peaks from natural radioactivity observed in the **uncorrelated** data (e.g., the 583 keV and 2614 keV γ rays from ^{208}Tl) were utilized. This re-calibration was performed for each HPGe detector, employing a linear calibration function that resulted in better alignment with the *offline* calibrated data. The peak fitting procedure used for this re-calibration will be presented alongside the peak identification analysis. It is important to note that the final calibration of the data is still an ongoing effort. However, for the preliminary identification of X-rays and γ rays performed in this work the mentioned calibration provides sufficient accuracy.

12.4 Line Identification & Signal Estimation of Excited States

As motivated in Chapter 3, the primary objective of these measurements is to extract the total OMC rate and partial rates to excited states of ^{136}Cs. To achieve this goal, it is crucial to determine the net signal and time evolution of γ rays emitted during the de-excitation of multipole states produced by OMC [56]. However, the first challenge lies in identifying the lines of interest amidst the background produced by X-rays, natural radioactivity, and beam-produced isotopes. This section describes the various types of signals expected to be observed in the data and the features utilized to identify them.

Signals, identifiers & classifiers

In order to comprehensively understand the full spectrum and detect fainter excitation lines, we first categorize the expected signals based on their origins and their corresponding time features $t_{\mu\gamma}$:

- Muonic X-rays (μX): High-energy[8] X-rays emitted within $\sim 10^{-13}$ s during the transition of the muon captured in a muonic orbit to the lowest energy state K(1s) (as described in Section 3.2). Their single and double escape peaks (SEP, DEP) are also often present in the spectra.
- De-excitation γ lines: These γ rays arise from the de-excitation following OMC (Equation 12.1). They originate not only from excited levels of ^{136}Cs but more frequently from ^{135}Cs, considering that neutron emission following OMC is around one order of magnitude more likely [56]. Both lines are of interest, as we can use the more intense γ rays from ^{135}Cs to estimate the total capture rate, and the ones from ^{136}Cs to obtain partial rates [56]. The time distribution $t_{\mu\gamma}$ of these lines follows an exponential decay with a characteristic time of $\mathcal{O}(100\,\text{ns})$, which is related to the OMC probability [56]. Consequently, these lines are considered delayed compared to the prompt μX signals.
- γ lines from beam-produced isotopes: Many of the OMC products of the $^{\text{enr}}$Ba target were unstable, with half-lives ranging from $\sim$15 min to $\sim$15 d. A few examples are ^{136}Cs ($T_{1/2}$=13 d) and $^{135\text{m}}$Cs ($T_{1/2}$=53 min).
- Natural radioactivity: The HPGe detectors, without dedicated shielding (such as lead layers), were especially exposed to sources of environmental radioactivity, such as from ^{238}U and ^{232}Th chains (discussed in Chapter 4). Lines from these chains, along with those from ^{40}K and cosmogenic ^{41}Ar[9], were observed, especially in the uncorrelated data.

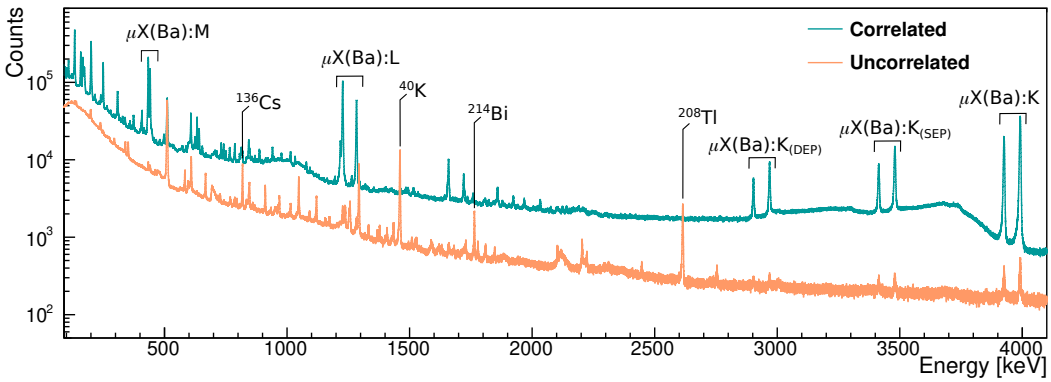

Figure 12.5: Correlated and **uncorrelated** spectra displaying prominent γ and μX lines.

8 They are $\sim$200 times more energetic than conventional X-rays, given the higher mass of muons compared to electrons.

9 ^{41}Ar is produced by neutron activation of atmospheric ^{40}Ar close to neutron-emitting targets.

Figure 12.5 shows two spectra[10], where many μX and γ lines are clearly observed. Their distinct signatures in the data are referred to as 'identifiers'. These identifiers are crucial in distinguishing different types of signals and understanding the origin of each line. Below are the identifiers we use for line identification:

I. Energy: The energies from γ rays emitted by isotopes from natural radioactivity and beam-produced isotopes are known with an accuracy better than 0.1 keV [57]. For the μX this information is extracted from a specific muonic X-ray database [161], which provides slightly less precise energy values. For the de-excitation lines, the energies from excitation schemes are extracted from [162] and present an uncertainty up to $\pm$0.5 keV.

II. Time ($t_{\mu\gamma}$): The time signature between Ge hits and C2 hits gives information on the correlation of events to a tagged muon. The μX are more intense at prompt $t_{\mu\gamma}$, while γ rays from excited states appear more clearly at delayed $t_{\mu\gamma}$, when the background of μX is reduced. The remaining signals appear at much longer time scales, being more clear in either the **uncorrelated** spectrum, or in the *beam-off* or *offline* data.

III. FWHM: By fitting the observed lines and comparing their resulting width to those obtained from calibration peaks, it is possible to understand whether the observed peak is composed of multiple lines with similar energy. Also, μX lines can be identified through their width, as their peaks are characterized by Doppler broadening [54].

IV. Intensity: Once lines were categorized using the previous identifiers, the comparison between their relative intensities and branching ratios (BR) was used to confirm whether they have been properly assigned to the right isotope (this applies only for the case the isotope had N>1 γ ray emissions with BR>5%). The branching ratios for γ rays from radioactive isotopes are precisely known [57]. The ones for excitation lines are much less precise, presenting uncertainties at the level of 50% [162].

As many lines may have similar energies, the timing information measured as $t_{\mu\gamma}$ is key to identify the peaks. To utilize this time information more effectively, we further categorize the correlated data into *prompt* and *delayed* events, in addition to the previous classifications. The resulting classification breakdown is presented in Figure 12.6.

In this breakdown, the events are initially classified as *prompt* if their $t_{\mu\gamma}$ values are less than 100 ns[11]. The remaining correlated events with $t_{\mu\gamma}$ values between 100 ns and 1000 ns are categorized as *delayed*. This distinction allows us to better identify the prompt μX and the delayed γ rays from excited states.

10 Unless otherwise specified, all the next spectra shown were measured with Ge channel 5 or 7.
11 This number is then adjusted once the lifetime of muonic atoms produced in the target is known.

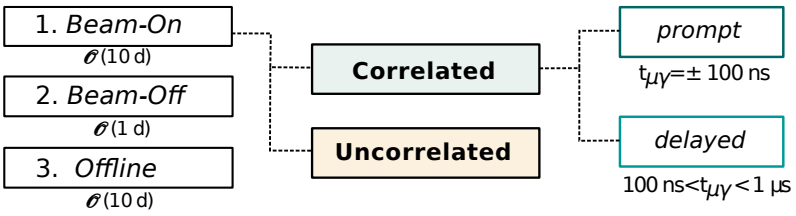

Figure 12.6: Schematic representation of the types of data classification. The order of magnitude of data taking time for the three measurement modes are shown as well as the time cuts for the *prompt* and *delayed* classifications.

Energy-time spectra and line identification

To observe the time signature of the radiation from different origins, we build spectra based on the event energy (identifier I) versus time $t_{\mu\gamma}$ (identifier II). Additionally, we separate the spectra according to the different classifiers (**correlated** *prompt* or *delayed*, **uncorrelated**, *beam-off*, and *offline*). This further helps in distinguishing radiation lines with different time characteristics. Given the large number of detected lines, the analysis of these spectra is performed for small energy windows. An example of such spectra is shown in Figure 12.7.

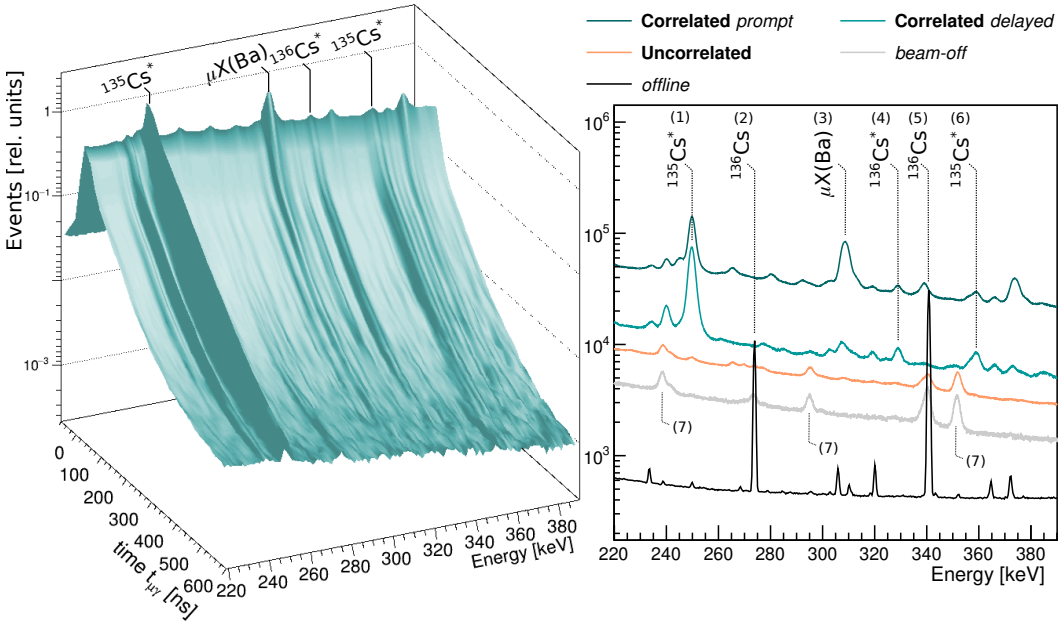

Figure 12.7: Energy-time distribution (220-385 keV vs. $t_{\mu\gamma}$ <600 ns) of **correlated** events during the irradiation of ^{enr}Ba. The *prompt* and *delayed* spectra shown on the right are projections of this spectrum for the corresponding time intervals. The $t_{\mu\gamma}$, **uncorrelated**, and *offline* spectra were normalized or re-scaled to improve visualization. Several lines are marked as examples, see text for details.

In this figure, the time signatures discussed earlier are clearly visible. Lines marked with numbers 1, 4, and 6 correspond to γ ray emissions resulting

from the de-excitation of isotopes formed by OMC in ^{enr}Ba. These lines are more prominent in the *delayed* spectrum. Line 3 corresponds to μX signals, which are mostly present in the *prompt* spectrum. Lines 2 and 5 originate from the decay of the beam-produced ^{136}Cs and are more visible in the *offline* spectrum due to its half-life of 13 d. The γ lines from these unstable beam-produced isotopes are mostly in the **uncorrelated**, *beam-off*, or *offline* spectra, depending on their lifetime. Lines indicated with 7 are from environmental radioactivity. Some of the marked lines partially overlap with others, an effect further investigated with the peak fitting procedure.

Over 100 γ rays and μX have been identified by comparing these spectra. This first identification was important to select 'de-excitation' lines, which we study in more detail to obtain the total and partial rates. To further validate the identification of these lines, a more quantitative approach is employed, where the peaks are fit to precisely determine the identifiers II-IV (time, FWHM and intensity). A particular focus is to study the line time evolution. This is achieved by fitting the decay in intensity over time, where the $t_{\mu\gamma}$ histogram is partitioned into time intervals of a few nanoseconds and the line intensity estimated in each interval [56].

However, many of the de-excitation lines from ^{136}Cs were faint, and their energies not precisely known. This often caused time-partitioned fits to fail in reproducing peaks. Therefore, these lines had to be fit first within $t_{\mu\gamma}$ intervals where their intensity exhibited a high signal-to-background ratio. To determine such intervals where faint peaks could be effectively fitted, the following procedure was employed.

Optimum interval (Δt^{opt}) & peak fitting

The optimum interval method aims to find the Δt^{opt} interval of the $t_{\mu\gamma}$ distribution that yields the highest signal-to-background ratio S_R for a given line of interest (LOI). The method consisted of calculating the signal S and Compton background B_C around a LOI within increasing $t_{\mu\gamma}$ intervals, and obtaining a signal-to-background ratio for each interval Δt, until minimum and maximum time boundaries ($t_{min/max}$) were found, as shown in Equation 12.5:

$$S_R(\Delta t) = \frac{S(\Delta t) - B_C(\Delta t)}{\sqrt{\sigma_B}} \tag{12.5}$$
$$t^{opt}_{min} < t_{\mu\gamma} < t^{opt}_{max}, \text{ with } \Delta t^{opt} = t^{opt}_{max} - t^{opt}_{min},$$

The boundaries $t_{min/max}$ for an optimized time interval were determined based on the point where further integration of time-binned sections decreased the signal-to-noise ratio for a given LOI. The investigated LOIs included: de-excitation lines from ^{136}Cs and ^{135}Cs, as well as a few μX lines, for comparison. The method is exemplified for two lines in Figure 12.8.

At first, the signal was estimated from a energy region spanning $\pm$1-2 keV around the expected mean of the LOI, while the noise was estimated from selected sidebands a few keV away from the mean. Once a preliminary

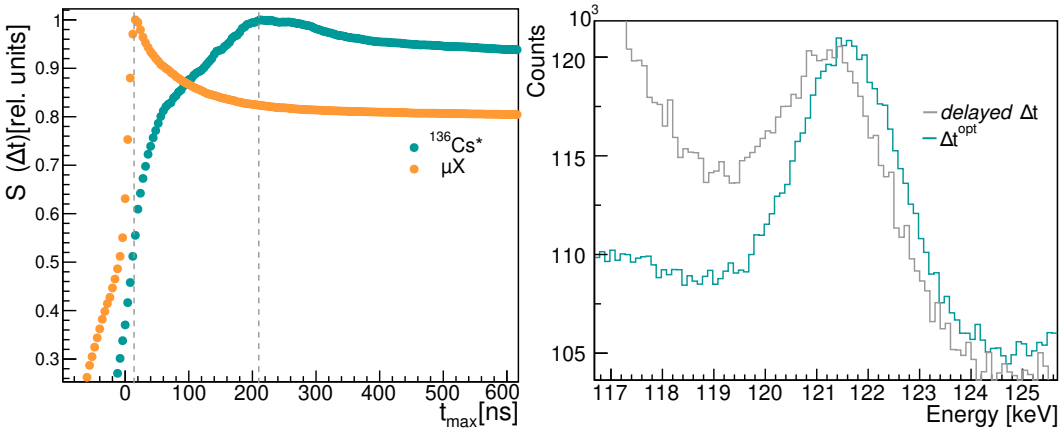

Figure 12.8: Left: S_R calculated for several t_{max} starting from -100 ns for two candidate μX and de-excitation γ LOIs with energies of 121.4 keV and 309.5 keV, respectively. The optimum t^{opt}_{max} values obtained are marked with dashed lines. The 121.4 keV γ line is plotted on the right for both the time interval of the *delayed* classification as well as for the optimum interval Δt^{opt}.

optimum interval Δt^{opt} was identified, the LOI became more prominent in relation to the background, as shown in Figure 12.8. The LOI was then fit using a combination of a Gaussian and a step function (details regarding these fits will be subsequently covered). With the Gaussian mean (μ) and standard deviation (σ) derived from the fit, the calculation for the optimized interval was repeated, estimating the signal within $\pm 3\sigma$ around the mean and the Compton background from the sidebands. As a result, new Δt^{opt} intervals were established, which are shown in Figure 12.9.

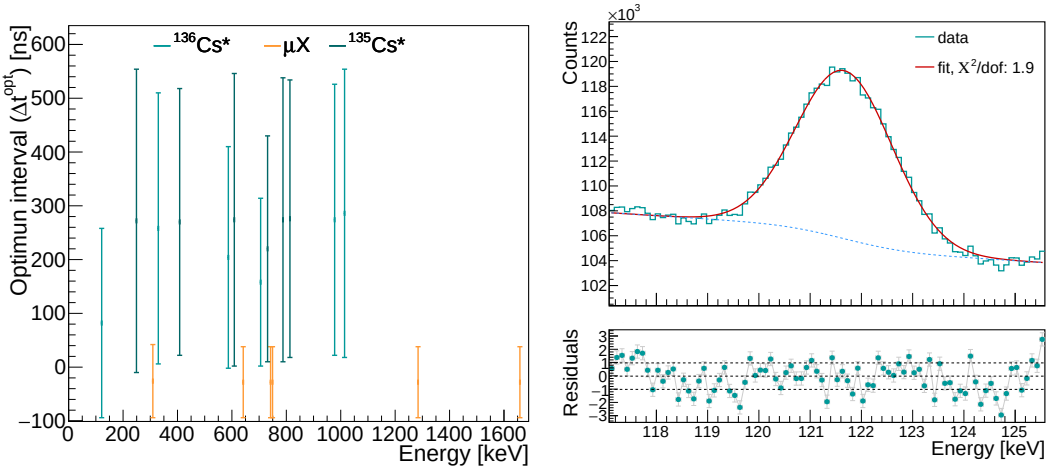

Figure 12.9: Left: Optimum Intervals obtained for several μX and de-excitation γ lines. Right: Spectrum around the 121.4 keV γ line for the Δt^{opt} interval shown on the left.

These intervals additionally serve as indicators of proper peak classification. All lines categorized as μX exhibit short optimal intervals, as expected from

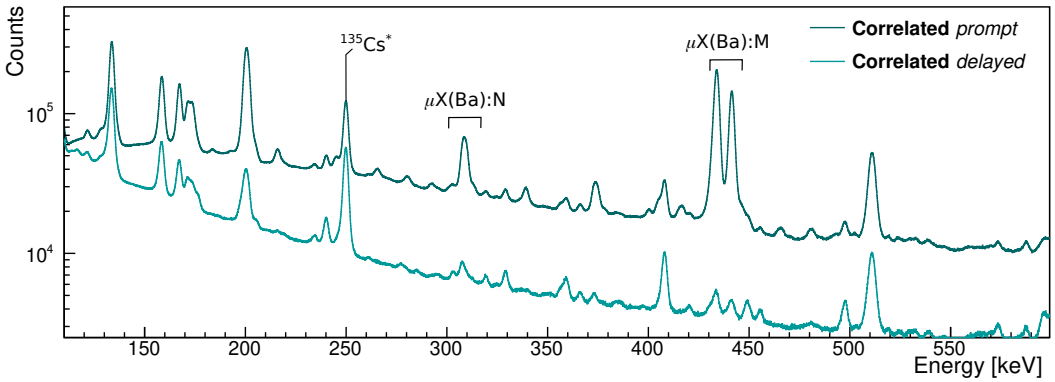

Figure 12.10: Correlated *prompt* and *delayed* spectra for the energy region between 100 keV and 600 keV.

their prompt emission. Their intervals extend from approximately -90 ns to 50 ns for the specific detector, reflecting the inherent C# and Ge hit time measurement uncertainty of approximately ± 100 ns. This uncertainty is more pronounced for low-energy γ rays, often absorbed in the detector surface where the electric field may be weaker [56]. This reduced time resolution, along with the high Compton background at low energies, may explain the shorter optimal interval for the 121 keV line, while all other lines identified as de-excitation γ rays have optimal intervals spanning over 350 ns. Further slight variations observed around 700 keV can be attributed to the emergence of significant background at later times in this region.

Following the determination of these intervals, the LOIs were fit in more detail within the optimized time interval Δt^{opt}. This peak fitting was performed around the mean μ of each LOI, using a region to model the signal spanning approximately $\pm 3\sigma$, where σ was determined from the previous Gaussian fit. Additional sidebands covering $\pm 3\sigma$ around the Gaussian peak were used to constrain the background. Given the densely populated spectrum, shown in Figure 12.10, the background within these sidebands was often not flat. In certain cases, an additional Gaussian was introduced to account for a secondary peak within the region.

The fitting procedure was based on a chi-squared minimization method. The signal was modeled using a combination of Gaussian and tail functions and the background with linear and step functions. These functions are described in detail in [163] and are listed below:

$$
\begin{aligned}
f_{\text{Gauss}}(E) &= \frac{n}{\sqrt{2\pi}\sigma} \exp\left[-\frac{(E-\mu)^2}{2\sigma^2}\right], \\
f_{\text{lin}}(E) &= a + b \cdot E, \\
f_{\text{step}}(E) &= \frac{d}{2} \operatorname{erfc}\left(\frac{E-\mu}{\sqrt{2}\sigma}\right),
\end{aligned}
\tag{12.6}
$$

$$f_{\text{tail}}^{left}(E) = \frac{c}{2\beta} \exp\left(\frac{E-\mu}{\beta} + \frac{\sigma^2}{2\beta^2}\right) \operatorname{erfc}\left(\frac{E-\mu}{\sqrt{2}\sigma} + \frac{\sigma}{\sqrt{2}\beta}\right),$$

$$f_{\text{tail}}^{right}(E) = \frac{c'}{2\beta'} \exp\left(\frac{E-\mu}{\beta'} + \frac{\sigma^2}{2\beta'^2}\right) \operatorname{erfc}\left(\frac{E-\mu}{\sqrt{2}\sigma} - \frac{\sigma}{\sqrt{2}\beta'}\right).$$

The left tail of the peak is attributed to imperfect charge collections, whereas the right tail may arise due to pile-up effects. Although μ and σ should ideally be fixed by well-established and calibrated values, these parameters were relatively loosely constrained, given the large uncertainties in the mean energy values for excitation lines from databases. Additionally, the resolution function for the peaks has not been definitively determined, as the calibration work is still in progress. As a result, μ was allowed to vary by ± 0.1 to 0.5 keV, depending on the specific line, and σ was allowed to vary by -15% (+5%) lower (larger) values compared to the estimate obtained by measuring the peak width at half maximum.

Background estimations from adjacent sidebands constrain the linear and step functions, with the latter further aligned to the same μ and σ of the Gaussian function. A selection of fitted excitation lines are presented in Figures 12.11 to 12.13, where each employed function is drawn for illustration.

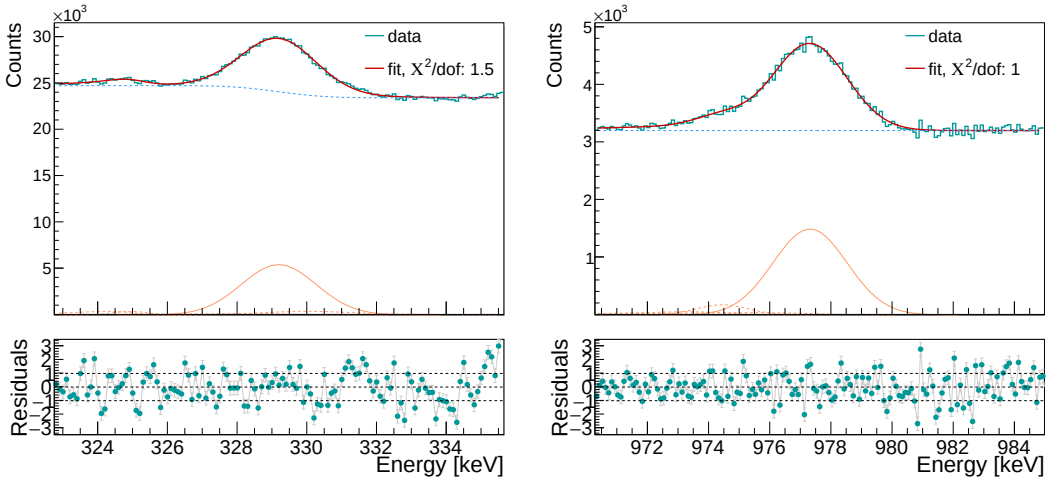

Figure 12.11: Measured spectra and fits of the 330.2 keV and 979.1 keV de-excitation γ rays from ^{136}Cs, histogrammed within the respective Δt^{opt} intervals. The individual functions used for the combined fit are also shown in dashed lines, except for the primary Gauss function, which is drawn in solid lines. Some functions exhibit minor contributions and may not be clearly visible.

Except for the 249.8 keV line, all fits yielded normalized chi-squared values (chi-square divided by the number of degrees of freedom) ranging between 1 and 1.9. However, given the large number of functions and relatively lose constraints, fits of peaks composed by two lines may result in a less accurate estimation of the Gaussian amplitudes. This is particularly pronounced for the overlapped 1013.7 keV and 1015.9 keV lines, as depicted in Figure 12.13.

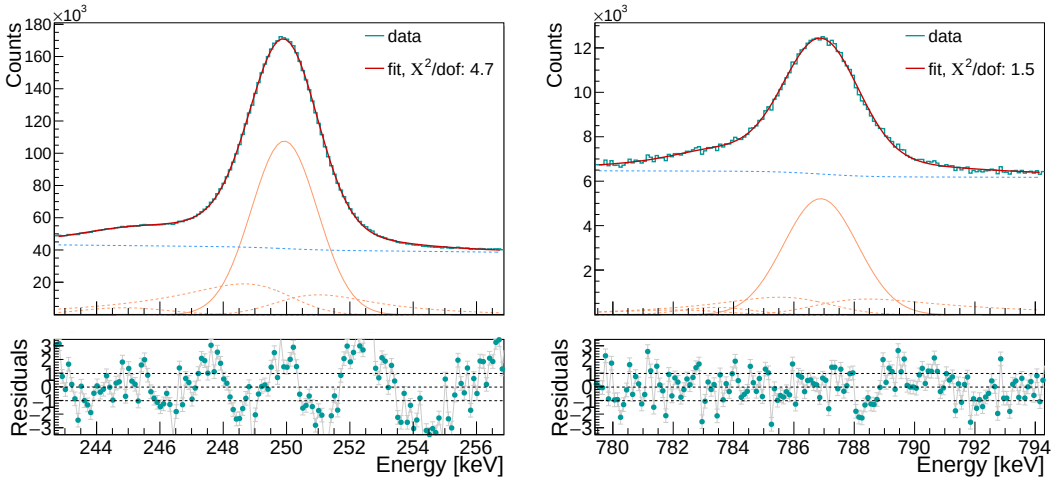

Figure 12.12: Measured spectra and fits of the 249.8 keV and 786.8 keV de-excitation γ rays from ^{135}Cs, histogrammed within the respective Δt^{opt} intervals.

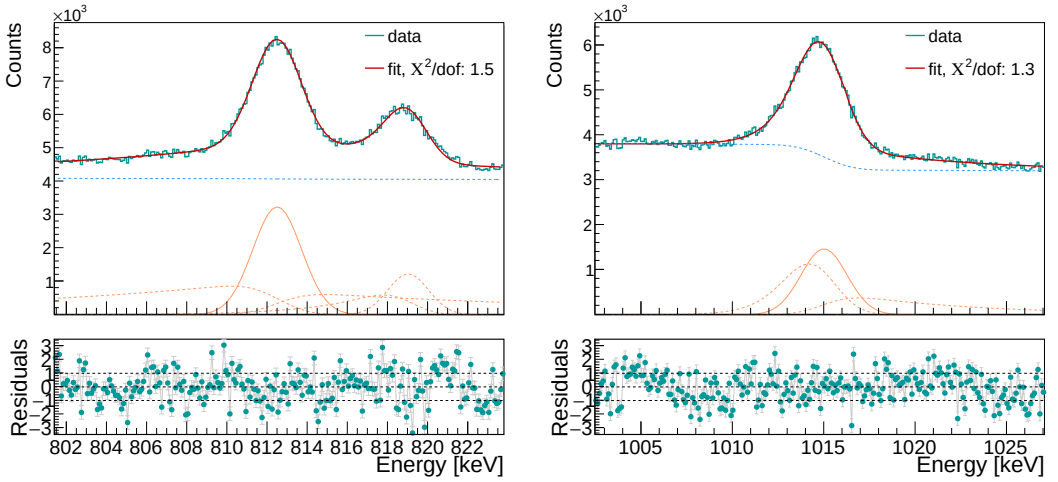

Figure 12.13: Measured spectra and fits of the 812.6 keV de-excitation γ ray from ^{135}Cs (left), fit along with a nearby γ ray from ^{135}Cs decay. The spectra and fits for a double peak composed of 1013.7 keV and 1015.9 keV de-excitation γ rays from ^{136}Cs are shown on the right.

Nonetheless, since the primary objective of this analysis is not to precisely determine the number of counts within a peak, but rather to estimate the line's time evolution, the fits are considered satisfactory. For the purpose of more accurate event count estimation, the incorporation of calibration inputs are necessary to achieve more stringent constraints.

LOI time evolution & muonic lifetime

After fitting the peaks within the optimized time interval Δt^{opt}, the fit parameters μ, σ, and the tail amplitudes relative to the Gaussian amplitudes are held constant while fitting the LOIs over time intervals of 40 ns. For each interval, the counts within the peaks are estimated by calculating the area of a symmetric Gaussian distribution with an amplitude derived from the fitting process. The resulting counts are histogrammed, yielding the time evolution of the γ lines shown in Figure 12.14.

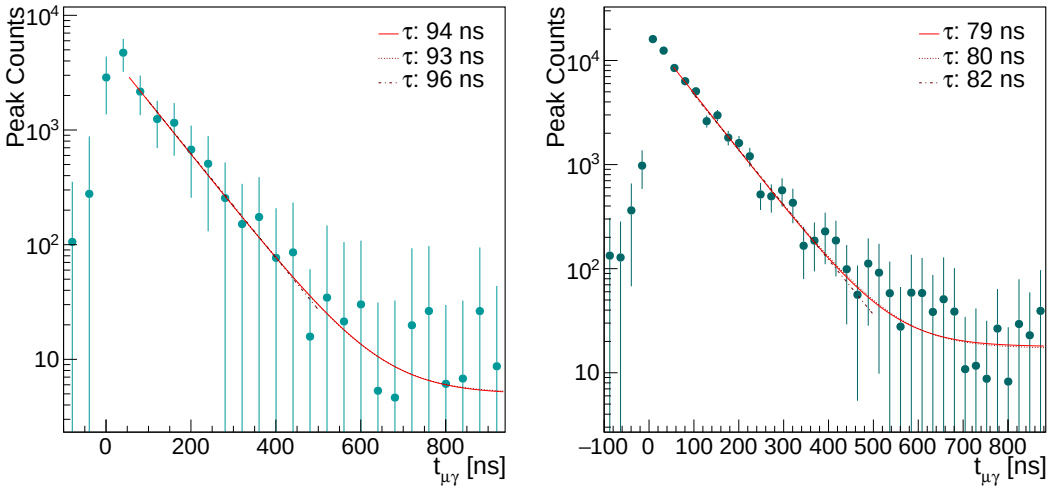

Figure 12.14: Distribution of peak counts from the 330.2 keV and 608.2 keV de-excitation γ rays from ^{136}Cs (left) and ^{135}Cs (right), displayed for 40 ns and 24 ns binnings, respectively. The τ values obtained by fitting the distribution in the ranges [50, 900] ns, [90, 900] ns and [100, 900] ns are respectively shown.

The decay time τ of de-excitation lines is related to the lifetime of the muonic atom [56]. To quantify τ, the time evolution of each LOI was fit with a sum of a constant term and an exponential function, the latter being characterized by the total muon disappearance rate λ_{tot} [56]:

$$f_{exp}(E) = a + \exp\left(\frac{-t_{\mu\gamma}}{\tau}\right), \text{ where } \tau = \frac{1}{\lambda_{tot}}. \tag{12.7}$$

The constant term accounts for a uniform background arising from random hits. The muon disappearance rate is directly related to the OMC rate, since it reflects both the probabilities for muon decay and for muon capture, as detailed in [56]. To assess the uncertainties in the obtained τ values, the fits were performed for three different time ranges, as shown in Figure 12.14.

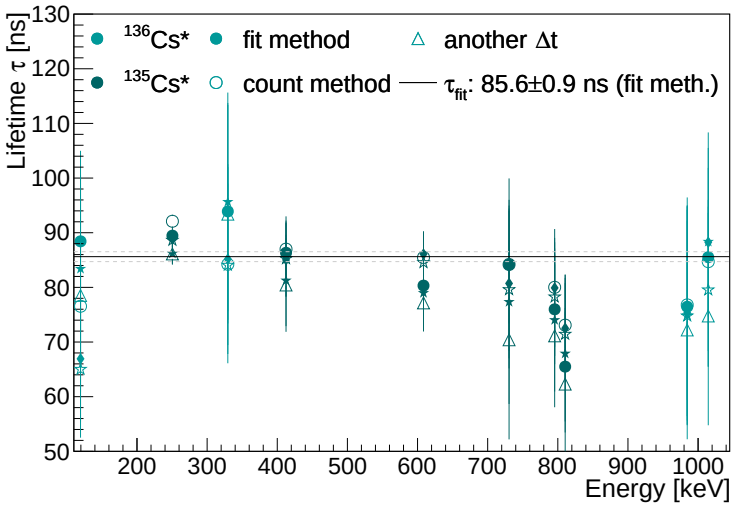

Figure 12.15: Lifetime values obtained from the 40 ns-binned time evolution of several LOIs. The rounded markers represent the values derived for a time range between 50 ns and 900 ns. The solid (dashed) lines indicate the error-weighted mean (and deviation) calculated using the fit results.

Additionally, a shorter time binning of 24 ns was investigated, leading to similar results. The variations in τ primarily originate from the time fitting ranges, as the time evolution is affected by uncertainties arising from the timing of C# and Ge hits. This uncertainty is detector and energy-dependent, thus resulting in variations of τ values derived from different lines and detectors. These results are combined for a given detector and an error-weighted average τ value is calculated for each Ge channel. Figure 12.15 shows the results obtained for the Ge channel 7.

To further validate the lifetime estimates, the time evolution of each LOI was additionally studied using a counting method (following the procedure described in Appendix A). The corresponding τ values obtained from fitting these distributions are also presented in Figure 12.15 and show that both methods agree. Fainter lines, such as the 330 keV line shown in Figure 12.14, yield larger errors for both the fitting and counting methods[12]. As a result, the mean value is predominantly influenced by the most intense lines. Yet, the consistency among all values reaffirms the proper classification of all candidate de-excitation lines shown in Figure 12.15.

Relative intensities of de-excitation γ rays

As aforementioned, comparing the relative intensities and BR of de-excitation γ lines can further validate their proper identification. For this comparison, the measured intensities must be corrected for the energy-dependent efficiency of the HPGe detectors. Using a preliminary efficiency function for HPGe detector 7, this study was performed. For each line, the fitting process was

12 In cases of faint lines within high background regions, like the 706.5 keV γ from ^{136}Cs, the fits failed to converge, and the line is omitted from the figure.

executed within the optimum interval, and the estimated peak counts were then normalized for efficiency, lifetime effects (as partial intervals are utilized for integrating peak counts), and the highest relative intensity. The results are summarized along with each investigated line in the next section, where only the mean values are compared in a qualitative matter, while potential errors, likely dominated by corrections such as efficiency, are not discussed.

12.5 SUMMARY OF IDENTIFIED LINES, CONCLUSIONS & OUTLOOK

In this work, methods for line identification in the densely populated ^{enr}Ba data were developed, leading to the identification of over 100 lines[13]. Among these, over twenty lines are categorized as de-excitation lines from ^{136}Cs and ^{135}Cs. Lines with minimal overlap with other μX and γ lines were selected for more detailed studies. The results of these analyses confirmed their correct classification through the identification of characteristic optimal intervals and the determination of decay times.

A summary of the in-depth studied de-excitation γ rays from ^{136}Cs is presented in Table 12.1, including their relative peak intensities. While a BR relationship exists for the 330.2 keV, and 1013.7 keV γ rays, their BRs have large uncertainty, ranging from 60 to 100%. Despite potential uncertainties in the intensity measurement of the latter line due to its peak-overlap structure (Figure 12.13), the relative intensities seem to be consistent.

Table 12.1: Energy levels, decay times and relative intensities of selected ^{136}Cs de-excitation γ rays. The listed decay times correspond to values obtained from the fit method within 50 to 900 ns, shown in Figure 12.15. The γ intensities are shown relative to the most intense line.

E(level)(keV)	J^{π}(level)	γ Energy (keV)	decay time τ (ns)	γ intensity
3684	14+	121.4	96	1.00
3257.8	13-	330.2, 1013.7	94, 86	0.70, 0.45
4086.7	15-	706.5	-	0.26
4359.2	16-	979.1	76	0.47
4396.1	16-	1015.9	86	0.49

Several other lines that should follow the emission of the identified lines above, such as the 406.4 keV, 729.8 keV, and 309.4 keV de-excitation γ rays from ^{136}Cs [162], seem to be observed in the spectra. However, due to their overlap with other μX and γ lines, they necessitate stricter fit constraints to be investigated accurately.

While the peak identification provided in this study is not yet final, as ongoing work continues in calibrating energy and efficiency parameters, the method presented here can be employed once these calibration parameters are finalized. Improved calibration will facilitate the fitting of overlapped peaks, which is essential for validating overall line identification.

13 The full list was provided to the collaboration and is not shown here.

As a by-product of this analysis, preliminary values for the total muon disappearance rates were obtained. The values obtained from data recorded by three HPGe detectors are shown in Table 12.2.

Table 12.2: Lifetimes τ obtained per detector using ten de-excitation γ rays as presented in Figure 12.15, or excluding low-energy (below 250 keV) γ rays.

Channel	Lifetime τ (ns)	Lifetime τ, exc. low E (ns)
Ge 5	85.9±0.7	82.2 ± 1.8
Ge 7	85.6±0.8	78.8 ±1.9
Ge 8	110.8±0.9	86.3 ±1.9

The values in Table 12.2 were obtained using the time ranges specified in Figure 12.15, where the starting time of 50 ns was based on the boundaries of the optimum interval for μX lines in Ge channel 7. However, other detectors appear to have poorer timing resolution, an effect especially observed in their time distributions of low-energy γ rays. This accounts for the significantly larger τ obtained for Ge channel 8, when low-energy γ rays are not excluded. This result indicates the importance of defining energy-dependent and detector-dependent time ranges based on the study of μX lines measured by these detectors.

While the obtained lifetimes (muon disappearance rates) are directly related to the total OMC rate and the relative γ intensities to relative partial rates, the results presented here are only indicative of these parameters. The lifetime τ reflects a not-yet corrected capture rate, as contributions from the free muon decay or from other Barium isotopes, carbon, and oxygen present in the target were not yet considered. The γ intensities may also have contributions from other higher-lying levels [56]. Additionally, as other analysis parameters such as calibrations are finalized, the peak fits should be conducted again for a more accurate estimation of peak counts and time evolution.

Despite these considerations, the investigations and analyses presented in this chapter are crucial steps toward identifying and characterizing de-excitation lines in the ^{enr}Ba dataset, laying the groundwork for establishing a final set of de-excitation lines and their associated results for the total and partial rates of OMC.

PART V

PASSIVE NEUTRINO AND DARK MATTER DETECTION WITH PALEOCCENE

13

PARTICLE DETECTORS READ OUT BY LIGHT-SHEET FLUORESCENCE MICROSCOPY

In this chapter, we shift focus to another field within neutrino research: the detection of reactor neutrinos through their coherent elastic scattering with nuclei. Here, we introduce PALEOCCENE, a novel concept aimed at detecting low-threshold nuclear recoils induced by neutrinos or dark matter. As this chapter lies beyond the central theme of $0\nu\beta\beta$-decay search explored so far in this thesis, we begin with a brief overview of the primary objectives and concept of PALEOCCENE. This overview is followed by the motivation for low-threshold dark matter and neutrino detectors, alongside an introduction to passive solid-state detectors. Given the broad scope of this project, these introductory sections are by no means exhaustive; their purpose is to provide the necessary context for comprehending the measurements conducted in this thesis as R&D for PALEOCCENE.

13.1 BRIEF OVERVIEW

Despite being five times more abundant than ordinary matter [164], dark matter has not yet been detected. To detect neutrinos, tons of sensitive volume or powerful beam-lines are usually required to obtain a few events per day [165–167]. The pursuit of dark matter detection and the exploration of neutrino interactions have driven numerous experiments to push technological boundaries [68, 71, 73, 168–173]. Most of the currently employed techniques rely on the collection of charge, photons or phonons produced within sensitive targets following particle interactions [68, 71, 73, 165–173]. The PALEOCCENE collaboration pursues a new approach: light-sheet fluorescence microscopy (LSFM) to read out color centers (CC) arising from dark matter or neutrino induced nuclear recoils in transparent crystals [174, 175].

These CCs are crystalline defects that can alter the color of materials through fluorescence, which is the same physical process previously referred to as wavelength shifting (Chapter 5). Despite their nanoscale dimensions, CCs may emit visible-wavelength photons upon excitation [174], facilitating their detection with optical microscopes. Moreover, CC-based detectors hold potential for exploring particle interactions at low-energy nuclear recoil thresholds, given that CCs require 10-50 eV nuclear recoil energy to form [174, 176].

To potentially establish CC fluorescence as a sensitive, low-threshold detection method for dark matter and neutrinos, a fast imaging method of individual CCs is essential and thus the scalable imaging offered by LSFM is particularly relevant [174, 175].

This work presents the first LSFM measurements of radiation-induced CCs within transparent crystals, demonstrating the method's potential to scan crystals that could work as passive particle detectors. Particularly for neutrino detection through coherent elastic neutrino-nucleus scattering (CEvNS), this method offers the advantage of ex-situ readout, enabling passive crystals to be more easily accommodated in the close proximity of a nuclear reactor. These low-threshold passive detectors would thus not only offer potential for the first reactor CEvNS detection but could also serve as nuclear nonproliferation safeguards [174]. The next section offers more background on this application as well as on the motivation of employing these detectors for dark matter detection.

13.2 MOTIVATION & BACKGROUND

Dark matter search at low-energy nuclear recoils

Substantial evidence supports the existence of dark matter [164, 177] – a type of matter that exerts a gravitational pull within our galaxy and universe, but is 'dark' because it does not interact with photons, unlike ordinary matter. A prominent dark matter candidate is the so-called WIMP (weakly interacting massive particle). As our solar system is immersed in dark matter, traveling across it at 220 km/s, we should constantly receive a flux of these particles. While most of WIMP particles are expected to traverse the Earth unnoticed, they may prompt observable signals when interacting with ordinary nuclei, inducing them to recoil. These nuclear recoils are the signal many WIMP-search experiments have been seeking to detect [68, 71, 73, 168–171]. The absence of such signals in experiments ranging from kilogram to ton scales yields constraints on WIMP mass and interaction cross section.

Prominent among these experiments are the noble-liquid-based detectors, such as the Xenon experiment [178], which have been setting limits on increasingly lower spin-independent interaction cross sections [171–173]. To cover the WIMP parameter space at low masses, low-energy threshold solid-state detectors operating at milikelvin temperatures are often employed. These detectors, such as CRESST and CDMS, collect phonons as the signal from a potential WIMP interaction [168, 169]. However, there has been a common background to this detection channel: phonon-based experiments have been detecting an unknown signal, leaving much of the low-energy WIMP search parameter space uncovered [168, 169, 179]. Given the low-energy threshold (tens of eV) expected for CC creation [174, 176], CC-based detectors could potentially fill this gap [174–176, 180], particularly by searching for sub-GeV WIMPs through spin-dependent interactions [174].

Nuclear reactor neutrinos & nonproliferation safeguards

Nuclear reactors emit intense fluxes of neutrinos, which originate from beta decays of fission fragments (A, B, ...) produced within the reactor core:

$$^{235}_{92}\mathrm{U} + \mathrm{n} \rightarrow \text{Fission Products A, B} + 3\mathrm{n} + \text{Energy},$$

$$\mathrm{A} \rightarrow \mathrm{A}' + e^- + \bar{\nu} \rightarrow \ldots$$

$$\mathrm{B} \rightarrow \mathrm{B}' + e^- + \bar{\nu} \rightarrow \ldots$$

Using a reactor source of neutrinos, the first detection of neutrinos was achieved by Reines and Cowan in 1956 [10], decades after the prediction of the existence of neutrinos by Pauli. This detection was achieved via measuring inverse beta decay (IBD) reactions:

$$\bar{\nu} + \mathrm{p} \rightarrow \mathrm{n} + e^+.$$

In this process, a neutrino interacts with a proton from a hydrogen-rich medium like water or an organic scintillator, producing a positron and a neutron, which result in $\mathcal{O}$(MeV) signals from positron annihilation and γ rays following neutron capture. This reaction requires neutrino energies above 1.8 MeV, a threshold established by the mass difference between initial and final states [181]:

$$\Delta\mathrm{m} = \mathrm{m_n} - \mathrm{m_p} + 2\mathrm{m_e}$$

Despite the moderate kinetic energy threshold and the small cross section of $\mathcal{O}(10^{-43}\,\mathrm{cm}^2)$ [182] for this interaction, IBD detectors have succeeded in observing neutrinos across diverse physics programs, spanning from the earliest neutrino discovery to neutrino flavor oscillation measurements, and more recently, reactor monitoring [10, 182, 183]. However, the inherent large-scale of IBD detectors limits their application for reactor monitoring aimed at nuclear nonproliferation efforts [182]. As a result, alternative detection methods, such as coherent elastic neutrino-nucleus scattering (CEvNS), have been proposed to address this challenge.

CEvNS is a neutral-current interaction between a neutrino and nucleus, where the neutrino interacts with the nucleus as a whole, transferring a small amount of momentum to it, causing a recoil:

$$\bar{\nu} + \mathrm{X} \rightarrow \bar{\nu} + \mathrm{X}.$$

The differential cross section for CEvNS is given by the equation:

$$\frac{d\sigma}{dT} = \frac{G_F^2}{2\pi} m_N \left(1 - \frac{m_N E_r}{2E_\nu^2}\right) Q^2 F^2(Q^2),$$

where G_F is the Fermi constant, m_N is the target nucleus mass, E_r is the nuclear recoil energy (=q^2/m_N), E_ν is the neutrino energy, Q is the weak charge, and $F(Q^2)$ is the nuclear form factor (=1 for $q^2 \rightarrow 0$) [183].

Unlike IBD, CEvNS imposes no kinetic threshold, being thus sensitive to low-energy neutrinos. Moreover, the cross sections for CEvNS can surpass those for IBD by up to two orders of magnitude [181], particularly for heavier target nuclei due to the quadratic cross section dependence on the neutron number of the target nucleus [183]. Consequently, CEvNS stands as a promising detection mechanism for reactor monitoring through compact detectors situated in proximity to reactors [174].

Yet, a challenge persists: CEvNS from reactor neutrinos remain unobserved to date. In fact, the first CEvNS observation was just recently accomplished by the COHERENT experiment, employing a modest-sized detector consisting of 14.6 kg of CsI[Na] scintillating crystals [76]. However, this detection was achieved by using a high-flux accelerator source of neutrinos with energies around 50 MeV [76]. Although the neutrino flux provided by the spallation neutron source (SNS) did not outmatch the flux of a Gigawatt (GW) nuclear reactor, it offered higher-energy neutrinos, as presented in Table 13.1. This enabled CEvNS observation at a threshold of 5 keV, while thresholds below 1 keV are necessary for the detection of reactor neutrinos CEvNS [181].

Table 13.1: Fluxes and maximum energies of common neutrino sources.

Source	Flux ($\nu_s/\mathrm{cm}^{-2}\,\mathrm{s}^{-1}$, at a given distance)	Maximum Energy
Sun	$\mathcal{O}(10^{11})$ (at Earth) [7]	$\lesssim$10 MeV
SNS	$\mathcal{O}(10^{7})$ (at 20 m from the source) [184]	$\lesssim$50 MeV
GW Reactor	$\mathcal{O}(10^{12})$ (at 20 m from the source) [182]	$\lesssim$8 MeV

Numerous dedicated experiments have been tackling the challenge of achieving low-energy detection thresholds and aiming at observing reactor neutrino CEvNS for the first time [185–187]. These efforts are motivated by the broad extent of physics that can be investigated through CEvNS interactions, which include investigations of nonstandard neutrino interactions, neutrino electromagnetic properties, neutron distributions within nuclei, and neutrino supernova detection [181, 182, 188].

Covering all these aspects exceeds the scope of this chapter, we will thus specifically focus on the application of CEvNS detectors as nuclear reactor monitors aimed at nuclear nonproliferation verification. This application can be facilitated by employing compact, low-threshold passive CEvNS detectors, such as those proposed by Paleoccene. In contrast to the resource-intensive large-scale IBD-based detectors, the scalability of such detector technology introduces the prospect of efficiently monitoring approximately 450 operational commercial nuclear reactors and several hundred research reactors, most of which falling under the inspection of the International Atomic Energy Agency (IAEA). The monitoring of these reactors is in line with the verification requirements for the Treaty on Nonproliferation of Nuclear Weapons [174, 182].

Before detailing further about the operation of these detectors as nuclear safeguards, we briefly overview the imprints of particle interactions in dielectric crystals and minerals – a foundational introduction for better comprehending the Paleoccene concept.

When particles interact with atoms in an insulating solid, such as a mineral or a transparent crystal, they can leave behind a trail of damage known as tracks. These tracks are metastable linear regions within the crystalline structure of the material, characterized by various forms of crystalline damage, including mechanical stress, local amorphization, or the presence of vacancies. These regions of 'localized melting of the crystalline structure', exhibit contrasting properties that resemble the passage of the particle.

Imaging these tracks has long been part of the palette of radiation detection methods [189]. For instance, imaging uranium fission tracks, as shown in Figure 13.1, has been an established technique for rock dating since the 1960s [190]. This method was also applied to estimate the interaction of dark matter particles in ancient muscovite mica samples [191]. However, conventional fission tracking techniques require etching the sample before optical microscope imaging, which is labor-intensive, destructive, and has a relatively high threshold for detection[1]. Consequently, this etching method is not well-suited for the purpose of detecting dark matter or neutrinos. An alternative approach is directly imaging tracks using high-resolution microscopy techniques [192], but these methods are not scalable.

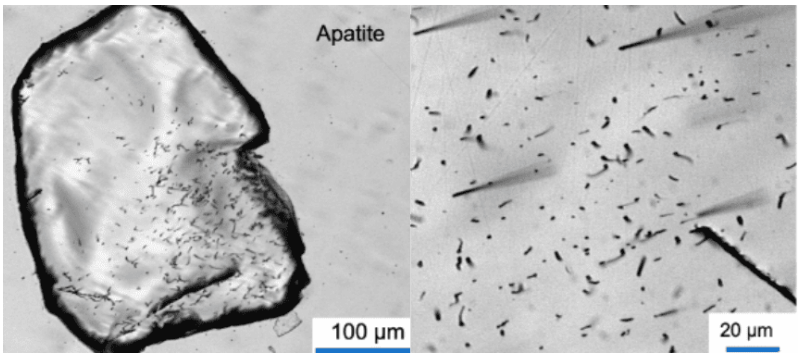

Figure 13.1: Etched fission tracks and dislocations in Apatite imaged with an optical microscope. Figure from [193].

Moving from the elongated, etchable damage tracks to smaller scales, various types of crystalline point defects can produce observable effects in crystals. Among these are CCs, which are classified into: electron excess (F-centers), hole excess, or complex centers [194]. CCs involve point defects such as vacancies, substitutional and interstitial defects (often including impurities), or a combination thereof. They can be *native* defects to the crystal or induced by irradiation [194]. Particles such as neutrons, ions, or γ rays may create these defects in crystals by either displacing atoms, generating new vacancy defects, and/or through ionization[2]. Well-know examples of CCs are the

1 The threshold depends on the specific energy loss per track length required for an etchable track to form [189].

2 The ionization process is more complex, as it can lead to the formation of CC defects by directly ionizing impurities (or defects complexes), or by transferring energy to electrons

nitrogen-vacancy (N-V) centers in diamond, which are currently intensively studied for applications in quantum sensing and quantum bits. These centers, composed of a complex of substitutional nitrogen impurities and a carbon vacancy, emit colors that dependent on the configuration and number of substitutional nitrogen atoms involved in the complex [196].

In this chapter, and within the PALEOCCENE context, we primarily focus on the F-type[3] of CCs, which consists of anionic vacancies occupied by unpaired electrons, as shown in Figure 13.2. Such a quantum system exhibits fluorescence, emiting visible light when excited by UV or visible light.

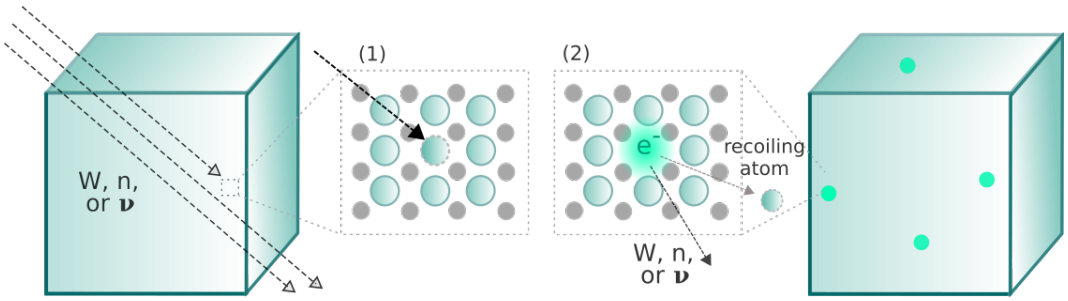

Figure 13.2: Interaction of particles such as neutrons, neutrinos (ν), or WIMPs with a nucleus in a target (1), can induce nuclear recoils. If the displaced atom is an anion, its vacancy can be filled by an electron, forming an F-center (2).

CCs, as other types of defects, have been employed to characterize materials [194, 197]. With the increasing pursuit for reaching low-energy thresholds, CCs have been recently proposed as potential signals for WIMP search detectors [176]. Certain materials have been identified to exclusively produce CCs in response to nuclear recoils or exhibit distinct colors for electron and nuclear recoils [198]. However, these features have been primarily investigated through far-field spectroscopy.

Building on these developments and on recent advancements in microscopy techniques, the PALEOCCENE concept was introduced in 2021 in a publication presenting sensitivity estimates for dark matter and CEvNS detection using CCs, along with the proposal of new CC readout and applications [174].

in the medium which may trigger further ionization or atom displacement. For the latter, it is worth noting that the energy required for these displacements is small (a few tens of electronvolts). Consequently, even though electrons are not highly effective in displacing atoms, electrons with energies in the range of a few hundred keV can still result in the generation of single-site vacancies within the crystal lattice [195].

3 We note that while some literature refers to F-centers as being any type of CCs (Farbzentren), here we refer to it only as defined.

PALEOCCENE (Passive low-energy optical color center nuclear recoil) is a multidisciplinary collaborative effort aimed at developing passive detectors of dark matter and neutrinos [174, 175]. To advance this goal, PALEOCCENE teams work on theoretical estimations, simulations, sample irradiation, fluorescence measurements using far-field spectroscopy, and LSFM measurements. This chapter focuses on the latter, which lies at the core of the PALEOCCENE concept – namely, the use of LSFM to read out CC signals induced by dark matter and CEvNS interactions in transparent crystals [175].

The concept in a nutshell

Here, we illustrate the concept for the reactor neutrino CEvNS application, where passive crystals of around 100 g would be placed near a nuclear reactor. The exposure to the large flux of neutrinos may induce nuclear recoils and consequently CCs in the crystal, as illustrated in Figure 13.2. If the nuclear recoil displaces an atom by approximately 1 nm (equivalent to an E_r of a few tens of electronvolts), the corresponding vacancy and associated CC can be long-lived at room temperature [174, 193].

After an exposure of approximately 90 days, the crystal undergoes an LSFM scan, where a thin light sheet illuminates sections of the crystals. The fluorescence emitted by the CCs upon excitation is recorded with precise ($\mathcal{O}$(µm)) x-y-z position and light intensity information, as depicted in Figure 13.3.

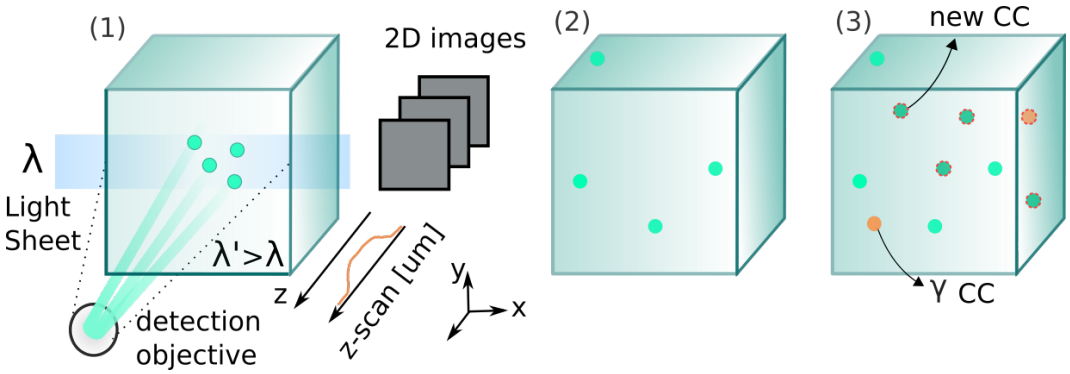

Figure 13.3: In LSFM, a thin light sheet illuminates a z-section of the sample x-y plane which is observed by a camera orthogonal to the light-sheet source (1). By incrementally shifting the sample along the z-axis, 3D images are generated. The scans acquired prior (2) and after the exposure (3) to the reactor can be compared. Feasible target materials should yield none or distinct response to γ rays (3).

By comparing the number and positions of CCs between pre- and post-exposure scans, it is possible to estimate the total neutrino fluence and, consequently, the reactor power. This data can be cross-checked against declared values, allowing for validation of reactor shutdown periods. Monitoring the reactor power is important within the context of nuclear nonproliferation

verification [174], providing means to prevent the diversion of plutonium, which is a fissile material well-suited for fabrication of nuclear weapons [182].

With the precise knowledge of CC positions within the crystal, Paleoccene offers a nuclear nonproliferation safeguard concept with a certain level of tamper-proof security. This is due to the fact that replacing a monitoring crystal with a new one would result in a distinct pattern of CCs that would differ from those recorded in the pre-exposure scan [174].

To mitigate the impact of cosmogenic background radiation, a moderate overburden of approximately 1.5 m depth is sufficient [174]. Given the compact size of the proposed detectors, creating small boreholes (⌀10 cm) at the required depth for overburden could be accomplished with relative ease. Being passive, these detectors offer unsupervised operation without the need for cryogenic and high voltage installations, unlike traditional reactor neutrino detectors [185–187]. They can operate at room-temperature and in close proximity to nuclear reactors, where active instrumentation and associated cryogenics are often not feasible.

For dark matter detection, the detectors should be placed in underground laboratories and the readout performed in-situ. Further details about this application, including sensitivity estimates and background sources for both reactor neutrinos and dark matter detection, can be found in [174].

Probing color centers with fluorescence microscopy

While passive detectors read out by microscopy have been utilized in the past, recent technological advancements on microscopy make this proposal attractive again. Particularly interesting is the use of fluorescence microscopy to image CCs, allowing to probe nanometer-sized atom dislocations resulting from low-energy recoils. As this techniques operates within optical wavelengths, it yields faster imaging compared to nanometer-scale microscopy methods such as transmission electron microscopy (TEM) and atomic force microscopy (AFM).

In fluorescence microscopy, a sample is excited with a specific wavelength of light, and the emitted fluorescent light is collected using a combination of filters, objective lenses and a camera. By filtering out the excitation wavelength, the signal emitted by fluorescent CCs can be effectively isolated in the images. The brightness of each imaged pixel can potentially provide information about the density of CCs within that pixel, possibly allowing for the differentiation between single-site vacancies and full tracks.

Fluorescence microscopy techniques vary in resolution and throughput. In ascending order of scan speed, traditional methods include confocal fluorescence microscopy, widefield fluorescence microscopy, and LSFM, also known as selective plane illumination microscopy (SPIM).

Although single CCs have been imaged using widefield and confocal fluorescence microscopes [199, 200], imaging CCs with LSFM offers further ad-

vantages: sharper imaging compared to widefield, reduced sample exposure (leading to minized bleaching of signals), and higher throughput [6].

The highest scan speeds have been demonstrated by LSFM setups, but until recently, there was no commercial setup providing fast 3D fluorescence microscopy of large (cm-sized) samples. This gave rise to the development of the mesoscale SPIM microscope (mesoSPIM), led by scientists at the UZH [6, 201, 202]. This novel setup has been employed in the measurements conducted in this thesis and is described within the next sections.

13.4 Measuring radiation-induced color centers in calcium fluoride

To study CCs with LSFM, CaF_2 crystals were acquired and irradiated with neutrons or γ rays. While many dielectric crystalline materials can present CCs [174, 176, 198], CaF_2 was initially selected due to its suitable excitation wavelengths [176]. Moreover, CaF_2 crystals can be easily obtained in several shapes and from diverse vendors. The specific samples and their respective irradiation are described below.

13.4.1 *Samples & irradiation*

The CaF_2 samples used in these experiments were mostly cubes of $1\,cm^3$ size, with all sides polished. The cubic shape and polish of the crystals were chosen in order to minimize multiple scattering of light in the sample. The samples stemmed from different vendors, and were either irradiated or left unirradiated (blank reference), as described below.

- **Cubic γ-irradiated crystals:** Samples acquired from *Crystran* [203] were irradiated in a ^{60}Co irradiator at Penn State University. The crystals, shown in Figure 13.4, received doses of 100 kRad and 5 MRad each (corresponding to fluences of up to $50 \cdot 10^{13} ph/cm^2$), being subsequently named after their received doses. Due to the isotropic nature of the radiation source and the low attenuation of 1.17 MeV and 1.33 MeV γ rays by 1 cm of CaF_2 [204], the deposition of energy by the γ rays in the crystal is expected to be uniform. Two other crystals from the same batch were left blank.

- **Cubic neutron-irradiated crystal:** sample acquired from *United Crystals* [205] and irradiated by Paleoccene collaborators at Virginia Tech at a neutron flux of 10^8 n/cm^2 provided by a lead-shielded Americium-Beryllium source. The irradiated sample is referred to as VT303, and a blank sample from the same batch is designated as VT306.

- **Disk-shaped neutron-irradiated crystal** 2 mm-thick disk with a diameter of 1 cm irradiated by Virginia Tech collaborators at a neutron flux of 10^{10} n/cm^2. This sample is named VT02.

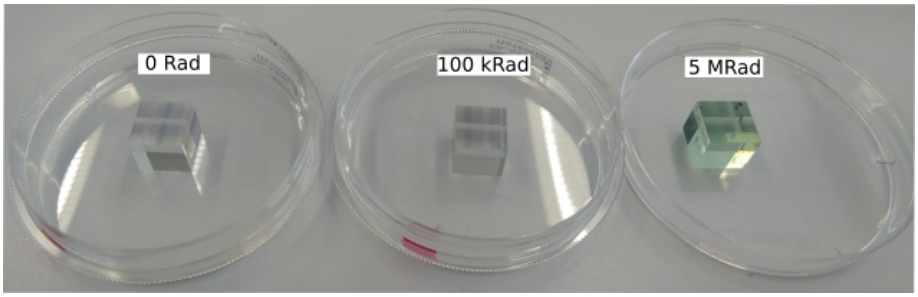

Figure 13.4: γ-ray irradiated CaF_2 crystals. The crystal with the highest radiation dose changed color to green.

13.4.2 *Fluorescence microscopy measurements*

The measurements were conducted using three types of fluorescence microscopes, each chosen for the specific features they offered, such as improved resolution, larger scan speed, and more precise color information.

The standard and benchtop mesoSPIM microscopes: These LSFM microscopes offer near-isotropic resolution imaging of cm-sized samples within minutes, eliminating the need to slice the sample as often required for large sample imaging. This capability is attributed to the long working distances of the objectives and the light-sheet optical sectioning, which allows for imaging CCs in 3D deep within crystals. The mesoSPIM resolution and scan speed can be adjusted using a set of automated lenses (with magnifications ranging from $0.8\times$ to $20\times$) and the light-sheet axial (z) step.

The standard mesoSPIM achieves a scan rate of approximately $1\,cm^3$ per 5 minutes at a 6 µm isotropic resolution [201]. Its upgraded version (benchtop) now attains 1.5 µm resolution in the x-y plane[4], with a scan speed up to $\sim 10\,cm^3$ per hour. Data file sizes range from $\sim$10 to 250 Gb $/cm^3$, depending on the scan mode. Both setups are shown in Figure 13.5.

In both mesoSPIMs, lasers provide the excitation light and sCMOS cameras (Hamamatsu Orca Flash) are employed. The light sheet is created by an electrotunable lens (ETL), and is swept axially, yielding uniform z-resolution across the field of view. Part of the upgrades for the benchtop mesoSPIM was dedicated to improving CC imaging. As presented in Table 13.2, the benchtop mesoSPIM features a significantly increased field of view, improved resolution, and higher throughput compared to the standard version. All these enhancements were achieved at decreased cost and footprint [6].

Widefield Leica Thunder 3D: This inverted fluorescence microscope provides a wide range of magnifications and features both a color camera and a monochromatic one. In addition to the fluorescence emission filter, this setup employs an excitation filter to ensure monochromatic excitation light[5].

4 And 3.3 µm axial resolution, defined by the thickness of the light sheet. For isotropic resolution, the sample can be rotated.

5 This filter is crucial in this context, as the LED light is delivered through the same objective used to collect the fluorescence light. LEDs are also generally less monochromatic than lasers.

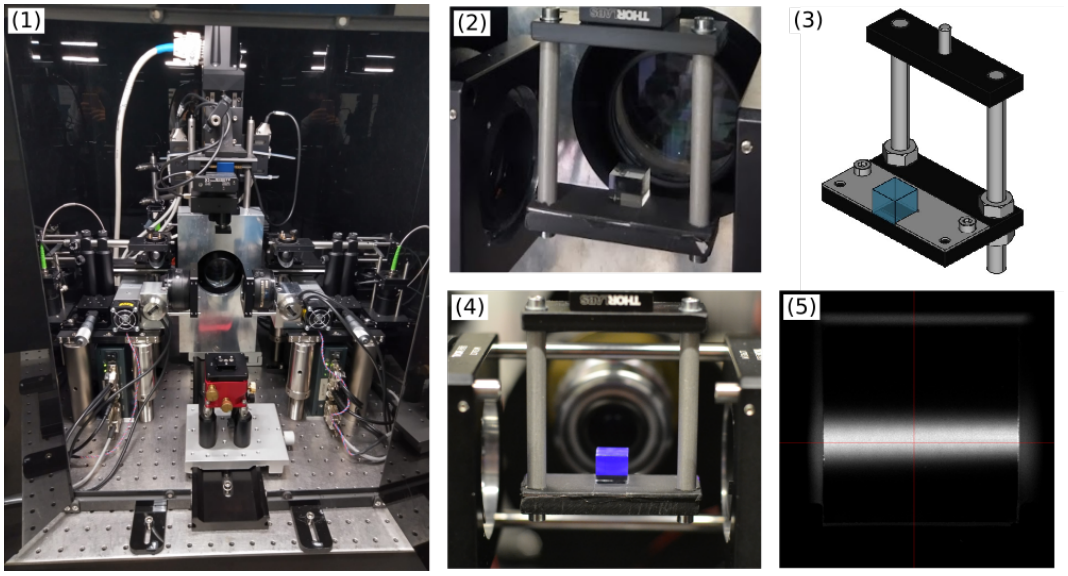

Figure 13.5: Images of: the standard mesoSPIM (1); a CaF_2 crystal prior to imaging (2) installed in a custom-made sample holder (3); the benchtop mesoSPIM (4) [6], where the illuminated transparent crystal appears bright blue, and a microscope image of a partially illuminated crystal (5).

Due to the restricted working distance of the Leica microscope and increased shadowing caused by background fluorescence from other illuminated planes, this microscope was primarily used to gather information about the color emitted by the CCs, utilizing its color camera.

Table 13.2 provides the specifications of the three employed microscopes, listing only the excitation wavelengths (λ_{exc}) and filters used in this work (though the setups offered more options). The quadband (quad) filter blocked light of the four respective wavelengths, while LP denotes a long-pass filter that blocks light above a specific wavelength.

Table 13.2: Microscopes specifications and employed settings. The working distance (WD) and travel ranges (TR) along the z-axis are shown for the Leica and mesoSPIM setups, respectively. For the Leica setup, pixel sizes (PS) are indicated only for the color camera. The field of view (FOV) refers to the number of camera pixels. All images were produced with a 16 bit depth, resulting in the listed image sizes.

Microscope	WD/TR	Cam. PS	FOV (pixels)	Im. Size
Leica Thunder 3D	0.17-10 mm	5.6 µm	2048x2048	8.4 MB
mesoSPIM (standard)	100 mm	6.5 µm	2048x2048	8.4 MB
mesoSPIM (benchtop)	100 mm	4.25 µm	5056x2960	30 MB

Magn.	λ_{exc} (nm)	Exc. / emission filters
5×-40×	390	375-405 / 415LP
0.6×-6×	405, 488, 561, 640	- / quad, 515LP, 594LP
0.8×-20×	405	- / quad

Methods

The CaF_2 crystals were placed in a custom-made sample holder designed for imaging crystals with the mesoSPIM (Figure 13.5). A mesoSPIM python-based software was utilized to select the microscope settings. These included selecting excitation wavelength, emission filter, laser intensity, galvo amplitude (which is associated with the coverage area of the light sheet), focusing, and translating (in x, y, z) or rotating the sample.

Given that refractive-index matching immersion was not utilized, the focus must be adjusted not only for one surface, but fully across the crystal. To accomplish this, features like scratches or dust particles on the frontal and back surface of the crystals were utilized[6]. To ensure proper crystal alignment and ETL parameter settings, the following procedure was followed: The laser motion was stopped, creating a laser 'line' within the crystal. While observing the sample through the microscope, adjustments were made to the ETL parameters and sample position until a very thin and focused line was achieved. This indicated the correct ETL parameter setting and minimized laser scattering within the sample.

To accurately assess the signal, samples were scanned both before and after irradiation or compared to a blank reference. Various magnification objectives and laser wavelengths were employed, and the corresponding emission filters listed in Table 13.2 were utilized to prevent excitation light from reaching the detectors.

To mitigate background fluorescence from surrounding materials, the sample holder was covered with the Metal Velvet™ absorbing foil from Acktar [140]. This was necessary as low levels of fluorescence may lead to bright features imaged with the mesoSPIM, given its sensitive camera and high-power lasers (100 mW). While the microscope itself is housed in an enclosure, ambient light was further minimized by turning off room lights before initiating scans.

Further background components were assessed through data analysis. For this purpose, the data taking involved acquiring background data through: i) Initiating scans with the light-sheet positioned outside the crystal to assess surface background; ii) Conducting scans with the laser switched off to evaluate camera noise; iii) Performing scans with partial illumination (using varied galvo amplitudes) to characterize stray light background.

As part of the acquired data included these background regions, a fiducialization of the 3D imaged volume was performed, where the region of interest (ROI) was defined by excluding scans close to the surface and non-illuminated parts, as illustrated in Figure 13.6.

To further validate measured signals as originating from CCs, multiple scans of the same sample were acquired, and correlation between regions in repeated scans (scan matching) was studied [206]. A summary of investi-

6 As the bulk of the crystals is highly transparent, focusing must be performed on the surfaces. Therefore, the crystals were not cleaned, as their surface dust was utilized as focusing markers.

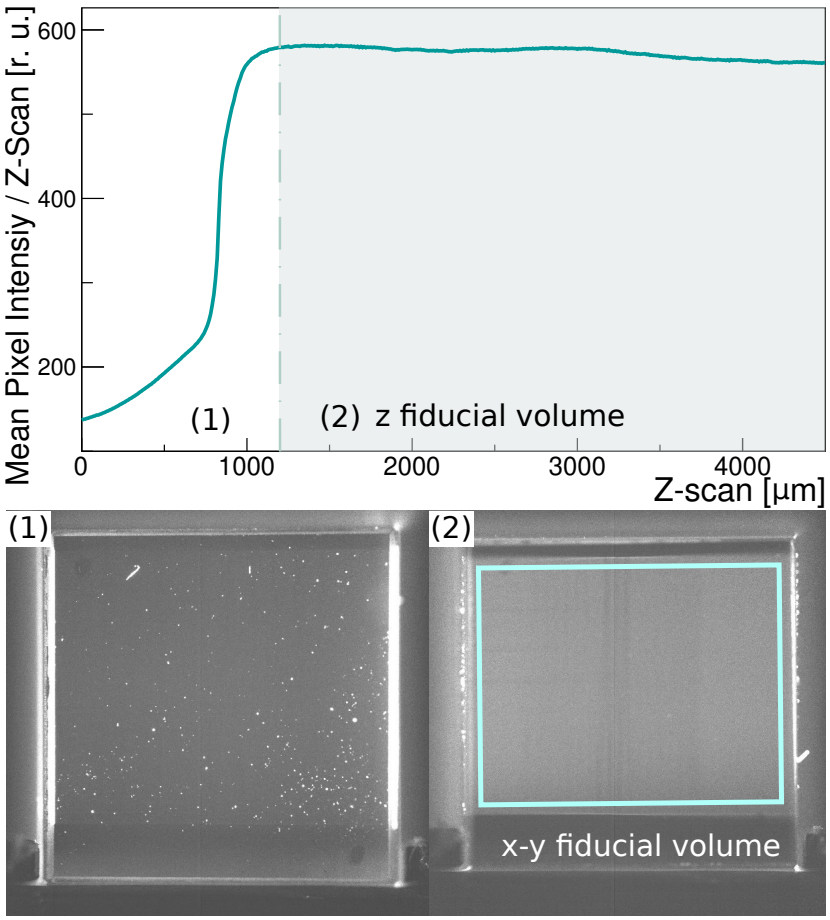

Figure 13.6: Top: Mean pixel intensity per z-scan within the x-y fiducial volume. The intensity is low at first, as the light-sheet does not touch the crystal yet, but it increases when z is at the surface, primarily due to bulk and/or dust fluorescence. Finally, the intensity stabilizes within the bulk (only z scans up to the middle of the crystal are shown). The z-fiducialization is defined within the stable region (2). Examples of surface scans (1) and fiducial scans (2) are shown. The x-y fiducial area is also indicated in the latter and the bright spots on the former are attributed to dust or scratches.

gated background sources and their corresponding background suppression methods are described below.

- Surface background: This background could arise from fluorescent contaminants (eg., as dust and oil) [120], or from centers that intensely scatter light (such as dust or scratches). Fiducialization effectively avoids this background by excluding surface scans/regions from the analysis.
- Stray light: Ambient light or fluorescence originating from regions other than the illuminated path within the crystal (such as from surrounding materials). It was mitigated by covering surrounding materials with absorbing foil, maintaining a dark environment, and can be further suppressed by the scan-matching technique.
- Filter Leakage: It is not known whether the filter presents any leakage. However, by comparing the signal from irradiated vs blank, we can rule out a net signal as originating solely from filter leakage. On a pixel-by-pixel basis, this can be further mitigated by the scan matching.
- Lens fluorescence: Glasses may exibit a low level of fluorescence [120]. Although this signal would appear in matched scans, its appearence across multiple z-planes would clearly distinct it from a single-site CC.
- Camera hot pixels: Defective camera pixels that more often yield a signal, which can be discriminated as in the case of lens fluorescence.
- Camera shot noise: Thermal noise, stemming from random thermal excitations, was estimated by taking data with the laser switched off.

The scan matching method and automated fiducialization are part of V. Aerne's MSc thesis [206] and not discussed here. The other aforementioned background suppression methods were investigated, utilizing primarily the comparison between images before and after irradiation (or irradiated vs blank), within the fiducialized volume.

Standard mesoSPIM results

The results from the 100 kRad crystal imaged at 1× magnification in response to several excitation wavelengths are presented in Figure 13.7. These results show a clear, well above the background, fluorescence signal observed from the illuminated region (a) of scans within the 100 kRad crystal. This signal is particularly intense in response to 405 nm excitation light measured with a quad filter, and it is suppressed when the 515LP filter is employed, indicating that the majority of the fluorescence emission lies below this wavelength.

The signal is more intense within the bulk fiducialized region of the crystal, showing that the primary source of signal is not from surface background, stray light, or lens fluorescence. A comparison of the signal from region (2) to the background measurement with the laser off indicates some level of stray light, albeit not significant in comparison to the signal within the ROI.

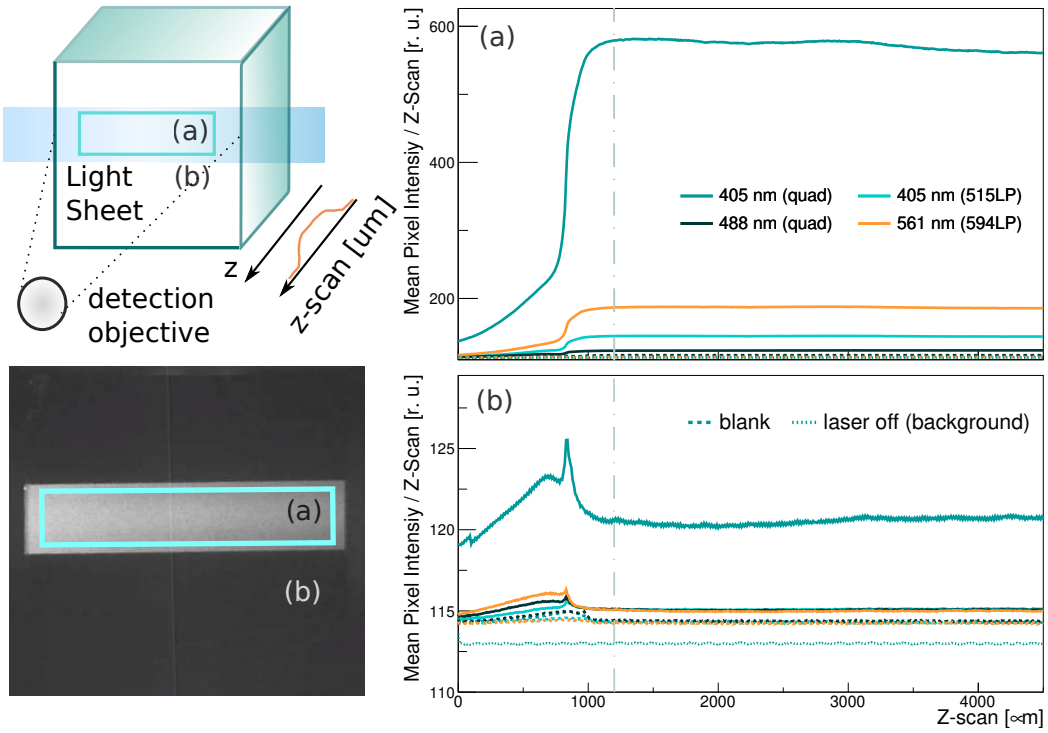

Figure 13.7: Mean pixel intensity per Z-scan measured from the 100 kRad sample (solid lines) within the ROI (a) and non-illuminated background region (b). Each curve corresponds to a 3D scan acquired in response to a specific wavelength and filter setting (displayed in different colors, as indicated in the legends). The measured intensity increases when the light sheet is at the surface and further increases (a) or decreases (b) when it is within the crystal, depending on whether the region is illuminated (a or b) or whether the crystal was irradiated (blank reference measurements are shown by dashed lines). The y-axis present different scales. The vertical line marks the boundary of the fiducialized z-region, utilized for the average values presented in Figure 13.8.

Utilizing the intensities extracted from planes within the fiducialized region, an average intensity was calculated for each measurement presented in (a), facilitating the comparison among the measurements. These results, displayed in Figure 13.8 (left), show that the blank sample yields signals comparable to the laser off background while the irradiated sample yields a signal above the background for all excitation wavelengths. These crystals were also scanned prior to irradiation, and the measured intensity from those scans was comparable to the background, as measured from the blank reference. This observation indicates that the measured signal cannot be attributed to intrinsic sample fluorescence variability within samples from the same batch.

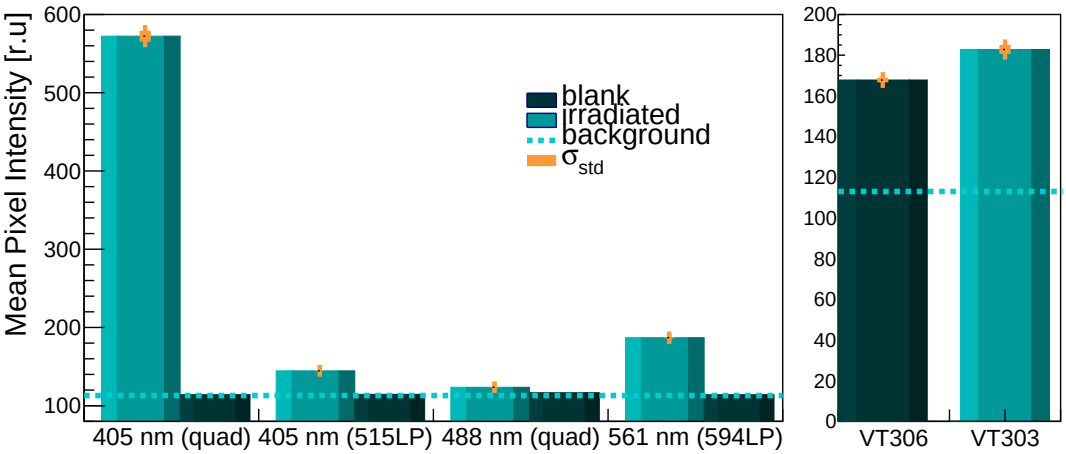

Figure 13.8: Quantification of crystal fluorescence from blank and irradiated (100 kRad) crystals imaged with different excitation wavelengths, and emission filters (left). The same comparison is performed for the blank and irradiated VT306 and VT303 samples (right), albeit only in response to 405 nm excitation. The background line represents the signal measured when the laser is off. The small error bars in orange show the standard deviation of average pixel intensities. The solid bars show the mean value of the distribution.

On the right of Figure 13.8, analogous results are shown for the neutron irradiated samples. However, in this case, both blank and irradiated samples yield signals above the background level. Although the irradiated sample yields a larger signal, no data from this sample was acquired prior to irradiation to evaluate whether this could be attributed to some intrinsic fluorescence variability within the sample batch.

benchtop mesoSPIM results

The enhanced magnification and reduced pixel sizes offered by the benchtop mesoSPIM revealed track-like structures in the images. A few of these structures were visually identified in one of the scans of the 100 kRad sample, and their presence was further confirmed by their appearance in the same positions during a repeated scan, as depicted in Figure 13.9.

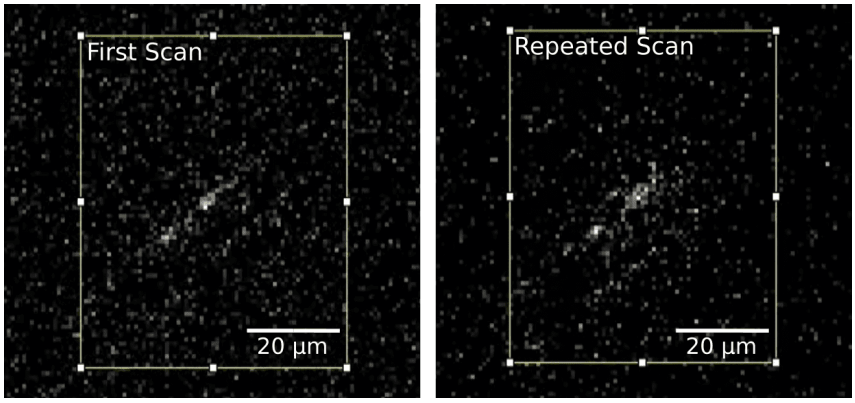

Figure 13.9: Exemplary z-planes exhibiting a track-like structure of approximately 20 µm observed in the same x-y-z positions of repeated scans from the 100 kRad sample imaged at 10×.

In this specific example, the track-like structure spanned around 6 z-planes and did not appear in the same x-y position across the other hundreds of z-planes. A detailed analysis of the correlation between matching points along this track, as compared to the expected correlation from random matching in the two acquired 3D scans, indicated that the track is unlikely to be a random feature. The correlation coefficient of the track matching points was several standard deviations above the mean value of the random noise distribution [206].

Leica results

Utilizing the Leica microscope in color camera mode, the fluorescence color emitted by three crystals were directly imaged, as shown in Figure 13.10.

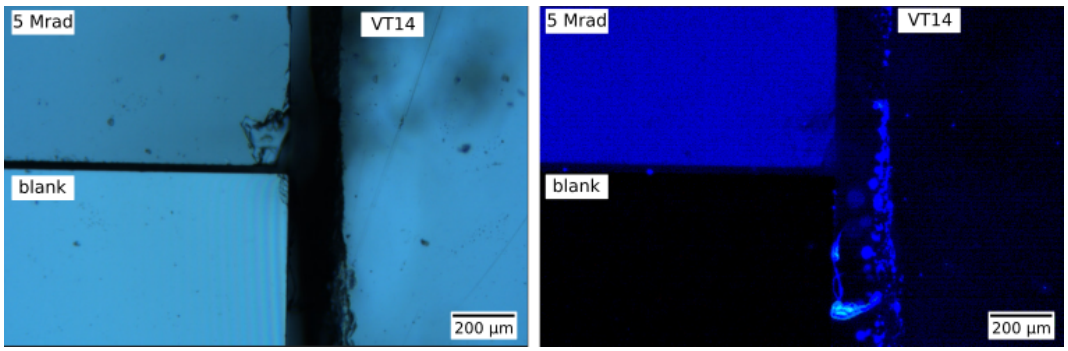

Figure 13.10: Left: Bright-field images of irradiated and blank crystals acquired without filters. Only a portion of each crystal is visible in the image. Right: The same crystals, in the same positions, imaged in fluorescence mode using 390 nm excitation light and corresponding filters, allowing only fluorescent light to be detected.

A blue emission is observed from the 5 MRad and VT14 irradiated samples, while no emission above the background level is observed from the blank crystal, a similar result to those obtained with the standard mesoSPIM.

13.4.3 *Spectroscopy measurements*

To further study the fluorescence of irradiated samples, the forward transmission and fluorescence spectra of blank and γ-irradiated samples were measured in response to light from 250 to 800 nm using a UV-vis spectrophotometer and an Edinburgh Instruments FS5 spectrofluorometer, respectively. The main results are shown in Figure 13.11.

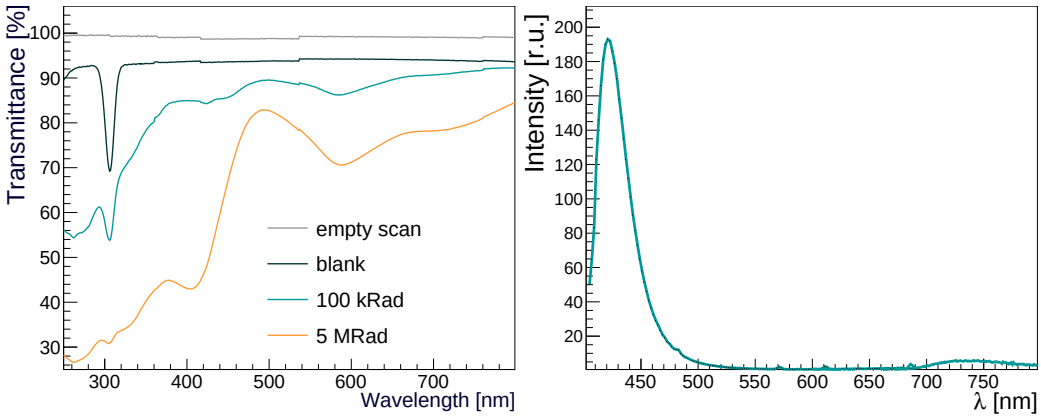

Figure 13.11: Transmittance spectra from blank and irradiated samples (left). Fluorescence spectrum (right) of 100 kRad irradiated sample measured in response to 400 nm light.

These results show an intense absorption by the 5 MRad irradiated sample at short wavelengths, particularly at ∼410 nm, as well as an intense emission at ∼425 nm. The fluorescence response to shorter excitation wavelengths (not shown, but measured down to 340 nm) consistently presented the emission peak at the same position. This result validates the observations obtained with the mesoSPIM: the irradiated crystals fluoresce in blue and the signal is not Raman scattering, which would otherwise move towards lower wavelengths in response to lower excitation wavelengths. A fainter emission peak at ∼740 nm is also observed and its intensity increases at larger (600 nm) excitation wavelengths. This also matches the results obtained with the mesoSPIM, where a significant fluorescent signal was measured in response to 561 nm light.

13.4.4 *ICPMS measurements*

After these measurements, the samples VT14 and 100 kRad were sent for inductively coupled plasma mass spectrometry (ICPMS) analysis with the goal of shedding light on the origin of CCs observed from CaF_2 samples. The focus was specifically to measure the concentrations of rare-earth elements, which are often present in minerals as impurities capable of inducing fluorescence. The obtained results revealed concentrations of ∼100 ppb of europium (Eu) and samarium (Sm) in both samples, which can fluoresce with emissions in the blue and red spectral wavelengths, respectively [207, 208]. The irradiation process might contribute to this fluorescence by providing electrons to these

ions. Normally found in their stable trivalent state[7] (Sm^{3+}, Eu^{3+}), these ions can transition to fluorescing divalent states (Sm^{2+}, Eu^{2+}) upon acquiring an electron [208, 209].

Given the substantial number of CaF_2 molecules ($\mathcal{O}(10^{10})$) in each cubic micrometer of the crystal, and considering that an imaging voxel has a volume of multiple cubic micrometers, the measured concentration levels are sufficient to result in several impurities within each imaged voxel.

13.5 CONCLUSIONS & OUTLOOK

This chapter introduced the first LSFM measurements of radiation-induced CCs in transparent crystals carried out with the cutting-edge mesoSPIM microscopes.

These measurements aimed not only to demonstrate the feasibility of CC imaging with LSFM, a cornerstone of the PALEOCCENE concept, but also entailed the development of imaging techniques and background estimation methods crucial for quantifying CCs in crystals. Within this context, the distribution of CCs across milliliters of material was analyzed, background sources were identified and investigated, and the color of the emitted CCs measured. Complementary measurement techniques, such as spectroscopy, were utilized to further enhance the overall understanding of these subjects.

With the mesoSPIM, fluorescence from γ-irradiated CaF_2 crystals was probed, demonstrating the device's capacity to image CCs at a quantitative level. Relevant outcomes from these investigations included the development of a data taking procedure and fiducialization method, based on the evaluation of specific background sources[8]. Additionally, comparisons were drawn between irradiated and non-irradiated samples, as well as among samples sourced from different vendors.

Utilizing the benchtop mesoSPIM, 'track-like' structures were imaged within the crystal and identified as likely intrinsic fluorescent features. While the origin of these features remains uncertain (one possibility being the trace left by a cosmic ray), this investigation highlights the benchtop mesoSPIM capability in imaging 'track-like' structures of CCs. The improved resolution at $20\times$ magnification will be valuable for future imaging of single CCs or alpha-induced tracks.

With the far-field measurements, the results obtained with microscopy were confirmed, such as excluding Raman as the signal source. Additionally, precise measurements of the wavelengths of absorption and emission revealed the extent of light absorption in irradiated crystals.

While the mesoSPIM data agrees with the far-field spectroscopy, several unique features are offered by the mesoSPIM. The capability for sectioned

7 In the case of CaF_2, these trivalent ions would occupy the place of Ca ions, with charge compensated by interstitial F^- ions [208].

8 This fiducialization is performed in a more quantitative, automated manner in [206], following these first studies.

imaging allows for precise delineation of a ROI, thereby mitigating surface-related background. Furthermore, this approach enables the quantification of CC distributions throughout the sample and facilitates the imaging of individual or clustered color centers with precise 3D positional information – a crucial feature for the concept of particle detectors discussed in this work.

The ICPMS assay provided valuable information about the origins of the fluorescence signals within the crystals. This analysis revealed the presence of rare-earth elements, specifically Eu and Sm, whose divalent states are now considered the likely source of the observed CCs, given that their known absorption and emission spectra align with the measurements in this study and with measurements conducted by other collaborators. This ICPMS assay was motivated by the observation of varying fluorescence levels across different crystal batches. Such variations could be attributed to varying impurity levels if impurities are accountable for the CCs. It is also worth noting that the presence of Sm and Eu, while confirmed at fractions of ppm, was listed in the suppliers' chemical assay as below the detection limit of 0.04 ppm.

In summary, this study demonstrated that LSFM can measure CCs induced in CaF_2 crystals by particle interactions, provided a good signal to background relation is attained. Within this work, collaborations with microscope developers were established, resulting in the upgraded benchtop microscope including dedicated design for the application here investigated [6]. This development is significant, given that improving mesoSPIM's capabilities enhances the practicality of PALEOCCENE detectors for dark matter search and nuclear safeguards. The role of LSFM, particularly the mesoSPIM, to rapidly and precisely image large volumes of crystals is pivotal for the imaging requirements of the PALEOCCENE concept.

The mesoSPIM could also find applications beyond particle physics, including fission track dating of transparent rocks. Employing the mesoSPIM for this purpose could facilitate the 3D imaging of minerals without the need for etching, offering a non-destructive and rapid method.

In conclusion, although still in its early stages of research and development, PALEOCCENE holds potential in the field of reactor CEvNS detection: it could enable a first reactor CEvNS detection with modest detector masses of 10 g [174], and it could also provide a scalable technology for nuclear non-proliferation safeguards, a critical application given the spread of nuclear reactors on a global scale.

SUMMARY & OUTLOOK

14 SUMMARY & OUTLOOK

An observation of $0\nu\beta\beta$ decay would shed light on major physics problems such as the origin of neutrino mass and the matter-antimatter asymmetry of the universe. Experiments advancing this research include not only those directly searching for this rare decay, such as GERDA and LEGEND, but also MONUMENT, which contributes to the calculations of nuclear matrix elements (NMEs) required for an accurate estimation of $m_{\beta\beta}$, the key parameter indicative of new physics involved in $0\nu\beta\beta$ decay.

This thesis presented analyses, simulations, and hardware R&D conducted within the context of these experiments. This work started with GERDA, which searched for $0\nu\beta\beta$ decay until November 2019, achieving a record-setting lower limit on $T^{0\nu}_{1/2}$ and a remarkably low background level [1]. This thesis included the characterization of data utilized in these results, specifically, the investigation of background rates before and after the 2018 upgrade during Phase II. The derived conclusions, primarily the confirmation that the upgrade did not introduce new background, lent further support to employing a unified background index for the entire Phase II data.

LEGEND-200 started assembly in 2020, aiming for a sensitivity to $T^{0\nu}_{1/2}$ exceeding 10^{27} yr. Its next phase, LEGEND-1000, demands a ten-fold background reduction to achieve a sensitivity to $T^{0\nu}_{1/2}$ beyond 10^{28} yr. Within the context of LEGEND, this thesis played a significant role by contributing to the development, construction, and characterization of the wavelength-shifting reflector (WLSR), designed to enhance light collection and background suppression achieved with the liquid argon (LAr) instrumentation.

To select materials for the WLSR of LEGEND-200, the reflectance, absorption, outgassing, and radiopurity of several WLSR materials were measured while the trade-offs between optical efficiency and mechanical stability were evaluated. Among the investigated materials, TPB-coated Tetratex® (TTX) emerged as the superior choice. However, achieving a stable and high-quality TPB-coated TTX necessitated the development of an in-situ TPB evaporation system. The design and construction of this system were realized as part of this thesis, and resulted in the successful evaporation of TPB onto 13 m^2 of the TTX shroud inside the LEGEND-200 cryostat.

The quality of the resulting TPB-coated TTX was investigated, along with PEN as an alternative to TPB. Light spectroscopy, microscopy, and LAr measurements combined with Monte Carlo simulations allowed to determine optical parameters such as the light yield (LY), reflectivity, and quantum efficiency (QE) of these materials in LAr. The low VUV reflectance of TTX measured in LAr (<17%) demonstrated the importance of using wavelength shifters not only to enable the detection of LAr scintillation with photosen-

sors non-sensitive to VUV light but also to enhance light collection through effective reflection.

The measured QE of PEN and TPB in LAr (∼69% and ∼85%, respectively), were the first estimations of the QE of TPB obtained with dedicated LAr measurements and of PEN's efficiency independent of TPB.

To optimize PEN-based WLSR, various reflectors coupled to PEN of different grades, thicknesses, and treatments, were characterized through microscopy and LAr measurements. While specific surface treatment and reflector choice did not significantly impact their LY in LAr, the poorer mechanical stability of 25 µm films arose as an issue affecting the accurate estimation of their LY. The most efficient WLSR configurations were 125 µm films not optically coupled to reflectors, and a laminate of thin PEN glued to Tyvek. A ready-to-use commercial aluminum-based PEN laminate emerged as an option providing a good balance between efficiency and ease of use.

In conclusion, the results obtained from the WLSR investigations presented in this thesis hold significant implications for optimizing detector designs and refining optical simulations of experiments using LAr. Information complementary to these measurements could be attained through dedicated experiments, such as precisely measuring the VUV absorption of TPB and determining the reflectivity of TTX and other reflectors in LAr in response to visible light.

While the measurements of this study were conducted ex-situ, the effectiveness of the WLSR introduced to LEGEND-200 was recently assessed in-situ through dedicated calibrations [127]. These evaluations revealed a remarkable threefold increase in light collection by the LAr system, compared to the previous design utilized in GERDA – an evidence that the WLSR developments undertaken in this thesis, and by the LAr instrumentation team, have successfully achieved their intended objectives. The enhanced background suppression achieved by collecting more light is still under study and will likely be understood with the first LEGEND-200 data release, planned for this year.

Looking ahead to the future of $0\nu\beta\beta$-decay search, the forthcoming results from MONUMENT hold potential to considerably reduce theoretical uncertainties in determining the $m_{\beta\beta}$ sensitivity of upcoming experiments. This, in turn, will yield a more precise understanding of the extent of the inverted mass ordering region that will be covered by these experiments. While the analysis presented in this thesis focused on the isotope relevant for NMEs of ^{136}Xe, MONUMENT also measured data pertinent to ^{76}Ge, both of which are the foremost isotopes currently driving $0\nu\beta\beta$-decay searches.

This work provided a thorough analysis of ordinary muon capture (OMC) in ^{136}Ba, with a focus on γ and x-ray line identification. This effort additionally yielded preliminary estimations of parameters directly related to the total and relative partial OMC rates. As refinements are applied to other analysis parameters, the eventual outcomes will serve to fine-tune and provide deeper insights into NME calculations, such as those provided in [55]. These results

play a pivotal role not only in enhancing the precision of $m_{\beta\beta}$ sensitivity estimations but also in providing an accurate value of $m_{\beta\beta}$ in case $0\nu\beta\beta$ decay is observed.

Given the wealth of potential new physics that can be probed through investigating neutrino properties and interactions, the scope of this thesis extended beyond $0\nu\beta\beta$ decay to the exploration of passive neutrino detectors with PALEOCCENE. The light-sheet fluorescence microscopy (LSFM) measurements of irradiated CaF_2 crystals presented in this work demonstrated the potential of the mesoSPIM light-sheet microscope in quantifying color centers in large volumes of crystals that could work as passive particle detectors. While this thesis presented only a fraction of the analysis and results obtained with the mesoSPIM, a substantial amount of findings were systematically analyzed by the MSc student V. Aerne, who undertook the task of processing the extensive dataset collected throughout this work.

Advancements involving LSFM testing for PALEOCCENE are set to evolve upon the groundwork laid by this thesis and the related MSc thesis. Future work will focus on verifying the initially observed signal from neutron-irradiated samples and exploring visualization of full tracks induced by ions and alpha particles. This R&D effort is pivotal in advancing PALEOCCENE from its early development stage to becoming effective detectors that could enable a first reactor CEvNS detection and potentially revolutionize the field of nuclear non-proliferation safeguards.

APPENDICES

A

RADIOPURITY ASSAY WITH THE GATOR FACILITY FOR γ-RAY SPECTROMETRY

One of the main background reduction techniques in rare-event search experiments such as LEGEND is the selection of radio-pure materials [63, 210, 211], as discussed in Chapter 4. The stringent background constraints of these experiments [39, 210] drive the need for highly sensitive radiopurity assay. The Gator facility meets this demand by providing a low-background environment for HPGe γ-ray spectrometry [2, 212]. Using Gator, we measured the radiopurity of the Tetratex® (TTX) used in LEGEND-200. The setup, simulation, analysis procedure, and radiopurity results for TTX are described in the following sections, showcasing a sample measurement. As part of this work, I additionally performed an update of the standard analysis[1] of samples measured in Gator, along with simulation cross-checks, which are detailed in this chapter and/or in a publication I co-authored [2].

A.1 THE SETUP, SAMPLE & MEASUREMENT

Gator is a low-background γ-ray counting facility, consisting of a 2.2 kg HPGe crystal shielded by layers of oxygen-free copper and lead. Located at LNGS, Gator stands as one of most sensitive setups worldwide for radiopurity assay with γ-ray spectroscopy, providing measurements of detector materials for GERDA, XENONnT and LEGEND [105, 210]. Gator's background rate is among the lowest in the field, as shown in Table A.1, where several of its features are compared to other HPGe γ-ray counting setups located in underground laboratories. Further details on Gator are provided in [2, 212].

Its spacious cavity, measuring 25×25×33 cm^3, enables the measurement of large samples, such as the TTX piece folded into a rectangular shape with dimensions 17×15.5×7.5 cm^3, shown in Figure A.1. This sample corresponds to the same batch of TTX used for the WLSR of LEGEND-200 (discussed in Chapters 8 to 11). With a weight of 930 g and a surface density of approximately 100 $g\,m^{-2}$, the folded rectangular TTX has a density of 0.47 $g\,cm^{-3}$.

The TTX sample was measured from March to May 2022 while the background data were acquired between October and December 2021, with respective effective live data durations of 53.2 d and 73.7 d. Detailed information about the measurement procedures, data selection, and calibration can be found in [2]. Both spectra are presented in Figure A.2, revealing that the rates measured from the TTX sample closely resemble those from the background. This highlights the necessity for Gator's exceptional sensitivity and an extended measuring time for this specific sample.

1 Compared to the previous analysis method employed, described in [212].

Table A.1: Location and overburden (in meter water equivalent [m.w.e]), HPGe crystal mass, efficiency (ϵ, as defined in [189]), energy resolution (FWHM at 1332 keV) and background rate (within 60-2700 keV) of Gator in comparison to other γ-ray screening HPGe detectors located in SURF [213], LNGS, Boulby [214], LSC [215], and LVdA [216]. Not all references provide the uncertainty in the count rate.

Detector	Location ([m.w.e.])	Mass [kg]	ϵ [%]	FWHM [keV]	Rate [cts/(kg·day)]
Gator	LNGS (3600)	2.2	100.5	1.98	(89.0 ± 0.7)
Maeve [211]	SURF (4300)	2.0	85	3.19	956.1
GeMPI 3 [217]	LNGS (3600)	2.2	98.7	2.20	(24 ± 1)
Belmont [211]	Boulby (2805)	3.2	160	1.92	135.0
GeOroel [215]	LSC (2450)	2.2	109	1.85	165.3
GeMSE [218, 219]	LVdA (620)	2.0	107.7	1.96	(88 ± 1)

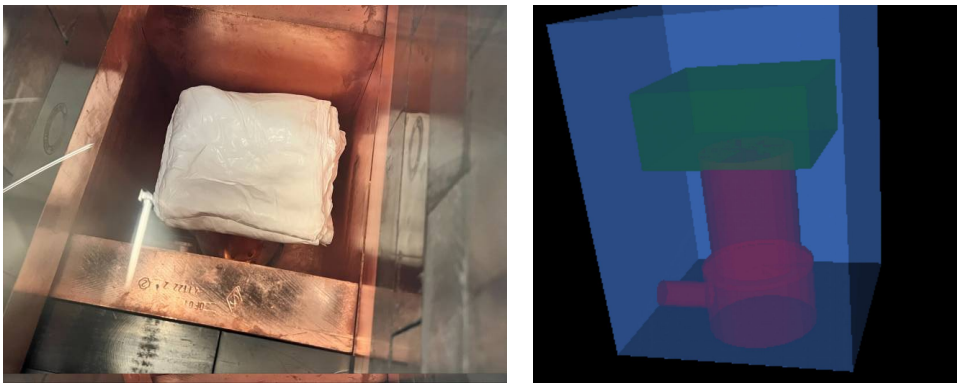

Figure A.1: Left: TTX sample inside the Gator facility, at the top of the HPGe detector. Right: Geant4 simulation of the TTX sample in Gator. Some parts of the setup (such as the lead shield) are not shown in the figure for clarity.

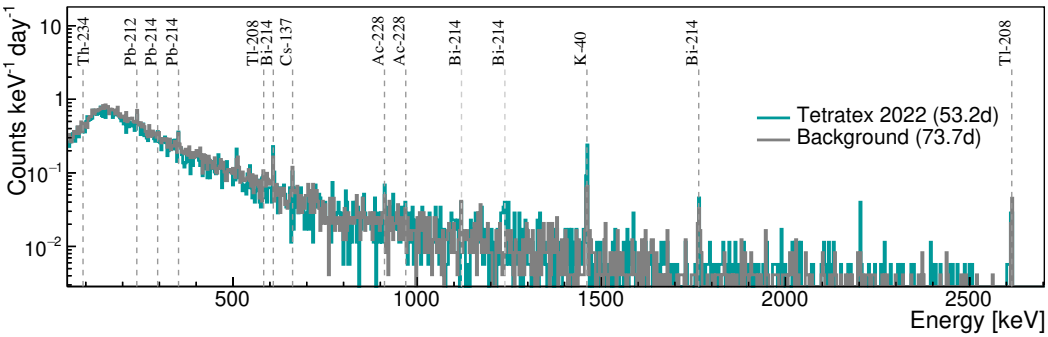

Figure A.2: Count rate measured with Gator for the TTX sample and background.

Prominent γ-ray lines

As shown in the decay chains presented in Figure 4.1, only a few isotopes produce γ rays with significant branching fraction (f_B >5%) and at energies where the detector is most sensitive (E_γ >90 keV[2]). Although the efficiency of HPGe detectors to γ rays peaks at low energies (∼150 keV), the increasing background at these energies limits the sensitivity in that region. Consequently, the selection of prominent γ-ray lines is primarily based on their f_B values.

For isotopes that do not emit 'prominent' γ rays, we assume these isotopes are in equilibrium with their short-lived daughter (e.g., ^{238}U in equilibrium with ^{234}Th) and calculate their activity based on the activity of the latter. In general, the following groups are assumed to be in secular equilibrium:

- The top of the ^{238}U decay chain (^{238}U, ^{234}Th, ^{234m}Pa);
- The part following ^{226}Ra (^{226}Ra, ^{214}Pb, ^{214}Bi);
- The top of the ^{232}Th decay chain (^{228}Ra, ^{228}Ac);
- And its subsequent daughters (^{228}Th, ^{212}Bi,^{208}Tl).

To determine the activity of these groups, specifically of ^{238}U, ^{226}Ra, ^{228}Ra (^{232}Th), and ^{228}Th, we rely on the specific γ lines marked in Figure 4.1.

For the top of the ^{235}U decay chain, there is only one prominent γ ray: the 185.7 keV (5.7%) line from ^{235}U. This line is often not observed, given the high Compton background at low energies and the low abundance of ^{235}U compared to ^{238}U[3]. However, we can use the relative abundance of these isotopes (ρ_r ∼0.7%) to determine the activity of ^{235}U based on the following relation between its abundance, activity and half-life with those from ^{238}U:

$$A_{235} = \rho_r \cdot A_{238} \cdot \frac{\tau_{238}}{\tau_{235}} = 0.04604 \cdot A_{238}.$$

Finally, the activities of ^{40}K, ^{137}Cs, and ^{60}Co are determined using their main γ lines with f_B >94%.

Simulation of γ-ray detection efficiency

The simulation of γ-ray detection efficiency for the TTX radiopurity assay was performed using the Geant4 software [144]. The simulation considered the exact geometry, chemical composition, and density of the materials present in the sample, detector, and cavity. Figure A.1 (right) shows part of the detector and sample geometries as implemented in Geant4.

2 This energy region, determined by [220], corresponds to where Gator can effectively detect and measure signals with significant efficiency and above the background noise.

3 Furthermore, there is a ^{226}Ra line close by, at 186.2 keV.

To cross-check and gain a better understanding of the modeling of Gator's γ-ray detection efficiency, as implemented in Geant4, two simulation modes were investigated.

- **Standard mode**: In this mode, the decays of isotopes were simulated, taking into account the entire decay chains for cases where an isotope decays into other isotopes. The resulting γ-ray emissions create a spectrum of energy depositions, which is used to determine the γ-ray detection efficiencies ε employed for the final results.
- **Gamma-only mode**: In this mode, instead of simulating isotopes and their decay chains, only the specific γ rays with energies corresponding to the expected prominent lines were simulated. The efficiency ε' obtained from this mode can be fitted using well-known functions for the efficiency of HPGe detectors [221].

In both simulation modes, $\mathcal{O}(10^7)$ primaries for each isotope (or γ ray) of interest were uniformly distributed throughout the sample. The subsequent γ-ray interactions and energy depositions were simulated within the modeled geometry via the built-in Monte Carlo method of Geant4. The final energy depositions within the HPGe crystal were stored in ROOT trees [160] for further analysis. The stored parameters included the position of each energy deposition within the crystal, the energy deposited in each of those steps (E_{hit}), and the total energy deposited (E_{tot}) per event in the crystal, shown in Figure A.3.

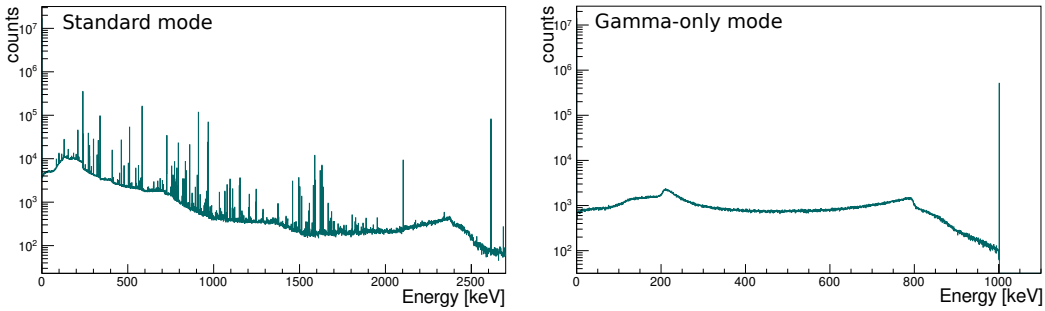

Figure A.3: Simulated spectra of total deposited energy (E_{tot}) for the ^{232}Th decay chain (left) and of ^{234m}Pa 1001 keV γ rays (right). For the simulation of decay chains or isotopes, many γ lines are observed in the E_{tot} spectrum (left). In the gamma-only mode (right), a sharp peak is observed at E_{tot}=E_γ, as well as the Compton edge at the maximum Compton energy (here ~800 keV), and the backscatter peak at ~200 keV.

The output spectra of the standard simulation mode exhibit peaks of varying intensities due to the interplay of the detector's efficiency as a function of energy, the f_B of each γ-ray line, and the reduction in efficiency caused by a sum-out effect, described in Figure A.4.

To derive the detection efficiency ε from the spectra obtained in the standard simulation mode, several steps are performed. First, the E_{tot} counts within

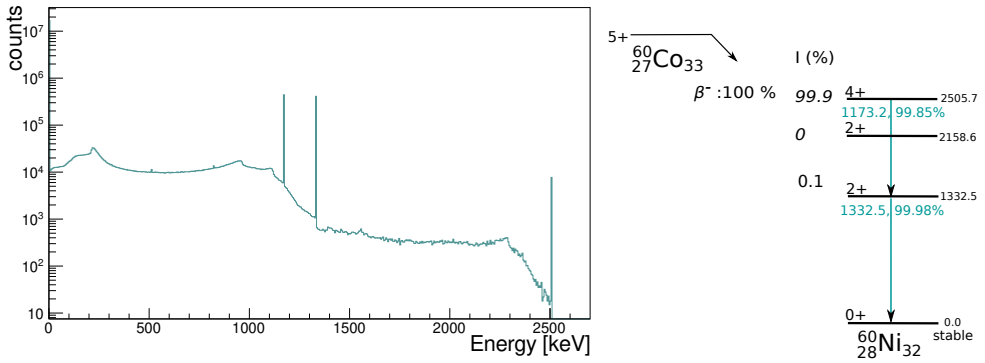

Figure A.4: Example of sum-out effect from ^{60}Co. The decay scheme [162] shows its two main γ lines, which are emitted in a cascade within $\mathcal{O}(ps)$ As a result, there is a certain probability of detecting their sum at ~2.5 MeV, as displayed by the E_{tot} simulated spectrum on the left. This leads to a decrease in the detection of the individual peaks, known as the sum-out effect. Other prominent γ-ray lines that undergo summation effects are marked in Figure 4.1.

the ROI centered around a specific γ-ray energy are integrated. Subsequently, the Compton background is subtracted to obtain the corrected number of counts within the full-energy peak (FEP). Next, this number is divided by the simulated number of decays. The resulting f_B weighted efficiency ($\varepsilon \times f_B$) is then divided by the f_B of the corresponding γ-ray line, resulting in the final detection efficiency ε. This value represents the probability of detecting a FEP of a γ ray given the total number of γ rays emitted at the same energy. The obtained efficiencies ε are presented in Figure A.5 (top).

In the gamma-only simulations, the efficiency ε' was directly obtained by dividing the Compton subtracted FEP counts by the number of simulated γ rays. The resulting values are presented in the same figure (bottom).

While the standard simulations are required for obtaining the actual detection efficiencies, the gamma-only simulation allows for observing the efficiency curve without the interference of sum-out effects. In this mode, the efficiency ε' depends solely on E_γ and the sample and setup geometry and materials. The efficiency curve exhibits a peak at around 150 keV: At lower energies, γ rays are often absorbed by the sample or non-sensitive layers around the detector; With increasing energies, γ rays undergo more often Compton scattering, resulting in a lower probability of full absorption at once, as shown in Figure A.6.

These high energy γ rays are also less likely to be fully absorbed within the HPGe crystal because their attenuation lengths become comparable to the crystal dimensions[4]. The combination of these scattering and absorption effects on the efficiency curve can be fitted with a sum of exponential functions, shown in Figure A.5 (bottom). The close alignment of the data with the

4 Attenuation coefficients of ~0.5 (0.06) cm^2g^{-1} for E_γ=100 keV (E_γ=1000 keV) result in attenuation lengths of ~0.4 cm and 3 cm (for a germanium density of ~5.3 gcm^{-3}), while the HPGe crystal has a radius of 4.1 cm and 8.1 cm of height.

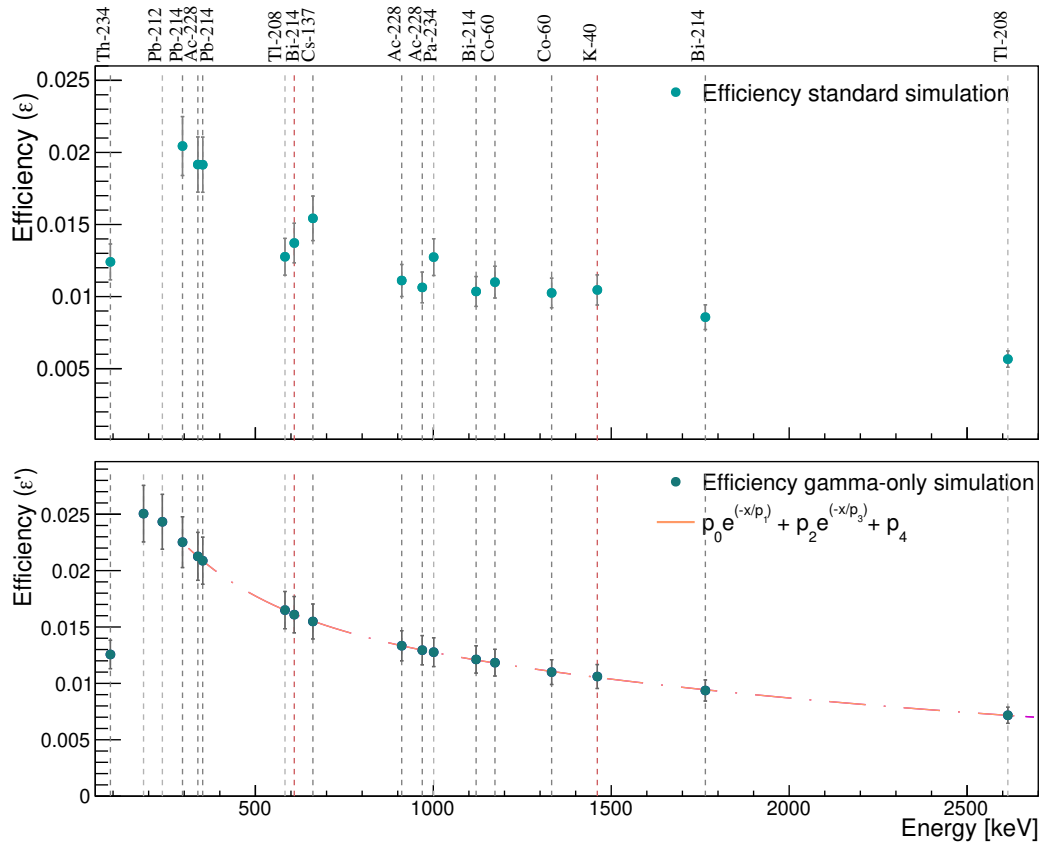

Figure A.5: Energy-dependent γ-detection efficiency ε' from the standard (top) and gamma-only simulations (bottom). The sum-out effects are clear in the former. The latter is fitted with a sum of exponentials above ∼300 keV, as in [221].

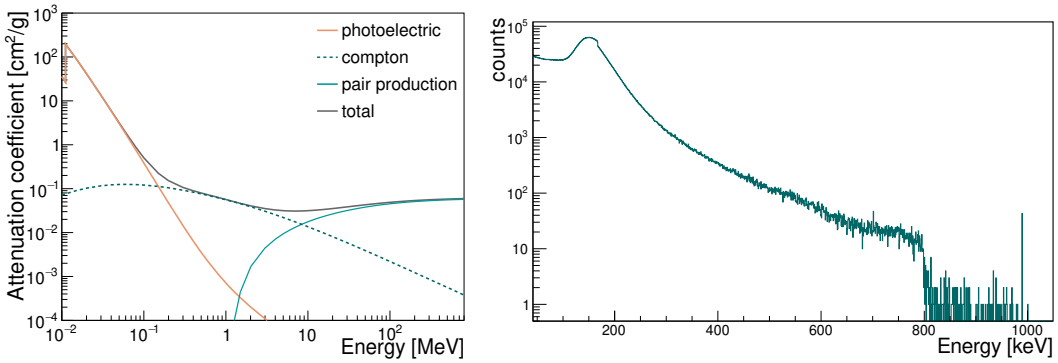

Figure A.6: Left: Mass attenuation coefficients for germanium for different scattering and absorption processes (data from [61]). The photoelectric absorption dominates below ∼100 keV, and Compton scattering dominates around 1 MeV. Right: E_{hit} simulated spectrum for 1001 keV γ rays. As γ rays of this energy have low probability of depositing their full energy at once, the peak at E_{hit}=E_γ is absent (as compared to the E_{tot} spectrum shown in the right of Figure A.3). The Compton edge is observable again at ∼800 keV and the backscatter peak at ∼200 keV.

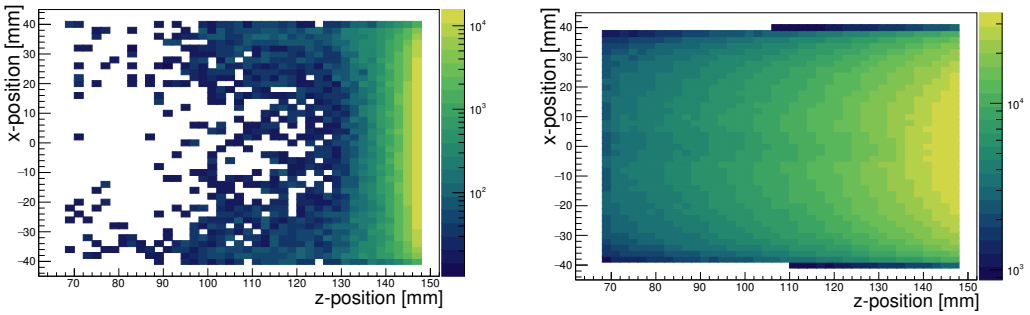

Figure A.7: x (radial) and z (longitudinal) position of energy depositions in the HPGe crystal for 100 keV (left) and 1000 keV (right) γ rays simulated inside TTX. Most of the low energy γ rays are stopped at the front of the detector, while high energy γ rays more often reach the bottom of the detector (low z position) or exit it again.

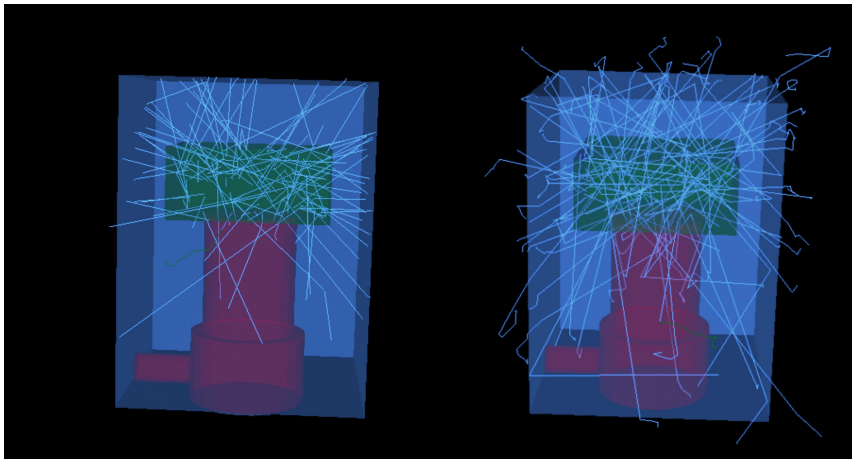

Figure A.8: Tracks of 100 keV (left) and 1000 keV (right) γ rays simulated with origin inside the TTX sample.

theoretical fit, without requiring additional parameters, suggests a reasonable modeling of the detector[5].

To gain a general understanding of these effects, the positions of simulated energy depositions in the HPGe crystal and visual examples of γ-ray tracks were studied. These visualizations, presented in Figure A.7 and Figure A.8, show the interactions of γ-ray energies of different energies within the crystal, providing information on the modeling of these interactions within the simulation framework. The comparison of these results to theoretical expectations for attenuation due to Compton scattering or full absorption within the detector (Figure A.6, left) demonstrates a satisfactory agreement, serving as a qualitative validation of the simulations.

5 The exact agreement of the simulation output with data has been investigated by [212] (in 2010) and is currently being investigated in more detail by another PhD student working with Gator

Analysis procedure

The measured sample spectrum was analyzed using a counting method. For each investigated γ-ray line, we counted the total (S_t), Compton (S_c), and Compton-subtracted (S) events within the region of interest ($\pm 3\sigma$ around E_γ) and at the Compton sidebands ($\pm 3\sigma$), as shown in Figure A.9. The same numbers were obtained for the background spectrum (B_t, B_c and B). B was then scaled by the time ratio between sample and background acquisition live-times ($t = t_S/t_B$), and the sample net signal S_{net} for a specific γ-ray line was calculated as:

$$S_{net} = (S_t - S_C) - (B_t - B_C) \cdot t = S - B \cdot t. \tag{A.1}$$

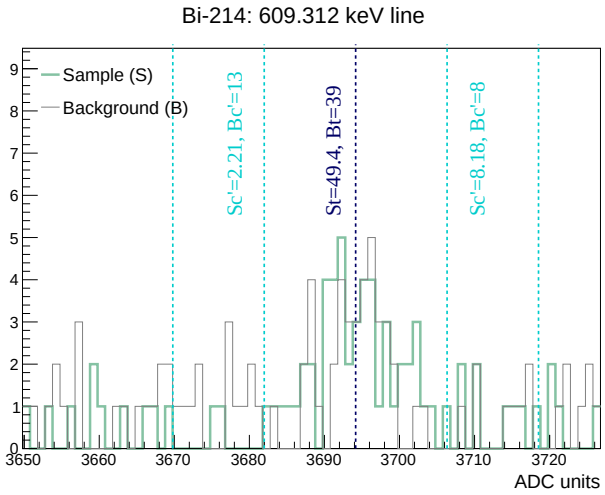

Figure A.9: TTX sample and background spectra around the ^{214}Bi 609.3 keV γ-ray line (in ADC units and not scaled for the time acquisition ratio). The signal region and its count numbers (S_t, B_t) are marked in dark blue. The Compton sidebands and their count numbers (S_C, B_C) are marked in cyan.

All uncertainties on x counts were calculated as $\sqrt{x+1}$. Based on the Compton and background counts, along with their uncertainties, we estimated the level of true net signal that leads to a certain probability of detection, knows as detection limit (L_d) :

$$L_d = f^2 + 2 \cdot f \cdot \sqrt{2} \cdot \sqrt{1 + \frac{f^2}{8} + S_c + \frac{(B_t - B_c)}{2} \cdot \frac{t_S}{t_B} + \left(\frac{(B_t + B_c)}{2} + 1\right) \cdot \left(\frac{t_S}{t_B}\right)^2}, \tag{A.2}$$

where f is the coverage factor for a given CL. Details on the general equation are provided by [222]. If S_{net} exceeds L_d, we report activity values. Otherwise, we report 90% CL upper limits. The values of S_{net} and L_d obtained for each prominent γ line with the two equations above are shown in Figure A.10, in comparison to the measured S_t, and B_t count numbers.

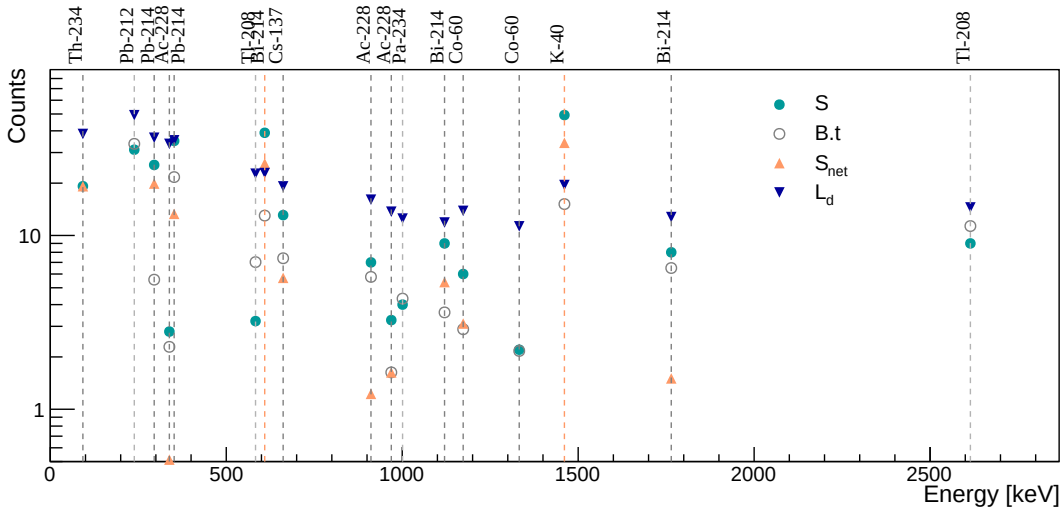

Figure A.10: L_d, S_{net}, and Compton subtracted number of counts measured for the sample (S), and background (B) for each investigated γ line. Here, B is shown multiplied by the acquisition time ratio (t). Lines with $S_{net} > L_d$ are marked in orange. For better visualization, no error bars are shown.

To convert S_{net} from a given γ-ray line to the specific activity A of the isotope, we use the following equation:

$$A[\mathrm{Bq/kg}] = \frac{S_{net}}{(\varepsilon \times f_B) \cdot m \cdot t_S}, \tag{A.3}$$

where m is the sample mass. The uncertainty on the activity takes into account the uncertainties on S_{net} and a 10 % systematic on the efficiency ε (described in [212]). If multiple lines of a given isotope are present in the spectrum with $S_{net} > L_d$, we calculate the activity as the error-weighted average. In the case of TTX, only two lines were observed with $S_{net} > L_d$, the ^{214}Bi 609.3 keV line and the ^{40}K line, as shown in Figure A.10. The activities of ^{226}Ra and of ^{40}K were estimated using these lines.

When only limits were available, the lowest upper limit was selected. For example, two energy regions were analyzed for ^{238}U: the 'double-line' of ^{234}Th at ∼92.6 keV[6], and the 1001 keV γ ray of $^{234\mathrm{m}}$Pa[7]. The 92.6 keV double-line yielded a slightly better limit, despite laying in a region of high Compton background. The resulting activities are shown and discussed in the next section.

6 For this line, a signal region slightly larger than the usual $\pm 3\sigma$ is employed.
7 With a f_B=0.8%, the $^{234\mathrm{m}}$Pa line was the only investigated line with $f_B < 5\%$.

Results

The values and upper limits of activity measured in the screening of the TTX sample are shown in Table A.2. The discussion of these results is within the relevant section of the TTX characterization work (Section 9.2).

Isotope	LEGEND-200 Batch (this work)	
	HPGe [mBq/kg]	HPGe [mBq/m^2]
^{238}U	<26.4	<2.64
^{226}Ra	0.97 ± 0.38	0.097 ± 0.038
^{228}Ra (^{232}Th)	<1.56	<0.156
^{228}Th	<1.48	<0.148
^{235}U	<1.21	<0.121
^{60}Co	<0.29	<0.029
^{40}K	7.20 ± 2.10	0.720 ± 0.210
^{137}Cs	<0.48	<0.048

Table A.2: Upper limits (90% CL) and values of activities measured in the γ-ray HPGe screening of the TTX sample. Values are also shown in mBq/m^2.

Outlook

As part of this study, the standard counting method and associated code used for analyzing samples in Gator were cross-checked and updated. This analysis method is specifically tailored for low-background counting, which is mostly the case for samples measured in Gator. This analysis approach offers the advantage of being easy to use, as it involves a counting method rather than requiring full spectral fits. However, for samples with a large number of counts, especially those with a high Compton background level, alternative methods should be considered

Additionally, cross-checks of the simulation code were performed, as presented in this appendix. Moving forward, it is recommended to focus on validating simulation parameters at low energies to enhance the accuracy of the simulation and more quantitatively investigate the simulation systematic uncertainties. By addressing these aspects, Gator's effective sensitivity in determining activity values for radiopurity assays can be enhanced, leading to more precise results.

B

OUTGASSING ASSAY OF TETRATEX

An outgassing setup available at our laboratory was used to assess the outgassing level from the specific TTX of LEGEND-200. The setup, described in detail in [130], mainly consists of a vacuum system, a stainless steel vacuum chamber for sample placement, and a residual gas analyzer (RGA) used to measure the outgassing in terms of partial pressure measured from each gas.

The TTX sample, weighing 5.5 g and with a surface area of 500 cm^2, was folded and inserted into the chamber. After several cycles of argon gas flushing, the setup was pumped to a vacuum level below 10^{-6} mbar within ∼1 h. Data acquisition using the RGA was performed multiple times over a period ranging from five hours to five days. The same procedures were carried out with an empty chamber as a control.

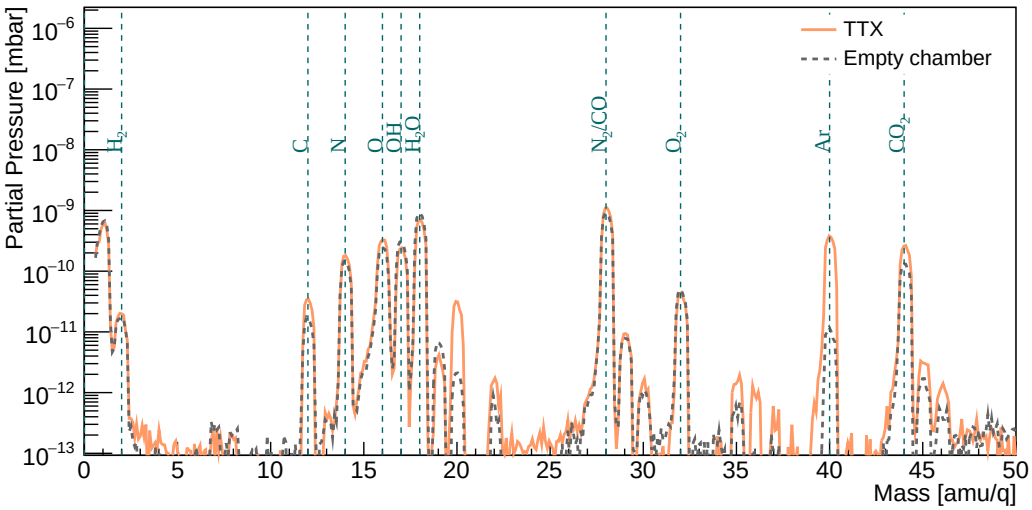

Figure B.1: Partial gas pressure as a function of atomic mass units per charge (amu/q) measured from the TTX sample and empty sample chamber. The main elements are identified by the vertical lines. Only two peaks seem to be higher for TTX: the one from argon, which is likely related to the flushing procedure, and the one from neon (at amu/q=20), which might also have the same origin.

The outgassing from the TTX material exhibited higher levels during the initial data takings but eventually stabilized after approximately two days. Only data acquired after outgassing stabilization are presented in Figure B.1, which shows the measured spectra after three days of pumping. The comparison with the empty chamber reveals that the outgassing from the TTX material is not significantly higher than that of the chamber, which possesses a comparable stainless steel surface area. Considering that the surface area of TTX in LEGEND-200 is much smaller than that of the cryostat (13 m^2 compared

to a few 100 m^2 of stainless steel), the outgassing from TTX is negligible for LEGEND-200.

This same type of outgassing assay was also employed during the design phase of the in-situ evaporator system. By comparing the outgassing levels of various plastic materials, such as polyamide-based pulleys, to that of the empty chamber, it was possible to assess their suitability for the evaporator system. The measurements of certain materials often revealed significantly high outgassing values, three to four orders of magnitude higher compared to the empty chamber. As a result, these materials, including polyamide-based pulleys, were avoided in the construction of the evaporator system.

C

WLSR CAMPAIGN DIFFERENCES AND DETAILS ON THE DATA ANALYSIS

C.1 SETUP AND PROCEDURES IN THE SECOND CHARACTERIZATION CAMPAIGN

Although the setup remained the same (Section 11.2), there were a few hardware and operational modifications made in the second characterization campaign. These differences are outlined below:

1. Additional LED: An extra LED and board were placed near the source, introducing a slight shading effect and potentially increasing outgassing within the sample volume.

2. Absorber: The absorber used to cover the setup had a smaller hole (⌀ 6 mm) for the source disk.

3. Shorter pumping times: The duration of the pumping process was reduced (∼20 h), resulting in a pressure before operation of approximately 10^{-4} mbar.

4. DAQ settings and equipment: The DAQ settings remained the same, and the NIM board and the voltage supply were not exactly the ones used in the previous campaign but were of the same types.

5. Data taking duration and voltage: Data was collected for a shorter duration (∼24 h) at a single voltage, unlike the first campaign which spanned several days and included different voltages.

6. PTFE filler treatment: The PTFE filler inside the cryostat (described in [3, 223]) was baked to facilitate its outgassing process and compensate for the shorter time between runs.

7. Additional heating element: A heating element was added at the bottom of the sample cell to accelerate the boiling of argon.

The first three factors may have contributed to a decrease in the LY observed in the absorber and sample measurements compared to the first campaign.

C.2 DAQ TRIGGER, DATA STABILITY & LY CORRECTION

In both campaigns, the DAQ trigger level was set to a few ADC units above the baseline ensuring the trigger was at the level of sPE. Despite the stability of the baseline, shown in Figure C.1, the mean values of the sPE peaks were

observed to slowly drift during the second campaign, as depicted in Figure C.2 (left). Possible factors for the drift included daily variations in PMT gain and less stability in the pressure and fill level of the cryostat. This drift was not a problem, given that each data set was calibrated using its sPE peak, resulting in a stable mean of the PE peaks, as shown in Figure C.2 (right) on the right.

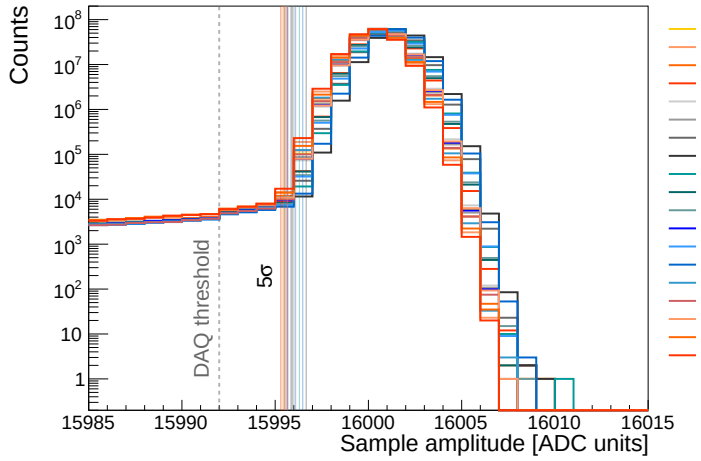

Figure C.1: Histogram of sample sizes (in ADC units) in the pre-trigger (baseline) region of various measurements and runs, represented with different colors. The DAQ threshold level and 5σ deviations for each histogram mean are also marked. The latter fall within one ADC unit range, indicating a stable baseline.

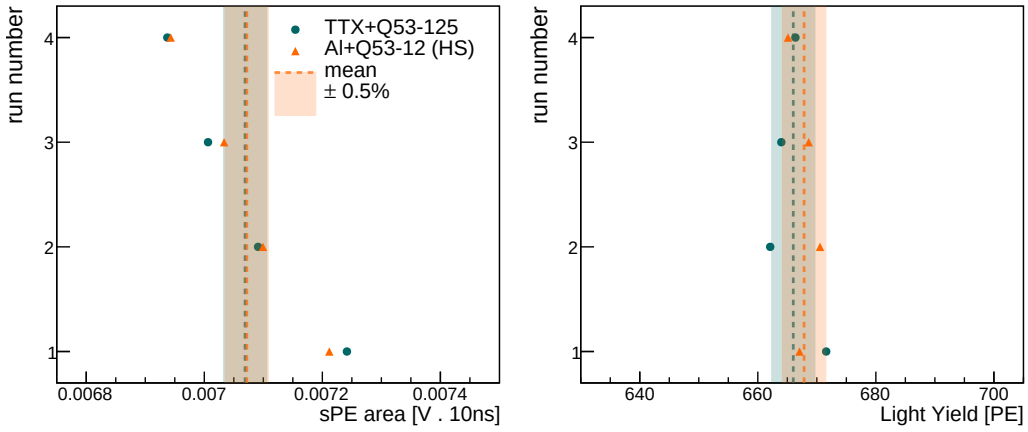

Figure C.2: Left: mean of sPE peak for several runs of two sample measurements. The vertical line and band shows the total average of these value ±0.5%. Right: Calibrated PE peak for these measurements, which agree within percent level, as shown by the bands.

To ensure comparability of the measurements, only the first ∼6 h of data taken immediately after the LAr filling and setup stabilization were selected for analysis in the second campaign. To assess the LY stability, the delayed

scintillation components, $\tau_{triplet}$, of the waveforms were fitted. The fit results, provided by the visiting student Sarthak Choudhary, are listed in Table C.1.

Table C.1: Triplet lifetime fit for the measurement of each PEN sample in the second campaign. Repeated measurements are shown in bold.

Measurement	$\tau_{triplet}$ [µs]	error [µs]
TTX+Q53-25 (MS)	1.13	0.01
TTX+Q51-50 (HS)	1.10	0.02
TTX+Q53-125 (MS)	1.11	0.01
TTX+Q53-125	**1.05**	**0.01**
TTX+Q53-125 (HS)	1.06	0.01
ESR+Q53-125	0.99	0.01
TTX+Q53-125	**0.97**	**0.02**
Al+Q53-12 (HS)	1.07	0.01
Tyvek+Q53-25	0.97	0.03

The triplet lifetime of pure argon is ∼1.3 µs, measured without wavelength shifting [85, 224]. Values measured with TPB, and possibly with PEN [4], can be slightly higher due to their delayed emission [224]. In the absorber configuration without WLS materials, $\tau_{triplet}$ was 0.96 ns, a low value that indicates the presence of impurities, mainly from the outgassing of the PTFE filler in the cryostat (discussed in [105]). The reduced $\tau_{triplet}$ and consequent quenching of LY becomes problematic only if significantly unstable, but most measurements presented in Table C.1 have $\tau_{triplet}$ values within 1.09±0.04 ns.

However, three measurements exhibited significantly lower values, ∼0.98 ns. The causes for the lower values were: introduction of impurities due an accidental reduction in pressure in the repeated measurement of **TTX+Q53-125**, and potentially increased outgassing from the laminate materials (Tyvek, SMP glue or ESR).

LY correction

To correct for the impurity-related relative quenching of LY, a dedicated measurement was performed to investigate the relationship between $\tau_{triplet}$ and measured PE. At the end of a measurement, the setup was gradually depressurized, resulting in the introduction of impurities. Figure C.3 shows the effect of impurity introduction on both $\tau_{triplet}$ and PE. From this dedicated measurement, we obtained the following relation:

$$\mathrm{PE} = p_0 + p_1 \cdot \tau,$$

where the fit resulted in p_0=134, and p_1=500, and τ corresponds to $\tau_{triplet}$. This function was utilized to correct the observed PE values for any given sample measurement (s), with:

$$\mathrm{PE}(s) = p_0 + p_1(s) \cdot \tau(s), \text{ or } p_1(s) = (\mathrm{PE}(s) - p_0) \,/\, \tau(s),$$

where we considered p_0 to be constant, as varying this parameter by $\pm 25\%$ did not significantly impact the results[1]. To compare the measurements, we selected a reference value of $\tau(ref)$ from TTX+Q53-125 MS, which had high PE and $\tau_{triplet}$ values. We then scaled the PE values of other samples based on their respective $\tau_{triplet}$ values in relation to the reference value:

$$\mathrm{PE}_{\mathrm{corr}}\,(s) = p_0 + (\mathrm{PE}(s) - p_0)\,/\tau(s) \cdot \tau(ref) =$$
$$p_0 \cdot (1 - \tau(ref)/\tau(s)) + \mathrm{PE(s)} \cdot \tau(ref)/\tau(s)$$

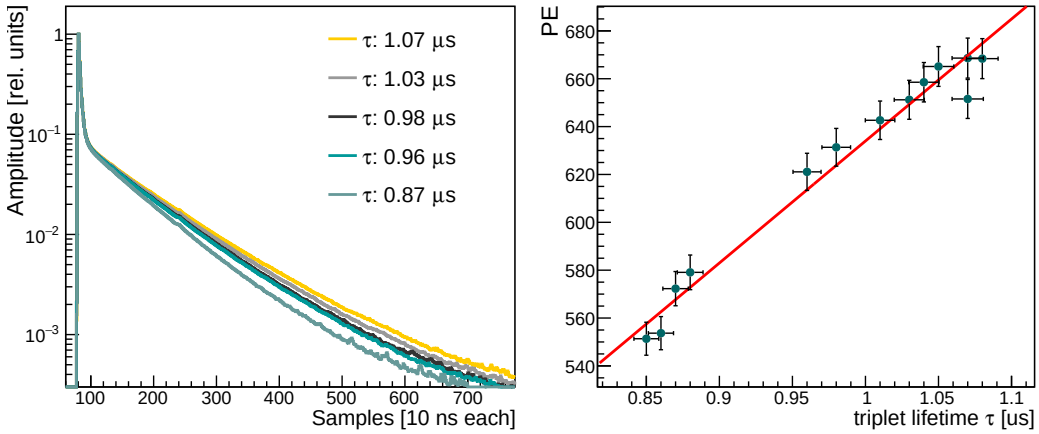

Figure C.3: Left: Stacked waveforms during depressurization and their respective $\tau_{triplet}$. Right: Relation of the LY (in PE) and $\tau_{triplet}$ fit with a linear function.

By applying this correction, we can more accurately compare the PE values of different samples, considering the variations in measured LY via their different $\tau_{triplet}$. This correction improves the agreement among the corrected LY values obtained from repeated measurements, as shown in the results section (Figure 11.10). Moreover, the trends observed in the four regions of LY values become more evident after the correction.

C.3 Optimization Studies of PEN-Based Laminates

Given that the refractive index of LAr is higher than that of air ($\sim$1.23 in the visible range), a few materials that are reflective in air may become transparent in LAr. To qualitatively investigate this phenomenon, the transparency of various PEN films coupled with reflectors was investigated in liquid nitrogen (LN2) and isopropanol, which have refractive indices around that of LAr (1.2 and 1.39 at $\sim$520 nm, respectively). The samples, listed in Table C.2, were immersed in either LN2 or isopropanol and illuminated with a UV lamp on the PEN side, as shown in Figure C.4.

1 Ideally, we would fit such a curve for each measurement, but this is not possible due to limited data availability. However, since the observed LY values did not largely vary, this correction based on the available data is expected to provide a reasonable representation for all measurements.

Table C.2: PEN combinations measured in LN2 and investigated as laminate options. All samples include PEN Q53 grade, 25 µm from Teonex. For details on the reflectors, see Chapter 11. Non-optically coupled samples are marked with 'nc', and adhesive samples with 'adh'

Sample name	coupling	reflector
ESR (nc)	-	ESR (non adhesive)
ESR (adh)	3M® adhesive	ESR (with adhesive)
TTX (nc)	-	Tetratex®
Mylar (adh)	-	Mylar® tape from Ruag
Tyvek (nc)	-	Tyvek® 1082D
Tyvek (g)(1)	UHU® polyvinylacetate glue	Tyvek® 1082D
Tyvek (g)(2)	Araldite® epoxy glue	Tyvek® 1082D
Tyvek (g)(3)	Poly Max® SMP glue	Tyvek® 1082D
Tyvek (g)(4)	Sikaflex® SMP glue	Tyvek® 1082D

The PEN film absorbed most of the UV light and emitted blue light. The intensity of light emitted by the PEN-reflector combination (frontal LY) was visually inspected, along with the presence of any blue light transmitted on the reflector side (back transparency). The latter indicated whether the coupled reflector was transparent to the shifted blue light. The aim was to identify a PEN-based WLSR that exhibited low transparency while keeping high light yield.

Figure C.4: ESR (adh) sample immersed in LN. The left image shows the blue light emitte by PEN which comes through the ESR reflector (back transparency). The image on the right shows the LY from the sample (frontal LY).

The qualitative observations were: With the exception of the Mylar (adh) sample, all samples exhibited some degree of transparency. However, the Mylar tape did not demonstrate a better frontal LY, which could be due to absorption by its adhesive, or suggest that, despite their observed transparency, conventional reflectors such as TTX, ESR, and Tyvek still reflected more blue light in LAr compared to Mylar. ESR (adh) appeared slightly more transparent, but due to the qualitative nature of the analysis, no definitive

conclusion could be drawn. TTX and Tyvek performed similarly, but TTX showed more shrinkage in LN2, possibly due to its lower rigidity. It was also observed that TTX became nearly transparent in isopropanol and remained so even after being removed from the isopropanol bath and until it dried. This indicates that the fibers of TTX were completely soaked in isopropanol. On the other hand, ESR and Tyvek did not exhibit this behavior and were not as transparent as TTX in isopropanol. Considering the mechanical stability and lower transparency in both cases, Tyvek was chosen for further optimization in the design of a laminate containing a coupled thin PEN film.

In the optimization of Tyvek-PEN laminates, an alternative approach was taken by testing different types of glues instead of using double-sided adhesives commonly found in commercial laminates (such as the PEN laminate investigated in Chapter 11). The aim was to minimize the number of layers, which can contribute to increased absorption. The production process of the laminate using glue is illustrated in Figure C.5.

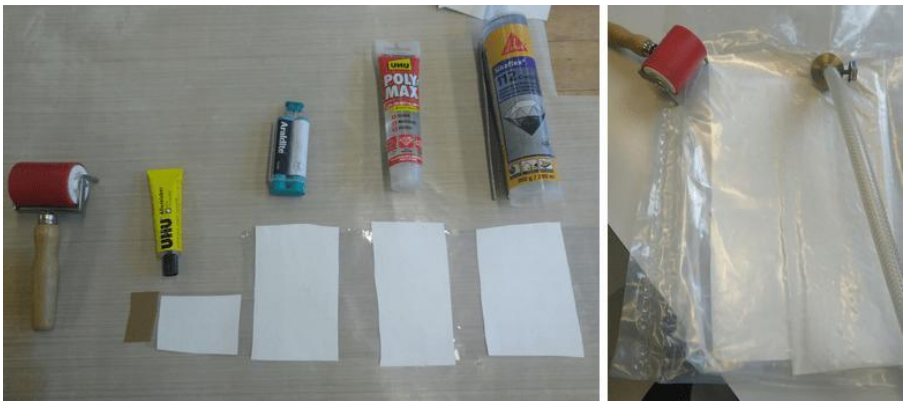

Figure C.5: Production process of laminates using glue: Tyvek and PEN films were sonicated in isopropanol to ensure cleanliness. The PEN film was then fixed on a table, glue was applied on top using a glue roll, and Tyvek was placed on top (left image). The combination was pressed together using a clean roll and immediately placed in a clean bag, which was vacuum-sealed and pressed again (right image). The film was left to dry for approximately 24 hours. Subsequently, UV bubble inspection, shrinkage inspection, and LN2 dunk tests were performed to assess the quality of the laminate.

The conclusions drawn from the tests conducted on each investigated sample, Tyvek (g)(1-4) are outlined below.

1. Tyvek (g)(1): The glue appeared less transparent. No shrinkage of the laminate was observed, and its appearance under UV light was satisfactory (no bubbles).

2. Tyvek (g)(2): The epoxy glue used in this sample was slightly yellowish and showed bubbling during mixing, some of it appeared to remain in the laminate. No shrinkage was observed, and it demonstrated high adhesive strength.

3. Tyvek (g)(3): The SMP glue used in this sample was transparent, but had a less liquid consistency, making it slightly harder to handle. It presented a satisfactory appearance under UV (no bubbles). No shrinkage was observed for a small piece, but the edges turned up slightly when producing a larger piece (over 100 cm^2). It had lower adhesive strength, and the PEN film could be detached if pulled.

4. Tyvek (g)(4): Its SMP glue was similar to that of Tyvek (g)(3), but the laminate exhibited shrinkage after drying (around one day). The final piece looked like a roll.

1-4: None of the laminates exhibited unusual shrinkage when immersed in LN2, and all of them appeared equally transparent compared to the ESR (nc) in LN2.

Based on the good transparency, low shrinkage and the low outgassing properties of the Poly Max® SMP glue [225], Tyvek (g)(3) laminate was selected for production as a large sample. This laminate was tested in the second PEN characterization campaign (Chapter 11). Its LY was satisfactory, surpassing the LY of thin films without coupling. After applying the triplet-lifetime correction, its LY was among the highest. However, it was observed that the outgassing of Tyvek resulted in a decrease in the effective LY due to the introduction of impurities. One possible solution to mitigate this outgassing is to increase the duration of the pumping process.

D

LIST OF HPGE DETECTORS IN MONUMENT

The eight HPGe detectors utilized in the 2021 irradiation campaign were mounted to the aluminum frame at an average distance of 15 cm from the target, seven of them were cooled by Big MAC cryostats, and one of them was cooled by an electrical Cryo-Pulse cryostat, as shown in Figure D.1.

Both Coax and BEGe are p-type detectors, while REGe are n-type Coax detectors with thin beryllium windows. Their full name describes channel ID, as identified in the analysis (Chapter 12), detector type, relative efficiency (represented by the first two digits), and energy resolution (FWHM at 1.3 MeV, represented by the last two digits). We note that the relative efficiency of each detector should not be taken as an estimate of the relative rate measured by each crystal, as their distances to the target were not completely uniform.

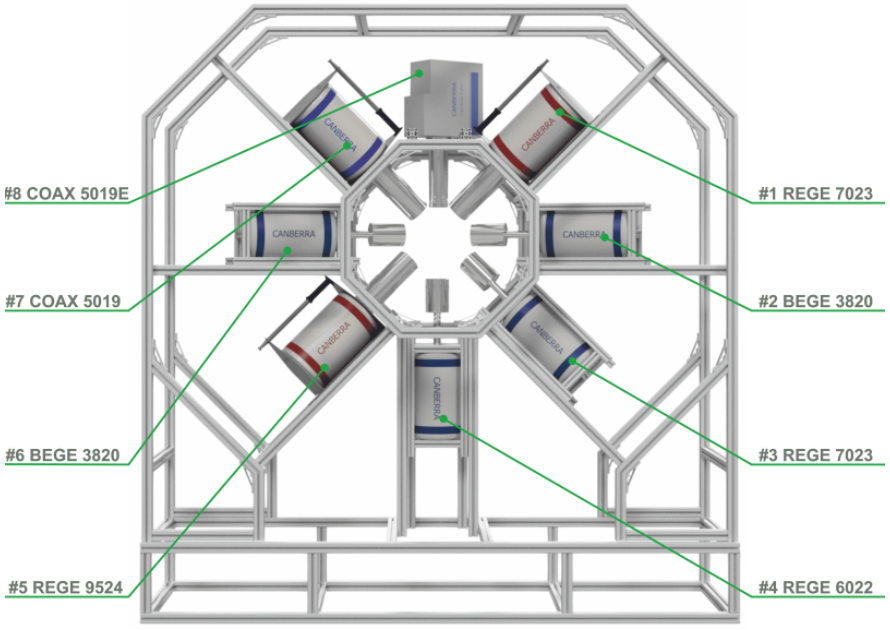

Figure D.1: MONUMENT setup during the 2021 campaign. Each detector is labeled according to a specific nomenclature. See text for details. Image credit: Egor Shevchik.

Prior to the assembly at PSI, the detectors owned by the collaboration were tested in a characterization campaign conducted at TUM. This characterization involved cooling the detectors, applying a certain bias voltage, exposing them to ^{60}Co or ^{133}Ba sources, and taking data with both a multi-channel analyzer and the LLAMA DAQ for each set voltage. The parameters measured included: leakage current, voltage at the test point, and FWHM. For each detector, the FWHM versus voltage was analyzed and the operation

voltage was defined as the point where increasing the voltage did not lead to improving the FWHM, as exemplified by Figure D.2.

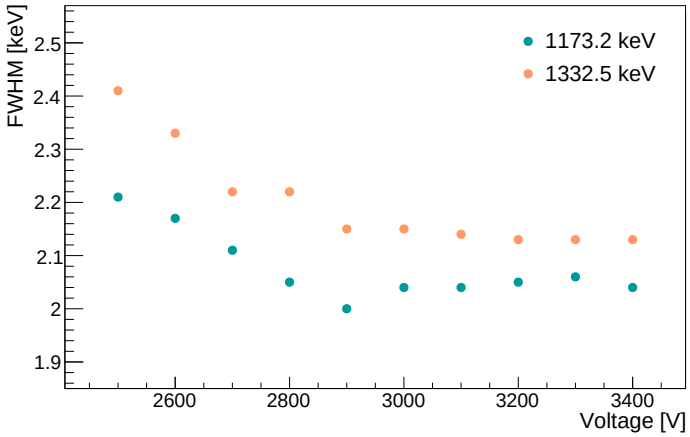

Figure D.2: FWHM measured for the two ^{60}Co lines at several voltages applied to the HPGe detector Coax 5019E.

BIBLIOGRAPHY

[1] **GERDA** Collaboration, M. Agostini et al. Final Results of GERDA on the Search for Neutrinoless Double-beta Decay. *Phys. Rev. Lett.*, 125(25): 252502, 2020, arXiv:2009.06079.

[2] G. R. Araujo, et al. The upgraded low-background germanium counting facility Gator for high-sensitivity Gamma-ray spectrometry. *J. Inst.*, 17 (08):P08010, 2022.

[3] V. H. S. Wu. Low Energy Calibration for GERDA and Characterization of Wavelength-shifters and Reflectors in Liquid Argon for LEGEND-200. Master's thesis, University of Zurich, 2021.

[4] G. R. Araujo, et al. R &D of wavelength-shifting reflectors and characterization of the quantum efficiency of tetraphenyl butadiene and polyethylene naphthalate in liquid argon. *Eur. Phys. J. C*, 82(5):442, 2022, arXiv:2112.06675.

[5] Sebastian Baum, et al. Mineral detection of neutrinos and dark matter. a whitepaper. *Physics of the Dark Universe*, 41:101245, 2023.

[6] Nikita Vladimirov, et al. The benchtop mesospim: a next-generation open-source light-sheet microscope for large cleared samples. *bioRxiv*, 2023.

[7] Raymond Davis. Nobel lecture: A half-century with solar neutrinos. *Rev. Mod. Phys.*, 75:985–994, 2003.

[8] Hitoshi Murayama. The origin of neutrino mass. *Physics World*, 15(5):35, 2002.

[9] E. Fermi. Versuch einer theorie der β-strahlen. i. *Zeitschrift für Physik*, 88(3):161–177, 1934.

[10] C. L. Cowan, et al. Detection of the free neutrino: a confirmation. *Science*, 124(3212):103–104, 1956.

[11] John N. Bahcall and Raymond Davis. Solar neutrinos: A scientific puzzle. *Science*, 191(4224):264–267, 1976.

[12] B. Pontecorvo. Inverse beta processes and nonconservation of lepton charge. *Zh. Eksp. Teor. Fiz.*, 34:247, 1957.

[13] B. Pontecorvo. Neutrino Experiments and the Problem of Conservation of Leptonic Charge. *Zh. Eksp. Teor. Fiz.*, 53:1717–1725, 1967.

[14] Samoil M. Bilenky. Bruno pontecorvo and neutrino oscillations. *Advances in High Energy Physics*, 2013.

[15] **Super-Kamiokande Collaboration** Collaboration, Y. Fukuda, et al. Evidence for oscillation of atmospheric neutrinos. *Phys. Rev. Lett.*, 81: 1562–1567, 1998.

[16] **SNO Collaboration** Collaboration, Q. R. Ahmad, et al. Direct evidence for neutrino flavor transformation from neutral-current interactions in the sudbury neutrino observatory. *Phys. Rev. Lett.*, 89:011301, 2002.

[17] Quote by I. Rabi. Retrieved in May 2023.

[18] Science by degrees. Standard Model of particles. Retrieved in May 2023.

[19] **Particle Data Group** Collaboration, R. L. Workman et al. Review of Particle Physics. *PTEP*, 2022:083C01, 2022.

[20] Boris Kayser. Neutrino physics. *eConf*, C040802:L004, 2004, arXiv:hep-ph/0506165.

[21] Chirality vs Helicity Chart. Retrieved in May 2023.

[22] Chirality, helicity, and the higgs. Retrieved in May 2023.

[23] M. Goldhaber, L. Grodzins, and A. W. Sunyar. Helicity of neutrinos. *Phys. Rev.*, 109:1015–1017, 1958.

[24] C. S. Wu, et al. Experimental test of parity conservation in beta decay. *Phys. Rev.*, 105:1413–1415, 1957.

[25] S. M. Bilenky and C. Giunti. Neutrinoless Double-Beta Decay: a Probe of Physics Beyond the Standard Model. *Int. J. Mod. Phys. A*, 30(04n05): 1530001, 2015, arXiv:1411.4791.

[26] Dr. Steve Boyd. Warwick Week - Neutrino Lectures. Lecture 2 - Neutrino mass and mass measurement (retrieved in May 2023).

[27] Stefano Dell'Oro, et al. Neutrinoless double beta decay: 2015 review. *Advances in High Energy Physics*, 2016:2162659, 2016.

[28] Frank F Deppisch. *A Modern Introduction to Neutrino Physics*. 2053-2571. Morgan Claypool Publishers, 2019. ISBN 978-1-64327-680-9.

[29] **APPEC Committee** Collaboration, A. Giuliani, et al. Double Beta Decay APPEC Committee Report. 2019, arXiv:1910.04688.

[30] **GERDA** Collaboration, M. Agostini, et al. Search for exotic physics in double- decays with GERDA Phase II. *J. of Cosmology and Astroparticle Physics*, (12):012, 2022.

[31] G. Benato. *Data Reconstruction and Analysis for the GERDA experiment*. PhD thesis, University of Zurich, 2015.

[32] Michael Duerr, Manfred Lindner, and Alexander Merle. On the quantitative impact of the schechter-valle theorem. *Journal of High Energy Physics*, 2011(6):91, 2011.

[33] Nu-fit neutrino oscillation parameters. Retrieved in July 2023.

[34] Giovanni Benato. Effective majorana mass and neutrinoless double beta decay. *Eur. Phys. J. C*, 75(11):563, 2015.

[35] S. R. Elliott, A. A. Hahn, and M. K. Moe. Direct evidence for two-neutrino double-beta decay in ^{82}Se. *Phys. Rev. Lett.*, 59:2020–2023, 1987.

[36] Michelle J. Dolinski, Alan W. P. Poon, and Werner Rodejohann. Neutrinoless Double-Beta Decay: Status and Prospects. *Ann. Rev. Nucl. Part. Sci.*, 69:219–251, 2019, arXiv:1902.04097.

[37] H. Gómez. Latest results of nemo-3 experiment and present status of supernemo. *Nuclear and Particle Physics Proceedings*, 273-275:1765–1770, 2016. 37th International Conference on High Energy Physics (ICHEP).

[38] Yoann Kermaidic for the GERDA MAJORANA and LEGEND collaborations. GERDA, MAJORANA and LEGEND towards a background-free ton-scale Ge-76 experiment, 2020. XXIX International Conference on Neutrino Physics.

[39] **LEGEND** Collaboration, N. Abgrall et al. The Large Enriched Germanium Experiment for Neutrinoless $\beta\beta$ Decay: LEGEND-1000 Preconceptual Design Report. 2021, arXiv:2107.11462.

[40] Matteo Agostini, et al. Toward the discovery of matter creation with neutrinoless double-beta decay. 2022, arXiv:2202.01787.

[41] **KamLAND-Zen Collaboration** Collaboration, S. Abe, et al. Search for the majorana nature of neutrinos in the inverted mass ordering region with kamland-zen. *Phys. Rev. Lett.*, 130:051801, 2023.

[42] D. Q. Adams, et al. Search for majorana neutrinos exploiting millikelvin cryogenics with cuore. *Nature*, 604(7904):53–58, 2022.

[43] D.R. Artusa, et al. Enriched TeO2 bolometers with active particle discrimination: Towards the CUPID experiment. *Phys. Lett. B*, 767:321 – 329, 2017.

[44] S. Andringa et al. (SNO+ Collaboration). Current status and future prospects of the SNO+ Experiment. *Advances in High Energy Physics, article ID 6194250*, 2016. DOI:10.1155/2016/6194250.

[45] **nEXO** Collaboration, G. Adhikari et al. nEXO: neutrinoless double beta decay search beyond 10^{28} year half-life sensitivity. *J. Phys. G*, 49(1): 015104, 2022, arXiv:2106.16243.

[46] **KamLAND-Zen** Collaboration, Koichi Ichimura. Recent results from KamLAND-Zen. *PoS*, NOW2022:067, 2023.

[47] Ruben Saakyan. Two-neutrino double-beta decay. *Annual Review of Nuclear and Particle Science*, 63(1):503–529, 2013.

[48] Jouni Suhonen and Joel Kostensalo. Double beta decay and the axial strength. *Frontiers in Physics*, 7, 2019.

[49] Markus Kortelainen and Jouni Suhonen. Nuclear muon capture as a powerful probe of double-beta decays in light nuclei. *J. of Phys. G: Nuclear and Particle Physics*, 30(12):2003, 2004.

[50] Jonathan Engel and Javier Menéndez. Status and future of nuclear matrix elements for neutrinoless double-beta decay: a review. *Reports on Progress in Physics*, 80(4):046301, 2017.

[51] Frank T. Avignone, Steven R. Elliott, and Jonathan Engel. Double beta decay, majorana neutrinos, and neutrino mass. *Reviews of Modern Physics*, 80(2):481–516, 2008.

[52] Javier Menéndez. On the importance of muon capture for neutrinoless double-beta decay studies. *Monument Collaboration Meeting*, 2023.

[53] A. Belley, et al. Ab initio calculations of neutrinoless $\beta\beta$ decay refine neutrino mass limits. 2023, arXiv:2307.15156.

[54] D.F. Measday. The nuclear physics of muon capture. *Physics Reports*, 354(4):243–409, 2001.

[55] Patricia Gimeno, et al. Ordinary muon capture on 136ba: Comparative study using the shell model and pnqrpa. *Universe*, 9(6), 2023.

[56] D. Zinatulina, et al. Ordinary muon capture studies for the matrix elements in $\beta\beta$ decay. *Phys. Rev. C*, 99:024327, 2019.

[57] S.Y.F. Chu, L.P. Ekstroem, and R.B. Firestone. Nuclear Data Website, Table of Radioactive Isotopes. Accessed in September 2022.

[58] G. Heusser. Low-radioactivity background techniques. *Ann. Rev. Nucl. Part. Sci.*, 45:543–590, 1995.

[59] ASTAR database: Stopping power and range for alpha particles. Accessed in May 2023.

[60] ESTAR database: Stopping power and range for electrons. Accessed in May 2023.

[61] XCOM database: Photon cross sections. Accessed in September 2022.

[62] **LEGEND** Collaboration, N. Abgrall, et al. The Large Enriched Germanium Experiment for Neutrinoless Double Beta Decay (LEGEND). *AIP Conf. Proc.*, 1894(1):020027, 2017, arXiv:1709.01980.

[63] M. Agostini, et al. Modeling of GERDA Phase II data. *Journal of High Energy Physics*, 2020(3):139, 2020.

[64] Yannick Müller. *PhD thesis under preparation*. PhD thesis, University of Zurich, 2023.

[65] **GERDA** Collaboration, M. Agostini et al. Upgrade for Phase II of the Gerda experiment. *Eur. Phys. J. C*, 78(5):388, 2018, arXiv:1711.01452.

[66] **GERDA** Collaboration, K.H. Ackermann et al. The GERDA experiment for the search of $0\nu\beta\beta$ decay in ^{76}Ge. *Eur. Phys. J. C*, 73(3):2330, 2013, arXiv:1212.4067.

[67] Christoph Wiesinger, Luciano Pandola, and Stefan Schönert. Virtual depth by active background suppression: Revisiting the cosmic muon induced background of GERDA Phase II. *Eur. Phys. J. C*, 78(7):597, 2018, arXiv:1802.05040.

[68] **DarkSide** Collaboration, P. Agnes, et al. DarkSide-50 532-day Dark Matter Search with Low-Radioactivity Argon. *Phys. Rev. D*, 98(10): 102006, 2018, arXiv:1802.07198.

[69] **DEAP** Collaboration, P A Amaudruz, et al. Design and construction of the DEAP-3600 dark matter detector. *Astropart. Phys.*, 108:1–23, 2019, arXiv:1712.01982.

[70] **DUNE** Collaboration, B. Abi, et al. The Single-Phase ProtoDUNE Technical Design Report. 2017, arXiv:1706.07081.

[71] Jui-Jen Wang. *MiniCLEAN Dark Matter Experiment*. PhD thesis, The University of New Mexico, 2017.

[72] **MicroBooNE** Collaboration, R. Acciarri, et al. Design and construction of the MicroBooNE detector. *JINST*, 12(02):P02017–P02017, 2017.

[73] **ArDM** Collaboration, J. Calvo, et al. Commissioning of the ArDM experiment at the Canfranc underground laboratory: first steps towards a tonne-scale liquid argon time projection chamber for dark matter searches. *J. Cosmol. Astropart. Phys.*, 2017(03):003–003, 2017.

[74] S. Amerio, et al. Design, construction and tests of the icarus t600 detector. *Nucl. Inst. and Meth. in Phys. Research*, 527(3):329–410, 2004.

[75] **MicroBooNE** Collaboration, R. Acciarri et al. A Proposal for a Three Detector Short-Baseline Neutrino Oscillation Program in the Fermilab Booster Neutrino Beam. 2015, arXiv:1503.01520.

[76] D. Akimov et al. Observation of coherent elastic neutrino-nucleus scattering. *Science 03 Aug*, 2017. DOI: 10.1126/science.aao0990 .

[77] T. Doke, et al. Absolute scintillation yields in liquid argon and xenon for various particles. *Jpn. J. Appl. Phys.*, 41(Part 1, No. 3A):1538–1545, 2002.

[78] M. Agostini, et al. Limit on the radiative neutrinoless double electron capture of ^{36} 36 ar from GERDA phase i. *The European Physical Journal C*, 76(12), 2016.

[79] Liquid argon properties table. Accessed in May 2023.

[80] P. Benetti et al. Measurement of the specific activity of Ar-39 in natural argon. *Nucl. Inst. and Meth. in Phys. Research 574 (1) 83-88*, 2007. arXiv:astro-ph/060313.

[81] **DEAP** Collaboration, R. Ajaj, et al. Electromagnetic Backgrounds and Potassium-42 Activity in the DEAP-3600 Dark Matter Detector. *Phys. Rev. D*, 100:072009, 2019, arXiv:1905.05811.

[82] P. Adhikari, et al. Precision measurement of the specific activity of ar-39 in atmospheric argon with the deap-3600 detector. *The European Physical Journal C*, 83(7):642, 2023.

[83] J. Xu et al. A study of the residual 39Ar content in argon from underground sources. *Astroparticle Physics, Volume 66, p. 53-60*, 2015. arXiv:1204.6011.

[84] **WArP** Collaboration, R. Acciarri et al. Effects of Nitrogen contamination in liquid Argon. *JINST*, 5:P06003, 2010, arXiv:0804.1217.

[85] M. Hofmann, et al. Ion-beam excitation of liquid argon. *Eur. Phys. J. C*, 73(10):2618, 2013, arXiv:1511.07721.

[86] Saint-Gobain BCF-91A datasheet.

[87] Mario Schwarz, et al. Liquid Argon Instrumentation and Monitoring in LEGEND-200. *EPJ Web Conf.*, 253, 2021.

[88] G. R. Araujo, T. Pollmann, and A. Ulrich. Photoluminescence response of acrylic (PMMA) and polytetrafluoroethylene (PTFE) to ultraviolet light. *Eur. Phys. J. C*, 79(8):653, 2019, arXiv:1905.03044.

[89] A. Neumeier, et al. Attenuation of vacuum ultraviolet light in pure and xenon-doped liquid argon —an approach to an assignment of the near-infrared emission from the mixture. *EPL*, 111(1):12001, 2015.

[90] R. Acciarri et al. Effects of Nitrogen and Oxygen contamination in liquid Argon. *Nucl. Phys. B Proc. Suppl.*, 197:70–73, 2009.

[91] **ICARUS** Collaboration, B. Ali-Mohammadzadeh et al. Design and implementation of the new scintillation light detection system of ICARUS T600. *JINST*, 15(10):T10007, 2020, arXiv:2006.05261.

[92] M. Kuźniak, et al. Polyethylene naphthalate film as a wavelength shifter in liquid argon detectors. *Eur. Phys. J.*, C79(4):291, 2019, arXiv:1806.04020.

[93] Okimichi Yano and Hitoshi Yamaoka. Cryogenic properties of polymers. *Progress in Polymer Science*, 20(4):585–613, 1995.

[94] Y. Efremenko, et al. Use of poly(ethylene naphthalate) as a self-vetoing structural material. *JINST*, 14(07):P07006–P07006, 2019.

[95] J. Asaadi, et al. Emanation and bulk fluorescence in liquid argon from tetraphenyl butadiene wavelength shifting coatings. *JINST*, 14(2):P02021, 2019, arXiv:1804.00011.

[96] C. Benson, G. O. Gann, and V. Gehman. Measurements of the intrinsic quantum efficiency and absorption length of tetraphenyl butadiene thin films in the vacuum ultraviolet regime. *Eur. Phys. J.*, C78(4):329, 2018, arXiv:1709.05002.

[97] C. H. Lally, et al. UV quantum efficiencies of organic fluors. *Nucl. Instr. Meth. in Phys. B*, 117(4):421 – 427, 1996.

[98] R. Francini et al. VUV-Vis optical characterization of Tetraphenyl-butadiene films on glass and specular reflector substrates from room to liquid Argon temperature. *JINST*, 2013.

[99] C. S. Chiu, et al. Environmental effects on TPB wavelength-shifting coatings. *JINST*, 7(07):P07007–P07007, 2012, arXiv:1204.5762.

[100] Stacie E. Wallace-Williams, et al. Excited state spectra and dynamics of phenyl-substituted butadienes. *J. Phys. Chem, 98, 1, 60–67*, 1994.

[101] Joshua R. Graybill, et al. Extreme ultraviolet photon conversion efficiency of tetraphenyl butadiene. *Appl. Opt.*, 59(4):1217–1224, 2020.

[102] J.M. Corning, et al. Temperature-dependent fluorescence emission spectra of acrylic (PMMA) and tetraphenyl butadiene (TPB) excited with UV light. *JINST*, 15(03):C03046–C03046, 2020.

[103] Y. Abraham, et al. Wavelength-shifting performance of polyethylene naphthalate films in a liquid argon environment. *JINST*, 16(07):P07017, 2021.

[104] M. G. Boulay, et al. Direct comparison of PEN and TPB wavelength shifters in a liquid argon detector. 2021, arXiv:2106.15506.

[105] L. Baudis, et al. Enhancement of light yield and stability of radio-pure tetraphenyl-butadiene based coatings for VUV light detection in cryogenic environments. *JINST*, 10(09):P09009–P09009, 2015.

[106] J. R. Lacowicz. *Principles of Fluorescence Spectroscopy*. 3. edition, Springer, 2006.

[107] Marcin Kuźniak and Andrzej M. Szelc. Wavelength shifters for applications in liquid argon detectors. *Instruments*, 5(1), 2021.

[108] L. Pertoldi. *Search for new physics with two-neutrino double-beta decay in GERDA data*. PhD thesis, Universitá degli Studi di Padova, 2021.

[109] Christoph Wiesinger. *No neutrinos not found First exploration of neutrinoless double beta decay half-lives beyond 1026 years*. PhD thesis, Nov 2020.

[110] L. Pertoldi. *From the public github repository of his thesis: "Search for new physics with two-neutrino double-beta decay in GERDA data"*. PhD thesis, 2021.

[111] LEGEND website. Accessed in May 2023.

[112] **GERDA** Collaboration, M. Agostini, et al. Pulse shape analysis in Gerda Phase II. *Eur. Phys. J. C*, 82(4):284, 2022, arXiv:2202.13355.

[113] **GERDA** Collaboration, M. Agostini, et al. Characterization of inverted coaxial ^{76}Ge detectors in GERDA for future double-beta decay experiments. *Eur. Phys. J. C*, 81(6), 2021, arXiv:2103.15111.

[114] M. Agostini, et al. GELATIO: A General framework for modular digital analysis of high-purity Ge detector signals. *JINST*, 6:P08013, 2011, arXiv:1106.1780.

[115] **GERDA** Collaboration, M. Agostini et al. Background-free search for neutrinoless double-beta decay of Ge-76 with GERDA. *Nature*, 544:47, 2017, arXiv:1703.00570.

[116] **GERDA** Collaboration, M. Agostini, et al. Probing Majorana neutrinos with double-beta decay. *Science*, 365:1445, 2019, arXiv:1909.02726.

[117] B. Majorovits et al. PEN as self-vetoing structural material. *AIP Conference Proceedings 1921, 090001 (2018)*.

[118] **GERDA** Collaboration, Agostini, et al. Liquid argon light collection and veto modeling in GERDA Phase II. *Eur. Phys. J. C*, 83(319), 2023, arXiv:2212.02856.

[119] Donaldson website. Accessed in May 2023.

[120] G. R. Araujo. Wavelength shifting and photon detection of scintillation light from liquid argon. Master's thesis, Tech. Univ. Munich, 2019.

[121] Goodfellow website. Accessed in May 2023.

[122] Data sheet of the Hamamatsu R955 PMT.

[123] D. Arun Kumar et al. Growth and characterization of organic scintillation single crystal 1,1,4,4-tetraphenyl-1,3-butadiene (tpb) using vertical bridgman technique. *Optical Materials*, 109:110286, 2020.

[124] A. Neumeier, et al. Attenuation of vacuum ultraviolet light in liquid argon. *Eur. Phys. J.*, C72:2190, 2012, arXiv:1511.07724.

[125] A. Lubashevskiy et al. Mitigation of^{42} Ar/^{42} K background for the GERDA Phase II experiment. *Eur. Phys. J. C*, 78(1):15, 2018, arXiv:1708.00226.

[126] F Edzards. The future of neutrinoless double beta decay searches with germanium detectors. *J. of Phys.: Conference Series*, 1690(1):012180, 2020.

[127] Patrick Krause. *PhD thesis under preparation*. PhD thesis, Technical University of Munich, 2023.

[128] B. Broerman, et al. Application of the TPB Wavelength Shifter to the DEAP-3600 Spherical Acrylic Vessel Inner Surface . *JINST*, 12:04017, 2017, arXiv:1704.01882.

[129] T. Pollmann. *Alpha backgrounds in the DEAP Dark Matter search experiment*. PhD thesis, Queen's University, 2012.

[130] M. Walter. *Background Reduction Techniques for the Gerda Experiment*. PhD thesis, Universität Zürich, 2015.

[131] Solange C. Amouroux, Dirk Heider, and John W. Gillespie. Characterization of membranes used in pressure driven composite processing. *Composites Part A: Appl. Science and Manufacturing*, 41(2):207–214, 2010.

[132] Alessia Bacchi, et al. Raman investigation of polymorphism in 1,1,4,4-tetraphenyl-butadiene. *J. of Raman Spectroscopy*, 44(6):905–908, 2013.

[133] A. Bacchi, et al. Exploration of the polymorph landscape for 1,1,4,4-tetraphenyl-1,3-butadiene. *CrystEngComm*, 16:8205–8213, 2014.

[134] A. Girlando et. al. Spectroscopic and structural characterization of two polymorphs of 1,1,4,4-tetraphenyl-1,3-butadiene. *Cryst. Growth Des.*, 10, 2010.

[135] Yikui Fan, et al. Effects of alpha particle and gamma irradiation on the 1,1,4,4-tetraphenyl-1,3-butadiene wavelength shifter. *Radiation Phys. and Chem.*, 176:109058, 2020.

[136] D. Stolp, et al. An estimation of photon scattering length in tetraphenyl-butadiene. *JINST*, 11(03):C03025–C03025, 2016.

[137] Andreas Leonhardt. Characterization of Wavelength Shifters for Rare Event Search Experiments with a VUV Spectrofluorometer. Master's thesis, TUM, 2021.

[138] M. Babicz, et al. A measurement of the group velocity of scintillation light in liquid argon. *JINST*, 15(09):P09009–P09009, 2020.

[139] Nina Hong, Ron A. Synowicki, and James N. Hilfiker. Mueller matrix characterization of flexible plastic substrates. *Appl. Surface Science*, 421: 518–528, 2017. 7th Inter. Conference on Spectroscopic Ellipsometry.

[140] Data sheet of the Metal Velvet™ foil from Acktar.

[141] Martin Janecek. Reflectivity spectra for commonly used reflectors. *IEEE Transactions on Nuclear Science*, 59(3):490–497, 2012.

[142] N. McFadden, et al. Large-scale, precision xenon doping of liquid argon. *Nucl. Inst. and Meth. in Phys. Research*, 1011:165575, 2021.

[143] **n_TOF** Collaboration, P. Žugec et al. Pulse processing routines for neutron time-of-flight data. *Nucl. Instrum. Meth. A*, 812:134–144, 2016, arXiv:1601.04512.

[144] **GEANT4** Collaboration, S. Agostinelli et al. GEANT4–a simulation toolkit. *Nucl. Instrum. Meth. A*, 506:250–303, 2003.

[145] **ArDM** Collaboration, J. Calvo et al. Measurement of the attenuation length of argon scintillation light in the ArDM LAr TPC. *Astropart. Phys.*, 97:186–196, 2018, arXiv:1611.02481.

[146] N. Ishida, et al. Attenuation length measurements of scintillation light in liquid rare gases and their mixtures using an improved reflection suppresser. *Nucl. Instrum. Meth. A*, 384(2):380–386, 1997.

[147] Data sheet for the R11065 bilenkyed PMT provided by Hamamatsu.

[148] H. H. Li. Refractive index of alkaline earth halides and its wavelength and temperature derivatives. *J. of Phys. and Chem. Reference Data*, 9(1): 161–290, 1980.

[149] P. Laporte, et al. Vacuum-ultraviolet refractive index of lif and mgf 2 in the temperature range 80–300 k. *J. of the Opt. Soc. of America*, 73: 1062–1069, 1983.

[150] Birgit Zatschler. *Attenuation of the scintillation light in liquid argon and investigation of the double beta decay of ^{76}Ge into excited states of ^{76}Se in the GERDA experiment*. PhD thesis, Dresden, Tech. U., 2020.

[151] D. et al. Mary. Understanding optical emissions from electrically stressed insulating polymers: Electroluminescence in poly(ethylene terephthalate) and poly(ethylene 2,6-naphthalate) films. *J. Phys. D: Appl. Phys.*, 30:171, 1999.

[152] Xiaoning Zhang, et al. Complex refractive indices measurements of polymers in visible and near-infrared bands. *Appl. Opt.*, 59(8):2337–2344, 2020.

[153] F. Neves, et al. Measurement of the absolute reflectance of polytetrafluoroethylene (PTFE) immersed in liquid xenon. *JINST*, 12(01):P01017, 2017, arXiv:1612.07965.

[154] Min K. Yang et al. Optical properties of Teflon® AF amorphous fluoropolymers. *J. of Micro/Nanolithography, MEMS, and MOEMS*, 7(3), 2008.

[155] MIDAS DAQ Wiki. Accessed in August 2023.

[156] A. Antognini, et al. Measurement of the quadrupole moment of 185-Re and 187-Re from the hyperfine structure of muonic X rays. *Physical Review C*, 101(5), 2020.

[157] Mario Schwarz. *Work under preparation*. PhD thesis, Technical University of Munich, 2023.

[158] Elisabetta Bossio. *Beyond the Standard Model physics searches with double-beta decays*. PhD thesis, Technical University of Munich, 2022.

[159] G. R. Araujo, et al. The monument experiment, a conceptual paper. *Publication under prepararation*, 2023.

[160] Rene Brun and Fons Rademakers. ROOT software V.06.

[161] Joint Institute for Nuclear Research. Muonic X-ray Catalogue. Accessed in September 2022.

[162] National Nuclear Data Center (NNDC) at Brookhaven National Laboratory. Nudat 3.0 Website. Accessed in September 2022.

[163] **GERDA** Collaboration, M. Agostini et al. Calibration of the Gerda experiment. *Eur. Phys. J. C*, 81(8):682, 2021, arXiv:2103.13777.

[164] **Planck** Collaboration, N. Aghanim et al. Planck 2018 results. VI. Cosmological parameters. *Astron. Astrophys.*, 641:A6, 2020, arXiv:1807.06209. [Erratum: Astron.Astrophys. 652, C4 (2021)].

[165] The Borexino collaboration. Comprehensive measurement of pp-chain solar neutrinos. *Nature volume 562, pages 505-510*, 2018. doi:10.1038/s41586-018-0624-y.

[166] **COHERENT** Collaboration, D. Akimov et al. First Measurement of Coherent Elastic Neutrino-Nucleus Scattering on Argon. *Phys. Rev. Lett.*, 126(1):012002, 2021, arXiv:2003.10630.

[167] K. Boudjemline et al. The calibration of the Sudbury Neutrino Observatory using uniformly distributed radioactive sources. *Nucl. Inst. Meth. A620:171-181*, 2010. arXiv:0912.2991.

[168] **CRESST** Collaboration, G. Angloher et al. Results on sub-GeV Dark Matter from a 10 eV Threshold CRESST-III Silicon Detector. 2022, arXiv:2212.12513.

[169] **CDMS** Collaboration, R. Agnese et al. Nuclear-Recoil Energy Scale in CDMS II Silicon Dark-Matter Detectors. *Nucl. Instrum. Meth. A*, 905: 71–81, 2018, arXiv:1803.02903.

[170] **DEAP** Collaboration, R. Ajaj, et al. Search for dark matter with a 231-day exposure of liquid argon using DEAP-3600 at SNOLAB. *Phys. Rev. D*, 100(2):022004, 2019, arXiv:1902.04048.

[171] **XENON** Collaboration, E. Aprile et al. Projected WIMP sensitivity of the XENONnT dark matter experiment. *JCAP*, 11:031, 2020, arXiv:2007.08796.

[172] **DarkSide-20k** Collaboration, C. E. Aalseth, et al. DarkSide-20k: A 20 tonne two-phase LAr TPC for direct dark matter detection at LNGS. *Eur. Phys. J. Plus*, 133:131, 2018, arXiv:1707.08145.

[173] **DARWIN** Collaboration, J. Aalbers, et al. DARWIN: towards the ultimate dark matter detector. *JCAP*, 1611:017, 2016, arXiv:1606.07001.

[174] Bernadette K. Cogswell, Apurva Goel, and Patrick Huber. Passive Low-Energy Nuclear-Recoil Detection with Color Centers. *Phys. Rev. Applied*, 16(6):064060, 2021, arXiv:2104.13926.

[175] K. Alfonso, et al. Passive low energy nuclear recoil detection with color centers – PALEOCCENE. In *2022 Snowmass Summer Study*, 3 2022.

[176] Ranny Budnik, et al. Direct detection of light dark matter and solar neutrinos via color center production in crystals. *Phys. Lett. B*, 782: 242–250, 2018.

[177] Marc Schumann. Direct Detection of WIMP Dark Matter: Concepts and Status. *J. Phys. G*, 46(10):103003, 2019, arXiv:1903.03026.

[178] **XENON** Collaboration, E. Aprile, et al. Physics reach of the XENON1T dark matter experiment. *JCAP*, 1604(04):027, 2016, arXiv:1512.07501.

[179] The EXCESS Workshop, 2021.

[180] Surjeet Rajendran, et al. A method for directional detection of dark matter using spectroscopy of crystal defects. *Phys. Rev. D*, 96:035009, 2017.

[181] Maitland Bowen and Patrick Huber. Reactor neutrino applications and coherent elastic neutrino nucleus scattering. *Phys. Rev. D*, 102(5):053008, 2020, arXiv:2005.10907.

[182] Adam Bernstein, et al. Colloquium: Neutrino detectors as tools for nuclear security. *Rev. Mod. Phys.*, 92:011003, 2020.

[183] C. Awe et al. High Energy Physics Opportunities Using Reactor Antineutrinos. 2022, arXiv:2203.07214.

[184] **COHERENT Collaboration** Collaboration, D. Akimov, et al. Simulating the neutrino flux from the spallation neutron source for the coherent experiment. *Phys. Rev. D*, 106:032003, 2022.

[185] **CONUS** Collaboration, H. Bonet, et al. Constraints on Elastic Neutrino Nucleus Scattering in the Fully Coherent Regime from the CONUS Experiment. *Phys. Rev. Lett.*, 126(4):041804, 2021, arXiv:2011.00210.

[186] **CONNIE** Collaboration, Alexis Aguilar-Arevalo, et al. Exploring low-energy neutrino physics with the Coherent Neutrino Nucleus Interaction Experiment. *Phys. Rev. D*, 100(9):092005, 2019, arXiv:1906.02200.

[187] **NUCLEUS** Collaboration, J. Rothe, et al. NUCLEUS: Exploring Coherent Neutrino-Nucleus Scattering with Cryogenic Detectors. *J. Low Temp. Phys.*, 199(1-2):433–440, 2019.

[188] M. Abdullah et al. Coherent elastic neutrino-nucleus scattering: Terrestrial and astrophysical applications. 2022, arXiv:2203.07361.

[189] G. Knoll. *Radiation Detection and Measurement*. John Wiley and Sons, New York, 2000.

[190] Fernando Abdala et al. *Enciclopedia of Geology*. 2. edition, Academic Press, 2021.

[191] D. P. Snowden-Ifft, E. S. Freeman, and P. B. Price. Limits on dark matter using ancient mica. *Phys. Rev. Lett.*, 74:4133–4136, 1995.

[192] Sebastian Baum, et al. Searching for Dark Matter with Paleo-Detectors. *Phys. Lett. B*, 803:135325, 2020, arXiv:1806.05991.

[193] **PALEOCCENE** Collaboration, Sebastian Baum, et al. Mineral Detection of Neutrinos and Dark Matter. A Whitepaper. *Accepted for publication by Physics of the Dark Universe*, 2023, arXiv:2301.07118.

[194] Richard J. D. Tilley. *Point Defects, Defects in Solids*. John Wiley Sons, Ltd, 2008. 1-44 pp. ISBN 9780470380758.

[195] Michael Moll. *Radiation Damage in Silicon Particle Detectors*. PhD thesis, Hamburg University, 1999.

[196] Nicholas Nunn, et al. Beauty beyond the Eye: Color Centers in Diamond Particles for Imaging and Quantum Sensing Applications. *Reviews and Advances in Chemistry*, 12(1):1–21, 2022.

[197] K. Masuda, et al. Novel techniques for high precision refractive index measurements, and application to assessing neutron damage and dose in crystals. *Nucl. Inst. and Meth. in Phys. Research*, 784:198–201,

2015. Symposium on Radiation Measurements and Applications 2014 (SORMA XV).

[198] Yossi Mosbacher, et al. Wide band spectroscopic response of monocrystallines to low dose neutron and gamma radiation. 2019.

[199] Zhiping Ju, et al. Preparations and applications of single color centers in diamond. *Advances in Physics: X*, 6(1):1858721, 2021.

[200] Maabur Sow, et al. High-throughput nitrogen-vacancy center imaging for nanodiamond photophysical characterization and ph nanosensing. *Nanoscale*, 12:21821–21831, 2020.

[201] F.F. Voigt, et al. The mesospim initiative: open-source light-sheet microscopes for imaging cleared tissue. *Nat Methods*, 16:1105–1108, 2019.

[202] The mesoSPIM initiative website. Retrieved in August 2023.

[203] Crystran website. Retrieved in July 2023.

[204] Attenuation coefficients and scattering table. Retrieved in March 2023.

[205] United Crystals website. Retrieved in July 2023.

[206] Valentino Aerne. Thesis under preparation. Master's thesis, University of Zurich, 2023.

[207] Z. Siti Rozaila, Nicolas Riesen, and Hans Riesen. Luminescence and photoionization of X-ray generated Sm2+ in coprecipitated CaF2 nanocrystals. *Dalton Trans.*, 50:16205–16213, 2021.

[208] H. Bill and G. Calas. Color centers, associated rare-earth ions and the origin of coloration in natural fluorites. *Physics and Chemistry of Minerals*, 3(2):117–131, 1978.

[209] Andy Edgar, et al. Optical properties of divalent samarium-doped fluorochlorozirconate glasses and glass ceramics. *Optical Materials*, 31: 1459–1466, 2009.

[210] **XENON** Collaboration, E. Aprile et al. Material radiopurity control in the XENONnT experiment. *Eur. Phys. J. C*, 82(7):599, 2022, arXiv:2112.05629.

[211] **LZ** Collaboration, D. S. Akerib et al. The LUX-ZEPLIN (LZ) radioactivity and cleanliness control programs. *Eur. Phys. J. C*, 80(11):1044, 2020, arXiv:2006.02506.

[212] L Baudis, et al. Gator: a low-background counting facility at the Gran Sasso Underground Laboratory. *JINST*, 6:P08010, 2011, arXiv:1103.2125.

[213] Brianna J. Mount, et al. Black Hills State University Underground Campus. *Applied Radiation and Isotopes*, 126:130–133, 2017. Proceedings of the 7th International Conference on Radionuclide Metrology – Low-Level Radioactivity Measurement Techniques.

[214] P.R. Scovell, et al. Low-background gamma spectroscopy at the Boulby Underground Laboratory. *Astroparticle Physics*, 97:160–173, 2018.

[215] Iulian Bandac. Ultra-Low Background Services in the LSC. Talk a the DS-Mat Parallel meeting at GSSI, 2019. Talk a the DS-Mat Parallel meeting at GSSI.

[216] Yvan Gonin, José Busto, and Jean-Luc Vuilleumier. The "La Vue-des-Alpes" underground laboratory. *Review of Scientific Instruments*, 74(11): 4663–4666, 2003.

[217] N. Ackermann, private communication.

[218] Diego Ramírez García, et al. GeMSE: a low-background facility for gamma-spectrometry at moderate rock overburden. *JINST*, 17:P04005, 2022, arXiv:2202.06540.

[219] D. Ramírez Garcia, private communication.

[220] A. Askin. *Material Screening and Selection for the XENON100 Dark Matter Experiment*. PhD thesis, Universität Zürich, 2012.

[221] H.M. Diab. HPGe Detector Efficiency Curve Evaluation for Low-Level Measurements. *Arab Journal of Nuclear Sciences and Applications*, 48(4): 53–59, 2015.

[222] Christian Hurtgen, Simon Jerome, and Mike Woods. Revisiting currie — how low can you go? *Applied Radiation and Isotopes*, 53(1):45–50, 2000.

[223] T. Mannel. Low-level radioactivity techniques for the neutrino-oscillation experiment double chooz. *Master Thesis, Technical University of Munich*, November, 2013.

[224] **DEAP** Collaboration, P. Adhikari et al. The liquid-argon scintillation pulseshape in DEAP-3600. *Eur. Phys. J. C*, 80(4):303, 2020, arXiv:2001.09855.

[225] Shintaro Minami Shunichi Hayashi Norio Miwa Junichiro Ishizawa, Kichiro Imagawa. Research on application of shape memory polymers to space inflatable systems. *Proceeding of the 7th International Symposium on Artificial Intelligence, Robotics and Automation in Space: i-SAIRAS 2003, NARA, Japan, May 19-23, 2003*.

ACKNOWLEDGMENTS

Growing up in a large family with five siblings and around 30 cousins in my generation, I have been fortunate to be surrounded by a diverse and inspiring group of people who have significantly influenced my history and personality from my earliest memories to this very moment. When I defended my PhD thesis on October 12th, I was surrounded by more than 30 individuals, including my supervisor, work colleagues, and friends. The remarkable parallels between the inspiration I have drawn from my family throughout my life and the invaluable lessons I learned from the exceptional individuals who were part of my PhD journey, contributing to the successful defense on October 12th, left me momentarily speechless. I was unable to fully express my gratitude to those who played pivotal roles in this journey. Fortunately, I now have the opportunity to do so in the last pages of this thesis.

First and foremost, I want to express my profound gratitude to my supervisor, Prof. Laura Baudis. Her commitment to advancing scientific knowledge and courage to embark on complex experimental endeavors in pursuit of solving intriguing physics problems have been a continuous source of inspiration for me. Joining her research group was a huge privilege, and the environment she fostered throughout my PhD journey allowed me to experiment and grow. I feel fortunate to have been part of a group that upholds the highest scientific standards, embraces open-mindedness toward new developments and methods, and secures the necessary funding that experimental physics demands. Her rapid responses, open-door policy, and unwavering support made me feel appreciated and assured that I was never alone in facing any challenges. I am genuinely thankful for that.

Next, I extend my thanks to every member of the Baudis group, both past and present. Each of you has left an impact on this work and has profoundly influenced my professional and scientific development. Thank you for the fruitful discussions, your knowledgeable scientific inputs, and the guidance in asking the right questions and achieving the best work practices. I am also thankful for the enjoyable coffee breaks, shared beers, moments by the lake, and the camaraderie we have shared over the years. Special thanks go to Pin-Jung, Marta, Jose, and Diego, who took the time to proofread this work. A more than special thanks goes to my fellow PhD colleagues Yannick, Ricardo, and Giovanni, who accompanied me for most of this journey, sharing both the celebratory moments and the challenges. Your support, whether in the lab, in understanding complex physics concepts, or simply adding humor to our days, has been motivating and deeply appreciated. You have all become dear friends with whom I look forward to sharing many more moments. While not everyone is mentioned by name, I genuinely thank all the group members – working with you has been an honor and a tremendous growth experience, both as a researcher and as a human being.

As this PhD journey involved even more individuals than the number of my family members, there are still many to acknowledge. I express my gratitude to GERDA and LEGEND members, especially to those with whom I worked as part of the liquid argon projects. I appreciate the indispensable contributions of the UZH mechanical and electronic workshops in bringing many of these projects to fruition. I also thank the PEN-measurements team members, who were part of several of the endeavors presented in this thesis. I must also thank the members of MONUMENT for the fun shifts, enjoyable coffee breaks, and valuable insights on the analysis. Special thanks to Eli and Danyia, who also took the time to proofread the 'monumental' chapter. My gratitude extends to the PALEOCCENE members for their warm welcome and support. Special thanks go to Nikita Vladimirov, whose excitement and expertise were essential in advancing this project at UZH, and to Prof. Patrick Huber, from whom I learned a great deal within the context of PALEOCCENE and who kindly reviewed this thesis. I also appreciate the contributions of master students Vera and Valentino, who willingly joined me in some of these experimental endeavors. Lastly in this group, I am grateful to Alan Poon and his group, who welcomed me in Berkeley for a month at the conclusion of this journey.

Finally, I warmly thank all my European-based friends, as well as my Brazilian-based friends and family, who were essential for me to reach this milestone. Catching up with friends and the warm welcome from my family and friends during my visits to Brazil were always refreshing, reminding me of life's most precious aspects. Last but certainly not least, I am deeply grateful to my beloved and dearest Tobi, who consistently supported me and filled my life with love and joy each day, making the PhD journey a smoother path.